A Microfluidic Platform for High-Precision Growth Quantification of Photosynthetic Microorganisms

Von der Fakultät für Mathematik und Naturwissenschaften der RWTH Aachen University zur Erlangung des akademischen Grades eines Doktors der Ingenieurwissenschaften genehmigte Dissertation

vorgelegt von

Master of Science (M.Sc.)

Lennart Ole Witting

aus Hamburg

Berichter: Prof. Dr. rer. nat. Wolfgang Wiechert
Prof. Dr.-Ing. Lars Blank

Tag der mündlichen Prüfung: 02.06.2026

Diese Dissertation ist auf den Internetseiten der Universitätsbibliothek verfügbar.

Eidesstattliche Erklärung

Ich, Lennart Ole Witting,

erkläre hiermit, dass diese Dissertation und die darin dargelegten Inhalte die eigenen sind und selbstständig, als Ergebnis der eigenen originären Forschung, generiert wurden. Hiermit erkläre ich an Eides statt:

1. Diese Arbeit wurde vollständig in der Phase als Promovierender dieser Fakultät und Universität angefertigt;
2. Sofern irgendein Bestandteil dieser Dissertation zuvor für einen akademischen Abschluss oder eine andere Qualifikation an dieser oder einer anderen Institution verwendet wurde, wurde dies klar angezeigt;
3. Wenn immer andere eigene- oder Veröffentlichungen Dritter herangezogen wurden, wurden diese klar benannt;
4. Wenn aus anderen eigenen- oder Veröffentlichungen Dritter zitiert wurde, wurde stets die Quelle hierfür angegeben. Diese Dissertation ist vollständig meine eigene Arbeit, mit der Ausnahme solcher Zitate;
5. Alle wesentlichen Quellen von Unterstützung wurden benannt;
6. Wenn immer ein Teil dieser Dissertation auf der Zusammenarbeit mit anderen basiert, wurde von mir klar gekennzeichnet, was von anderen und was von mir selbst erarbeitet wurde;
7. Teile dieser Arbeit wurden zuvor veröffentlicht. Eine vollständige Auflistung ist im Anhang unter 'Publications' zu finden.

Düsseldorf, Juni 2026
Lennart Ole Witting

Preface

This thesis contains the results from research I conducted from June 2022 until the end of 2025 at the Institute of Bio- and Geosciences: Biotechnology (IBG-1), that is part of the Forschungszentrum Jülich (FZJ) GmbH in Jülich, Germany. It was carried out specifically within the 'Microscale Bioengineering' research group, which is headed by Dr. Dietrich Kohlheyer. The research was conducted within the broader context of subproject A07 from CRC1535, 'MibiNet: Microbial Networking - From Organelles to Cross-Kingdom Communities', which is based at the Heinrich Heine University Düsseldorf (HHU), but involves cooperation with research institutions such as the FZJ. The overarching goal of this subproject is to study endosymbiosis by isolating and cultivating individual cyanobacteria in picoliters of fluid.

The aim of this thesis was to lay the groundwork for these studies by establishing cyanobacteria cultivation in microfluidic photobioreactors. To achieve this, the existing single-cell cultivation technology was upgraded to include environmental control of the two main parameters that influence photosynthesis: Light intensity (Chapters 3–5) and CO_2 concentration (Chapter 6). Proof-of-concept studies were then conducted on common cyanobacteria model organisms. Furthermore, characteristics of the microfluidic platform were derived by comparing the microfluidic growth data to growth data acquired using a commercial photobioreactor. In the later stages of the project, the developed platform was used in two biological case studies: One related to project A07 (Chapter 7) and the other related to the circadian biology of cyanobacteria (Chapter 8). Finally, future applications of the platform are discussed (Chapter 9).

As a bioengineer by training, I could not have conducted this research project without the help of an interdisciplinary group of researchers. I am sincerely grateful to them.

First, I would like to thank the head of the 'Microscale Bioengineering' research group, Dr. Dietrich Kohlheyer, for the supervision of my research. He was always attentive and supportive. Furthermore, he always made time for me when I needed support, and his critical questions helped me to improve my work. I would also like to thank Prof. Dr. Wolfgang Wiechert, head of IBG-1, and Prof. Dr. Lars Blank for reviewing and supervising my thesis. Johannes Seiffarth (FZJ) and Dr. Katharina Nöh (FZJ) developed the image analysis pipeline, without which none of this work would have been possible. Dr. Marion Eisenhut (BU), Jan Mathis Hofer (HHU), Dennis Hasenklever (HHU), Tim Schulze (BU) and Prof. Dr. Andreas Weber (HHU) worked with me in the context of CRC1535 - MibiNet. I would like to thank them for patiently answering all of my questions about cyanobacteria. Furthermore, I would like to thank Birgit Sute and her supervisor, Dr. Eric von Lieres, for

their collaboration on the CO_2 transport simulations and evaluation of the light cone shape emitted by the ringlight. I am grateful to Martin Beyß (FZJ) for fixing the STL light engine when it stopped working in early 2024.
I would also like to thank Prof. Dr. Ilka Axmann (HHU), Florian Stirba (HHU), and Anika Wiegard (HHU). At a conference in 2024, Ilka approached me about investigating their circadian mutant strains using our microfluidic platform. This collaboration gave my research an unexpected new direction, and the results are summarized in Chapter 8 of this thesis. I would like to thank Daniel Klein for his help in designing and fabricating the various custom-built components mentioned in Chapter 3. Moreover, I would like to thank Nadja Glöck from the Helmholtz Nano Facility for her advice and for fabricating the master molds for PDMS soft lithography. Finally, I would like to thank the Local Organizing Committee of the ISPP2025 for awarding me with the 'ISPP2025 Outstanding Young Student Award' and for allowing me to present my research in the form of an oral presentation at the conference in Qingdao, China.

I would like to thank Agnes Müller-Schröer for taking care of organizing the lab. Thanks to her excellent organizational skills, I never had to worry about missing materials, and everything was always where it should be. I would like to thank Matthias Pesch, Michelle Bund, Nina Dolven and Keitaro Kasahara for accompanying me on my doctoral journey. Your passionate work motivated me to keep going. Even when work in the lab was frustrating, you made sure I had a good day. Matthias Pesch and Benita Lückel often accompanied me on my daily commute from Aachen to the research center, turning even being stuck in traffic into an enjoyable experience. Furthermore, I would like to thank Bastian Wollenhaupt and Matthias Rieb for welcoming me to the group in 2023 and for training me. I would also like to thank Julius Nohr, Anton Stratmann, Arne Kayserling, Lena Friebel, Phillip Ernst and Patrick Gref for being such great colleagues. All the people mentioned above made my time at the research center very enjoyable.

Last but certainly not least, I would like to thank my parents for their constant support and encouragement throughout my academic journey. Without them, I would not have been able to pursue it.

Düsseldorf, Juni 2026
Lennart Ole Witting

Abstract

Conventional methods of quantifying microbial growth, such as optical density or backscatter measurements, cannot distinguish between cell division, growth and changes in morphology. This issue is particularly pertinent for phototrophic microorganisms, given that circadian regulation is known to affect these variables with a 24-hour period. Furthermore, in conventional photobioreactors, self-shading of cells inevitably creates light-intensity gradients, which makes it difficult to determine the amount of light impinging on a cell. This thesis addresses these issues by outlining the development of a novel experimental platform for phototrophic microorganisms. Microfluidic cultivation technology is used to restrict cell growth to monolayers, ensuring constant and accurate illumination. Combined with time-lapse imaging at single-cell resolution, this technology enables the precise quantification of the relationship between light intensity and growth rate. In addition, cell division and cell growth can be distinguished. Furthermore, the experimental platform can test multiple light intensities and CO_2 concentrations simultaneously, thus accelerating the acquisition of growth data.

The first part focuses on setting up the platform and conducting proof-of-concept studies. First, a ringlight connected to an LED was integrated into the microscope's periphery to provide precisely regulated illumination for photosynthesis. The design enables the ringlight to illuminate the cultivation chip either homogeneously or with a spatial light intensity gradient, allowing multiple intensities to be tested simultaneously. Stable long-term cultivation for up to twelve days was demonstrated for cyanobacteria as well as extremophile microalgae. No CO_2 limitations were observed during microfluidic cultivation in ambient air. Moreover, the CO_2 concentration in the monolayer growth chambers can be controlled by flushing defined gas mixtures through a CO_2 control layer. This allows growth under CO_2 limiting conditions to be studied. The method, in combination with Python-based workflows for cell segmentation, allows multiple cyanobacteria strains to be characterized in parallel in just four days.

In the second part, the device is employed in two biological case studies to investigate fundamental properties of cyanobacteria. (i) The characterization of *Synechocystis* mutants lacking the ability to synthesize intracellular glycogen as carbon storage ($\Delta glgC$ mutant) and (ii) the development of a method for reporter-free observation of the circadian rhythm in individual *Synechocystis* cells. In both studies employing single-cell resolution time-lapse imaging revealed effects occurring within individual cells otherwise masked in bulk cultivation, thereby demonstrating the advantages of the device. Finally, the potential applications of the device in future research studies regarding phototrophic microorganisms are discussed.

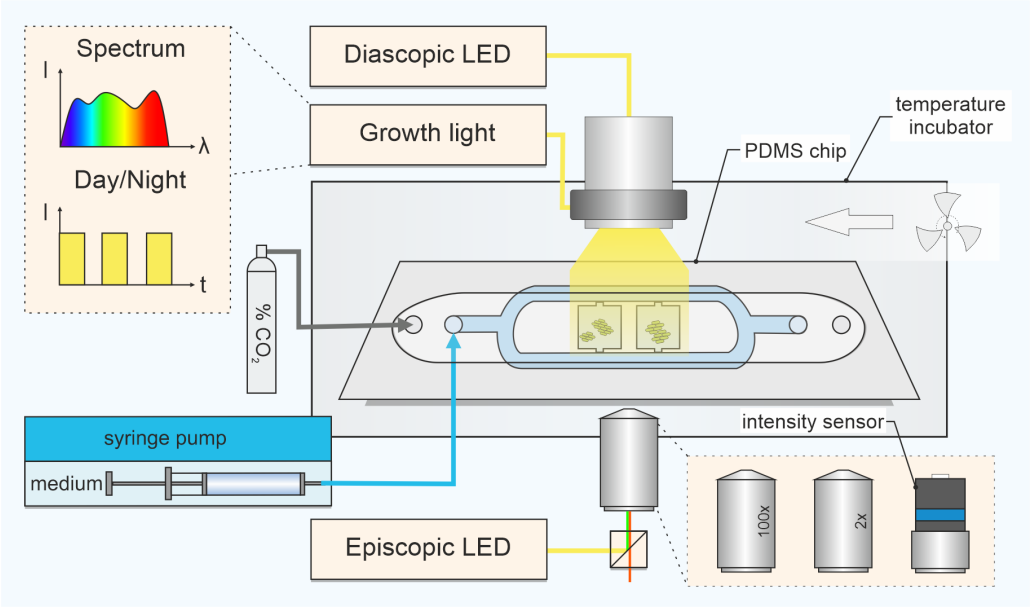


Fig. 1: Overview of the proposed microfluidic cultivation platform to study phototrophic microorganisms. The platform includes a microscope housed in a temperature-controlled incubator. To provide illumination for photosynthesis, a third illumination option was added by equipping the condenser with a ringlight connected to a growth-light source with full spectral control in the PAR. A light-intensity sensor, which is integrated into the microscope's objective revolver, was used to measure the precise light intensity to which the cells were exposed. During imaging, the growth light is turned off, and phase-contrast and fluorescence imaging of the cultivated microorganisms are performed using the diascopic and episcopic light paths. A syringe pump continuously perfuses the growth medium at a constant flow rate. Adding a CO_2 perfusion chamber connected to a premixed CO_2 bottle to the setup enables control of the CO_2 concentration around the microorganisms. The figure was reproduced from Ref. [1] with permission from the Royal Society of Chemistry.

Zusammenfassung

Konventionelle Methoden zur Quantifizierung mikrobiellen Wachstums, wie beispielsweise Messungen der optischen Dichte oder der Rückstreuung, können nicht zwischen Zellteilung, Wachstum und Veränderungen der Morphologie unterscheiden. Dieses Problem ist besonders relevant für phototrophe Mikroorganismen, da bekannt ist, dass die zirkadiane Regulation diese Variablen in einem 24-Stunden-Zyklus beeinflusst. Außerdem führt in herkömmlichen Photobioreaktoren Selbstbeschattung von Zellen zwangsläufig zu Lichtintensitätsgradienten, weshalb es schwierig ist, die auf eine Zelle einwirkende Lichtmenge genau zu bestimmen. Diese Arbeit befasst sich mit diesem Problem, indem sie die Entwicklung einer neuartigen Versuchsplattform für phototrophe Mikroorganismen beschreibt. Die mikrofluidische Kultivierungstechnologie gewährleistet eine konstante, präzise gesteuerte Beleuchtung, indem sie das Zellwachstum auf Einzelzelllagen beschränkt. In Kombination mit Zeitrafferaufnahmen mit Einzelzellauflösung ermöglicht diese Technologie eine genaue Quantifizierung des Zusammenhangs zwischen Lichtintensität und Wachstumsrate sowie die Unterscheidung zwischen Zellteilung und Zellwachstum. Darüber hinaus kann die experimentelle Plattform mehrere Lichtintensitäten und CO_2-Konzentrationen gleichzeitig testen und so die Erfassung von Wachstumsdaten beschleunigen.

Der erste Teil konzentriert sich auf die Einrichtung der Plattform und beinhaltet Proof-of-Concept-Studien. Zunächst wurde ein mit einer LED verbundenes Ringlicht in die Peripherie des Mikroskops integriert, um eine präzise regulierte Beleuchtung für die Photosynthese zu gewährleisten. Das Design ermöglicht es, das Ringlicht so zu konfigurieren, dass der Kultivierungs-Chip entweder homogen oder mit einem räumlichen Lichtintensitätsgradienten beleuchtet werden kann. Dadurch können mehrere Intensitäten gleichzeitig getestet werden. Eine stabile Langzeitkultivierung von bis zu zwölf Tagen wurde sowohl für Cyanobakterien als auch für extremophile Mikroalgen demonstriert. Während der mikrofluidischen Kultivierung in Umgebungsluft wurden keine CO_2-Limitierungen beobachtet. Die CO_2-Konzentration in den Wachstumskammern kann gesteuert werden, indem definierte Gasgemische durch eine CO_2-Kontrollschicht durchgespült werden. Dies ermöglicht die Untersuchung des Wachstums unter CO_2-limitierenden Bedingungen. In Kombination mit Python-basierten Workflows zur Zellsegmentierung ermöglicht diese Methode die parallele Charakterisierung mehrerer Cyanobakterienstämme in nur vier Tagen.

Im zweiten Teil wird die experimentelle Plattform in zwei biologischen Fallstudien eingesetzt, um grundlegende Eigenschaften von Cyanobakterien zu untersuchen. (i) Die Charakterisierung von *Synechocystis*-Mutanten, denen die Fähigkeit zur Synthese von intrazellulärem Glykogen als Kohlenstoffspeicher fehlt (Δ*glgC*-Mutante) und (ii) die Entwicklung

einer Methode zur reporterfreien Beobachtung des zirkadianen Rhythmus in einzelnen *Synechocystis*-Zellen. In beiden Studien konnten mittels Zeitrafferaufnahmen mit Einzelzellauflösung Effekte aufgedeckt werden, die in einzelnen Zellen auftraten und unter Standardkultivierungsbedingungen nicht erkennbar gewesen wären. Dadurch wurden die Vorteile des Geräts demonstriert. Abschließend wurden die potenziellen Anwendungen des Geräts in zukünftigen Studien zu phototrophen Mikroorganismen diskutiert.

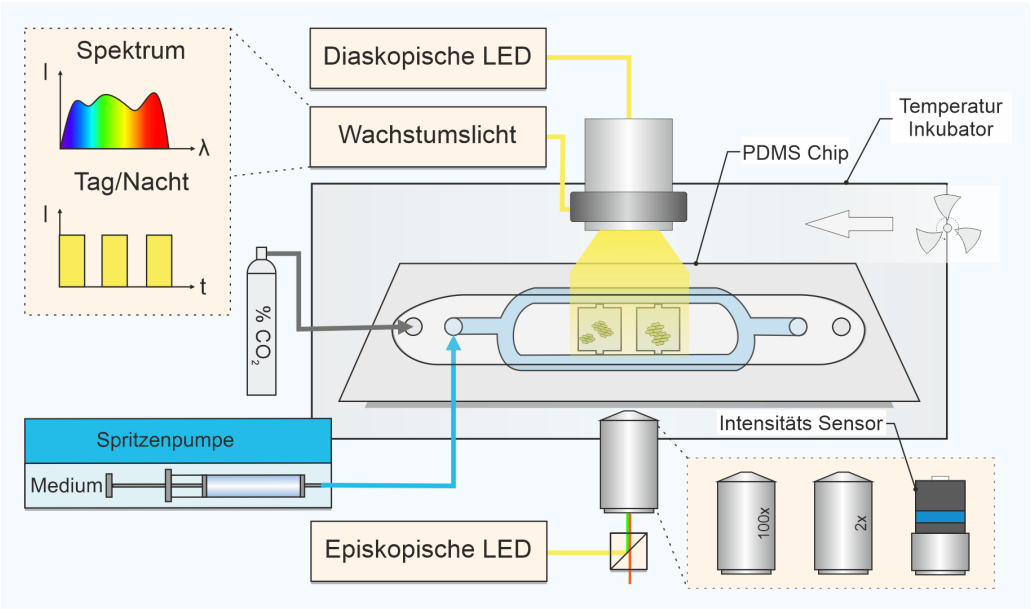


Fig. 2: Übersicht über die mikrofluidische Kultivierungsplattform zur Untersuchung phototropher Mikroorganismen. Die Plattform beinhaltet ein Mikroskop, das in einem temperaturgeregelten Inkubator platziert ist. Um Licht für die Photosynthese bereitzustellen, wurde ein dritter Lichtweg hinzugefügt, indem der Kondensor mit einem Ringlicht ausgestattet wurde, das an eine Wachstumslichtquelle mit vollständiger Spektralsteuerung im PAR angeschlossen ist. Ein Lichtintensitätssensor, der in den Objektivrevolver des Mikroskops integriert ist, wird verwendet, um die genaue Lichtintensität zu messen, der die Zellen ausgesetzt sind. Während der Bildgebung wird das Wachstumslicht ausgeschaltet und die Phasenkontrast- und Fluoreszenzbilder der kultivierten Mikroorganismen werden unter Verwendung des diaskopischen und episkopischen Lichtwege durchgeführt. Eine Spritzenpumpe sorgt für eine kontinuierliche Perfusion des Wachstumsmediums mit konstanter Durchflussrate. Durch Hinzufügen einer CO_2-Perfusionskammer, die mit einer Flasche mit vorgemischtem CO_2 verbunden ist, kann die CO_2-Konzentration um die Mikroorganismen herum gesteuert werden. Die Abbildung wurde mit Genehmigung der Royal Society of Chemistry aus Ref. [1] übernommen.

List of acronyms

Miscellaneous

CBB Calvin-Benson-Bassham-cycle

CCM Carbon concentration mechanism

CFD Computational fluid dynamics

mCGG Microfluidic concentration gradient generator

DAQ-device Data acquisition device

DI Deionized

DL Deep learning

DFT Discrete Fourier transformation

FOV Field of view

PFD Photon flux density

PAR Photosynthetically active radiation

PFS Perfect focus system

PS Photosystem

ROI Region of interest

STL Spectra Tune Lab

LHC Light-harvesting complexes

OD Optical density

MC Multi-Cultivator 1000-OD

Enzymes

cscB Sucrose permease

glgC ADP-glucose pyrophosphorylase

RuBisCo Ribulose-1,5-bisphosphate carboxylase/oxygenase

sps Sucrose phosphate synthase

Chemicals

ATP Adenosine triphosphate

ADP Adenosine diphosphate

Cl Chloramphenicol

DMSO Dimethyl sulfoxide

GAP Glyceraldehyde-3-phosphate

G-1-P Glucose-1-phosphate

G-6-P Glucose-6-phosphate

IPA Isopropyl alcohol

IPTG Isopropyl-β-D-1-thiogalactopyranosid

Km Kanamycin

PDMS Polydimethylsiloxane

RuBP Ribulose-1,5-biphosphate

Sp Spectinomycin

Microorganisms

B. braunii *Botryococcus braunii*

C. glutamicum *Corynebacterium glutamicum*

C. merolae *Cyanidioschyzon merolae* 10D

C. sorokiniana *Chlorella sorokiniana*

E. coli *Escherichia coli*

G. sulphuraria *Galdieria sulphuraria* 074

PCC7942 *Synechococcus elongatus* PCC7942

PCC6803 *Synechocystis* sp. PCC6803

S. elongatus *Synechococcus elongatus*

UTEX2973 *Synechococcus elongatus* UTEX2973

C. reinhardtii *Chlamydomonas reinhardtii*

Research institutions

BU Bielefeld University

FZJ Forschungszentrum Jülich

HHU Heinrich Heine University Düsseldorf

IBG-1 Institute of Bio- and Geosciences: Biotechnology

Contents

Eidesstattliche Erklärung iii

Preface vi

Abstract viii

Zusammenfassung x

List of acronyms xiii

1 Introduction 1

1.1 Theoretical background . . . 3

1.2 Why use single-cell resolved microfluidic cultivation? . . . 11

1.3 Microfluidic devices for the cultivation of cyanobacteria . . . 13

1.4 Scope of this thesis . . . 26

2 General experimental protocols 28

2.1 Laboratory scale cultivation . . . 28

2.2 Microfluidic cultivation . . . 32

2.3 Other protocols . . . 39

I Platform development and proof-of-concept studies 41

3 An illumination system to drive photosynthesis during microfluidic cultivation 42

3.1 Introduction . . . 42

3.2 A ringlight-based illumination system to drive photosynthesis . . . 44

3.3 A sensor for accurate and reproducible light-intensity measurements . . . 50

3.4 Conclusion & Outlook . . . 52

4 Homogeneous growth light illumination **53**

4.1 Introduction . . . 53

4.2 Materials & Methods . . . 53

4.3 Results & Discussion . . . 57

4.4 Conclusion & Outlook . . . 67

5 Linear light-intensity gradient illumination **68**

5.1 Introduction . . . 68

5.2 Materials & Methods . . . 70

5.3 Results & Discussion . . . 73

5.4 Conclusion & Outlook . . . 84

6 Dynamic CO_2 control **86**

6.1 Introduction . . . 86

6.2 Materials & Methods . . . 86

6.3 Results & Discussion . . . 94

6.4 Conclusion & Outlook . . . 99

II Biological use cases **101**

7 Engineering building blocks for a synthetic vacuole **102**

7.1 Introduction . . . 102

7.2 Materials & Methods . . . 104

7.3 Results & Discussion . . . 107

7.4 Conclusion & Outlook . . . 118

8 Reporter-free observation of the circadian rhythm in individual Synechocystis cells **120**

8.1 Introduction . . . 120

8.2 Materials & Methods . . . 122

8.3 Results & Discussion . . . 127

8.4 Conclusion & Outlook . . . 134

9 Conclusion & Outlook **136**

Bibliography **xxv**

Publications **xxxiii**

List of Figures **xxxvi**

List of Tables **xxxviii**

A Supplementary protocols **xl**

A.1 Fabrication of the replication master with maskless lithography xl

A.2 Default values for image registration with the *Correct 3D drift* Fiji plugin . xli

B Master mold designs for soft lithography **xlii**

C Technical drawings **xlvi**

C.1 Connection of the STL light engine to the ringlight input used for reference measurements and measurements with the aspheric condenser lenses. . . . xlvi

C.2 Connection of the STL light engine to the ringlight input with reduced distance xlix

C.3 Comparison of the two approaches to maximize the intensity emitted onto the cultivation plane li

C.4 Fixation of the ringlight around the microscope condenser liii

C.5 3D printed master molds for soft lithography liv

C.6 Miscellaneous lv

D Supplementary data **lvii**

D.1 Characterization of the Mounted LED lvii

D.2 Mean Single-cell area across colonies lix

D.3 Single-cell area distribution analysis lxi

D.4 Single-cell area over light-intensity analysis lxvi

D.5 *Single-cell traces* for the experiment displayed in Fig. 7.5 (b) lxvii

D.6 Improved simulation approach lxviii

1 Introduction

Microalgae and cyanobacteria are morphologically diverse, photosynthetic microorganisms found in marine and terrestrial habitats. They can be distinguished from terrestrial plants because they lack roots, stems, and leaves [2, 3]. Microalgae are eukaryotic organisms, whereas cyanobacteria are prokaryotic organisms. The latter are ancient, morphologically diverse bacteria that emerged over 2.5 billion years ago. They were the first organisms to perform oxygenic photosynthesis, significantly impacting the evolution of life. (See Fig. 1.1). Even today, cyanobacteria play a significant role in the formation of molecular oxygen and nitrogen fixation in the world's oceans [4]. In fact, marine microalgae are responsible for half of the global oxygen production [5]. Unlike heterotrophic organisms, which extract energy from the degradation of organic molecules, photosynthetic microorganisms like microalgae perform photosynthesis (See Eq. 1.1). During this process, the light energy delivered by impinging photons is captured and stored as chemical energy in organic substances. Inorganic CO_2 is used as a carbon source. In this equation $h{\cdot}\nu$ represents the energy delivered by the impinging photons [5].

$$6\,CO_2 + 12\,H_2O \xrightarrow{h\cdot\nu} C_6H_{12}O_6 + 6\,O_2 + 6\,H_2O \tag{1.1}$$

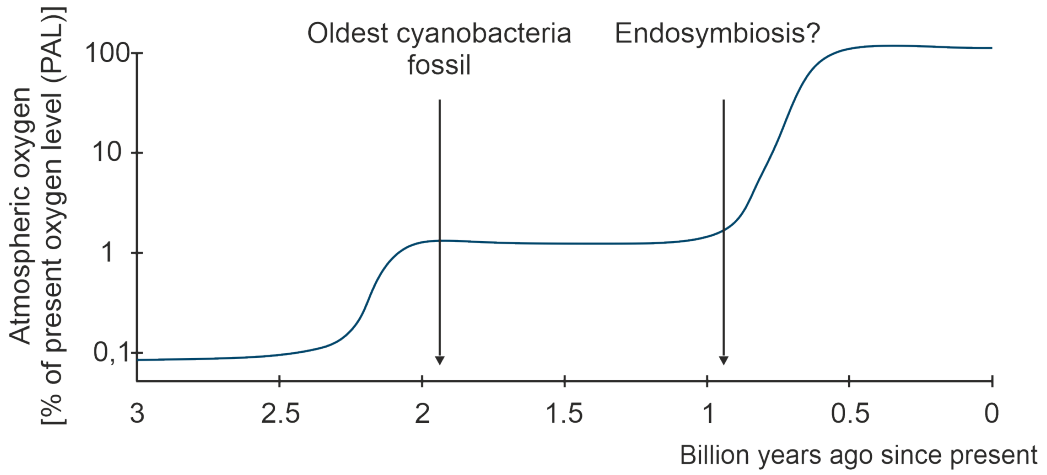


Fig. 1.1: Development of the oxygen concentration in the Earth's atmosphere. Cyanobacteria were the first organisms to perform oxygenic photosynthesis, thereby transforming our planet. The first global increase in oxygen concentration coincided with their first appearance on Earth. A second rise in oxygen concentration coincided with endosymbiosis. The figure was adapted from Shih [6] with permission from Elsevier.

As illustrated in Fig. 1.1, cyanobacteria had a significant impact on the history of our planet. They are therefore of interest in geological and evolutionary studies, as well as in biotechnology, environmental research, and fundamental biology.

Biotechnology: Microalgae are possible producers of biofuels or high value chemicals, such as pigments, proteins or vitamins [2, 5, 7]. Their biomass can be used as a food supplement for humans or as feed for aquaculture [2]. Furthermore, new concepts for producing valuable chemicals are being developed. These concepts involve engineering microalgae to share the products of photosynthesis by cultivating them alongside heterotrophic microorganisms that produce chemical compounds. Hence, producing valuable chemicals from just light and CO_2 [8, 9]. Of the 40,000 to 60,000 identified species of microalgae, fewer than 15 strains are currently used in industrial production. Current industrial processes include producing food supplements with the genera *Spirulina* and *Chlorella*, as well as producing the red pigments astaxanthin and β-carotene using *Haematococcus* and *D. salina* strains, respectively [2].

Environmental research: Most microalgae species grow in water, while some grow on rocks, soils, snow or on other plants. In nature, they are known to live in symbiosis with ciliates or corals or in the form of lichens [10]. As is well known, the concentration of carbon dioxide in our atmosphere has risen from approximately 290 parts per million (ppm) to around 400 ppm since the beginning of the pre-industrial era, leading to a rise in temperature and the acidification of the world's oceans [11, 12]. This climate change is known to make harmful algal blooms more likely. These blooms are characterized by a sudden increase in microalgae growth, followed by the collapse of aquatic ecosystems. However, the exact mechanisms that trigger these blooms remain unknown [13]. Therefore, studying the effects of rising temperatures and lower pH levels on microalgae can help us mitigate the impact of global warming on our planet and its ecosystems.

Fundamental biological studies: It is widely accepted that photosynthesis evolved only once. This subsequently led to an increase in oxygen concentration between 2.2 and 2.4 billion years ago, known as the Great Oxygenation Event [6]. Between 1 and 0.64 billion years ago, the evolution of chloroplasts led to a further increase in the concentration of atmospheric oxygen to near-present-day levels. It is widely accepted that these chloroplasts can be traced back to a single cyanobacterium that was engulfed by a heterotrophic host and subsequently evolved into the photosynthetic organelles found today [14]. Further research into this process, known as endosymbiosis, is expected to improve our understanding of phototrophic eukaryotes and general microbial interactions. Furthermore, cyanobacteria were among the first microorganisms to be fully sequenced. In fact, the first fully sequenced

photosynthetic organism was the popular cyanobacteria model organism *Synechocystis sp.* [15, 16].

1.1 Theoretical background

1.1.1 Basics of photobiotechnology

Photosynthesis in cyanobacteria

In eukaryotic cells, photosynthesis only occurs inside chloroplasts. However, it is believed that all chloroplasts evolved from cyanobacteria. For simplicity, hereafter photosynthesis is explained for cyanobacteria. All processes are analogous to those occurring in the chloroplasts of microalgae. As shown in Fig. 1.2, the process of photosynthesis can be divided into light and carbon reactions.

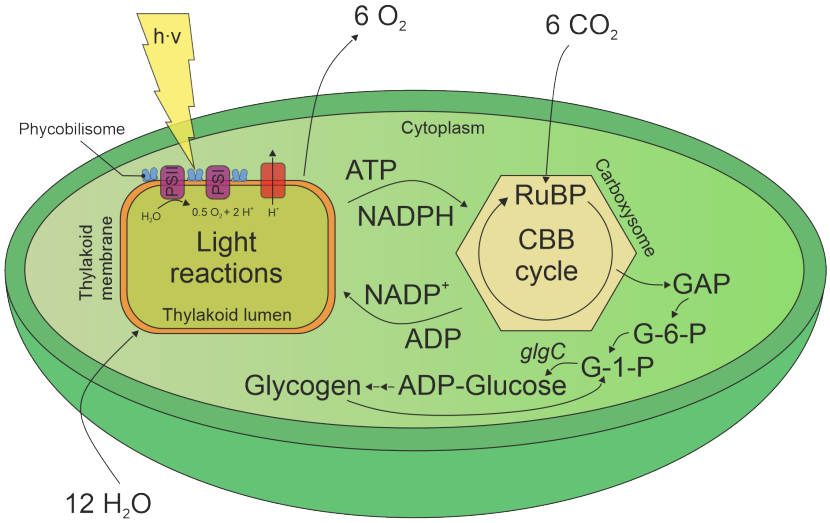


Fig. 1.2: Photosynthesis in cyanobacteria. The light reactions occur in the thylakoid lumen, while the carbon reactions occur in the cytoplasm and carboxysomes. During the light reactions, water is split into oxygen and hydrogen ions. The resulting cross-membrane proton gradient is used for ATP synthesis. Electrons are excited by impinging photons and shuttled through multiple protein complexes before being used to synthesize NADPH. ATP and NADPH are used to catalyze reactions in the CBB cycle and to synthesize glucose from GAP. This results in the formation of new ADP and $NADP^+$.

Light reactions: Cyanobacteria are prokaryotic cells, meaning they lack organelles. However, they form bilayer lipid membranes with embedded pigment-protein complexes known as thylakoid membranes. These membranes create closed fluid compartments within the cytoplasm known as the thylakoid lumen. During the light reaction, photons are captured by a subgroup of these pigment-protein complexes known as Light-harvesting complexes (LHC). The pigments include chlorophyll and carotenoids. In cyanobacteria, the main LHC are protein complexes bound to the thylakoid membrane known as phycobilisomes. For each captured photon, one electron is excited to a higher energy state. Noteworthy, each photon excites only one electron regardless of its energy. Consequently, the wavelength of the impinging photons does not influence the result. The LHC then funnel the excited electrons to another group of nearby pigment-protein complexes, known as Photosystem (PS). The two known PSs are numbered in order of their discovery: PSI and PSII. Both of them contain a central chlorophyll molecule that absorbs light at 680 nm and 700 nm for PSII and PSI, respectively.

PSII catalyzes the splitting of H_2O into O_2 and H^+ within the thylakoid lumen. This creates a proton gradient across the thylakoid membrane. The gradient is then used to catalyze the synthesis of energy-rich Adenosine triphosphate (ATP) from Adenosine diphosphate (ADP) via a transmembrane ATP-synthase. The electrons resulting from the splitting of water are exited by photons and shuttled through further complexes toward PSI. While some are used to reduce $NADP^+$ to NADPH (z-scheme), other electrons are permanently cycled through PSI (cyclic electron transport), whereby ATP is the only product. This cyclic electron transport is necessary to maintain the correct ATP/NADPH ratio [2, 10]. To conclude the reaction happening during the light reaction can roughly be summed up by Eq. 1.2:

$$2\,H_2O + 2\,NADP^+ + 3\,ADP + 3\,P_i \xrightarrow{h\cdot\nu} O_2 + 2\,NADPH/H^+ + 3\,ATP \qquad (1.2)$$

Carbon reactions: The central component of the carbon reactions is the Calvin-Benson-Bassham-cycle (CBB). In cyanobacteria, the CBB occurs in the carboxysome, while in eukaryotic algae, this cyclic reaction occurs in the chloroplast stroma. It can be divided into three steps.

(i) Carbon fixation: A CO_2 molecule is added onto the C5 body Ribulose-1,5-biphosphate (RuBP) through covalent bonding. This step is catalyzed by the enzyme Ribulose-1,5-bisphosphate carboxylase/oxygenase (RuBisCo); one of the most abundant proteins on Earth. The resulting molecule is unstable and quickly breaks into two C3 bodies.

(ii) Reduction: In the second step, the resulting C3 bodies are phosphorylated and reduced, consuming the ATP and NADPH formed during the light reactions. The product of the second step is Glyceraldehyde-3-phosphate (GAP). One of three GAP molecules leaves the cycle, and serves as a precursor for the synthesis of glucose or glycogen.

(iii) Regeneration: In the third step RuBP is synthesized from the remaining GAP molecules under ATP consumption.

The whole reaction can be summarized by Eq. 1.3 [2].

$$3\,CO_2 + 6\,NADPH/H^+ + 9\,ATP \longrightarrow GAP + 6\,NADP^+ + 9\,ADP + 8\,P_i \tag{1.3}$$

This means, that in order to synthesize two molecules of GAP twelve molecules of NADPH and 18 molecules ATP are needed. However, further ATP is needed for the synthesis of glucose from GAP. Measurements as well as thermodynamic calculations have shown that under ideal conditions eight photons are needed to fix one molecule of CO_2 [2, 17]. These are grossly simplified descriptions of the complex processes that occur during photosynthesis. For a more detailed description the reader is referred to other authors e.g. [2, 10, 17, 18].

Light as a substrate in biotechnology

In heterotrophic cultivation, organic molecules are added to the culture medium to provide energy for the cultivated microorganisms. By contrast, in photobiotechnology, light is used as a substrate from which the microorganisms can extract energy. The biggest difference between these energy sources is that, unlike in heterotrophic cultivation, the substrate cannot be mixed by stirring the culture broth. The physical phenomenon that humans refer to as 'light' are actually electromagnetic waves with a wavelength between 380 and 780 nm. This range is being refereed to as visible light. As displayed in Fig. 1.3 wavelengths down till 10 nm are called UV-light and electromagnetic waves with wavelengths up to 1 mm are refereed to as Infrared-Light [10]. In physics electromagnetic radiation can be described either as a wave or as a particle. Both providing physicals properties, that can be used to describe certain phenomena [19].

During photosynthesis, light energy is captured by shifting electrons within pigments to higher energy levels. This energy is transferred to other molecules and is ultimately stored in ATP. While photons with higher energy can shift electrons to higher energy levels, these levels relax too quickly to be passed on. Any excess energy is converted into heat. Therefore, the rate of photosynthesis depends only on the number of photons absorbed by the LHC, not on the energy stored inside these photons. Consequently, researchers studying

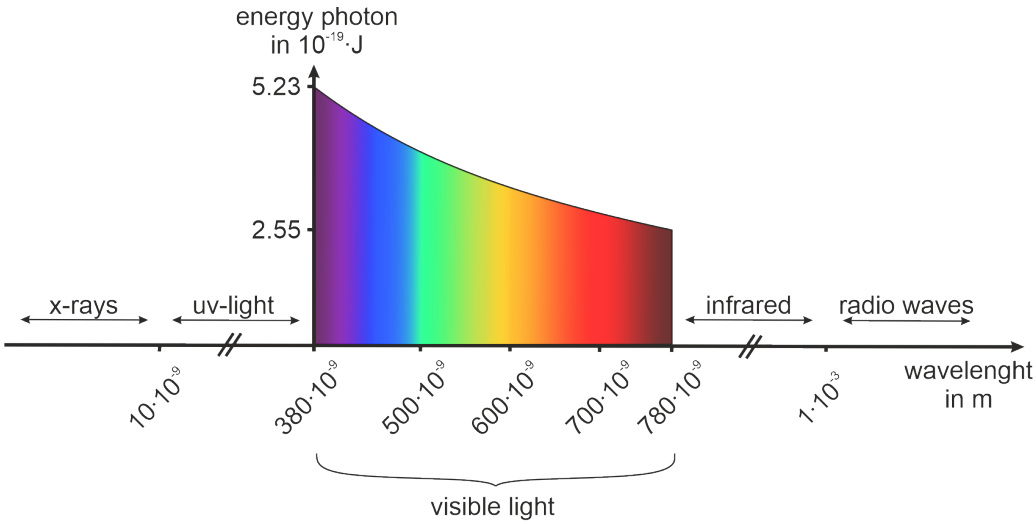


Fig. 1.3: The spectrum of electromagnetic waves. Electromagnetic waves with wavelengths between 380 and 780 nm fall within the visible spectrum. Those with longer wavelengths are called infrared and radio waves. Those with shorter wavelengths are called UV-light and X-rays.

photosynthesis consider light to be more like a particle than a wave. They measure light as the flux of photons per square meter per second, referred to as Photon flux density (PFD). The energy stored inside the impinging photons is important for energetic considerations and can be calculated from the PFD using Eq. 1.4.

$$I_e = \int_{\lambda_{min}}^{\lambda_{max}} PFD(\lambda) \cdot h \cdot \frac{v_L}{\lambda} \cdot d\lambda \tag{1.4}$$

Therein I_e is the Irradiance, h is the Plank constant ($6.626 \cdot 10^{-34} J \cdot s^{-1}$), v_L is the speed of light ($2.998 \cdot 10^8$ m$\cdot s^{-1}$), λ is the wavelength and $PFD(\lambda)$ is the PFD of photons with the wavelength λ.

However, the spectrum of the used light should always be mentioned alongside the intensity, because the absorption of photons highly depends on the wavelength. Chlorophyll for instance, has two absorption peaks. One at $\approx$ 380 nm and one at $\approx$ 680 nm. An absorption minimum is present between $\approx$ 500 - 600 nm, giving phototrophic organisms their typical green color. The flux of absorbed photons is equal to the flux of impinging photons multiplied by the wavelength- and strain-specific absorption coefficient. In photobiotechnology, this process parameter is called the absorption cross-section [2, 20]. The Photosynthetically active radiation (PAR) of photons was traditionally believed to be 400 and 700 nm. How-

ever, since the discovery of cyanobacteria that can use wavelengths up to 760 nm, the exact definition of PAR has been debated again [5, 21].

In photobiotechnology the PFD is usually measured in $\mu E \cdot m^{-2} \cdot s^{-1}$. Whereby 1 E equals 1 mol of photons. In this thesis, the terms PFD and light intensity are used interchangeably to describe the same phenomenon. For most of the cultivation experiments in this thesis, the LED light source was programmed to emit ideal black body radiation (See Eq. 1.5).

$$PFD(\lambda) \propto \frac{\lambda^{-4}}{e^{\frac{h \cdot v_L}{\lambda \cdot k \cdot T}} - 1} \tag{1.5}$$

Therein λ is the wavelength, *PFD(λ)* is the PFD of photons with the wavelength λ, k is the Bolzmann constant ($1.38 \cdot 10^{-23} J \cdot K^{-1}$), T is the temperature v_L is the speed of light ($2.998 \cdot 10^8$ m$\cdot s^{-1}$), and h is the Plank constant ($6.626 \cdot 10^{-34} J \cdot s^{-1}$).

By inserting the surface temperature of the Sun ($T_S \approx 5800$ K), the spectrum of light emitted by the Sun onto Earth can be replicated.

CO_2 as a substrate in biotechnology

As can be seen from Eq. 1.1, the second most important process parameter when working with microalgae is the abundance of CO_2. When considering liquid cultures, CO_2 is provided from CO_2 dissolved in the culture medium. On plates, CO_2 is also provided from the surrounding air. When CO_2 is dissolved in an aqueous solution, a small fraction (less than 1 %) reacts with the abundant H_2O and forms carbonic acid. The carbonic acid dissociates almost completely into bicarbonate and carbonate. This results in a pH change of the medium [22, 23].

$$CO_{2(aq)} + H_2O \longrightarrow H_2CO_3 \longrightarrow HCO_3^- + H^+ \longrightarrow {CO_3}^{2-} + H^+ \tag{1.6}$$

The resulting increase in H^+ molecules causes the acidification of the world's oceans [24]. Furthermore, this is why the pH correlates with the concentration of dissolved CO_2, which is exploited for routine CO_2 measurements in aqueous solutions, either by using an electrode (Severinghaus electrode) or by pH-sensitive dyes [25]. As with all photoautotrophic organisms, the fixation of CO_2 in microalgae is catalyzed by the enzyme RuBisCo [2]. In cyanobacteria RuBisCo is stored inside a microcompartment called a carboxysome [26]. In eukaryotic microalgae, it is stored in the stroma of the chloroplast. Remarkably, cyanobacteria possess a mechanism that concentrates CO_2 around RuBisCo in the carboxysomes to concentrations up to 1,000 times higher than in the surrounding environment. This Carbon concentration

mechanism (CCM) includes carbonic anhydrase enzymes within the carboxysome to convert HCO_3^- into CO_2, a protein shell hindering the diffusion of CO_2 out of the carboxysome and a number of active CO_2 and HCO_3^- transporters located in the plasma and thylakoid membrane. For a detailed summary of the several transport mechanisms inside cyanobacteria the reader is referred to other authors [23, 26, 27]. In conventional photobioreactors, CO_2 is typically supplied by bubbling air through the culture broth. In open systems, it is also supplied by direct mass transfer from the fluid surface. Since the CO_2 concentration is typically a limiting factor, CO_2-enriched air is often used to reach higher growth rates. In lab scale photobioreactors CO_2 can also be provided by adding $NaHCO_3/Na_2CO_3$ to the medium [2]. Please note that the amount of CO_2 is usually expressed as a percentage (%) or as parts per million (ppm). Thereby, 1 % CO_2 is equal to 10,000 ppm CO_2.

Further media components

In order to grow, microalgae require additional medium components besides carbon dioxide as a carbon source and photons as an energy source. The macronutrients nitrogen and phosphorus are incorporated into many biomolecules and should be supplemented in higher amounts [28]. Hydrogen diphosphate, dihydrogen phosphate and ammonia are frequently used as buffer [2]. Metal ions also need to be supplemented. RuBisCo for instance requires Mg^{2+} as a cofactor and Mg^{2+} is also part of Chlorophyll. Fe is build into the LHC. Vitamins can also be necessary medium components [2]. Microalgae can be found in both seawater and freshwater. Therefore, maintaining the appropriate salinity level is crucial to avoid cell damage. Several waste waters can be utilized as a complex medium for growing microalgae [28]. Popular media for culturing freshwater and seawater microalgae, as well as cyanobacteria, are TRIS-acetate-phosphate buffer medium (TAP medium), enriched artificial seawater (EASW), and BG11, respectively. The abbreviation of the latter medium stands for **B***lue-***G***reen Algae Medium Number* **11**. For mixotrophic or heterotrophic growth multiple organic carbon sources can be supplemented [2]. Attention should also be drawn towards the pH value, since the concentration of H^+ has an effect on the dissociation of carbonic acid. Thus influencing the transport of inorganic carbon from the air into the culture medium and from the medium into the microalgae [28].

Temperature

The medium temperature can directly influence microalgae growth by influencing reaction and transport rates of the cell metabolism. This, in turn, impacts growth rates and biomass composition [28]. Temperature also has an indirect influence by affecting the solubility of CO_2 in an aqueous medium [5]. This alters the availability of inorganic carbon for photosyn-

thesis. When cultivated in open systems, the temperature of the medium is determined by the ambient temperature and the impinging sunlight. In closed bioreactors and microfluidic devices, however, temperature is usually controlled.

1.1.2 Quantification of microbial growth

Exponential growth

The most basic mathematical equations for describing bacterial growth have not changed since Jacques Monod milestone contribution to microbial growth kinetics. Generally, the growth of a bacterial culture is considered exponential, when the doubling time t_d is constant over time. In this case, the growth rate μ, as defined in Eq. 1.7, is constant over time [29, 30].

$$\frac{\ln 2}{t_d} = \mu = \frac{\ln c(t) - \ln c(0)}{t - t_0} \tag{1.7}$$

Therein μ is the growth rate, t_d is the doubling time, c is the concentration of cells in a bacterial culture and t is the time.

In biotechnology, the concentration of cells in a liquid culture is typically measured by determining the Optical density (OD). The relationship between the OD of a given liquid and the concentration of a solute, in this case bacteria, is defined by the Lambert–Beer law (Eq. 1.8).

$$\ln \frac{I_{\lambda,0}}{I_\lambda} = \underbrace{\epsilon_\lambda \cdot c \cdot d}_{=OD_\lambda} \quad \Leftrightarrow \quad I_\lambda = I_{\lambda,0} \cdot e^{-\epsilon_\lambda \cdot c \cdot d} \tag{1.8}$$

Therein $I_{\lambda,0}$ is the incident intensity of a light beam of the wavelength λ radiated into the culture broth, I_λ is the remaining intensity of the beam after it passed through the distance d of the liquid, ϵ_λ is the extinction coefficient of the solute at the wavelength λ. The concentration of the solute, or bacteria in this case, is denoted by c.

If it is assumed, that ϵ_λ and d are constant throughout the whole cultivation, ϵ_λ and d cancel out after inserting Eq. 1.8 into Eq. 1.7. This assumption is usually well-justified, especially for d, since the dimensions of a bioreactor typically don't change. For ϵ_λ, however, this is not always the case; morphological changes or the formation of inclusion bodies can affect the value for ϵ_λ. The OD of microalgae cultures is commonly measured between 730 and

750 nm [31]. Instead of measuring the amount of light transmitted through the culture, backscatter measures the amount of light scattered by a probe. In modern biotechnology, OD measurements are often complemented by cytometric methods such as Coulter counters and FACS. However, these offline methods require sampling, which makes it difficult to observe time-dependent processes. Microfluidic cultivation, on the other hand, offers the possibility for non-invasive long-term online observation of cells [32].

Modeling the dependency of the growth rate on the PFD

In photoautotrophic microorganisms, the chemical energy gained from photosynthesis is used for survival and proliferation. When the growth rate is plotted against the impinging energy in the form of the PFD (Fig. 1.4), several regions can be identified. In the first region, there is a linear relationship between the growth rate and the PFD. Here, the availability of photons limits growth. In the second region, a higher PFD does not yield a higher growth rate because photosynthesis is limited by a reaction rate of the carbon reactions. In the third region, growth is inhibited by the PFD [10].

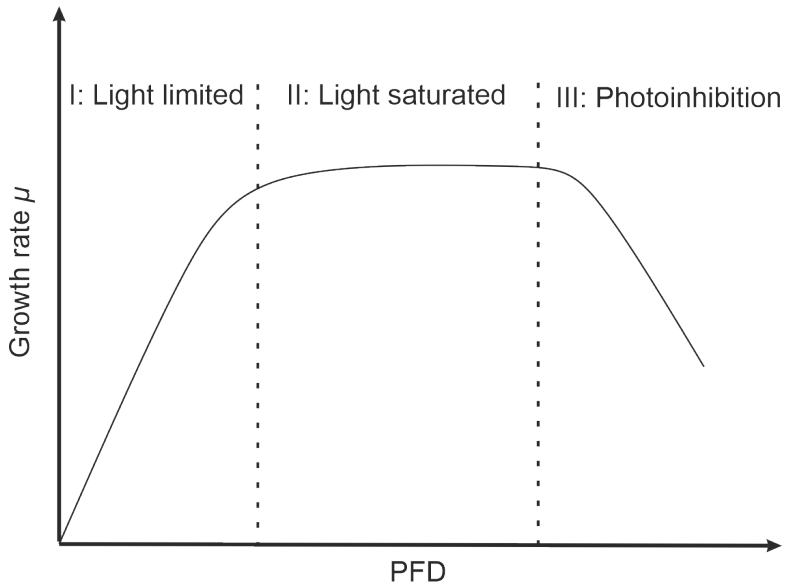


Fig. 1.4: The dependency of microalgae growth on light intensity. At low light intensities, growth rates increase linearly as light intensity rises. In a second region, however, the growth rate becomes independent of light intensity and the CO_2 concentration limits the growth rate. Ultimately, excessive light can inhibit growth.

A variety of models describing this relationship between growth rate and the light-intensity are described in literature [33]. The hyperbolic tangent model [34] and the shape-modified

Monod kinetic model [35] worked well to describe the data presented in this thesis. The hyperbolic tangent model was chosen for data fitting. However, this model only accounts for regions I and II. Photoinhibition was not considered.

$$\mu(PFD) = \mu_{max} \cdot \tanh \frac{\alpha \cdot PFD}{\mu_{max}} \tag{1.9}$$

Therein 1.9 μ is the growth rate, μ_{max} is the maximal growth rate, PFD is the applied photon flux density and α is the initial slope of the hyperbolic function.

The physical meanings of the parameters μ_{max}, α and $PFD_{1/2}$ were derived as follows:

Maximum growth rate μ_{max}:

$$\mu_{max} = \lim_{PFD \to \infty} \mu(PFD) = \mu_{max} \cdot \underbrace{\lim_{PFD \to \infty} \tanh \frac{\alpha \cdot PFD}{\mu_{max}}}_{=1} \tag{1.10}$$

Initial slope α:

$$\alpha = \lim_{PFD \to 0} \mu'(PFD) = \frac{\mu_{max} \cdot \alpha}{\mu_{max}} \underbrace{\lim_{PFD \to 0} \frac{1}{\cosh^2 \frac{\alpha \cdot PFD}{\mu_{max}}}}_{=1} = \alpha \tag{1.11}$$

Half maximum growth rate $\mathbf{PFD_{1/2}}$:

$$\frac{\mu_{max}}{2} = \mu(PFD_{1/2}) \Leftrightarrow \frac{1}{2} = \tanh \frac{\alpha \cdot PFD_{1/2}}{\mu_{max}} \Leftrightarrow PFD_{1/2} = \underbrace{\tanh^{-1} 0.5}_{\approx 0.55} \cdot \frac{\mu_{max}}{\alpha} \tag{1.12}$$

1.2 Why use single-cell resolved microfluidic cultivation?

Lab-scale cultivation devices for cyanobacteria commonly include microtiter plates, shake flasks, bubble columns, flat-panel reactors, stirred tank reactors and tubular reactors [36]. For production scale processes also open systems such as raceway ponds and inclined surface reactors can be used [2]. Of these, only microtiter plates are applicable for automated high-throughput screening [36]. Microtiter plates can be illuminated homogeneously [37] or with differing light intensity between individual wells, to further increase experimental throughput

[38, 39]. This is especially important when cultivating phototropic organisms due to their slow growth in comparison to many heterotrophic bacteria. Nevertheless, all the above-mentioned systems suffer from fundamental physical restrictions concerning the distribution of light and dissolved nutrients within the bioreactor.

When a beam of light travels through the culture broth of a conventional photobioreactor, its intensity is reduced due to scattering and absorption of the light by microorganisms and miscellaneous particles leading to the formation of a light-intensity gradient. Unlike in heterotrophic fermentation, where such concentration gradients concerning the substrate can be resolved by mixing of the fermentation broth, light can not be mixed by convective transport. Near gradient-free substrate concentration can be reached by highly diluted cultures and specific reactor geometries [2]. The decrease in light-intensity as a function of reactor depth is often modeled assuming the Lambert-beer law 1.8, therefore ignoring light scattering. In Eq. 1.8 ϵ_λ is exchanged with the wavelength and strain specific absorption cross-section. Therefore, an exponential decrease in light intensity is expected.

Under unfavorable conditions, all the cases shown above - light limitation, light saturation, and photoinhibition - can occur in the same bioreactor at the same time. When scaling up a process, researchers regularly use the mean light intensity from this gradient to compare devices. Additionally, microorganisms are mixed by convection and travel continuously through the culture broth, experiencing different light intensities along the way. These microbial lifelines also include fluctuations in parameters such as pH, temperature, and dissolved nutrients (e.g. CO_2). This problem becomes even more complex when considering that in batch processes an increase in biomass concentration leads to a permanently changing light gradient [2, 36, 40].

The term 'microfluidics' describes the field of research concerned with the knowledge and manipulation of fluid in structures of micrometer scale. Since its establishment, microfluidics has been successfully applied in material science, healthcare, and biotechnology. For instance, microfluidic devices can be used to produce nanoparticles for drug delivery and to manufacture diagnostic pregnancy tests, blood glucose monitoring test strips and urine test strips [41]. Another important application in biotechnology are microfluidic cultivation devices, mainly fabricated from Polydimethylsiloxane (PDMS), for single-cell analysis. These devices can be used to investigate various factors, such as population heterogeneity, cell morphology, cell migration and cell-to-cell interaction, as well as the impact of microbial lifelines [40, 42].

For these applications, PDMS offers unique advantages, such as its biocompatibility with a wide range of microorganisms and its permeability to a number of gases, including CO_2

[43]. Furthermore, there is no evidence of reaction products forming between PDMS and CO_2 [44]. Thus enabling microalgae cultivation under stable and non-limiting CO_2 concentrations. Concerning the cultivation of phototrophic microorganisms PDMS, offers the advantage of high and uniform transmission of light within PAR [45]. This, combined with the ability to restrict growth to a single cell layer, enables homogeneous and stable illumination of all microorganisms within a colony. Hence, eliminating the just-mentioned limitations. Conventional cultivation techniques primarily use batch cultivation, while continuous cultivation is difficult to implement. In most microfluidic cultivation devices, the growth medium is supplied continuously, which eliminates changing nutrient concentrations as a limiting factor. Although more challenging, achieving microfluidic batch cultivation at the single-cell level is also possible [46].

It should be noted that these devices are analytical tools, rather than bioreactors for production purposes. For instance, microfluidic devices can be used to acquire precise correlations of light intensity and CO_2 concentration with growth rates. These can then be used in photobioreactor modeling approaches, reducing the experimental effort required for photobioreactor scale-up.

1.3 Microfluidic devices for the cultivation of cyanobacteria

Given the obvious advantages of single-cell cultivation devices for phototrophic growth quantification — such as monolayer growth for constant and precise illumination, as well as stable and non-limiting CO_2 concentrations — preliminary work on this topic has been conducted by other researchers. This section begins with a concise literature review, followed by the definition of the scope of this thesis. The literature review focuses on the cultivation of microorganisms in artificially structured microenvironments. Droplet microfluidic approaches were not considered. Due to the large number of publications on the subject of microfluidic single-cell analysis, most of this review concentrates on phototrophic cultivation. However, the section on CO_2 also features heterotrophic microorganisms due to the limited literature on this subtopic. It should be noted that research groups are conducting research on phototrophic microorganisms using non-structured or structured agarose pads [47–51]. Furthermore, single-cell cultivation of *Synechococcus elongatus* (*S. elongatus*) has been employed in circadian research to visualize the circadian rhythm in individual cells [52–55]. The latter application is further discussed in chapter 8 of this thesis. However, these studies focus on image analysis and fundamental biology. The focus of this review is on microstructured devices that enable the quantification of growth parameters for phototrophic microorganisms. It evaluates the devices based on three main criteria.

- **Simple design:** Simplicity and robustness are key considerations to ensure that the new methods are accessible to non-technical specialists with minimal training. Many innovative systems are still too laborious, resulting in few real applications.
- **Multi-value/parameter testing:** As microalgae grow slowly compared to other microorganisms, it is particularly important to be able to test multiple values of a process parameter or multiple process parameters simultaneously or over time (e.g. dynamic medium switching).
- **Single cell resolution:** The obvious advantages are that population heterogeneity, morphology, and changes in autofluorescence can be observed, and the light intensity experienced by single cells can be precisely measured.

The results of the analysis based on these criteria are summarized in Tab. 1.1 - 1.3. Tab. 1.1 summarizes the results for devices that enable investigation of different lighting conditions, Tab. 1.2 summarizes the results for devices that enable investigation of medium components and Tab. 1.3 summarizes the results for devices that enable investigation of the impact of CO_2 on microalgae growth. An overall summary of the reviewed literature is displayed in Tab. 1.4. If an author is mentioned twice, a superscript "*" indicates this, authors from the IBG-1 are indicated with a superscript "+".

1.3.1 Microfluidic devices for the investigation of lighting conditions

As displayed in Fig. 1.5 these devices can be sorted into two categories: Devices, that illuminate the microfluidic cultivation chip with uniform illumination and create different light-intensities and or day/night rhythms by shading parts of the cultivation chip [56, 57] and devices that illuminate the chip with structured light, thus eliminating the need for on-chip shading [58–61]. In detail:

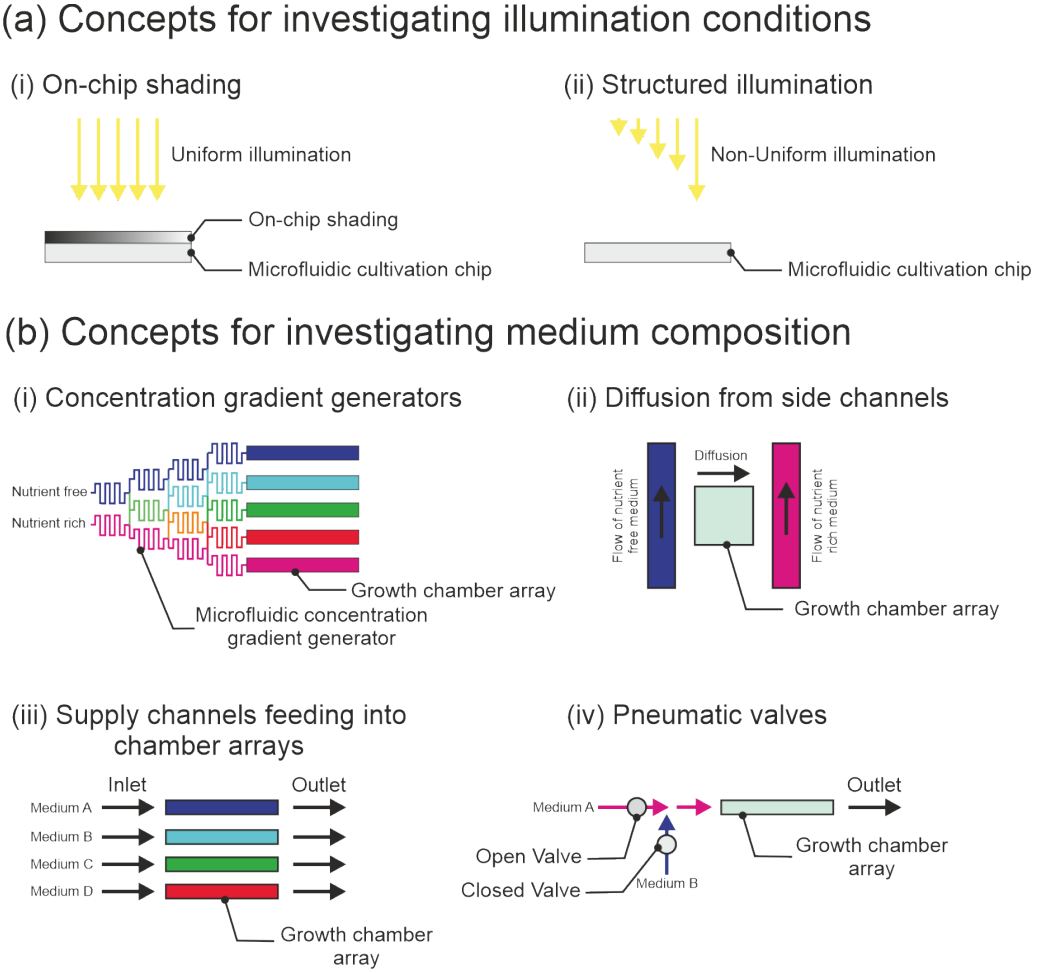


Fig. 1.5: Concepts for investigating different media or light regimes in a microfluidic experiment. (a) Two approaches can be used to investigate different light regimes in a single microfluidic experiment. (i) One approach is to uniformly illuminate the cultivation chip. Then, different light regimes can be created by shading parts of the chip. (ii) Another approach is to structure the light projected onto the cultivation chip. (b) Different approaches are used to investigate the effect of different media on microalgae. (i) Using a Microfluidic concentration gradient generator (mCGG) feeding into different growth chamber arrays multiple dilutions of a single nutrient can be investigated simultaneously. (ii) The same result can be achieved by placing the chamber arrays between parallel flow channels perfused with nutrient-free and nutrient-rich media. However, this method only works if the material allows sufficient diffusion of the nutrient. (iii) Different media can also be investigated by connecting the chamber arrays to independent supply channels fed by distinct inlets. (iv) Pneumatic valves can be used to dynamically change the medium in a chamber array.

Kim et al.: [62] proposed a four-layer microfluidic PDMS chip that enables the cultivation of microalgae under eight different light intensities and day-night cycles. From bottom to top, the device consists of:

1. A cultivation layer with eight rows containing eight culture chambers each, all of which are connected to the same medium inlet and outlet. Each of the circular culture chambers (Volume of 54 nL) contains five single-cell trapping structures (Volume of 0.43 nL).
2. A light intensity control layer consisting of a microfluidic mCGG connected to eight parallel flow channels (Fig. 1.5, (b, i)). This layer was used to create a gradient of Deionized (DI) water and black dye. This leads to different light-intensities in each row of the cultivation layer (Fig. 1.5, (a, i))
3. A light-dark cycle control layer consists of an inlet for black dye and one for DI water. Pneumatic valves are used to periodically fill eight parallel flow channels with either DI water or black dye, thus creating eight different day/night cycles. These channels are perpendicular to those in the layer below.
4. A light-blocking layer ensures isolated light conditions in each circular culture chamber.

The light source is positioned above the microchip. Time-lapse imaging combined with automated image analysis is used to determine colony size and evaluate growth of *Botryococcus braunii* (*B. braunii*). Endpoint nile red staining protocols were developed to evaluate lipid production. This approach is versatile, enabling single-cell resolution and precise high-throughput data acquisition. However, the system is quite complex, which hinders its usage.

Graham et al.: [60] introduced a cultivation system consisting of a PDMS chip placed on an illumination unit. The system allows controlling the light intensity and spectrum for each of the 238 photobioreactors individually (Fig. 1.5, (a, ii)). It was used to investigate the effects of different illumination regimes on the growth of *Synechococcus elongatus* PCC7942 (PCC7942). Imaging of cyanobacteria at single-cell resolution is not possible, and growth rates are derived from the increasing chlorophyll fluorescence in the photobioreactors. The system does not restrict growth to monolayers. Therefore, self-shading of cells is avoided. It is noteworthy that a follow-up publication uses the same illumination system.

In this publication, a 1 mm thick hydrogel containing *Chlamydomonas reinhardtii* (*C. reinhardtii*) cells is placed on the illumination unit [61]. After 48 hours, the hydrogel is removed and lipid staining is performed. Growth is analyzed by imaging chlorophyll autofluorescence and the lipid content of the cells is analyzed by imaging the fluorescence of the lipid stain. Although this approach is highly innovative, it only allows for endpoint

determination. It does not reach single-cell resolution and does not involve artificial microenvironments.

Castaldello et al.: [57] designed a 3-channel PDMS device, each channel connected to two rows of four photobioreactors. Each individual photobioreactor has a volume of 20 µL. Neutral density filters are placed on the different rows of chambers to produce eight different light intensities from a homogeneous light source (Fig. 1.5, (a, i)). Growth rates of the microalgae strain *Scenedesmus obliquus* are calculated from chlorophyll autofluorescence measurements. The design of the device is elegant and easy to use. However, the 20 µL volume of the compartments is quite large in comparison to other devices; single-cell analysis was not possible [57].

Liu et al. and Kim et al.: used an agarose-based array of photobioreactors to investigate the growth of *C. reinhardtii* in four consecutive publications. Each photobioreactor always measures 100 x 100 x 100 µm. In their studies the chlorophyll fluorescence inside the photobioreactors is tracked using episcopic time-lapse imaging. The change in chlorophyll fluorescence is assumed to be proportional to a change in cell number and therefore used to calculate growth rates.

1. Kim et al. 2015 [13] studied the effect of an ammonium gradient on *C. reinhardtii*. To create the concentration gradient, the photobioreactor array is placed between parallel flow channels spaced 2 mm apart. One channel is perfused with standard minimal medium and the other with nitrogen-depleted minimal medium (Fig. 1.5, (b, ii)). The result is a nitrogen concentration gradient between the flow channels. This study belongs in the next subsection: 'Investigation of medium composition'.

2. Liu et al. 2020 [13] expanded the concept pioneered in the previous study by adding an orthogonal flow channel. This creates an orthogonal gradient of nitrogen and phosphorus. This study belongs in the next subsection: 'Investigation of medium composition'.

3. Liu et al. 2022 [58] modified a light microscope by inserting a half-moon mask into the diascopic light path to create a linear light-intensity gradient across the array of photobioreactors (Fig. 1.5, (a, ii)). The dependency of *C. reinhardtii* growth on light intensity is studied. The study also features an LED matrix-based light-intensity gradient generator for a 96-well plate [59].

4. Liu et al. 2024 [58] combined the light-intensity gradient with an orthogonal nitrogen gradient in their most recent study.

Tab. 1.1: Microfluidic devices for the investigation of lighting conditions. Microfluidic devices for investigation lighting conditions. Simple design: (Good: + , Neutral: o , Weak: -), Multi-value/parameter testing: (Good: + , Neutral: o , Weak: -), Single-cell resolution (Good: +, Neutral: o, Weak: -).

Author	Simple design	Multi-value/ parameter testing	Single-cell resolution
Kim et al. [56]	-	+	+
Graham et al. [60]	o	+	-
Castaldello et al. [57]	+	o	-
Liu et al. [13, 58, 59]	+	+	o

1.3.2 Microfluidic devices for the investigation of medium composition

According to Fig. 1.5 four main concepts can be used to investigate the effect of media on the growth of microalgae. (i) A mCGG feeding into growth chamber arrays [63–67]. (ii) Diffusion based gradients between parallel supply channels [13, 56, 58]. (iii) Separate supply channels for each growth chamber array [68, 69] and (iv) pneumatic values for dynamic medium exchanges [55, 70]. In detail:

Zheng et al.*: [63] used a multilayer microfluidic device to test the toxicity of chemicals on microalgae. The bottom layer contains a mCGG with eight output channels. The top layer contains 16 microfluidic photobioreactors, each with a volume of 240 nL. A semi-porous membrane is placed between the two layers to allow nutrients to diffuse towards the microorganisms while containing the microalgae within the culturing chambers. The bottom and top layers are made from PDMS, while the semi-porous membrane is made from polycarbonate. The setup enables the online measurement of the chlorophyll autofluorescence and the concentration of cells.

Bae et al.: [64] constructed a microfluidic chip that consists of a mCGG with eight output channels. A row of five photobioreactos, each with a volume of 0.28 nL, is connected to each output channel. The device was used to optimize the sodium acetate concentration for a mixotrophic *C. reinhardtii* culture. The growth rate is calculated from fluorescence intensity. A lipid staining method is used to investigate the lipid content.

Eu et al.: [70] presented a microfluidic platform that enables the cultivation of microalgae under controlled environmental conditions for up to five days. The chip contains two rows of four photobioreactors. Twelve medium supply channels are used in conjunction with 14 valves to control the medium within the photobioreactors. Four additional channels, in conjunction with two valves, are used for cell loading and harvesting. The effect of different medium compositions on microalgae cells was studied using this setup, with a control experiment always running in parallel. Growth rates are tracked using time-lapse microscopy, while lipid content is measured using nile red staining.

Kwak et al.: [71] published a microchip made from PDMS with two rows of eight photobioreactors. Each chamber contains approximately 176 µL and is connected to individual input and output channels. Growth rate determination is performed by measuring the OD at 680 nm.

Yang et al.: [65] used a similar concept as Bae et al. for medium optimization of the cyanobacterium PCC7942. Here, the mCGG has six output channels leading into six photobioreactors, each containing 400 µL. The OD was measured at 730 nm.

Luke et al.: [55] fabricated a microfluidic device based on PDMS for cultivating microalgae under dynamic environmental conditions. The device includes a 0.7 mm radius photobioreactor. Its height is adjustable for different species. It yielded a volume of 1.9 nL for *Synechocystis* sp. PCC6803 (PCC6803), 1.13 nL for PCC7942 and 5 nL for *Chlorella sorokiniana* (*C. sorokiniana*). It also includes two media ports, two waste ports and a cell loading port. The streams from the two media ports can be dynamically mixed in a user-defined ratio. This so-called Dial-a-Wave system was used to investigate the response of *C. sorokiniana* to fluctuating nitrogen concentrations. The number of cells present within the photobioreactor as well as their size is quantified using time-lapse microscopy and automated image analysis.

Yu et al.: [68] presented microfluidic device for observing PCC6803. The microfluidic chip contains two rows of 48 photobioreactor, each with a volume of 40 nL. This design allows each photobioreactor to be addressed individually with a separate medium. The number of cell and their surface area is analyzed by taking microscopic images every 10 minutes, followed by automated image analysis.

Paik et al.: [66] constructed a mCGG with two inlets and seven outlets connected to perfusion bioreactors. The device is built from two PDMS modules: one containing the mCGG and the other the photobioreactors. Permeable membranes are placed between them. The system was used to investigate the effect of the NH_4^+/PO_4^{2-} concentration on lipid production in *C. reinhardtii*.

Zheng et al.*: [67] published a microfluidic device to reduce experimental effort for toxicity test on microalgae. The designs always includes a dilution network connected to photobioreactors. Different dilution and mixing networks are applied. The photobioreactor are always 2 mm long and 1.2 mm wide. The dilution and mixing networks are designed by modeling of equivalent electric circuits. Microalgae cells are observed with an inverted microscope. The growth rate and motility of the cells were investigated using image analysis of fluorescence pictures of individual cells.

Westerwalbesloh et al.$^+$: [69] used a PDMS microfluidic chip composed of four arrays of 400 photobioreactors. Each array is fed by a separate inlet. The volume of each photobioreactor is approximately 32 pL. Time-lapse microscopy and computer-aided image analysis are used to determine the track the number of cells in a photobioreactor. The chip was used to evaluate the effect of different PFD on the growth of *C. sorokiniana*. Although used for a different purpose in the cited study, the four inlets allow different medium to be applied in parallel experiments. Therefore, the system is considered in the context of medium optimization in this review.

Tab. 1.2: Microfluidic devices for the investigation of medium composition. Simple design: (Good: + , Neutral: o , Weak: -), Multi-value/parameter testing: (Good: + , Neutral: o , Weak: -), Single-cell resolution (Good: +, Neutral: o, Weak: -).

Author	Simple design	Multi-value/ parameter testing	Single-cell resolution
Zheng et al.* [63]	-	+	o
Bae et al. [64]	+	o	o
Eu et al. [70]	-	+	+
Kwak et al. [71]	o	o	-
Yang et al. [65]	+	o	-
Luke et al. [55]	+	o	+
Yu et al. [68]	-	+	+
Paik et ak. [66]	o	o	-
Zheng et al.* [67]	-	+	o
Westerwalbesloh et al.$^{+}$ [69]	+	-	+

1.3.3 Microfluidic devices with On-Chip CO_2-Control

The implementation of on-chip O_2 control during microfluidic cultivation has previously been undertaken by other researchers. Concepts include mini-incubators [72] or integrated on-chip O_2 perfusion chambers [73]. The same concepts can be used for CO_2 control; however, the equilibrium mentioned in Eq. 1.6 makes CO_2 control a bit different. Also, due to their slow growth, fast switching is not necessary. Due to the limited amount of literature on CO_2 control for microalgae, the scope of the review has been widened in this section to include devices for other microorganisms. Nevertheless, only a few studies were found. In several of the above-discussed studies, the microfluidic chips are placed in an incubator with an enriched CO_2 concentration [37, 38, 55, 62, 68, 71]. In other studies inorganic carbon is supplied by adding bicarbonate to the medium [65, 74]. This was not considered to be *on-chip CO_2 control*.

Microalgae

Choi et al.: [75] used a PDMS microfluidic platform to study the movement of *C. reinhardtii* towards favourable concentrations of HCO_3^-, using an HCO_3^- gradient. The microfluidic device consists of two reservoirs, one for cells and one for nutrients, connected by a channel. A circular observation chamber with a volume of approximately 2.5 nL is

located between the two reservoirs. Microchannels filled with agarose, placed between the nutrient reservoir and the observation chamber, allow HCO_3^- to diffuse towards the cell reservoir while hindering microalgal movement, thus the concept is similar to Fig. 1.5 (b, ii). This creates a HCO_3^- concentration gradient along the connecting channel. Chemotaxis was evaluated by manually counting the number of cells inside the observation region.

Xu et al.: [76] developed a microfluidic poly(methyl methacrylate) (PMMA) device consisting of eight culture chambers, each with a volume of 5 µL (0.5 mm depth, 1 mm width, 10 mm length). They used a mCGG to create eight different CO_2 concentrations between 50 and 280 ppm (Fig. 1.5 (b, i). CO_2 was delivered from underneath through a semipermeable membrane. Furthermore, the CO_2 concentration was simulated with COMSOL. The system was used to study the effect of CO_2 concentrations lower than 269 ppm (ambient air) on the growth of *C. reinhardtii*.

Yusuf et al.: [77] used a mCGG to create six different CO_2 concentrations on a chip (Fig. 1.5 (b, i). The mCGG and the photobioreactors are created using a milling machine. While the material used is not explicitly stated, the paper implies the use of a rigid see-through polymer block. The mCGG is sealed from above. The 19.25 µL culture chamber is placed on top of the mCGG, with the outlets feeding into it. The microalgae species *Picochlorum* sp. is used as the model organism in this case study. Microalgal growth is investigated by taking images with a microscope.

Mammalian cell

Forry and Locascio: [78] developed a microfluidic PDMS device for cultivating mouse fibroblasts. The cultivation chamber has a volume of about 45 nL. CO_2 is delivered to the culture chamber by diffusion from a side channel. CO_2 is indirectly measured by pH detection using a pH-sensitive dye. An equilibrium between the cultivation chambers and the CO_2 supply channel (5% CO_2) is reached within 5 minutes.

Takano et al.: [79, 80] developed a microfluidic device comprising two cell culture compartments, each with a volume of 78 nL. The PDMS chip is surrounded by an outer water reservoir filled with a bicarbonate/carbonate buffered solution. This prevents evaporation of water from the cell culture compartments and buffers the CO_2 concentration in the cell culture medium. CO_2 incubation of COS-7 (mammalian cell culture) cells is maintained for 17 days. In a subsequent publication, the formulation of the medium reservoir is modified to control CO_2 and O_2 levels simultaneously.

Tab. 1.3: Microfluidic devices with On-Chip CO_2-Control. Simple design: (Good: + , Neutral: o , Weak: -), Multi-value/parameter testing: (Good: + , Neutral: o , Weak: -), Single-cell resolution (Good: +, Neutral: o, Weak: -).

Author	Simple design	Multi-value/ parameter testing	Single-cell resolution	CO_2 validation method
Microalgae				
Choi et al. [75]	+	-	o	Fluorescein tracer experiments
Xu et al. [76]	o	o	o	COMSOL simulation
Yusuf et al. [77]	+	o	o	-
Mammalian cell				
Forry and Locascio [78]	o	-	+	pH sensitive dye
Takano et al. [79, 80]	o	-	+	Direct pH measurement

1.3.4 Evaluation of the preliminary literature

The results of the literature review are summarized in Tab. 1.1 for the illumination control, 1.2 for the nutrient control and 1.3 for the CO_2 control. An overall summary of the previously presented studies is shown in Tab. 1.4. From the analysis of these tables the following conclusions are drawn:

- Many 'microfluidic' devices for the cultivation of microalgae are presented in literature. Thereby the term 'microfluidic' is used loosely for devices across different magnitudes of fluid volumes (From 32 pL to 400 µL). Microfluidic devices, that limit cell growth to monolayers and enable growth analysis at single-cell resolution were spars.
- Microfluidic devices are commonly applied to investigate how nutrients or the concentration of nutrients influence the growth of microalgae. The number of parallel conditions was similar to that of microtiter plates. Some devices are more sophisticated than others. Only two authors used dynamic changes in the medium. Luke et al. [55] enabled the mixing of two media in a defined ratio (Dial-a-wave) [55]. The device presented by Eu et al. [70] allows the user to switch between four different media.
- Not many devices, enable the parallel investigation of different CO_2 concentrations or light intensities. Except from the devices presented by Liu et al. [58, 59] and Castaldello et al. [57] these cultivation devices used are among the most sophisticated and versatile. This also makes them the most complicated to use and the most prone to experimental failure. The devices by Liu et al. and Castaldello et al. are elegant and easy-to-use. However, their cultivation chambers are high-volume and do not allow growth analysis at single-cell resolution.
- All devices meant for CO_2 control were capable of single-cell analysis, however the images were of low magnification and poor quality in comparison.
- Dual-parameter investigation was demonstrated in three case studies:
  - The one by Nguyen et al. [61]. In this study, the illumination system was based on that presented by Graham et al. [60]. However, the study did not include defined microstructures or single-cell analysis. Additionally, the system only allowed endpoint measurements.
  - Two case studies from Liu et al., one involving a dual nutrient gradient [13] and the other a light-intensity and nutrient gradient. However, these studies did not include single-cell analysis, and growth was not restricted to monolayers.

Tab. 1.4: Comparison of microfluidic devices for the cultivation of microalgae. *: same author, + author from the IBG-1.

Author	Size compartments	Number compartments	Parallel Conditions	Dynamic control
		Illumination		
Kim et al. [62]	54 nL	64	64	No
Graham et al. [60]	27 nL	Two designs; either 120 or 280	120 or 280	No
Castaldello et al. [57]	20 µL	24	6	No
Liu et al. [13, 58, 59]	1 nL	64	64	No
		CO_2		
Choi et al. [75]	2.5 nL	1	1	No
Xu et al. [76]	5 µL	8	8	No
Yusuf et al. [77]	19.25 µL	1	6	No
		Medium components		
Zheng et al.* [63]	240 nL	16	8	No
Bae et al. [64]	0.28 nL	40	8	No
Eu et al. [70]	0.76 nL	8	2	Yes
Kwak et al. [71]	176 µL	16	16	No
Yang et al. [65]	400 µL	6	6	No
Luke et al. [55]	1,9 nL/1,13 nL/5 nL	1	1	Yes
Yu et al. [68]	40 nL	96	96	No
Paik et al. [66]	n/a	7	7	No
Zheng et al.* [67]	240 nL	n/a	n/a	No
Westerwalbesloh et al.+ [69]	32 pL	1600	4	No

1.4 Scope of this thesis

This thesis aims to overcome fundamental limitations of conventional photobioreactors by establishing a novel microfluidic experimental platform. These limitations include the inability to uniformly illuminate all cells within a photobioreactor and the inability independently observe cell division, growth and morphological changes. Here, microfluidic cultivation in monolayer growth chambers to avoid self-shading of cells is combined with time-lapse imaging at single-cell resolution to enable independent observation of cell growth, morphology, and division. The design aspects of the microfluidic platform are listed in Tab. 1.5.

To the best of the author's knowledge, there is currently no device that fulfills these requirements sufficiently. The following pages outline the development process and subsequent application of the experimental platform. The first chapter, lists general protocols, e.g. for conducting microfluidic experiments, maintaining cultures and 3D printing. The rest of this thesis is split into two parts.

Part I: features the development of the platform alongside proof-of-concept experimentation. First, a growth-light system to drive photosynthesis is constructed and characterized, followed by cultivation under homogeneous growth-light illumination. Next, a protocol is developed for conducting experiments with a light-intensity gradient. Finally, CO_2 control is added. Parts of the results in the first part of this thesis were published in Witting et al. [1].

Part II: presents two case studies in which the microfluidic cultivation platform helped answer biological questions by revealing phenomena masked during bulk cultivation by enabling discrimination between cell morphology, cell growth, and cell division. In both studies mutant cell lines from the genus *Synechocystis* are analyzed.

- A case study aimed at characterizing *Synechocystis* strains that lack the ability to synthesize glycogen as internal carbon storage. Light intensity gradients and homogeneous cultivation with a day/night rhythm were applied here. Furthermore, the concept of integrating nutrient spiking into the setup to compensate for glycogen deficiency at night was tested and discussed.
- A case study aimed at investigating the circadian rhythm in *Synechocystis*. Circadian rhythms were observed in both the phase-contrast intensity of individual cells and the average phase-contrast intensity of the entire population. Therefore, the phase shift and period of the rhythm in individual cells must be highly similar throughout the entire population.

Tab. 1.5: Design aspects of the microfluidic experimental platform presented in this thesis.

Restriction	Design aspect	Implementation
Self-shading of cells	Monolayer growth	Growth chamber height should match microorganism diameter Illumination from a direction orthogonal to the cultivation plane
Differentiation between cell growth cell division and cell morphology	Single-cell imaging	Use of a transparent polymer (PDMS) for cultivation chip production
Slow growth of phototrophic microorganisms	Dual parameter investigation of light intensity and the CO_2 concentration	Linear light-intensity gradient Dynamic CO_2 control
Microfluidic devices are often complex, thus hindering application	Straightforward and user-friendly design	Keep the microfluidic structures as simple as possible Integrate environmental control into the microscope's periphery, if possible

2 General experimental protocols

In the past, microfluidic single-cell cultivation devices developed at the IBG-1 were mainly used to evaluate growth parameters of industrially important heterotrophic microorganisms such as *Corynebacterium glutamicum* (*C. glutamicum*) or *Escherichia coli* (*E. coli*) [32, 81, 82]. Consequently, most preculture protocols prior to microfluidic experiments were optimized for heterotrophic microorganisms. Although some experience with microalgae has been gained previously [69], most of the workflows presented in this section were developed as part of this thesis or adapted from collaborating working groups.

2.1 Laboratory scale cultivation

2.1.1 Continuous cyanobacteria cultivation in shake flask

For phototrophic cultivation, a commercial LED panel (GrowLight Duo, Venso EcoSolutions, Germany) was placed on an incubation shaker (Inkubationsschüttler 3031, GFL, Germany). Using a spectrometer (Li-180, LI-COR, US), the growth light was set to emit approximately 20 - 30 $\mu E \cdot m^{-2} \cdot s^{-1}$. Cyanobacteria were cultivated in 100 ml shake flasks with chicane filled with 30 mL of BG11 medium. These were cultivated at 110 rpm continuous shaking and a temperature of 30 °C. Every 14 days, 2 mL of culture was propagated into fresh medium. For the first 24 hours after propagation, the flasks were covered with a white cloth to reduce light exposure. Antibiotics were added to the growth medium as needed to ensure genetic stability. Stock solutions were prepared and stored in the freezer as aliquots. All respective concentrations are listed in Tab. 2.1. The OD at 720 nm of the shake flask culture was measured using a benchtop photometer (UV-1800, Shimadzu, Japan). These measurements were collected in an Excel spreadsheet to monitor the growth of the cyanobacteria in the shake flask culture (Fig. 2.1). If contamination occurred, the permanent culture was restarted from the cryo stock. The cyanobacteria were therefore first plated from the cryo stocks. After the plate had been successfully incubated for around two weeks, the liquid culture was inoculated from it.

Antibiotic	Final concentration [µg·mL^{-1}]	Stock concentration [mg·mL^{-1}]	Supplier
Kanamycin (Km)	25	50	Carl Roth
Chloramphenicol (Cl)	10	34	Cayman Chemical
Spectinomycin (Sp)	20	20	Cayman Chemical

Tab. 2.1: Concentration of antibiotics during permanent shake flask culture.

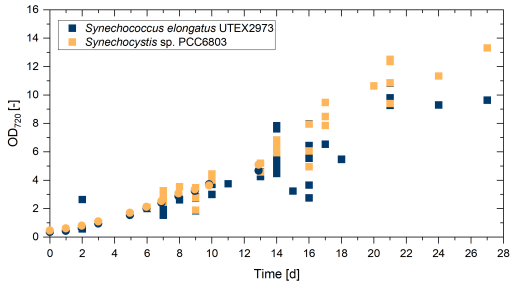


Fig. 2.1: Growth of cyanobacteria model organisms in a shake flask culture. The OD_{720} was measured once at the beginning of the project to estimate the growth rate (circles) and regularly to calculate the inoculation volume for Multi-Cultivator 1000-OD (MC) cultivation (squares). The estimated doubling times for *Synechococcus elongatus* UTEX2973 (UTEX2973) (blue) and PCC6803 (orange) were 77.4 and 85.9 hours, respectively.

2.1.2 Multi-Cultivator cultivation

A commercial photobioreactor (Fig. 2.2) (Multi-Cultivator 1000-OD, Photon Systems Instruments, Czech Republic) was used for precultivation and growth rate estimation of cyanobacteria. The Multi-Cultivator was equipped with an additional aeration tube to enable parallel cultivation with ambient air and CO_2 enriched air. The aeration tube for CO_2 enriched air was connected to a CO_2 controller (CO_2-Controller 2000, PECON, Germany), while ambient air was supplied by the built-in pump. The cultivation tubes were inoculated to an OD_{720} of 0.1 in BG11 growth medium. Precultures for microfluidic experiments were performed with ambient air and a PFD of 80 µE·m^{-2}·s^{-1}. The temperature was set according to that of the experiment. Samples for microfluidic cultivation were collected via a three-way valve and transferred to a sterile syringe. A custom Python script was used for the data plotting and growth rate calculation. The calculation of the growth rate included the following steps: (i) All OD_{720} values under 0.05 and over 0.4 were cut off. (ii) The natural

logarithm of the cutoff OD_{720} over time was formed. (iii) A linear model was fitted onto the natural logarithm using *numpy* [83]. (iv) The slope of the linear model is the growth rate.

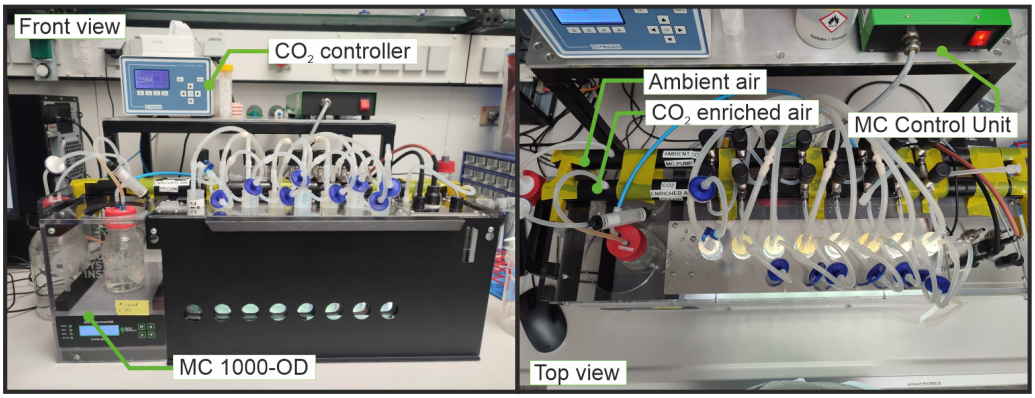


Fig. 2.2: Multi-Cultivator 1000-OD photobioreactor. Left: Front view. Right: Top view. The images show the device undergoing parallel cultivation in eight separate cultivation tubes. The light-intensity and regime (Day/Night), strain and growth medium can be controlled for each cultivation tube individually. A CO_2 device and an additional gas dispenser were manually added to the setup. This enabled the device to bubble some tubes with ambient air and others with CO_2-enriched air. All tubes are operated with the same temperature.

2.1.3 Preparation of liquid BG11 growth medium

All stock solutions were prepared in advance and stored in the refrigerator at 4 °C. After weighing the components, the solutions were sterile filtered, except for the HEPES buffer. This solution was adjusted to a pH of 7.5 with NaOH and then autoclaved. The composition of the stock solution and the final concentration of each component are indicated in Tab. 2.2. One or two liters of medium were usually prepared every four to six weeks. The following steps were involved in preparing the final mixture from the stock solution:

1. Fill a glass bottle with half of the desired final volume of DI water.
2. Add the appropriate volumes of stock solution under sterile conditions.
3. Fill the solution up to the desired final volume with DI water using a measuring cylinder.
4. Stir for at least two minutes.
5. Sterile filtration of the mixture into a sterile glass bottle.
6. Store at room temperature for a maximum of six weeks.

Tab. 2.2: Composition of the BG11 liquid growth medium. The number before the name of the stock solution (e.g. 1000 x) indicates the concentration factor.

Stock solution	Component	Stock Concentration [g/L]	Concentration [g/L]
100 x Macronutrients	$NaNO_3$	149.6	1.496
	$MgSO_4$ x 7·H_2O	7.5	0.075
	$CaCl_2$ x 2·H_2O	3.6	0.036
	Citric acid	0.650	$6.500 \cdot 10^{-3}$
	EDTA-Na_2	0.100	$1.000 \cdot 10^{-3}$
1000 x Trace metal	H_3BO_3	2.860	$2.860 \cdot 10^{-3}$
	$MnCl_2$ x 4·H_2O	1.810	$1.810 \cdot 10^{-3}$
	$ZnSO_4$ x 7·H_2O	0.222	$2.220 \cdot 10^{-4}$
	Na_2MoO_4 x 2·H_2O	0.391	$3.910 \cdot 10^{-4}$
	$CuSO_4$ x 5·H_2O	0.079	$7.900 \cdot 10^{-5}$
	$Co(NO_3)_2$ x 6·H_2O	0.049	$4.947 \cdot 10^{-5}$
1000 x K_2HPO_4	K_2HPO_4	30.480	0.030
1000 x Na_2CO_3	Na_2CO_3	20.030	0.020
1000 x Fe-NH_4-citrate	Fe-NH_4-citrate	6	$6.00 \cdot 10^{-3}$
20 x HEPES Buffer	HEPES	238.3	4.766

2.1.4 Preparation of BG11 agar plates

The protocol for preparing BG11 agar plates involved the following steps:

1. Preparation of a double-concentrated BG11 mixture. The previously mentioned protocol was therefore followed, with the volume of each stock solution doubled.
2. Prepare a mixture of 3 g of Bacto agar in 100 ml of DI water, then autoclave the mixture.
3. Mix the two solutions in a 1:1 ratio.
4. Pour the solution into plastic petri dishes.
5. Store in the refrigerator at 4 °C.

2.1.5 Cyropreservation & plating out cyanobacteria

Two-milliliter reaction tubes were used for cryopreservation. At least three tubes were prepared for each strain. The protocol included the following steps:

1. Take a 2 mL sample from the shake flask culture during exponential growth. Ideally, the OD_{720} should be between 1 and 3.
2. Spin the sample in a centrifuge (MiniSpin Plus, Eppendorf, Germany) for five minutes at 4,000 rpm and room temperature.
3. Discard the supernatant using a pipette.
4. Resuspend the pellet in 200 µL of fresh BG11 growth medium.
5. Add 25 µL of autoclaved Dimethyl sulfoxide (DMSO) and mix.
6. Quickly freeze the reaction tubes at -80 °C.

To plate out the cyanobacteria, the reaction tubes were removed from the freezer. Then, a small amount of the frozen culture was transferred onto sterile BG11 plates. The plate was sealed with laboratory film and incubated at 30 °C. For the first 24 hours, the plate was covered with a cloth. After one to two weeks, a visible cyanobacteria lawn began to form on the plate. Using a sterile pipette tip bent at a 90° angle, some material was scraped from the lawn into a 1.5 mL reaction tube containing 500 µL of BG11 growth medium. The contents of the reaction tube were mixed and transferred into a shake flask containing 30 mL of BG11 growth medium. From this point on, the culture was treated as described above.

2.2 Microfluidic cultivation

2.2.1 Cultivation chip design & production

The microfluidic designs used in this study were created using CleWin5 (WieWeb Software; Netherlands). Starting from an existing design, a series of layouts were created to optimize microfluidic bioreactors for the growth of phototrophic microorganisms. The master molds for the newly designed layouts consist of a 4" silicon wafer carrying two layers of SU-8 photoresist. These were fabricated at the Helmholtz Nano Facility [84] using maskless lithography. For a more detailed process description, the reader is referred to App. A: Tab. A.1 and to Witting et al. [1]. As illustrated in Fig. 2.3, the workflow for PDMS molding and subsequent chip fabrication included the following steps:

1. Mix PDMS and curing agent (SYLGARD™184 Silicone Elastomer Kit) in a 10:1 ratio.
2. Remove air bubbles in an exicator at about 200 mbar for at least 45 minutes.
3. Clean the silicon wafer with Isopropyl alcohol (IPA).
4. Pour the mixture onto the cleaned wafer and bake for at least two hours at 80 °C.
5. Remove the polymerized PDMS from the silicon wafer and subsequently cut it manually.
6. Wash the PDMS chips under a fume hood. First: 45 min in n-pentan to remove uncured monomers. Then: Twice for 45 min in aceton to remove residual n-pentan.
7. Dry the chips overnight under a chemical fume hood.
8. Collect the chips after drying overnight and store them in a clean petri dish until use.

For standard experiments, the thickness of the culture chips was 3-5 mm. For experiments with integrated CO_2 control, the height of the cultivation layer was reduced to approximately 1 mm. The final chip assembly was typically performed one to three days before or on the day of the experiment. The parameters for the O_2 plasma treatment are listed in Tab. 2.3. The standard assembly protocol involved the following steps:

1. Punch the inlet and outlet holes into the PDMS using a 0.5 mm disposable biopsy punch (World Precision Instruments, USA).
2. Clean the culture chips and a glass substrate (39.5 mm x 34.5 mm x 0.175 mm, Schott AG, Germany) with IPA. For the long cultivation chips, different substrate dimensions were used: 50 mm x 25 mm x 0.175 mm or 70 mm x 25 mm x 0.175 mm.
3. Transfer the cultivation chip and glass substrate into a plasma oven (Femto Plasma Cleaner, Diener Electronics, Germany). It is important that the side of the cultivation chip containing the cavities faces upwards.
4. Perform O_2 plasma treatment for 25 seconds (Tab. 2.3).
5. Flip the side of the cultivation chip with the cavities onto the glass. If necessary: Aid the bonding process by gently tipping the PDMS with the tip of a metal tweezer.
6. Place the bonded chip in an oven at 80 °C for two minutes.

Tab. 2.3: Standard parameters for oxygen plasma treatment.

Parameter	Setting
Evacuation pressure	0.16 mbar
Pressure during O_2 gassing	0.80 mbar
Plasma power	510 W

For experiments with integrated CO_2 control, the following steps were performed prior to the process described above:

1. Rinse the thin cultivation layer and the CO_2 perfusion chamber using IPA.
2. Transfer of the cultivation chip and the CO_2 perfusion chamber into the plasma oven on a carrier glass slide.
3. Perform O_2 plasma treatment for 50 seconds (Tab. 2.3).
4. Flip the CO_2 perfusion chamber onto the side of the cultivation chip without structures for microfluidic cultivation. If necessary: Aid the bonding process by gently tipping the PDMS with the tip of a metal tweezer.
5. Place the bonded chip in an oven at 80 °C for five minutes.

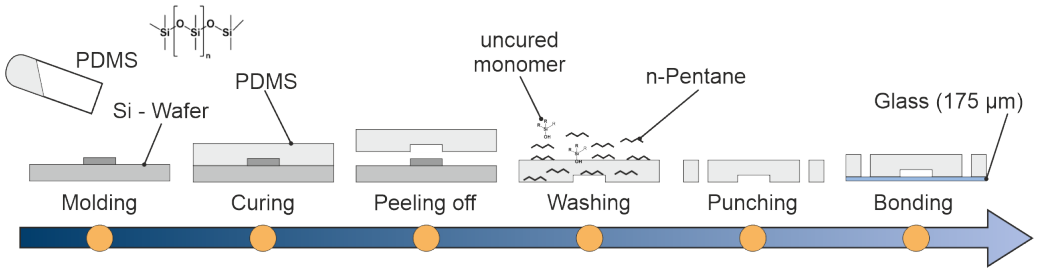


Fig. 2.3: Moulding and assembly of microfluidic cultivation chips. Soft lithography was mostly performed according to a published protocol [85]. Small deviations from the published protocol were implemented to perform light-gradient experiments (different type of glass substrate) and the CO_2 control experiments (bonding the CO_2 perfusion chamber to the cultivation layer).

2.2.2 Time-lapse microscopy

All the experiments presented in this thesis were conducted using the same microscopy setup. (Ti-E, Nikon, Japan). A list of all peripheral devices can be found in Tab. 2.4.

Tab. 2.4: Microscopy setup and peripheral devices.

Hardware		
Part	Product name	Manufacturer
Camera (Right side)	DS-Fi3	Nikon (Japan)
Camera (Left side)	Andor Zyla	Oxford Instruments (Great-Britain)
Temperature Incubator	Incubator NL 2000	Pecon (Germany)
Heating Unit	Heating Unit 2000	Pecon (Germany)
Temperature Controller	TempController 2000-2	Pecon (Germany)
Syringe pump	neMESYS Low Pressure	Cetoni (Germany)
Episcopic lamp	SOLA SE II	Lumencor (USA)
Diascopic lamp	pE-100	CoolLED (Great-Britain)
Data acquisition device (DAQ-device)	USB-6008	National Instruments (USA)
Software		
Part to control	Name & Version	Manufacturer
Microscope	NIS-Elements AR 4.51.00	Nikon (Japan)
Microscope	NIS-Elements AR 4.40.00	Nikon (Japan)
Syringe pump	QmixElements 32-bit	Cetoni (Germany)

Experiments involving cyanobacteria were conducted using PTFE tubing (PTFE 1/1" OD, 0.5 mm ID, CS Chromatographie, Germany). General Purpose Dispense-Tips (Nordson, Germany) were used to connect the tubing to the syringes. To connect the tubing to the cultivation chip inlet, the plastic was removed from the dispense-tip. The residual metal needle was connected to the tubing on one side and plugged into the cultivation chip on the other. The inflow and outflow tubing were prepared in bulk and stored until needed. Starting a microfluidic experiment involved the following steps:

1. Place the cultivation chip in the incubator and preheat it overnight to minimize focus loss.
2. If applicable, calibrate the light-intensity gradient, set the light intensity, or program the day/night cycle. A detailed description of these steps is provided later in the text.
3. Focus the Plan Apo λ 100× Oil Ph3 DM objective (Nikon, Japan) onto the cultivation chip using immersion oil (Immersion Oil F 30cc, Ibidi, Germany).

4. Connect the pre-assembled outflow tubing. 5 mL reaction tubes (Eppendorf, Germany) were used to collect the outflowing medium.
5. Carefully fill the medium into 3 mL sterile plastic syringes (Omnifix-F 3 mL, Braun, Germany). Then connect them to the tubing. Mount the syringes in the syringe pump. Flush the chip with medium at a rate of 200 nL·min^{-1} for at least 20 minutes.
6. If necessary, rotate the camera to align the chambers straight, and then recalibrate the objective.
7. Take a sample from the MC. Dilute the sample if needed.
8. Inoculate microorganisms into the cultivation chip using the technique described by Probst et al. [86].
9. Turn on the built-in Perfect focus system (PFS). Manually select chambers. Set the time interval and imaging methods. For each chamber, the x- and y-position as well as the PFS offset are saved.
10. Start the experiment.
11. If needed, correct the focus around two to four hours after the start of the experiment.

Generally many reasons can lead to experimental failure. Sometimes, the entire experiment is lost; at other times, growth fails in one or more of the growth arrays. Where possible, results from multiple partly failed experiments were combined for analysis. In some cases, the analysis was stopped at the point where the experimental failure began. General advice for avoiding the reasons for failure shown in Fig. 2.4 are:

- Subfigure 2.4 (a): If possible avoid high salt concentration as these can lead to precipitation. Sterile filtrate the medium before usage for the same reason.
- Subfigure 2.4 (b): Avoid conducting experiments on warm, humid summer days. Experience has shown that plasma bonding fails more frequently under these weather conditions, leading to focus loss and non-monolayer cultures.
- Subfigure 2.4 (c): Meticulously check the tubing and medium syringes for residual air bubbles. Even a single air bubble can kill all the bacteria in a growth array.
- Subfigure 2.4 (d): Although it is not possible to work in a completely sterile environment, keep open lids containing medium or bacterial cultures closed for as short a time as possible. Thoroughly disinfect the microscope and workplace after every experiment. In the case of cyanobacteria, be thorough with the permanent shake flask culture. Renew the culture if necessary.

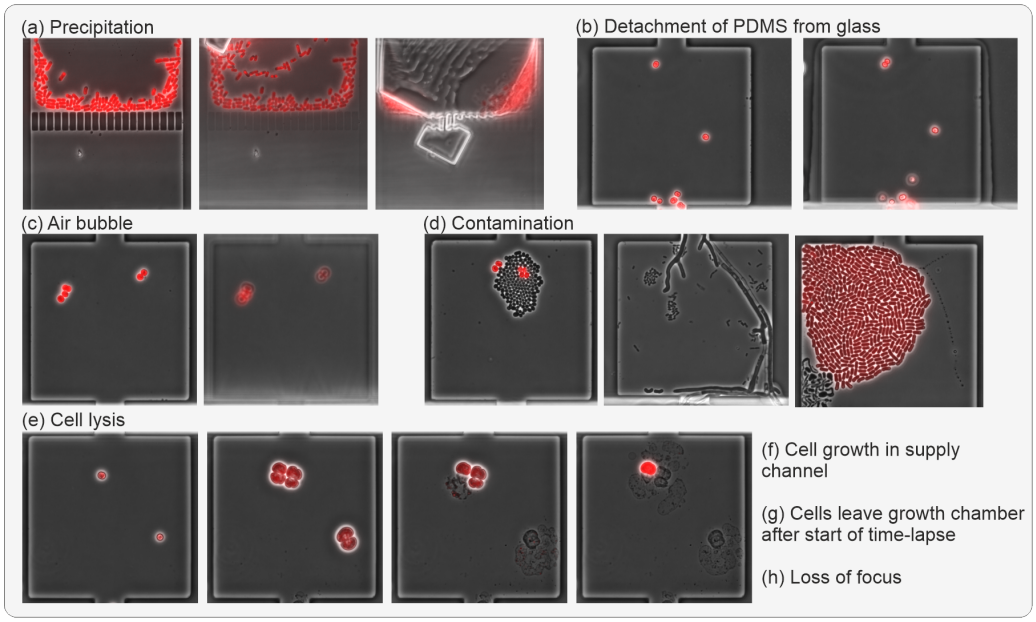


Fig. 2.4: Frequently experienced reasons for experimental failure. (a) Time-lapse images of an *S. elongatus* strain in a microfluidic co-culture chamber [87]. During the time-lapse experiment, a high concentration of NaCl led to the formation of NaCl crystals inside the supply channels and growth chambers, resulting in a failed experiment. (b) Time-lapse images of a PCC6803 strain in a microfluidic growth chamber. In this example, poor bonding quality caused the chamber to detach, resulting in a loss of focus. Although cell growth continued, image segmentation was of poor quality, so no quantitative data could be acquired from this experiment. (c) Time-lapse images of a PCC6803 strain in a microfluidic growth chamber. This example illustrates how an air bubble in the supply channel can dry out the growth chamber, leading to cell death. No growth was observed even when the growth medium was flowing again. (d) Images from various time-lapse experiments in which contamination occurred. Left: Growth chamber inoculated with a PCC6803 strain (red) and a cocooid contamination (black). Although the growth medium (BG11) did not contain a carbon source, growth of the contamination was observed. Middle: Growth chamber inoculated with a *E. coli* strain and a fungal contamination. Right: Growth chamber inoculated with a *S. elongatus* strain (red) and a contamination (black). Although the growth medium (BG11) did not contain a carbon source, growth of the contamination was observed. (e) Time-lapse images of a PCC6803 strain in a microfluidic growth chamber. This example illustrates how insufficient chamber height can result in cell lysis. (f) Cell growth in the supply channel can lead to channel clogging, which hinders growth in the growth chambers due to limited nutrient supply. (g) In experiments where cells were flushed out of growth chambers after the time-lapse started, the microscope imaged empty growth chambers, thus creating unusable data. (h) A loss of focus, for example due to the thermal expansion of the cultivation chip, leads to poor cell segmentation quality. No quantitative data can be acquired from such images.

- Subfigure 2.4 (e): Make sure that the chamber height is suitable for the bacteria being cultivated, as mechanical stress can cause cell lysis.
- Subfigure 2.4 (f): Flush medium at an elevated volumetric flow rate (e.g. 1000 nL · min^{-1}) for at least 20 min after inoculating. If needed, inoculate bacteria from the outflow.
- Subfigure 2.4 (g): Set a moderate flow rate after post-inoculation flushing (e.g. 200 nL · min^{-1}). After 1 - 2 h after experimental start, check whether bacteria are still present; if not, choose a new chamber.
- Subfigure 2.4 (h): Preheat the cultivation chip overnight. Correct the focus after 2–4 hours from the start of the experiment.

2.2.3 Post experimental workflow

After the experiment was finished, the tubing and cultivation chip were discarded. The metal needles and tips were collected and stored in ethanol. The needles and tips were regularly cleaned in an ultrasonic bath and dried for reuse. The microscope and workplace were disinfected. The .nd2 file was split using the command (*File -> Import/Export -> Split Multipoints ...*). Some chambers were manually discarded for three main reasons: (i) Poor image quality. (ii) No growth. (iii) Cells were flushed out of the chamber shortly after the experiment began. The data files were loaded individually into Fiji [88]. Image sequences were registered using the *Correct 3D drift* plugin [89]. The code for the plugin was modified to change the default values (See App. A: Fig. A.1). The images were then rotated (*Image -> Transform -> Rotate*), cropped (*Image -> Crop*) and exported (*File -> Save As -> Tiff...*) as an .tif files. Finally, the .tif files from one channel on a microfluidic were uploaded as a dataset onto an OMERO server [90] for storage and further processing. In order to train the Deep learning (DL) cell segmentation model, 20 exemplary image crops were selected using microbeSEG [91] and annotated semi-automatically using the ObiWan-Microbi tool [92]. Based on the annotated data, the Omnipose [93] cell segmentation model was finally fine-tuned. Using the OMERO Python API whole datasets or specific .tif files can be loaded into a jupiter notebook and segmented using their identifier [94]. Using the trained model, cell instances were segmented. In most cases a superordinate script (*ScalingAnalysis.ipynb*) was used to sequentially process all .tif files of a dataset with the same cell-segmentation script and to perform group statistics afterwards. If needed, notebooks were designed to perform meta analysis on multiple *ScalingAnalysis.ipynb* scripts.

The core of the segmentation notebook always consisted of the following steps:

1. Loading of the image sequence from OMERO.
2. Perform segmentation.
3. Rendering a video indicating the segmentation.
4. Filtering artifacts by size or fluorescence intensity or both.
5. Rendering a video indicating the filtered segmentation.
6. Perform data analysis e.g. calculate growth rate.

Calculation of growth rates according to an exponential model included the following steps:

1. The timeframe was manually selected to include the period between the start of exponential growth and overflow of the chamber or the end of cultivation. Where segmentation errors occurred, the timeframe was adjusted to exclude them from the analysis while ensuring there were enough timepoints for a trustworthy analysis.
2. Forming of the natural logarithm of the cell area or cell count.
3. Fitting a linear model onto the natural logarithm within the selected timeframe using *numpy* [83].
4. The growth rate is the slope of the linear model. In most cases the processed data was imported into Origin2020 Pro (Origin Lab, USA) to create figures.

In total 116 microfluidic experiments were performed during the three-year period of work on this thesis. Over 8 TB of image data was produced. Of these, 3,391 image sequences containing 304,138 phase-contrast images were cropped and uploaded to the OMERO server. The average duration of an experiment was at four days. A total of 28,849,128 cell instances were segmented in these. When merged, these cells cover an area of approximately 61 mm^2.

2.3 Other protocols

2.3.1 3D printing

In order to establish the cultivation platform of phototrophic microorganisms, custom-built components had to be integrated into the periphery of the microscope. Prototypes of

custom-built components, such as the custom connectors and master molds for perfusion chambers, were made using 3D printing. The 3D printing workflow included the following steps:

1. Design of the prototype in a CAD software (SolidWorks 2016, Daussault System, France) and converting the design to .stl format.
2. Load the .stl file into the 3D printer software (PreForm), add support structures if necessary, and finally load the file into the 3D printer (Form 3B, Formlabs, USA).
3. Remove the part from the 3D printer. If necessary, rinse with IPA to aid removal from the stage.
4. Clean in an IPA bath for 20 minutes to remove residual resin (Form Wash, Formlabs, USA).
5. Removal of support structures.
6. Post curing (Form Cure, Formlabs, USA).

Tab. 2.5 lists the 3D printing parameters. While the prototypes were produced by 3D printing, the final designs were produced in-house from metal. The main material used was black anodized aluminum to prevent reflections on the optical components.

Tab. 2.5: Process parameters for 3D printing.

Part	Printing		Curing	
	Resin	Layer thickness [mm]	Time [min]	Temp [°C]
Adapter ring for aspheric condenser lens	Grey V4	0.025	60	60
Connector for mounted LED	Tough 2000 V1	0.05	60	70
Connector for LI190R sensor	Tough 2000 V1	0.05	15	70
Master mold for tilted chip	Grey V4	0.025	60	60
Master mold for CO_2 perfusion chamber	Model V3	0.050	60	60

Part I

Platform development and proof-of-concept studies

3 An illumination system to drive photosynthesis during microfluidic cultivation

Parts of this chapter have been published in peer-reviewed journals (I) [1]. Some results were presented as an oral presentation (II) or posters (II, V) at international conferences. Daniel Klein helped to conceptualize some custom-connectors. The drawings he created are indicated in the respective figure description.

3.1 Introduction

When cultivating microalgae under a microscope, providing adequate illumination for photosynthesis is critical [49]. Some authors have reported using the built-in lamp of the diascopic light path to illuminate cyanobacteria on agarose pads or inside PDMS cultivation chips [49, 59, 70]. Others reported using a second lamp coupled into the diascopic light path in combination with a motorized shutter to switch between growth and imaging light [48]. Other growth light sources include external bulbs [56], an LED backlight combined with episcopic imaging from above [60], a circular cool white light LED array fixed around the microscope condenser [47, 52], or a ringlight connected to an external light source [95]. Another publication features a system in which an LED connected to a heat sink was mounted in the microscope's objective turret. During imaging, the objective was moved into the light path and the LED was switched off. This allowed precise control of the illumination. However, objectives that require the use of immersion oil, such as the objective used in this thesis, cannot be used in this setup [69]. Therefore, the magnification was limited. The following requirements were specified for the illumination system used in this thesis:

1. Independence from the diascopic light path. Thus enabling the cultivation chip to be illuminated broadly and the imaging light to be focused.
2. A homogeneous distribution of the light intensity over the cultivation chip area.
3. No temperature increase resulting from the lamp's off-heat or infrared radiation.
4. The option to use an oil objective is available to enable higher magnifications.
5. Ability to shut off the growth light during imaging to enhance image quality.

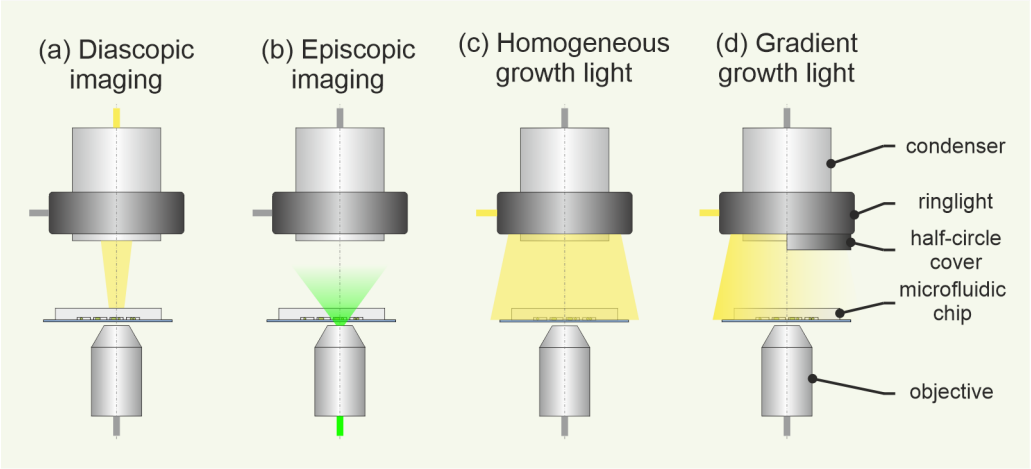


Fig. 3.1: The proposed ringlight illumination system. Overview over the illumination system for phototropic cultivation. A ringlight is mounted around the microscope condenser providing controlled illumination for photosynthesis. (a) During time-lapse imaging the ringlight illumination is temporary turned off to avoid optical interference. Then, the diascopic light path is used for phase contrast imaging. (b) For fluorescence imaging the episcopic light path is used. (c) The ringlight enables homogeneous illumination of the microfluidic chip. (d) A linear light-intensity gradient is generated when shading half of the ringlight emitter-surface with a half-circle cover. The Fig. was reproduced from Ref. [1] with permission from the Royal Society of Chemistry.

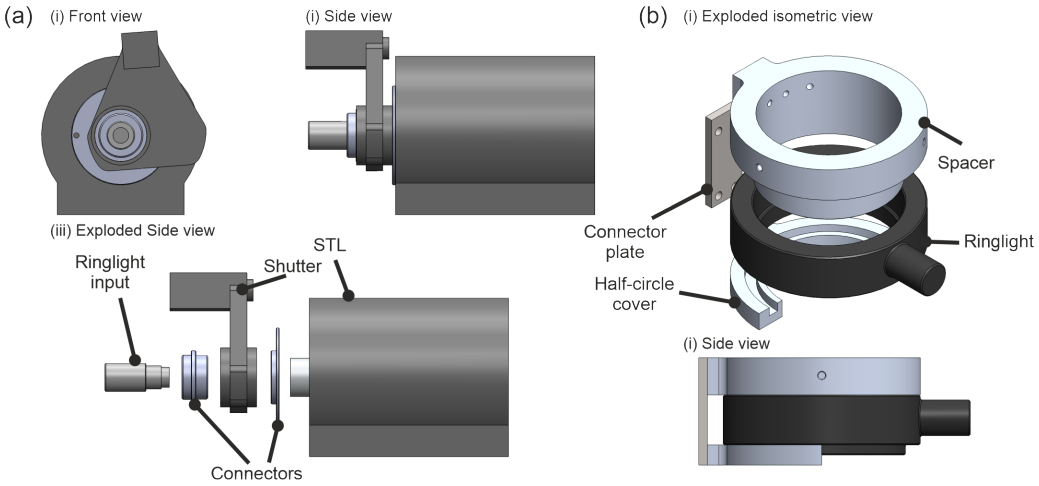


Fig. 3.2: Custom-built components for STL to ringlight illumination system. (a) The connection between the rebuilt STL, shutter and ringlight input. (b) Fixation of the ringlight around the microscope condenser. Technical drawings of the individual components can be found in App. C (a: Fig. C.6 - C.7, b: C.9 - C.12). Subfigure (b): Drawing by DK.

3.2 A ringlight-based illumination system to drive photosynthesis

3.2.1 Establishing a third light-path to deliver energy for photosynthesis

Here, a waveguide with a ringlight end (A08630 Midi Ringlight, Schott AG, Germany) is used to provide illumination for photosynthesis. The ringlight end of the waveguide is fixed around the microscope condenser. The growth light is coupled to the waveguide's other end. The waveguide's optical fiber (Schott A2 glass optical fibre) exhibits nearly equal transmission properties across the PAR spectrum (manufacturer information). As illustrated in Fig. 3.1 this creates an additional light path. This means that the light beam of the diascopic light path can be focused to optimize image quality (Köhler illumination), while the growth light illuminates the entire chip. Thus, requirements 1. and 4. are met. As is discussed in Chapter 5 of this thesis, the chosen method allows the light path to be manipulated using a half-circle cover to create a linear light intensity gradient over the length of the cultivation chip. For reproducible positioning of the ringlight a spacer ring was designed. The spacer also includes an attachment to screw the half-circle cover securely to the ringlight (See Fig. 3.2 (b). The technical drawings can be found in App. C (Fig. C.9 - C.12).

3.2.2 Comparison of two growth-light sources

As part of this thesis two different kinds of light sources were coupled into the ringlight and integrated into the microscope periphery to serve as a light source for photosynthesis. (i) A light engine with full spectral control in PAR (Spectra Tune Lab (STL), LEDMOTIVE, Spain) (ii) A LED with a fixed spectrum (MWWHL4, Thorlabs, USA). The specific advantages of the two growth light sources are:

Spectra Tune Lab (STL)

- Full flexibility in PAR.
- Integrated active cooling for heat dissipation.
- Ensured long term stability of the light intensity due to spectral output control.
- A linear power-setting to output-intensity correlation, that facilitates precise light-intensity control.
- Time-dependent output control enables the modulation of events such as dawn and dusk or changes in the light spectrum during an experiment.

Fixed-spectrum LED

- Cost-efficient. (See Tab. 3.1)
- No need for an additional shutter because the LED can be turned on and off using the microscope software.
- Passive cooling by a heat sink.
- Space-saving.

In summary, the STL is a highly sophisticated light engine that offers high experimental precision and enables the modulation of complex illumination scenarios. For experiments requiring constant light intensity and spectrum, the fixed-spectrum LED is a cost-efficient alternative (See Tab. 3.1). Both growth-light sources were successfully integrated into the microscope periphery. However, the majority of the cultivation experiments presented in this thesis were conducted using the STL as the growth light source.

The integration for the different growth light sources into the microscope periphery was performed as follows:

Fixed-spectrum LED: The LED driver for the fixed-spectrum LED can be connected to the microscope's Data acquisition device (DAQ-device) and controlled by the microscope's control software (See Tab. 2.4). Therefore, no additional shutter was needed to turn off the growth light during imaging (Requirement 5. fulfilled). To connect the LED to the waveguide a concentric reducer (See App. C: Fig. C.16 and Fig. 3.3) was designed and printed (See Tab. 2.5).

Tab. 3.1: Cost comparison of different growth light sources. All prices except the ringlight are from January 2024. The price of the ringlight is from September 2023.

Spectra Tune Lab		Fixed-spectrum LED	
Part	Cost [€]	Part	Cost [€]
Light engine (Spectra Tune Lab)	5550	LED (MWWHD3)	74.73
Shutter (IQ35-1375)	1925	LED Driver (LEDD1B T-Cube)	322.86
Shutter controller (Lambda SC Controller)	869.18	Connection cable (CAB-LEDD1)	17.17
Ringlight (A08630)	643	Ringlight (A08630)	643
Sum:	8987.18	Sum:	1057.76

STL light engine: To control the STL the provided software (μWAVE STL release 1.3.1, LEDMOTIVE, Spain) is used. In the software each of the ten LED channels can be controlled individually. Additionally, light sequences can be programmed, and spectra can be uploaded or downloaded. To shut of the light engine during imaging an external shutter (IQ35-1375, Sutter Instruments, USA) is needed (Requirement 5. fulfilled). The shutter controller (Lambda SC Controller, Sutter Instruments, USA) can in turn be connected by the microscope's control software. One objective during the design process of the custom-connectors was to maximize the light-intensity emitted by the ringlight onto the cultivation plane. One reason for the energy loss is that the lamp's output diameter (d = 29 mm) is significantly larger than the waveguide's input diameter (d = 7.6 mm). To solve this two approaches were considered.

(i) Condenser lens: One solution was to place an aspheric condenser lens on the lamp's diffuser (ACL3026U, Thorlabs, GB). The goal was to focus the light beam emitted by the STL onto a smaller diameter. To fix the lens to the STL a connector ring to hold the lens (Fig. 3.3 c) was designed and fabricated (Tab. 2.5). The ring connected the shutter to the STL via an adapter ring. Technical drawing for the connection as used for the measurements with the lenses and the reference measurements can be found in App. C (Fig. C.1 - C.5).

(ii) Reduced distance: The second approach was to minimize the distance between the lamp output and the waveguide input. Therefore, the internal housing of the STL was opened and modified to allow the lamp's output to penetrate deeper into the shutter, hence reducing the distance between lamp's output and the ringlight input from 26.3 to 4.8 mm. This distance was measured using a drawing that is included in App. C (Fig. C.8). The built-in diffuser lens was permanently glued to the output with commercial glue. The final connectors are illustrated in Fig. 3.2 (a).

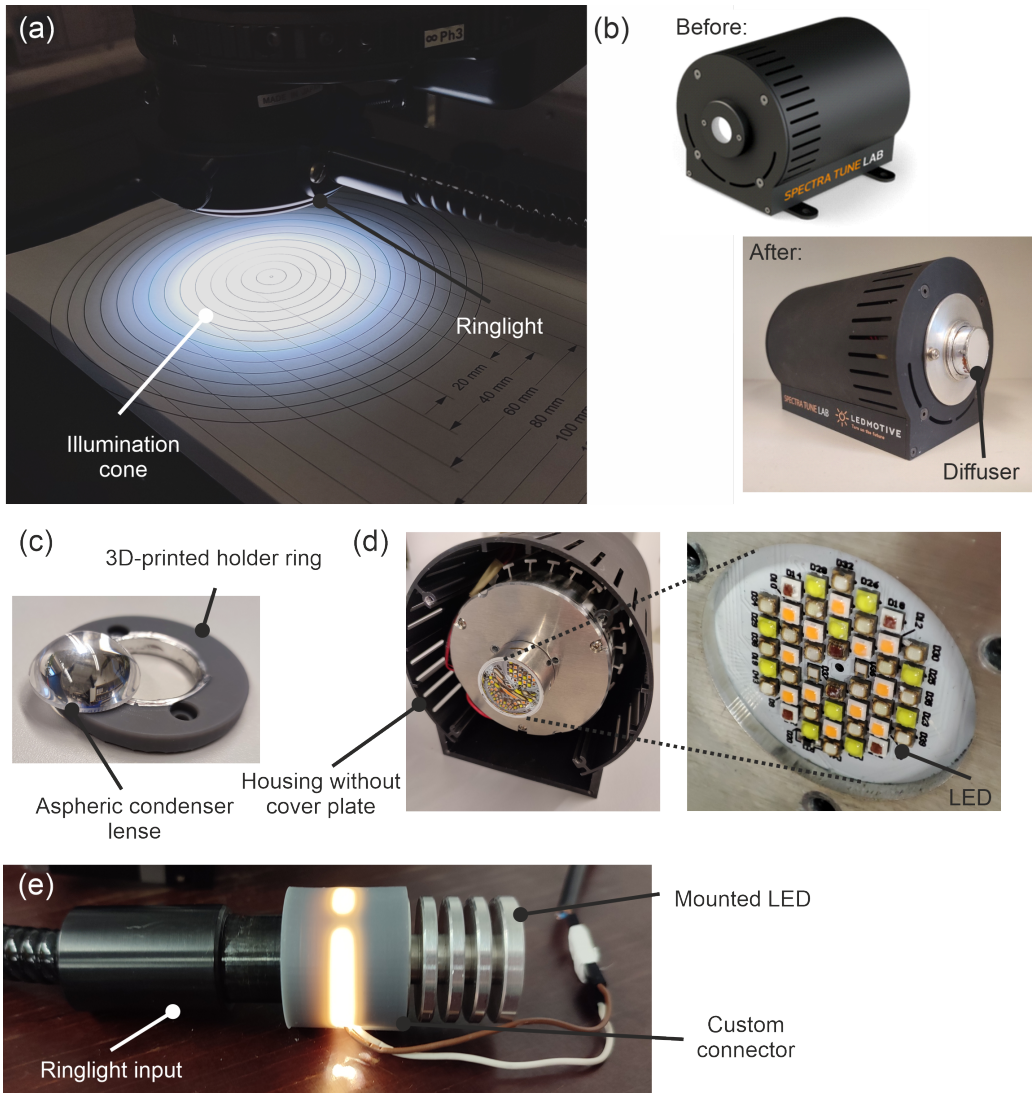


Fig. 3.3: Miscellaneous pictures of the proposed illumination system. (a) The ringlight emitting a homogeneous light cone onto the cultivation plane. (b) The STL as supplied by the manufacturer (Before). The image was copied from the supplier's website. And after rebuilding it to minimize the distance between the lamp output and the ringlight input. (c) Picture of the condenser lens and the custom 3D-printed holder ring used to connect the lens to the lamp. (d) The STL without cover plate. The individually controllable LED channels were further magnified. (e) Picture of the connection between the fixed-spectrum LED and the ringlight.

3.2.3 Characterization of the ringlight illumination system

To characterize the growth light source to ringlight connection the following experiments were performed.

Light intensity: The system was assembled and a spectrometer (Li180, LI-COR Biosciences; US) was placed in the cultivation plane. Light intensities were measured for three different scenarios: (i) Reference (ii) Condenser lens (iii) Minimized distance.

Temperature: The growth light source was set to emit light at maximum power. A temperature sensor (MTC-20/2SD, NPI Electronic Instruments, Germany) was molded into a cultivation chip and was placed in the cultivation plane. The microscope incubator was preheated to 30 °C. The temperature inside the chip was recorded manually.

Homogeneity: A microscopy calibration slide of homogeneous color and density (Chroma Technology, USA) was placed in the cultivation plane. A Plan Apo λ 2× objective (Nikon; Japan) was focused on the top of the slide. The growth-light source was turned on. Images at different power setting of the growth-light source were taken using the Andor Zyla scientific camera. The images were imported into Fiji and transformed into an 8-bit image. The histogram and mean pixel intensity of the images were calculated in Fiji. Then, the 8-bit image was uploaded to OriginPro 2020 for plotting.

Emitted light cone: The Li180 spectrometer was mounted on the x-y-stage of the microscope. The distance between the ringlight and the spectrometer was adjusted to match the distance between the cultivation plane and the ringlight during phototropic cultivation. To measure the light intensities, the spectrometer was moved along a straight line intersecting the center of the ringlight. The data was approximated using a third-degree polynomial fit. The total photon flux ($PF_{Cultivation}$) through the cultivation plane was then calculated using Eq. 3.1.

$$PF_{Cultivation} = \int_0^{2\pi} \int_0^{R} PFD(r) \cdot r \, d\varphi \, dr \overset{\varphi=2\pi}{=} 2\pi \int_0^{R} PFD(r) \cdot r \, dr \tag{3.1}$$

Therein $PF_{Cultivation}$ is the photon flux through the cultivation plane, *PFD(r)* is the PFD measured at position r, φ is the angle and R is the radius of the light cone.

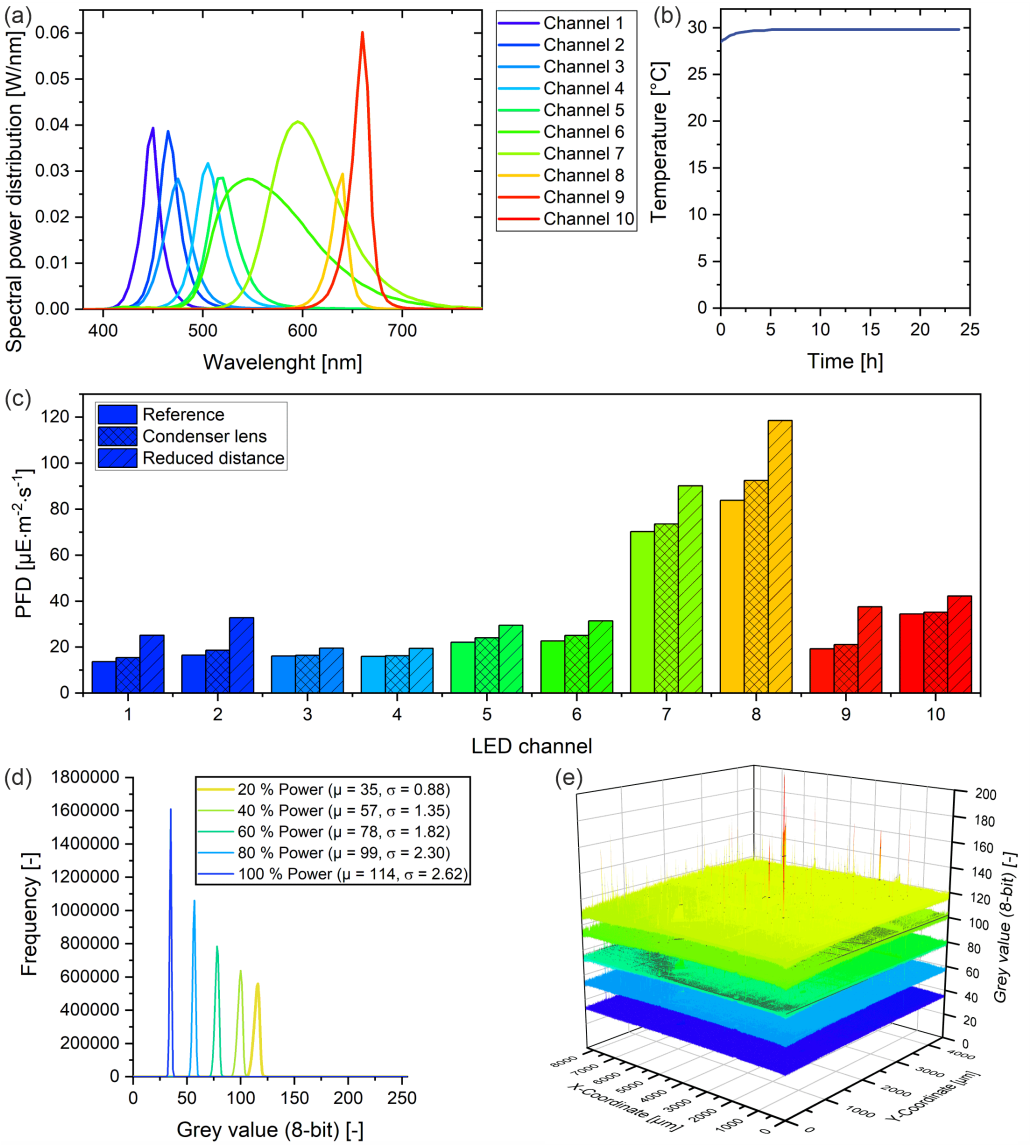


Fig. 3.4: Characterization of the STL ringlight illumination system. (a) Spectral power distributions of the ten LED channels of the STL growth light source. The information was supplied by the manufacturer. (b) Quantification of the temperature interference by the growth light at maximum power output. The incubator was set to 30 °C. (c) Direct light-intensity measurements of all 10 LED channels of the STL growth light source. The two coupling approaches (i: Condenser lens; ii: Reduced distance) are compared to the reference. (d) & (e) Quantification of illumination homogeneity. Left: Pixel intensity histogram of the individual images at different power settings of the growth light source. µ: Mean pixel intensity in the respective image, σ: Standard deviation of the pixel intensity in the respective image. Right: Images of the calibration slide illuminated at different power settings of the growth light source.

Energy loss: To quantify the energy lost by the coupling of the STL to the ringlight the energy projected onto the cultivation plane was compared to the energy emitted by the STL using Eq. 3.2.

$$\eta_{STL} = 1 - \frac{PF_{Cultivation}}{PF_{STL} \cdot (\frac{d_{Ringlight}}{d_{STL}})^2} \tag{3.2}$$

Therein η_{STL} is the energy loss by the coupling, $PF_{Cultivation}$ is the photon flux through the cultivation plane at maximum power of the STL, PF_{STL} is the Photon Flux emitted by the STL at maximum power setting. The value was calculated from the manufacturer value (14.87 W) using Eq. 1.4 and the respective spectrum. $d_{Ringlight}$ is the input diameter of the ringlight (7.6 mm) and d_{STL} is the output diameter of the STL (29 mm).

The results from the characterization of the STL growth light illumination system are displayed in Fig. 3.4. Analog data for the fixed-spectrum LED can be found in App. D (Fig. D.1 D.3 and D.2). Using the second approach (ii: Reduced distance), the increase in light intensity projected onto the cultivation plane was greater than with the first approach (i: Condenser lens) for all ten LED channels. In total intensities were 314.82, 338.02 and 446.20 µE·m^{-2}·s^{-1} for the reference, the condenser lens and the reduced distance approach respectively. The summarized intensity gain was 7.4 % and 41.7 % for the first and second approach, respectively. Therefore, this approach was chosen for the rest of this thesis, and the lamp was modified permanently (Fig. 3.3 b). Nor the lamp's off heat neither adsorption of electromagnetic waves did influence the temperature inside the cultivation chip (Requirement 3. fulfilled). The heterogeneity in the pictures of the calibration slide depends on the growth-light system, the camera, the light path of the microscope or the calibration slide itself. Although it was not possible to distinguish these effects, it can be concluded that the inhomogeneity of the growth-light system is less than 2.37 %. The value for the fixed-spectrum LED was at less than 3.75 % (Requirement 2. fulfilled). The energy loss was calculated for the final setup of the illumination system (Approach ii.). At full power of the lamp a total of 0.52 µE·s^{-1} were calculated to be emitted onto the cultivation plane. Using Eq. 3.2 the energy loss during the coupling was calculated to be 89.05 %.

3.3 A sensor for accurate and reproducible light-intensity measurements

A major advantage of microfluidic cultivation systems over conventional photobioreactors is their ability to avoid cellular self-shading by restricting cell growth to monolayers. Therefore, highly accurate correlations between growth rate and light intensity can be obtained [59, 96]. In this work, the light intensity was measured directly under the culture chip, with only the 175 µm thick glass between the intensity sensor and the cultivation plane. To increase the practicality and reproducibility of these measurements, a Terrestrial Quantum Sensor

(LI-190R, LI-COR Biosciences; USA) was purchased. The sensor was mounted in the Ti-E microscope using a custom-made connector (Tab. 2.5) and a PMMA thread (M25 x 0.75) compatible with the objective turret. For reproducible measurements, the sensor was moved into the light path and raised to a fixed z coordinate, comparable to the position of the cultivation chip. The sensitivity of the vertical distance between the ring light and the microfluidic chip to light intensity was characterized by measuring the light intensity at different z-coordinates. Moving 2 mm up or down from the measurement height changed the intensity by 2.5 and 2.9 %, respectively. This led to the conclusion that small changes in the vertical distance (e.g. when correcting Köhler illumination) can be made after the intensity measurement without significantly compromising its accuracy. It is possible to connect the sensor to a DAQ-device (e.g. the one listed in Tab. 2.4). The electrical current can be read using the microscope software and be converted in PFD using a correlation given by the manufacturer. Hence, additional automatizing is feasible.

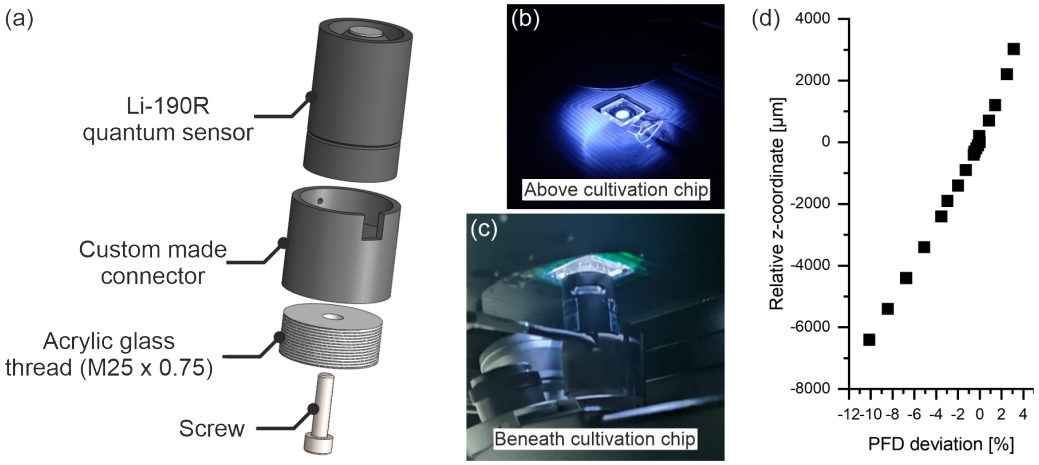


Fig. 3.5: L190R quantum sensor mounted into microscope objective turret. (a) CAD drawing of the custom-made connector and the acrylic glass tread. A more detailed drawing of the connector displaying the dimension can be found in App. C (Fig. C.15). (b) The light-intensity sensor in the light path seen from above the cultivation chip. (c) and beneath the cultivation chip. (d) The dependence of the light intensity on the vertical distance between the intensity sensor and the ringlight. The cultivation plane is at the relative z-coordinate of zero. There the reference light intensity was measured for the calculation of the light intensity deviation. SubFig. (a) was reproduced from Ref. [1] with permission from the Royal Society of Chemistry.

3.4 Conclusion & Outlook

Five requirements for an illumination system to drive photosynthesis during time-lapse microscopy are defined at the beginning of the chapter. Two of these requirements are met by using a ringlight fixed around the microscope condenser to illuminate the microfluidic chip from above.

- **Requirement 4:** Since the illumination comes from above, the objective revolver can be used freely, enabling the use of oil objectives.
- **Requirement 1:** The ringlight creates an additional, independent light path, enabling the diascopic light path to be optimized for imaging.

Two sources of growth light are presented: A sophisticated, albeit expensive, light engine and a cheaper, although less flexible, fixed-spectrum LED. Connections to the ringlight were designed for both light sources. The connection to the light engine was designed for high coupling efficiency. These were characterized to demonstrate that Requirements 2, 3, and 5 are met.

- **Requirement 5:** Both growth lights can be shut off during imaging, thereby enhancing image quality.
- **Requirement 2:** Homogeneous illumination across the cultivation chip is displayed in Fig. 3.4 d + e for the STL and Fig. D.3 for the fixed-spectrum LED.
- **Requirement 3:** The growth-light illumination does not affect the temperature inside the cultivation chip (See Fig. 3.4 b).

Furthermore, a light-intensity sensor was integrated into the microscope periphery. Going forward, it could be beneficial to integrate the STL the fixed-spectrum LED and the light-intensity sensor into the microscope software. This would allow the experimental procedure to be further automated. The next three chapters demonstrate how the developed illumination system can be used for phototrophic cultivation. First, it is used with homogeneous growth light illumination; then, the generation of a linear light gradient is introduced. Finally, dynamic CO_2 control is added.

4 Homogeneous growth light illumination

Parts of this chapter have been published in peer-reviewed journals or on preprint servers (I, III and VI) [1, 94]. Some results were presented as an oral presentation (II) or posters (II, V) at international conferences. Data and the applied code are publicly available (I - III).

4.1 Introduction

This chapter demonstrates the applicability of the proposed illumination system for the cultivation of cyanobacteria and eukaryotic microalgae under well-defined homogeneous illumination. First, the growth behavior within distinct growth chambers is shown. Then the results of multiple cultivations at different light-intensities are summarized. The resulting growth kinetic is then compared to growth rates within the MC. From this comparison system characteristics are derived and discussed. Parts of the results in this chapter were published in Witting et al. [1].

4.2 Materials & Methods

4.2.1 Strains

The vast majority of the microfluidic cultivations performed in this thesis were carried out with the cyanobacteria genera *Synechococcus* and *Synechocystis*. In order to show the system's versatility the extremophile microalgae strains *Galdieria sulphuraria* 074 (*G. sulphuraria*) and *Cyanidioschyzon merolae* 10D (*C. merolae*) were cultivated.

Extremophile microalgae: Both strains, *G. sulphuraria* and *C. merolae*, belong to the Cyanidiophyceae class. These unicellular red algae lack the red protein pigment found in other red algae. They are found worldwide, growing at temperatures of up to 56 °C and pH values between 0.05 and 5 [97]. The strain *G. sulphuraria* and *C. merolae* were obtained from another working group at the IBG-1. In turn, they received the strains from the institute for plant biochemistry at HHU. The *G. sulphuraria* strain 074 was originally isolated at Mount Lawu in Indonesia [98], whereas *C. merolae* 10D was first isolated from hot spring water sampled in Naples, Italy [99].

Cyanobacteria: *Synechococcus* are a genus of unicellular marine cyanobacteria with a substantial role in marine carbon fixation. They are widely distributed around the globe but are most abundant in tropical and subtropical environments. Their cell length typically lies between 0.5 - 2 µm and their diameter lies between 0.5 and 1 µm [5, 100]. UTEX2973 was isolated in 2011 from the non-axenic *S. elongatus* UTEX 625 strain and described in 2015 by Yu et al. [101]. The strain used in this thesis was provided by cooperation partners at the HHU and maintained in permanent culture throughout the duration of this thesis project. Therefore, genetic drift cannot be excluded. PCC7942 originated from a water sample taken by students during a university course at California State University. Since then, it has grown to fame within the cyanobacteria community [102]. Two mutated forms of the PCC7942 were used in the first part of this thesis.

cscB: This strain was provided by cooperation partners at the Technical University of Munich, but was originally engineered at Harvard Medical School [103]. It was designed to express a Sucrose permease (cscB) from *E. coli* and integrate it into its cell wall upon Isopropyl-β-D-1-thiogalactopyranosid (IPTG) induction. *S. elongatus* naturally accumulates intracellular sucrose in its cytoplasm to counteract osmotic stress from high extracellular salt stress. Therefore, when the growth medium is supplemented with salt (e.g. 150 mM NaCl) and IPTG (0.1 mM), the strain exports sucrose into its environment.

cscB sps$_{6803}$: In this strain, the Sucrose phosphate synthase (sps) gene from a PCC6803 strain was inducibly (by IPTG) overexpressed in PCC7942 cscB. sps catalyzed a part of the reaction from GAP to sucrose. Hence, the strain exports sucrose into it's environment upon IPTG induction without salt stress [104]. The strain was received from the institute for synthetic microbiology at HHU. They, in turn, received the strain directly from the laboratory where it was engineered. Initially, these strains was intended for use in a co-culture project, in which the exported sucrose would be fed to a heterotrophic partner that consumes sucrose. This project never progressed beyond the preliminary stage. However, a lot of kinetic growth data on the strain was gathered and is presented in this part of the thesis.

PCC6803: Cyanobacteria from the genus *Synechosystis* are described as coccoid spherical cells that divide into perpendicular planes [105]. The strain *Synechocystis sp.* PCC 6803, isolated in 1968 from freshwater samples taken in California [106, 107], has been the subject of much research. Attention was later drawn to this strain when Kaneko et al. sequenced it in 1996 [16]. This made it the fourth organism whose genome had been completely sequenced. Among phototrophic organisms, *Synechocystis sp.* PCC 6803 was the first to

be fully sequenced [15]. It has served as a popular model in cyanobacteria research ever since.

4.2.2 Microfluidic cultivation

The cultivation parameters for *G. sulphuraria* and *C. merolae* are given in Tab. 4.1. Layout iii. from wafer #1 (See Fig. 5.4) was used. *Synechococcus* cultivation was performed at 37 °C in BG11 medium [108]. For all cyanobacteria cultivations shown in this chapter, wafer #0 (See Fig. 5.4) was used. The growth light was first programmed to emit Planck's radiation distribution at 5800 K, mimicking the spectrum emitted by the sun [109]. Then the power setting was changed until the desired PFD was measured in the cultivation plane. In each experiment 15 - 20 chambers were collected per cultivation channel. Ideally one cell was inoculated into the middle of a growth chambers. Where possible, the chambers were chosen to be distributed across the chip to reduce the risk of a subchannel clogging ruining the experiment.

Tab. 4.1: Cultivation parameters for extremophile microalgae.

Strain -	Medium -	Light-intensity [$\mu E \cdot m^{-2} \cdot s^{-1}$]	Day/Night rhythm [h_{Day}/h_{Night}]	Temperature [°C]
G. sulphuraria	Modified Allen, pH 2	30	24/0	40
C. merolae	MA2, pH 2.25	50	16/8	37

4.2.3 Growth of UTEX2973 in the Multi-Cultivator

For comparison UTEX2973 was cultivated in the MC. Cultivations were performed with ambient air ($\sim$ 400 ppm CO_2), 3 % CO_2 (30,000 ppm) and 5 % CO_2 (50,000 ppm) enriched air bubbled through the culture broth. The general protocol is described in section 2.1.2. All cultivations were performed at 37 °C. The OD_{720} correlates linearly to biomass in the range from 0.05 - 0.4.

4.2.4 Determination of growth rates during microfluidic cultivation

After the experiment, time-lapse image files were prepared according to the description in Chapter 2. To analyze the data under homogeneous growth light illumination tailor-made

Python notebooks were implemented. A group statistics notebook was created for each experiment to retrieve data from each chamber, calculate the mean growth rate and the standard deviation. Then, a higher-order notebook retrieved data from all experiments and plots the mean growth rates and standard deviations for each experiment over the PFD. Furthermore, statistical notebooks were employed to count the number of images analyzed and the number of cells segmented within these images. Data analysis after each experiment consistent of the following steps:

1. Fine-tuning of artifact filtering using an example chamber.
2. Sequentially performing the segmentation for all image files using *ScalingAnalysis.ipynb*.
3. Manual inspecting of all segmentation notebooks. If needed, correction of filters or timeframe for growth rate fitting.
4. If applicable, discard chambers with bad segmentation quality.
5. Execute group statistics notebooks.
6. Update notebooks collecting data from multiple experiments.

4.2.5 Single cell area distribution within a growth colony

The coordinates of the center of the colony was calculated using Eq. 4.1. The distance of the respective cell to the center of the colony center d_n was calculated using Eq. 4.2.

$$\begin{pmatrix} x_{center} \\ y_{center} \end{pmatrix} = \begin{pmatrix} min\{x_1, x_2, ..., x_n\} + \frac{max\{x_1,x_2,...,x_n\}-min\{x_1,x_2,...,x_n\}}{2} \\ min\{y_1, y_2, ..., y_n\} + \frac{max\{y_1,y_2,...,y_n\}-min\{y_1,y_2,...,y_n\}}{2} \end{pmatrix} \tag{4.1}$$

$$d_n = \sqrt{(x_n - x_{center})^2 + (y_n - y_{center})^2} \tag{4.2}$$

Therein x_{center} and y_{center} are the x and y coordinates of the center of the colony. x_n and y_n are the coordinates of the n^{th} cell. The cell area of single-cells was then plotted over their respective distance d_n to the colony center.

Linear fits were calculated through the data to evaluate whether the single-cell area and distance are correlated. For this analysis a custom Python notebook was designed.

4.2.6 Quantum Yield

In photosynthesis research the photosynthetic efficiency, defined as the ratio of energy stored in biomass to the received energy, is often used to compare processes [2]. In light-driven physical processes more generally, the quantum yield is defined as the number of resulting events per photon. Here, the Quantum Yield was defined as total amount of accumulated biomass per total amount of impinging photons (Eq. 4.4). The total number of photons impinging on the growth colony over a specific timeframe P_{Total} was calculated using Eq. 4.3.

$$P_{\text{Total}} = \int_{t_0}^{t} \text{PFD} \cdot A(t)\, dt = \text{PFD} \int_{0}^{t} A_0\, e^{\mu t}\, dt = \text{PFD} \cdot \frac{A_0}{\mu} \left(e^{\mu t} - e^{0}\right) \tag{4.3}$$

$$\Phi = \frac{\Delta A \cdot h_{Chamber}}{P_{Total}} = \frac{\mu \cdot h_{Chamber}}{PFD} \tag{4.4}$$

Therein P_{Total} is the total number of photons impinging on the colony over the course of the time t, PFD is the applied PFD during the cultivation, $A(t)$ is the size of the colony at time t, A_0 is the size of the colony at t_0, μ is the growth rate, Φ is the quantum yield, $h_{chamber}$ is the height of the growth chamber and ΔA is the increase of the area occupied by the growth colony.

To calculate the photoconversion efficiency the denominator in Eq. 4.4 has to be multiplied by the strain specific absorption coefficient for each wavelength. Then, it must be converted into the total amount of impinged energy using Eq. 1.4. The nominator could be transformed by multiplying the cell volume with the volumetric energy density of *S. elongatus*. However, measuring the volumetric energy density lies beyond the scope of this thesis.

4.3 Results & Discussion

4.3.1 Extremophile microalgae

Time-lapse sequences for one exemplary growth chamber per strain are shown in Fig. 4.1. Due to their unusual morphology, the DL segmentation algorithm trained on *Synechococcus* did not correctly segment *C. merolae* and *G. sulphuraria* cells. In the case of *G. sulphuraria*, ten different growth chambers were selected and the number of cells was counted manually. *G. sulphuraria* is known to accumulate four to 32 daughter cells, called autospores, within its cell wall before hatching [97, 110]. Remarkably, in all ten observed chambers, 8 autospores were released from the initial cell, then each of the 8 offspring released 16 autospores. At the

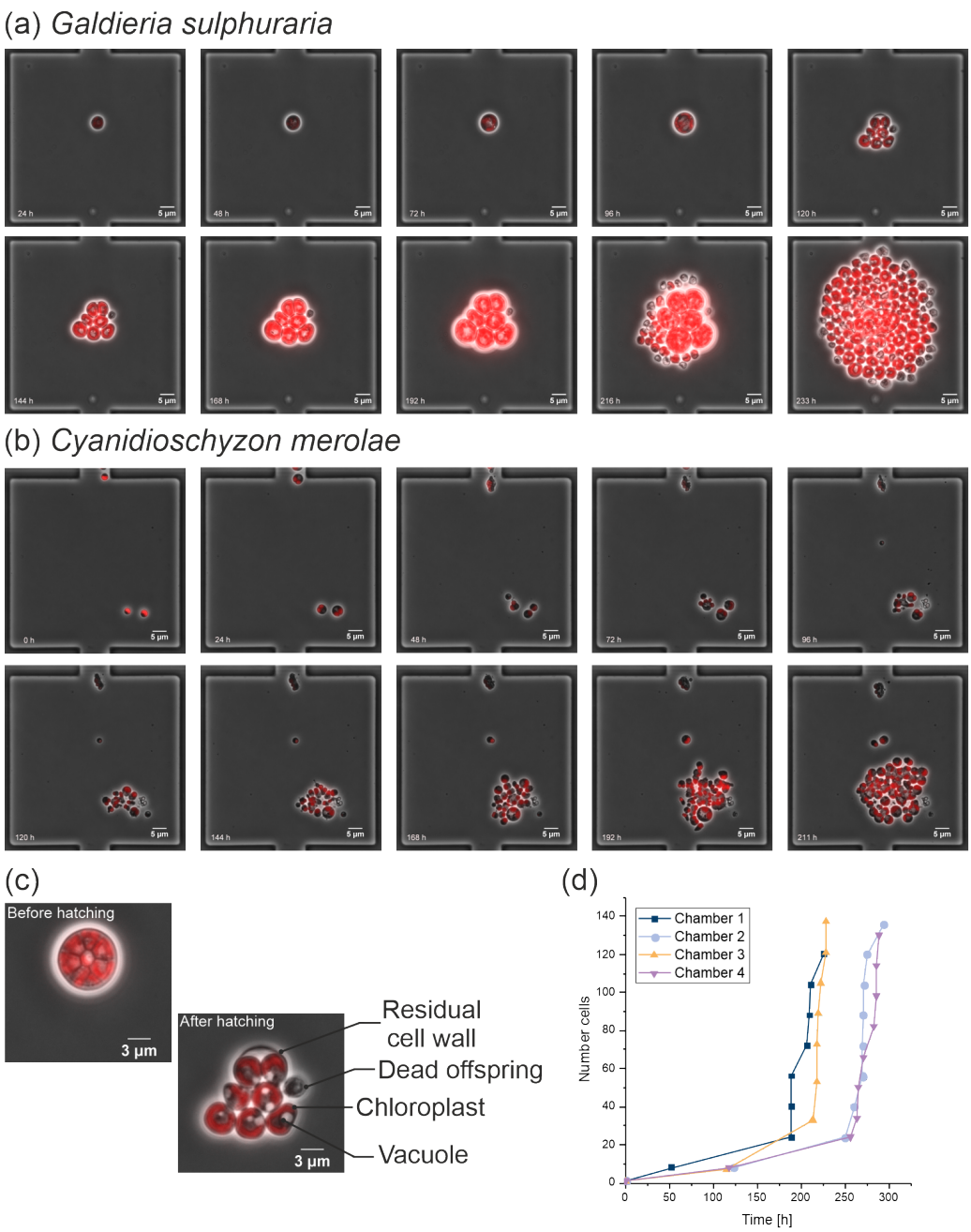


Fig. 4.1: Growth of extremophile microalgae. (a) Growth of *G. sulphuraria* over 233 h. (b) Growth of *C. merolae* over 211 h. (c) Close up on the hatching process of *G. sulphuraria*. (d) Manual cell count of *G. sulphuraria* in four distinct growth chambers.

end of cultivation, the third generation of cells was fully released in four growth chambers. In these growth chambers, growth rates were calculated from the time difference between the hatching of the first eight offspring and the second hatching event. Using the Eq. 1.7 a growth rate of 0.020 ± 0.004 was calculated. By cultivating the extremophile microalgae the following extreme aspects were demonstrated:

- **Low pH:** The cultivation was stable despite the extremely low pH of the growth medium (pH = 2).
- **High temperature:** The system can be operated at 40 °C.
- **Long term stability:** Stable cultivation of *G. sulphuraria* was performed over 301.5 h.

4.3.2 Growth behavior in distinct growth chambers

Fig. 4.2 shows the growth of UTEX2973 and PCC7942 cscB at light intensities between 10 and 140 $\mu E \cdot m^{-2} \cdot s^{-1}$. A total of 21,489 images containing 4,352,948 cells were segmented and analyzed. Several independent experiments were performed and the entire cultivation time under homogeneous growth-light illumination lasted roughly 38 days. Detailed growth data of two exemplary microbial colonies is shown in Fig. 4.2 c - e. The dependency of the growth rate on PFD is shown in Fig. 4.2 f.

Synchronous cell division of *Synechococcus*, as previously reported by Martins et al. [47], was also observed here and is evident from the sawtooth pattern when plotting the mean single-cell area over time. Synchronous division was observed within distinct growth colonies, but not between colonies in different growth chambers on the same growth array (See App. D: Fig. D.4 and D.5). It is characterized by the steady increase in mean cell size, followed by a sudden decrease as image-based cell segmentation eventually results in two independent, but smaller cells at the end of each cell division cycle.

Overall cells became smaller over the course of the cultivation. This effect was independent of colony size and light-intensity. An indicator for an external stimulus, that each cell experiences equally. In another study it was shown that as colonies grow bigger the diffusion of medium components with small concentrations can not be assumed to be equally distributed throughout the colony thus hampering growth in the middle of the colony [111]. In this case, only a slight correlation was found between the area of individual cells and the distance to the center of the colony. This correlation was weaker for larger colonies. If nutrient limitation were causing the decrease in cell size, a greater

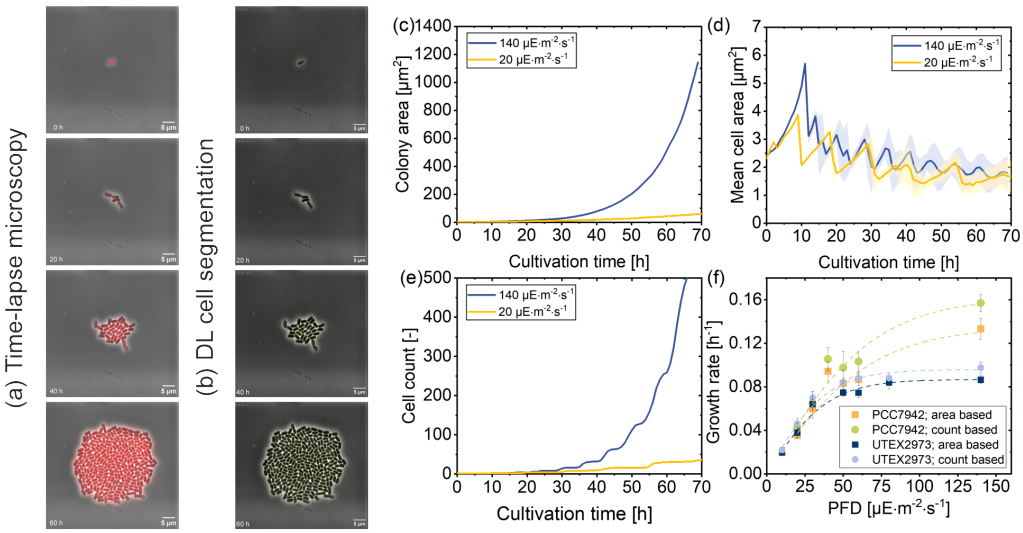


Fig. 4.2: Synechococcus growth at different light-intensities under homogeneous and constant growth-light illumination. (a) Data was acquired by time-lapse microscopy, recording phase contrast and chlorophyll fluorescence images. (b) Images were preprocessed in Fiji before cell instance segmentation was performed using a DL model that was trained on annotated sample images. DL based cell segmentation was performed on phase contrast images to derive cell number (and area) over time from which growth rates were determined using an exponential growth model. (c) Total cell area of segmented cells over the cultivation time. (d) Mean cell area per frame over cultivation time (e) Number of segmented cells over the cultivation time. (f) Colony based growth analysis derived from image data at single-cell resolution of UTEX2973 and PCC7942 cscB (In the legend indicated as PCC7942) under homogeneous illumination. These replicates were obtained from multiple chambers on the same chip, but the corresponding light-intensity was varied over several independent experiments (cultivation time approximately 38 days). The figure was reproduced from Ref. [1] with permission from the Royal Society of Chemistry.

Tab. 4.2: Number of analyzed chamber growth chamber with cell growth for the data shown in Fig. 4.4 and 4.2 F.

Organism	PFD [µE·m^{-2}·s^{-1}]							
	10	20	30	40	50	60	80	140
PCC7942	-	11	29	14	27	13	-	23
UTEX2973	13	10	24	-	13	27	5	15

Tab. 4.3: Growth rate and quantum yields calculated for distinct colonies of UTEX2973.

Parameter	140 µE·m^{-2}·s^{-1}	20 µE·m^{-2}·s^{-1}
Cell count based growth rate [h^{-1}]	0.105	0.064
Cell area based growth rate [h^{-1}]	0.093	0.050
Quantum yield [mm^3·µmol^{-1}]	0.00018	0.00071

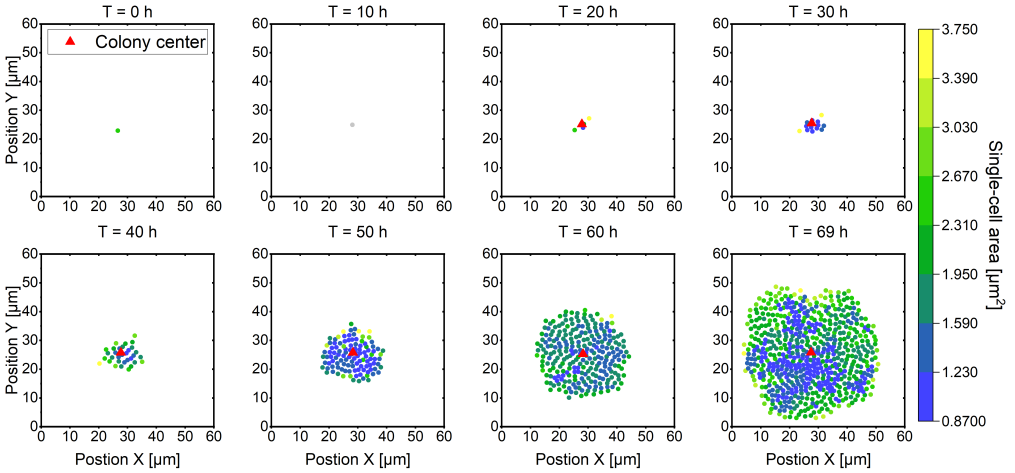


Fig. 4.3: Distribution of the single-cell area in a distinct growth colony. Visualisation of the distribution of the single-cell area within the growth colony illuminated at 140 µE·m^{-2}·s^{-1}. The position of the center of the colony (Eq. 4.1) is marked with a red triangle. For the full analysis, including all timepoints for both colonies the reader is referred to App. D.

correlation would be expected in larger colonies (Fig. 4.3 and App. D: Fig. D.6 D.7 D.10 D.8 D.9 and D.11). The fact that the same reduction occurred in both colonies is another indication of a size-independent reduction of the cell size: After 65 h of cultivation, 480 cells occupying an area of 783 µm^2 were present in the chamber illuminated 140 µE·m^{-2}·s^{-1}, whereas 32 cells occupying an area of 52 µm^2 were present in the chamber illuminated at 20 µE·m^{-2}·s^{-1}. Therefore, a nutrient deficiency can be excluded as a factor causing the smaller cells. The same is true for the light-intensity: The illumination to drive photosynthesis was provided from a direction orthogonal to the plane of monolayer growth. Therefore, the colony size does not influence the amount impinging photons per cell.

In image based single-cell analysis, the colony averaged growth rate can be derived from the total cell number in the respective growth chamber or the total area occupied by the colony. The reduction in cell size over the cultivation time decelerates the cell area based

growth rate measurement. Hence, the difference in the comparison between count based and area based growth rate calculation as shown in 4.2 f. For the rest of this thesis, the growth rate is calculated based on the increasing overall area of cells within the microfluidic growth chamber. This is due to the shrinking size of cyanobacteria cells and the discrete nature of the cell count measurement.

The quantum yield describes how much biomass can be produced per photon. In conventional photobioreactors, the operator can measure the incident light-intensity and the accumulation of biomass. However, knowledge of how much light is actually impinging on the single-cell is limited. Here, cells were grown in monolayer, therefore the amount of photon impinging on a cell per time unit is precisely known. The calculation of the quantum yield according to the derived formula (Tab. 4.3) reveals more efficient transformation of photons into biomass at 20 $\mu E \cdot m^{-2} \cdot s^{-1}$ than at 140 $\mu E \cdot m^{-2} \cdot s^{-1}$. As is discussed in the next section, when the light intensity is 140 $\mu E \cdot m^{-2} \cdot s^{-1}$ the limiting factor for cell growth is no longer the available light intensity. This makes the utilization of photons less efficient.

4.3.3 Growth kinetics of S. elongatus strains

The growth data in Fig. 4.4 and Fig. 4.2 f is typical for phototropic organisms. In the light-limited region, a linear growth rate dependence on the PFD is observed [2]. When further increasing the light-intensity, in the light-saturated region, the growth rate reaches a plateau and is limited either by the CO_2 uptake rate or by the rate limiting enzymatic step in the carbon reactions [10]. By increasing the CO_2 concentration, higher growth rates can be achieved to some extent, until no further growth-rate increase is achieved. The data in these figures were assembled from distinct experiments operated at various light-intensities. Each datapoint shows the mean growth rate and standard deviation calculated from multiple growth chambers. The number of analyzed growth chambers for each datapoint is shown in Tab. 4.2.

Literature research on growth models for photoautotrophic microorganisms, heavily relied on the review by Lee et al. [33]. Several therein described growth models were fitted onto the growth data. The Monod kinetic model tended to overestimate the maximum growth rate. By adding a shape coefficient m [35] the maximum growth rate can be corrected, however no physical meaning can be extracted for the shape parameter. The hyperbolic tangent model worked well [34] to describe the data. While no physical interpretation can be derived for the *tanh()*, it allows relatively easy derivation and integration. Hence, the decision to use the hyperbolic tangent model in this thesis. The parameters derived from

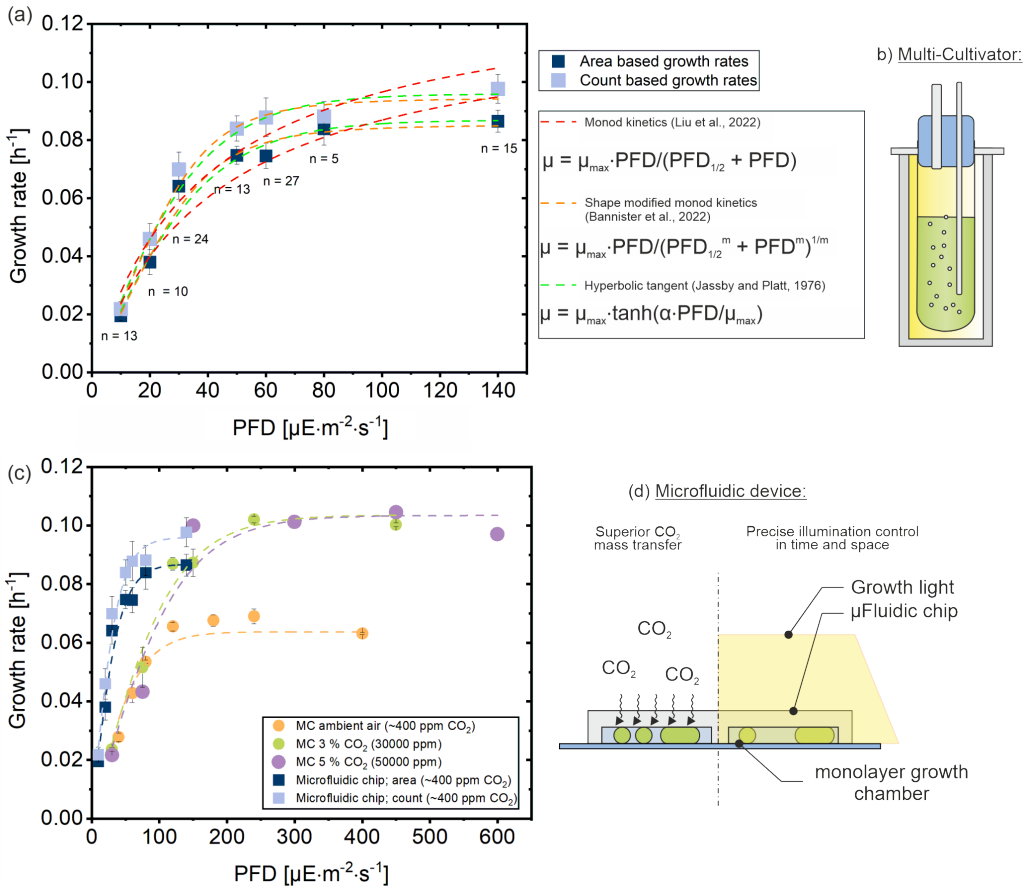


Fig. 4.4: Growth of UTEX2973 in the microfluidic chip and MC. (a) Multiple growth models were fitted onto the growth data. In this thesis the hyperbolic tangent model was most commonly used to describe the growth data (b) Schematic representing cultivation in the MC. Cyanobacteria growth in the MC is hampered by self-shading of cells and slow mass-transfer of CO_2. (c) Colony based growth analysis derived from image data at single-cell resolution of UTEX2973 under homogeneous illumination in comparison to laboratory-scale MC cultivation (n=2). The microfluidic device was operated without CO_2 control. The ambient air had a CO_2 concentration of approximately 400 ppm. The MC cultivations were performed with ambient and with CO_2 enriched air. (d) Schematic representation of cyanobacteria cultivated in the microfluidic chip. This cultivation technique offers unique advantages like precise illumination without self-shading of cells and a high exchange-surface to cultivation-volume ratio.

fitting Eq. 1.9 onto the data in Fig. 4.4 f are shown in Tab. 4.4. The growth kinetics can be compared according to two aspects. (i) The CO_2 availability, that mainly effects the value of μ_{max} and (ii) the incident light-intensity in the light limited region, which mainly effects the value of α. No correlation between the single-cell area and the light-intensity was found (See App. D: Fig. D.12 and D.13).

CO_2 availability: Supplying ambient air, the maximum growth rate of UTEX2973 cultivated inside the microfluidic chip, was higher than the growth rate of this strain cultivated in the laboratory scale MC. This is due to the fact, that under these conditions the effective CO_2 concentration was higher in the microfluidic device than in the MC. PDMS is known for its high permeability to a range of gases. If the upper side of the chamber closed of by PDMS is considered in gas exchange an exchange-surface to cultivation-volume ratio of 0.97 μm^{-1} can be calculated. In the microfluidic device all cyanobacteria are in direct contact with the PDMS, hence CO_2 is diffusing directly to the cyanobacteria and growth of the culture cannot limit the CO_2 supply.

Inside the MC cultivation tubes however, CO_2 is provided by bubbling air through the culture broth. The air bubbles have a low residence time and rather big diameters resulting in inefficient mass transfer of CO_2 into the culture broth. Inside the culture broth the aqueous CO_2 is mixed by convective and diffusive mass transfer. Cyanobacteria can then take up CO_2 or carbonic acid by active or passive transport [23]. This constitutes are complex and hard to simulate mass transfer problem. Nevertheless, the data clearly shows that when ambient air is supplied, the effective CO_2 concentration is lower in the MC than in the microfluidic device. Therefore, in the MC the CO_2 availability is limiting growth in the light saturated region. Additional MC cultivations were performed at 3% (30000 ppm) and 5% CO_2 aeration, enabling higher maximum growth rats. No further growth-rate increase was observed at 5% in comparison to 3%, indicating saturated photosynthetic capacity in the MC. Under these conditions, the value for μ_{max} was comparable between the cell count based growth rate in the microfluidic device and the MC.

As shown in Fig. 4.2 d, the cell size in the microfluidic device decreased over cultivation time, which corrupted the growth rate measurement. In this case, the growth rate estimation based on the colony area was considered more reliable. This means that under increased CO_2 concentration UTEX2973 grew a bit faster in the MC, than in the microfluidic device. The values correspond to 7.97 h and 6.73 h t_d values for the microfluidic device and the MC, respectively.

OD measurements are well established and have been used extensively in biotechnology for a long time because of their simplicity. However, they are not considered the most reliable tool. This is because the OD-to-biomass correlation is often nonlinear at higher OD values and because changes in cell morphology, cell growth, and cell division cannot be distinguished. Consequently, the difference in μ_{max} should not be over-interpreted; it may simply be an inaccuracy in the OD measurements. Perhaps the cell size also changed during the cultivation in the MC. Growth rates derived from the microfluidic device can be considered more accurate and reliable.

Incident light-intensity: The initial slope, α, of the growth curve indicates the relationship between the PFD and the growth rate in the light-limited region of phototropic growth. A comparison of the values shows that the slope was steeper in the microfluidic device. Thus, in the microfluidic device the maximum growth rate of UTEX2973 was reached at lower light-intensities than in the MC. Noteworthy, light-intensities between different cultivation systems for photoautotrophic organisms are often not comparable. Within the microfluidic device cells are cultivated in strict monolayer. The light-intensity was measured directly under the cultivation chip; only the 175 µm thick glass slide was separating the cultivation chamber from the intensity sensor. The light engine is equipped with an on-board CMOS spectrometer ensuring spectral precision an accuracy. Regular measurements were taken after each experiment to ensure that the PFD had remained constant. No deviations were ever noticed, even after week-long cultivation.

Tab. 4.4: Model parameters for cultivation of UTEX2973 and PCC7942 in the microfluidic device and in the MC under homogeneous growth-light illumination.

Condition	μ_{max} [h^{-1}]	α [$(h \cdot \mu E \cdot m^{-2} \cdot s^{-1})^{-1}$]	$PFD_{1/2}$ [$\mu E \cdot m^{-2} \cdot s^{-1}$]
UTEX2973			
Cell area	0.087	$2.16 \cdot 10^{-3}$	22.11
Cell count	0.096	$2.49 \cdot 10^{-3}$	21.14
MC ambient CO_2	0.064	$9.46 \cdot 10^{-4}$	37.01
MC 3 % CO_2	0.103	$8.71 \cdot 10^{-4}$	65.30
PCC7942			
Cell area	0.135	$1.92 \cdot 10^{-3}$	38.55
Cell count	0.162	$2.31 \cdot 10^{-3}$	38.50

In the MC cells are suspended in the culture broth and mixed by the sparged air. On their way through the photobioreactor cells are exposed to different light-intensities. It is also unclear at what distance from the LED panel the manufacturer measured the light-intensity. Both parameters, light-intensity and CO_2 concentration, can not be compared between devices. Whereby the system presented in this thesis yields a more accurate representation of the relationship between these parameters and the growth rate of cyanobacteria. Therefore, it is reasonable to assume that the PFD within the microfluidic device is the actual intensity of light impinging on the cells.

A comparable result was also reported by Luke et al. [55]. They compared doubling times between shake flask culture and their microfluidic device for the PCC7942 WT strain. At 50 $\mu E \cdot m^{-2} \cdot s^{-1}$, the t_d values were 12.8 and 7.3 h for the shake flask and their device, respectively. At 100 $\mu E \cdot m^{-2} \cdot s^{-1}$, the t_d values were 6.4 and 5.7 h for the shake flask and their device, respectively. Note that in their publication, the shake flask and the microfluidic device were kept in an incubator with 5 % CO_2.

4.4 Conclusion & Outlook

This chapter demonstrated the ability of the illumination system to provide the light necessary for photosynthesis during microfluidic cultivation. The system's ability to operate stably over long periods of time (301.5 hours), at high temperatures (40 °C) and extreme pH values (pH = 2) was demonstrated by cultivating the microalgae strains *G. sulphuraria* and *C. merolae*. However, most of the cultivations shown in this chapter were carried out using the two *S. elongatus* strains UTEX2973 and PCC7942 cscB. Because the system is capable of single-cell resolution, the growth rate can be determined by considering different values: (i) The number of cells present in the growth chamber; and (ii) the total area that the colony occupies. Due to the observed decrease in cell size and the continuous nature of the colony area curve, growth rates are calculated based on the total colony area of the colony for the rest of this thesis.

As more light intensities were investigated, the knowledge of growth kinetics increased. A comparison showed that the hyperbolic tangent model was the best fit for the growth data. Furthermore, UTEX2973 was cultivated in the MC and the growth kinetics of both systems were compared. The three main advantages of the microfluidic system were demonstrated: (i) Monolayer growth to avoid self-shading of cells. (ii) Superior CO_2 mass-transfer due to the extremely high surface-to-cultivation volume ratio. (iii) Continuously supplied growth medium to avoid nutrient limitation. Therefore, since growth was not limited by CO_2 or nutrient availability, the data shown here can be used as ground-truth data in biotechnology.

However, the MC can apply eight different light intensities per cultivation. In contrast, eight independent experiments are needed to investigate eight light intensities with the current setup. If each experiment lasts four days, 32 days of cultivation are required. The next chapter introduces a method to generate a light-intensity gradient over the length of the cultivation chip and cultivate cyanobacteria under the gradient, which solves this issue.

5 Linear light-intensity gradient illumination

Parts of this chapter have been published in peer-reviewed journals or on preprint servers (I and III) [1, 94]. Some results were presented as an oral presentation (II) or posters (II, V) at international conferences. Data and the applied code are publicly available (I - III).

5.1 Introduction

Initially, several concepts were considered for investigating a range of light intensities in a single experiment. In principle, changing the light intensity over time would be an easy option. However, this would remove the possibility of simultaneous day/night cycles. Furthermore, if the temporal dimension were reserved for a change in light intensity, changes in CO_2 concentration would have to be implemented spatially, which is more challenging than a spatial light intensity gradient.

The first concept for a spatial light intensity gradient was inspired by the work of Kim et al. [56]. PDMS mixed with black dye was formed into a triangular shape using a 3D printed master mold (Tab. 2.5). This was then bonded to a standard PDMS cultivation chip, creating a linear intensity gradient when illuminated from above (Fig. 5.1). Two prototypes were fabricated: One with and one without an integrated gas perfusion chamber. Drawings of the master mold are placed in App. C (Fig. C.14). However, this concept was quickly discarded for three main reasons:

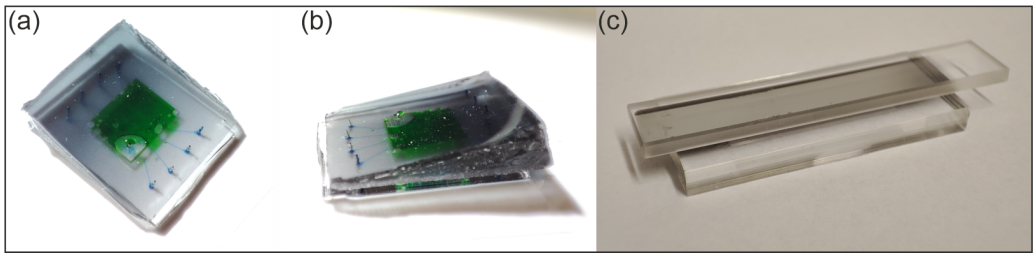


Fig. 5.1: Alternative light-intensity gradient concepts. (a) & (b) For the tilted cultivation chip PDMS was mixed with black dye and moulded into a triangular shape. This was then bonded to a thin cultivation layer. This tilted cultivation chip concept of creating a spatial light-intensity gradient was abandoned shortly after this prototype was made. (c) A continuously graduated ND filter was placed on a 24 mm cultivation chip made from wafer #1. On wafer #1, the inlets & outlets are spread out to allow the ND filter to be placed on the chip.

- Difficult calibration due to irreversible bonding of the triangular PDMS piece onto the cultivation chip.
- The irreversible bonding inevitable leads to heterogeneous image brightness during normal time-lapse imaging.
- A µm sized wave-shaped structure resulting from the 3D printing process was seen during microscopy of the triangular PDMS piece.

As an alternative, rectangular continuously variable ND filters (Thorlabs, GB) placed on top of the cultivation chip were considered (Fig. 5.1). The special coating of these filter is designed to result in a linear increase of the optical density from 0.04 to 2 (or 4) over a length of 50 cm. This results in an exponential decay of the transmission ($\tau = 10^{-OD}$). It was considered to use a small engine to move the filter over the cultivation chip and remove it during imaging. On the other hand, it was found that a linear light-intensity gradient can be created by shading half of the ringlight. This technique is similar to the one proposed by Liu et al. [58, 59], while enabling the diascopic light path to be used for imaging. After considering the advantages and disadvantages of both techniques, it was opted by move forward with the half shaded ringlight concept.

Variable ND Filter:

- **Advantage:** Broader light-intensity range.
- **Disadvantage:** Exponential decay of transmission.
- **Disadvantage:** Inlets and outlets need to be spaced out to make space for filter. This makes handling more difficult.
- **Disadvantage:** More automation (integration of engine) needed.
- **Disadvantage:** Extremely sensitive coating.
- **Disadvantage:** Finding the right alignment was extremely difficult.
- **Disadvantage:** High prize per filter ($\approx$ €100).

Half-Shaded ringlight:

- **Advantage:** Easy and simple generation of light-intensity gradient facilitates calibration.

- **Advantage:** No further automation necessary.
- **Advantage:** No physical obstacles in light path facilitates integration of gas control.
- **Disadvantage:** Long cultivation chip required.
- **Disadvantage:** More limited light-intensity range.

5.2 Materials & Methods

5.2.1 Measurements to investigate the shape of the light cone

The Field of view (FOV) of a microscope is determined by the magnification of the objective, the size of the sensor inside the camera and the lens used to couple the camera to the microscope light path. Using the 2x objective in combination with the Andor Zyla camera (Tab. 2.4) yielded a FOV of roughly 8315 x 7016 µm. Because the objective can not be moved relative to the ringlight, this method was not suitable for broader measurements of the shape of the light cone. For these measurements of homogeneous and gradient illumination, the sensor spot of the Li-180 Spectrometer was mounted on the x-y-stage. By moving the condenser holding the ringlight, the distance between the sensor and the ringlight was set to be the same as the distance between the ringlight and the cultivation plane (approximately 31.3 mm). Using the x-y stage, the spectrometer was moved along a horizontal line intersecting the center of the ringlight, making light-intensity measurements at each location. After initial tests, this procedure was automated by using the spectrometer software to measure the PFD and NIS-Elements to move the x-y-stage.

5.2.2 Calibration of the light-intensity gradient

The light-intensity gradient was calibrated before each experiment to assign a specific light-intensity for all cultivation chambers. Each calibration procedure included the following three main steps:

(i) Using the LI-190R Terrestrial Quantum Sensor under homogeneous illumination of the growth light, the PFD in the PAR [$\mu E \cdot m^{-2} \cdot s^{-1}$] was measured at various power settings [%] in the light engine's control software. A linear correlation was found between power setting and the resulting PFD.

(ii) Instead of the cultivation chip, a microscopy calibration slide of homogeneous color and density (Chroma Technology, USA) was mounted in the same optical plane. Using the 2x objective, the microscope was focused on the top surface of this calibration slide. Then bright-field images of the calibration slide were taken with the Zyla camera under homogeneous growth-light illumination at various power settings. A linear correlation between the light engine's power settings and the averaged camera gray-values was found. By replacing the power levels with the corresponding PFD values from i), a linear correlation between camera pixel gray-values and PFD can be derived.

(iii) Finally, the half-circle cover was installed to generate the light-intensity gradient. Bright-field images of the calibration slide under gradient illumination at specific power settings were taken. During capture, no additional microscopy illumination was applied. The light-intensity gradient illumination resulted in linearly increasing camera gray-values, resolving the gradient at camera resolution. By replacing the gray values with the corresponding PFD using the correlation from (ii), the light-intensity gradient can now be described as linear function of PFD over position. The slopes and intercepts of the linear correlation of the PFD over the x-coordinate in the images of the gradient were again linearly correlated with the power setting (Eq. 5.1).

(v) All images were loaded into *ImageJ* and combined into a stack. If necessary, artifacts such as scratches on the calibration slide surface or dust particles were cut out manually. The image stack was then uploaded onto the OMERO server. The actual parameterization of Eq. 5.1 was done using a custom Python notebook (*Calibration.ipynb*). The results were then loaded into an Excel template. There, the power setting and position to achieve the desired light intensity range were calculated. The cultivation chip was then placed in the microscope. Using the 2x objective, the desired position was fixed and saved in NIS-Elements. Later Eq. 5.2 was used to calculate the light-intensity for each specific growth chamber. The change in light-intensity over the length of a specific growth chamber (l = 60 µm) was found to be negligible compared to the overall gradient.

$$PFD(x,P) = \underbrace{\{b_{Intercept} + m_{Intercept} \cdot P\}}_{b_{meta}(P)} + \underbrace{\{b_{Slope} + m_{Slope} \cdot P\}}_{m_{meta}(P)} \cdot x \tag{5.1}$$

$$PFD_{Chamber_i} = b_{meta}(P) + m_{meta}(P) \cdot d \cdot (i - i_0) \tag{5.2}$$

Therein *PFD(x,P)* is the light-intensity along the gradient, x is the coordinate along the light-intensity gradient, P is the power setting in the lamp software, b and m are the intercept and

slope of the respective linear correlation. d is the distance between two growth chambers, i is an integer used to identify the position of a particular growth chamber along the length of the light intensity gradient. i_0 is the identifier i of the first growth chamber appearing in the FOV (from the left) of the 2x objective.

5.2.3 Microfluidic cultivation

The experiment itself was mostly started and carried out according to the description in Chapter 2, except that special attention was paid to the following aspects:

- **Position of growth chambers:** The growth chambers selected for time-lapse microscopy should be evenly spaced out along the light-intensity gradient.
- **Time to process one imaging loop:** The time to perform an imaging loop should be minimized. Trial and error tests showed that the x-y-stage motion speed should not exceed 0.25 mm·s^{-1} to ensure a stable PFS. The longer chip design further increased the motion time. Therefore, the outermost arrays were not used when selecting the growth chambers. Furthermore, the *Optimize* command within NIS-Elements was regularly used to optimize the order of the growth chambers. Images were taken only every 2 h. In general, a loop duration of less than 10 min was considered to be applicable. When designing the latest generation of cultivation chips for light-intensity gradient experiments (See Fig. 5.4) minimizing loop duration was considered a key design aspect.
- **Correct positioning during illumination:** For successful light intensity gradient experiments, the correct positioning of the culture chip when not imaging is key. The position of the chip was fixed with the 2x objective and stored in NIS-Elements. When programming the time-lapse sequence, the previously fixed position was always set as the last position to ensure that the x-y-stage always moves back to the correct position.
- **Retrieving data on chamber position:** For the data analysis pipeline to work, the position of a certain growth chamber within the growth chamber array must recognizable from the file name. Therefore, when selecting growth chambers, the coordinate was named according to the respective growth chambers identifier. Later the name must also be used for naming the respective .tif file uploaded onto the OMERO server.

5.2.4 Data analysis

After successful cultivation, cleaning up, saving the data, image pre-processing and calculating growth rates for single growth chambers was conducted according to descriptions in chapters 2 and 4. A group statistics notebook tailored for analyzing light-intensity gradient experiments was designed. This notebook involved the following steps:

1. Retrieving growth rates and chamber identifiers from each growth chamber and combining these into a *pandas* [112] dataframe. The data was previously exported as a .csv file by each *Growth_Rate.ipynb* notebook when executing it.
2. Retrieving the parameterization of Eq. 5.1. The data was exported as a .csv file when executing calibration notebook.
3. Input of values for i_o and P (Compare Eq. 5.2).
4. Assigning a specific light-intensity for each growth chamber using Eq. 5.2.
5. Plotting of the data.
   (a) A heatmap displaying the position of a growth chamber along the gradient and orthogonal to the gradient. The growth rate is indicated by the color.
   (b) A plot displaying the growth rate over the light-intensity.
6. If applicable, retrieving the growth data under homogeneous illumination (Compare chapter 4) as an internal standard.
7. Fitting the growth model (Eq. 1.9) onto the data using *curve_fit* from *SciPi* [113]
8. Plotting the growth data with the internal standard and the growth model.
9. Exporting the data as an .csv file for further analysis.

The .csv files containing the growth rate data over light intensity was uploaded to OriginPro 2020 for plotting and further data analysis. If necessary, data from multiple experiments were combined for comparison.

5.3 Results & Discussion

5.3.1 Characterization of the light-gradient created by the half-circle cover

First, the whole length of the gradient was characterized by moving the sensor spot of a spectrometer along a horizontal line that intersects the center of the circular light cone.

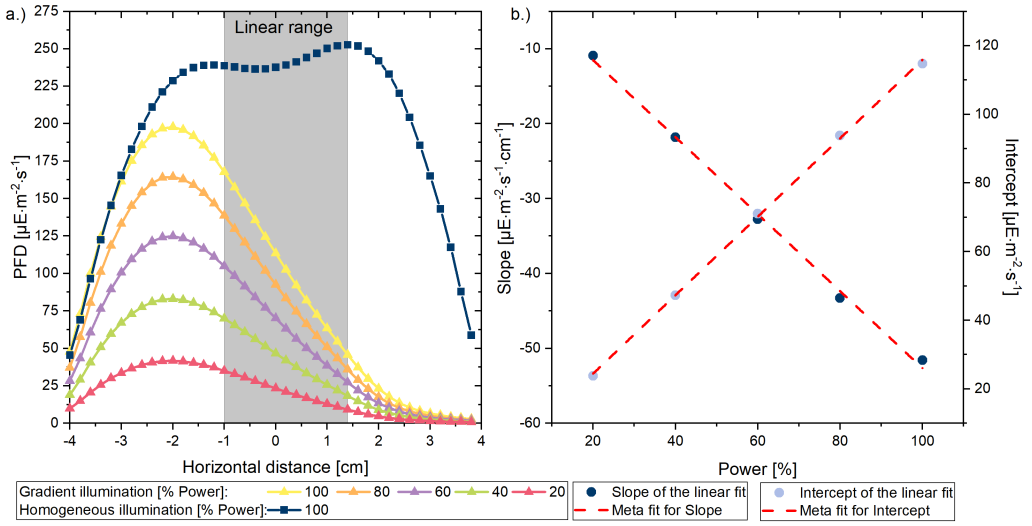


Fig. 5.2: Characterization of the light cone emitted by the ringlight. (a) PFD measurements along a horizontal line intersecting the geometric center of the light cone. Measurements were taken with and without a cover. Measurements with the half-circle cover were taken at varying power settings of the STL. Within the shaded region the dependency of the PFD to the horizontal distance can be modeled by an linear equation. (b) The slopes and intercepts of the linear correlations were plotted against the applied power setting. This relationship can be modeled by a linear equation.

Fig. 5.2 shows the resulting light-intensity profiles. It is noteworthy, that the diversion of the light intensity for homogeneous growth-light illumination shown in Fig. 5.2 (a) is not relevant, since cultivations with homogeneous growth-light illumination were performed using a short chip layout. The shape of the profiles for gradient illumination are similar at all power settings. A linear increase of the light-intensity is present between 1.5 and (-1) cm. Within this range a linear fit was performed onto the data for each power setting. In Fig. 5.2 (b) the resulting slopes and intersects are plotted over the applied power setting of the STL. The data shows that the use of Eq. 5.1 is justified to model the light-intensity gradient within the linear range.

5.3.2 Evaluation of the pre-experimental calibration procedure

Before the above described calibration procedure was established multiple options were considered. The first idea was to take picture's of the cultivation chip itself. This approach was quickly proofed inefficient. The structures, especially the edges of the supply channel and growth chambers, created a large amount of stray light, resulting in poor quality horizontal gray value averages. Two problems arose when cropping out the structures: (i) The resulting

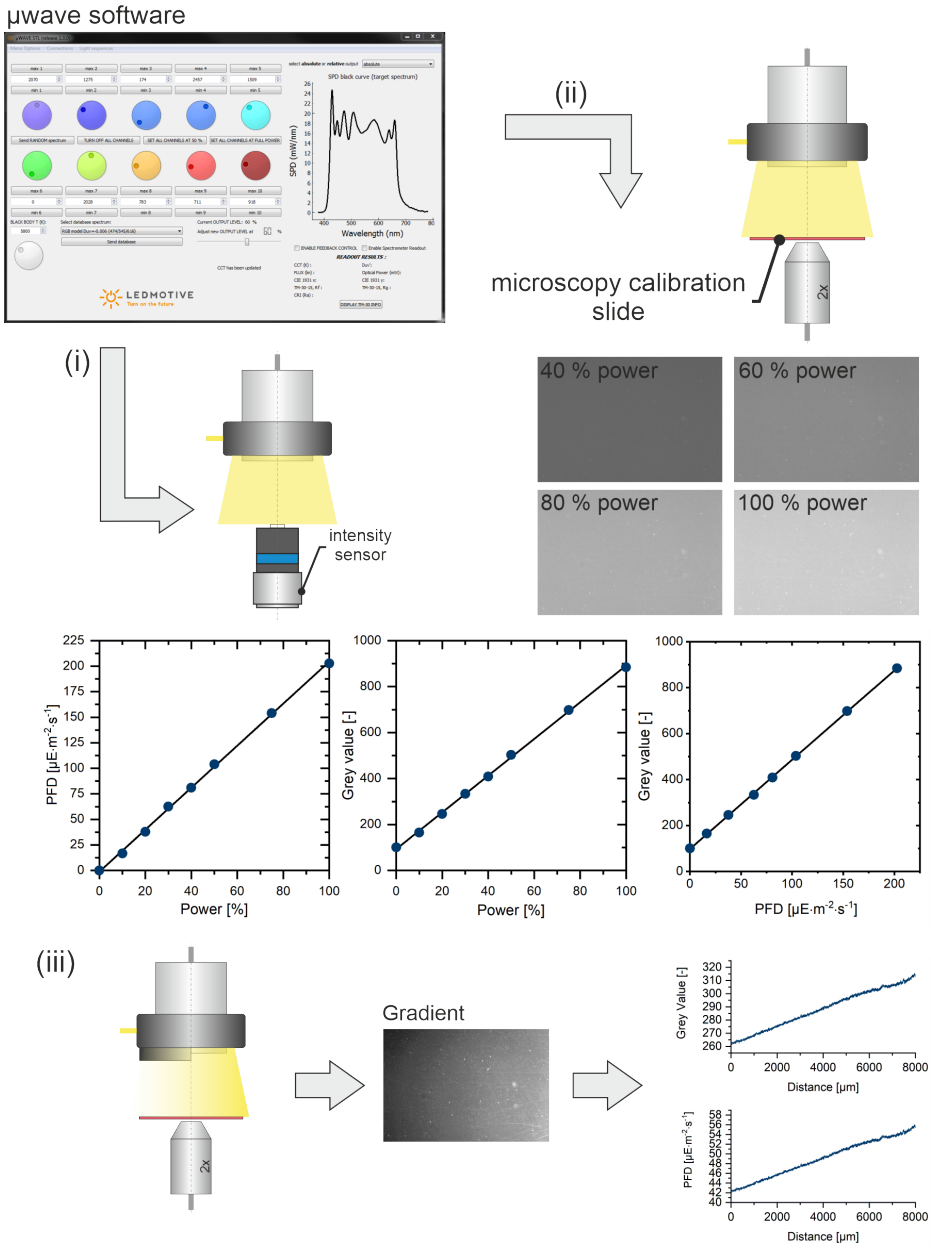


Fig. 5.3: The pre-experimental calibration procedure. (i) First the power setting of the STL light engine was correlated to the PFD in the PAR. (ii) Then the power setting of the light engine was correlated to the gray value in pictures of a microscopy calibration slide taken with a 2x objective. Here homogeneous growth light illumination was applied (iii) In the next step the half circle cover was installed. The resulting calibration was used to correlate the gray value to PFD in a picture of the microscopy calibration slide. All correlation show a $R^2 > 0.99$. The figure was reproduced from Ref. [1] with permission from the Royal Society of Chemistry.

images were quite thin, so intensity spikes resulting from dust particles or scratches were not averaged out vertically. (ii) The overall gray value in the background was too low, leading to an insufficient signal-to-noise ratio. Increasing the exposure time kept the signal-to-noise ratio constant because the point spread from the structures and particles also increased. To fix this the horizontal strip was added to the design of wafer #1 (See Fig. 5.4). The idea was to fill the horizontal strip with a fluorescein solution in order to increase the signal-to-noise ratio. Unfortunately, the emitted intensity was too low. By using a fluorescent calibration slide the signal-to-noise ratio proved sufficient for calibration (See Fig. 5.3). This approach has one disadvantage: the calibration must be performed before the cultivation chip is placed in the light path. Therefore, small adjustments to the distance between the ring light and the cultivation plane can occur, e.g., to apply Köhler illumination. However, these adjustments are negligible. (See Fig. 3.5). Cropped versions of the images were uploaded to the OMERO server and processed by a custom Python script. Correlations between light intensity and power setting, as well as between gray value and power setting, consistently showed R^2 values over 0.99. The final process is summarized in Fig. 5.3.

5.3.3 Optimization of the cultivation layout for light-gradient cultivation

All the experiments involving cyanobacteria that were presented in the previous chapter were performed using wafer 168. A two-step optimization was then conducted based on this design to improve the layout for light-gradient experiments with cyanobacteria. The layouts as well as the design of the growth chambers are shown in Fig. 5.4, further design parameters are listed in Tab. 5.1. The considerations made during the first optimization step, which led to wafer #1, were as follows:

Tab. 5.1: Design parameters of microfluidic layouts designed for light-intensity gradient cultivation. An explanation of the length parameters listed here is depicted in Fig. 5.4.

Layout (Wafer, Layout)	Area whole chip (w_t [µm] x h_t [µm])	Area chamber arrays (w_a [µm] x h_a [µm])	Number chambers (Columns x Rows)
#1 i.	39 x 18	24 x 7.7	40 x 32
#1 ii.	31 x 18	16 x 7.7	40 x 32
#1 iii.	23 x 18	8 x 7.7	40 x 32
#2 i.	53 x 12	25 x 5.6	140 x 12
#2 ii.	43 x 12	30 x 5.6	200 x 12
#2 iii.	41 x 12	40 x 5.6	260 x 12

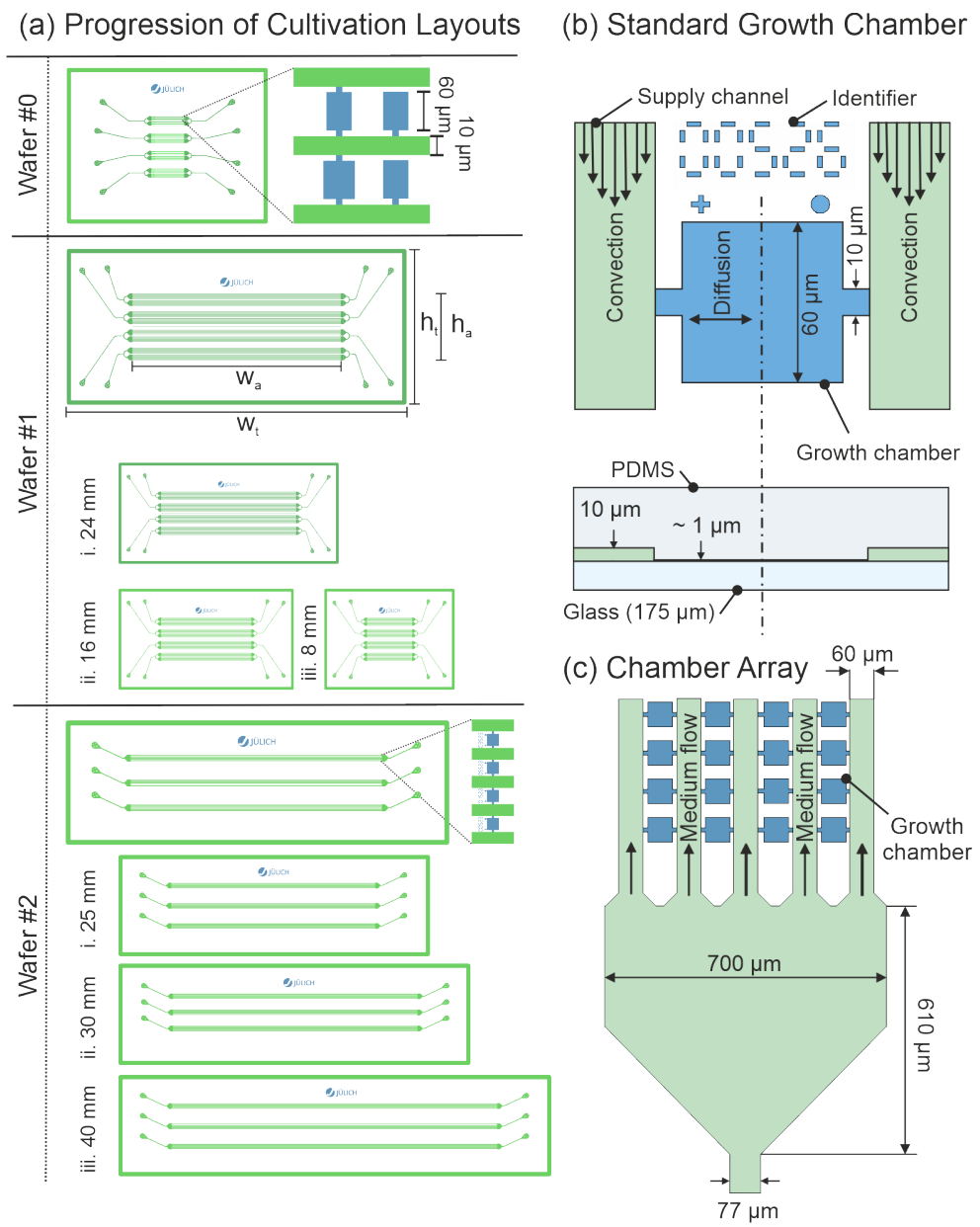


Fig. 5.4: Progression of microfluidic cultivation layouts. (a) Initial experiments were conducted using an already existing design. A two-step optimization was conducted to optimize the design for the cultivation of phototropic microorganisms. Each wafer contains multiple copies of each layout. (b) From wafer #1 onwards a standard growth chambers design was used. The chambers are 60 x 60 µm in size and are connected to the supply channel by a 10 x 10 µm inlet. (c) The growth chambers are interconnect by parallel supply channels. For the full layouts the reader is refereed to App. B: Fig. B.1 - Fig. B.4.

- **Uniformity of growth chamber design:** Wafer 168 included a variety of growth chamber designs as seen in Fig. 5.4 (a). Thereby, not even all variations are shown in the figure. To improve comparability and reproducibility a standard growth chamber design was created and used in all subsequent designs. The following considerations were made:
  - **Size:** The size of 60 x 60 µm was chosen to fill the microscopy camera's FOV when using the 100x objective.
  - **Shape:** The narrow entrance was selected to prevent cyanobacteria from leaving the chamber after inoculation.
- **Growth array length:** In order to take advantage of the full range of the light-intensity gradient the length of the chamber array was extended. The array length of the short layout iii. was picked to fit FOV of the 2x objective.
- **Inlet & Outlet spread:** To make space for the variable ND Filter, the Inlets & Outlets were spread outwards.
- **Chamber numbering:** For unambiguous identification of growth chambers and their position on the chip, a numbering system was added. The numbers were placed next to each growth chambers. The utilized system was the product of master thesis done at the IBG-1.
- **Horizontal calibration strip:** A horizontal strip was added between the growth arrays for potential calibration purposes. As mentioned previously, this approach was unsuccessful.

Most of the results shown in the latter part of this chapter and the next were produced using layout i from wafer #1. Layout iii. was used for cultivating extremophile microalgae, which is shown in the previous chapter. The layout was also used for various other cultivations. However, some issues with the design were observed over time and corrected in the second step of the optimization process.

- **Chamber numbering:** During the design of wafer #1 a mistake was made in the code responsible for generating the chamber identifiers. The identifier were usable, but not optimal. This was fixed.
- **Horizontal calibration strip:** The concept of using the horizontal strip for calibration of the light-gradient did not prove to be successful. Hence, the strip was omitted.
- **Inlet & Outlet spread:** Because the idea of using the variable ND Filter was rejected, the Inlets & Outlets were tilted inwards again. A small angle was kept, to facilitate CO_2 control as is explained in the next chapter.

- **Layout width:** Reducing the width of the chamber arrays and the overall width reduced the travel distance of the x-y-stage, thereby reducing the time needed for imaging. This also improved overall handling.
- **Layout length:** Testing showed, that the layouts ii. and i. were too short for light-gradient cultivation. For wafer #2 the length of the growth array was further increased.
- **Number chambers:** The number of growth chamber columns was increased to facility chamber selection and cell inoculation.

When comparing layout i from wafer #1 with layout i from wafer #2 the total area covered by the growth chamber arrays was reduced by 25 % (Compare Tab. 5.1). It should be pointed out, that the problem of the duration to process an imaging loop mainly stems from the age of the microscopy equipment. It was observed, that in a more modern version of the setup (Ti-E 2, Nikon, Japan), the movement speed of the x-y-stage can be set to higher values without failure of the PFS. However, acquiring a whole new microscopy setup was not a viable option.

5.3.4 Results from light-intensity gradient experiments

Fig. 5.5 shows some exemplary results from light-intensity gradient cultivation using layout i. from wafer #1. The parameters derived from fitting Eq. 1.9 to the different datasets are listed in Tab. 5.2. In Subfigure 5.5, the results are additionally compared to the results under homogeneous growth light illumination, as shown in the previous chapter (Fig. 4.4 and 4.2 f). This comparison confirms that the proposed calibration method is suitable for robustly assigning of light intensities to growth chambers. Although experiments under homogeneous illumination cover a wider range of light intensities, the derived model parameters did not differ significantly. Thus, experimental time was drastically reduced: The experiment under gradient illumination lasted four days, whereas 32 days were needed to gather the data under homogeneous illumination. In this experiment, different dilutions of the BG11 growth medium were perfused through the channels of the microfluidic chip. Growth was observed in channels filled with undiluted and 0.5·BG11. The model parameters between these dilutions did not differ significantly. This confirmed that the growth of UTEX2973 was not limited by nutrient availability. No growth was observed in 10- and 100-fold diluted BG11 growth medium. This could be caused by either nutrient limitation or osmotic pressure.

The strain of PCC7942 (sps_{6803}) used in Subfigure 5.5 (b) was engineered by another group to export sucrose into its environment upon IPTG induction [104]. The applied light

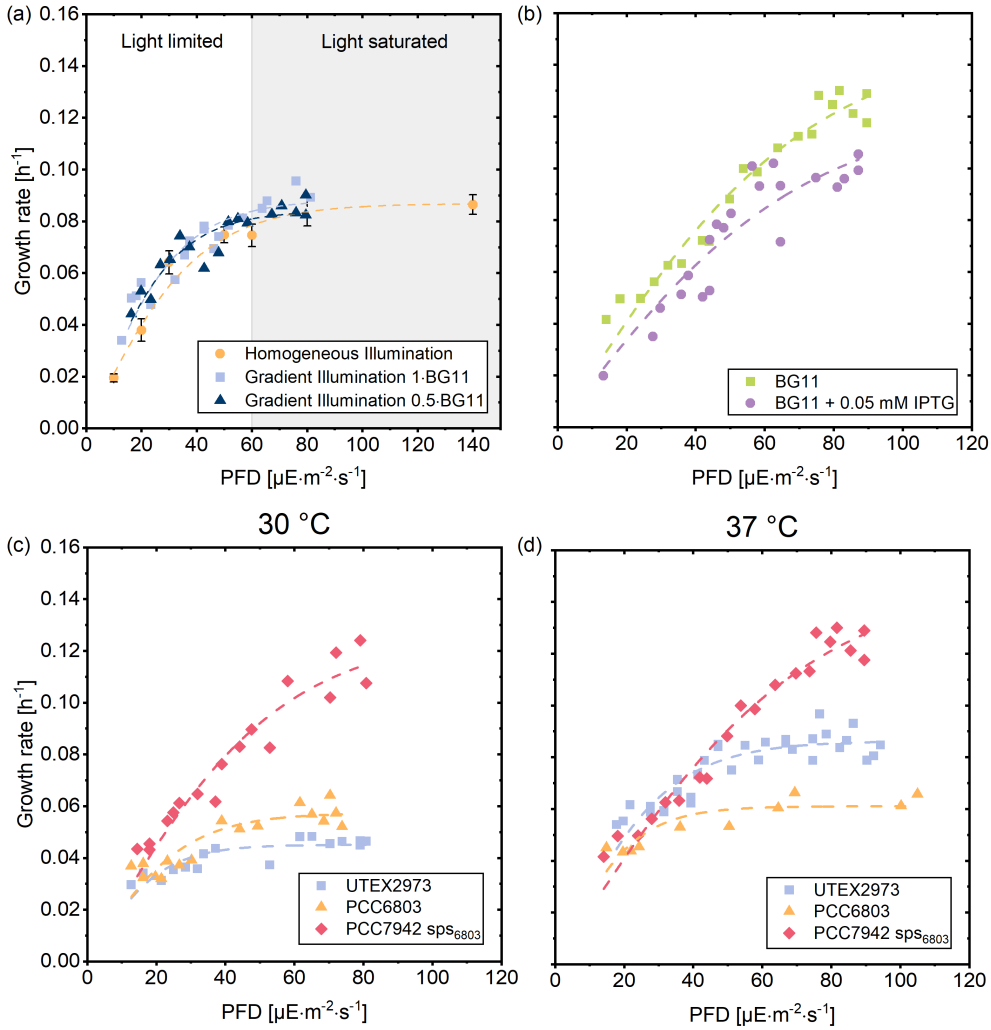


Fig. 5.5: Results from various light-intensity gradient experiments. (a) Comparison of results for UTEX2973 under light-intensity gradient illumination and under homogeneous illumination. Under light-intensity gradient illumination, each data point resembles growth inside distinct chambers from a single, continuously performed experiment. Datapoints for homogeneous illumination were obtained from multiple chambers on the same chip, but the corresponding light-intensity was varied over several independent experiments. (b) Growth of PCC7942 sps$_{6803}$ with and without IPTG induction. Growth of UTEX2973, PCC6803 and PCC7942 sps$_{6803}$ at (c) 30 °C and (d) 37 °C. Subfigure (d) was reproduced from Ref. [1] with permission from the Royal Society of Chemistry.

intensity range was insufficient to explore the behavior of the strain in the light-saturated region; therefore, the μ_{max} parameters shown are merely rough estimates. The value for α, on the other hand, can be trusted more. Nevertheless, it becomes apparent that, as light intensities rise, the growth rates under IPTG induction are significantly lower than those without IPTG induction. This shows that some energy derived from photosynthesis is allocated to exporting sucrose rather than cell growth. In the future, the experiment should be repeated with higher light intensity values. As can be seen from Fig. 5.2, at 100 % power of the STL, the range goes roughly from 50 to 160 $\mu E \cdot m^{-2} \cdot s^{-1}$. This experiment was preliminary work for a co-culture project. The idea was to place the sucrose-consuming *E. coli* W [114] and the sucrose-exporting strain PCC7942 sps_{6803} in a microfluidic growth chamber. Unfortunately, the project did not progress beyond the preliminary stage.

Subfigures (c) and (d) of Fig. 5.5 compare the growth rates of the strains UTEX2973, PCC6803, and PCC7942 sps_{6803} at 30 °C and 37 °C. Each channel was loaded with one of the respective strains. One of the strains was replicated in the spare channel. The results shown in Subfigure (c) of Fig. 5.5 were derived from one distinct experiment. The results in Subfigure (d) were stitched together from multiple partly failed experiments. Nevertheless, subfigure (c) demonstrates that growing all strains at once is feasible. The applied light-intensity range was sufficient to explore the growth dynamics of PCC6803 and UTEX2973 at both temperatures. The growth of PCC6803 was not heavily influenced by the temperature change. The value of μ_{max} for UTEX2973 was reduced by almost 50 % at 30 °C compared to 37 °C. As in Subfigure 5.5 (b), the light-intensity range does not reach high enough to explore the light-saturated region of PCC7942 sps_{6803}. However, it can be said that the temperature change did not greatly influence the growth rates. Furthermore, this strain grew fastest at both temperatures. This demonstrates the ability to quickly phenotype cyanobacteria strains with a precise correlation between light intensity and growth rate. However, it also demonstrates that the system lacks the flexibility required for working with bacteria that exhibit significantly different growth kinetics.

Yu et al. were observing the remarkable high growth rate of 0.33 for UTEX2973. However, the strain used in this work was not acquired directly from the University of Texas culture collection and furthermore shaken in permanent culture for over a year, therefore it is questionable whether the strain still shows the same genotype as in the paper by Yu et al.[101]. The growth rate of 0.04 h^{-1} for PCC6803 at 20 $\mu E \cdot m^{-2} \cdot s^{-1}$ observed by Luke et al. matches the data reported here [55]. Graham et al. reported a maximum growth rate of 1.19 ± 0.02 d^{-1} (0.049 h^{-1}) for *S. elongatus* within their microfluidic device [60].

Tab. 5.2: Model parameters for the data presented in Fig. 5.5 and Fig. 5.6. The data marked with an asterisk (*) represent the same dataset, but are used for comparison in two different contexts: (b) IPTG vs. no IPTG, and (d) 30°C vs. 37°C.

Condition	μ_{max} [h^{-1}]	α [$h^{-1}\cdot(\mu E\cdot m^{-2}\cdot s^{-1})^{-1}$]	$PFD_{1/2}$ [$\mu E\cdot m^{-2}\cdot s^{-1}$]
Fig. 5.5			
Subfigure (a)			
Homogeneous illumination	0.087	$2.16\cdot10^{-3}$	22.11
BG11	0.088	$2.70\cdot10^{-3}$	17.97
0.5·BG1	0.084	$2.78\cdot10^{-3}$	16.82
Subfigure (b)			
0 mM IPTG*	0.151	$2.09\cdot10^{-3}$	39.67
0.05 mM IPTG	0.123	$1.73\cdot10^{-3}$	39.13
Subfigure (c)			
UTEX2973	0.045	$2.15\cdot10^{-3}$	11.55
PCC6803	0.057	$2.09\cdot10^{-3}$	15.07
PCC7942 sps_{6803}	0.27	$2.33\cdot10^{-3}$	30.01
Subfigure (d)			
UTEX2973	0.086	$2.77\cdot10^{-3}$	17.11
PCC6803	0.061	$2.77\cdot10^{-3}$	12.01
PCC7942 sps_{6803}*	0.151	$2.09\cdot10^{-3}$	39.67
Fig. 5.6			
UTEX2973			
Day 1	0.085	$2.47\cdot10^{-3}$	18.82
Day 2	0.089	$2.87\cdot10^{-3}$	16.94
Day 3	0.094	$2.59\cdot10^{-3}$	19.95
Day 4	0.094	$2.65\cdot10^{-3}$	19.67
PCC7942 cscB			
Day 1	0.150	$2.35\cdot10^{-3}$	35.11
Day 2	0.163	$2.37\cdot10^{-3}$	37.69
Day 3	0.133	$2.67\cdot10^{-3}$	27.38

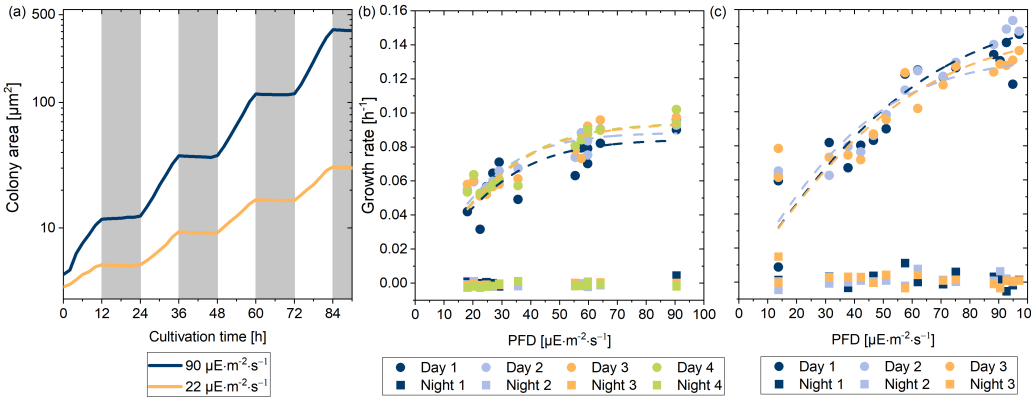


Fig. 5.6: Combined day/night rhythm and light-intensity gradient cultivation. (a) Colony area over cultivation time for UTEX2973 at two different light intensities. Each line represents a colony in a separate growth chamber. However, both growth chambers are on the same cultivation chip. A 12-hour day and 12-hour night cycle was applied during the cultivation. The shaded region indicates the night. (b) Growth rate over light intensity for UTEX2973. Growth rates were calculated based on 12-hour intervals. Each data point represents growth within a distinct growth chamber. (c) Growth rate over light intensity for PCC7942 cscB. The growth rates were calculated based on 12-hour intervals. Each data point represents growth within a distinct growth chamber. All the data shown in the plot was generated from a single experiment. Subfigures (a) and (b) were reproduced from Ref. [1] with permission from the Royal Society of Chemistry.

5.3.5 Combined day/night rhythm and light-intensity gradient cultivation

Fig. 5.6 shows an experiment in which a 12-hour day and 12-hour night cycle was applied simultaneously to the light-intensity gradient. This provides further support for the argument against a light-intensity gradient over time. In this case, it would not be possible to cultivate under a simultaneous day/night rhythm and a light-intensity gradient. In this experiment, two growth channels were inoculated with UTEX2973 and one with PCC7942. A fourth channel inoculated with PCC6803 exhibited growth in only three independent growth chambers. As can be seen in Fig. 5.6, cell growth stops rapidly after the onset of night. Conversely, exponential growth quickly resumes once the growth light is turned back on. It is worth mentioning that images were only taken once per hour. Therefore, what happens during the first hour of the night remains unclear. The parameters obtained by fitting Eq. 1.9 to the data are listed in Tab. 5.2. For UTEX2973, the value for μ_{max} was slightly higher on the third and fourth day than on the previous day. This finding could be due to a primary adaptation phase, or it could be statistical noise. For PCC7942, only the values for the first three days are listed because the growth chambers were already full on the fourth day due to the higher light intensities. In this case, the value for μ_{max} differs greatly from one day to the next. However, these values should not be overstated. The same issue reported in the previous

paragraph also applies to this experiment. For cultivating strains with significantly different growth kinetics, the range of light intensities is insufficient to explore the light-saturated range for all strains.

5.4 Conclusion & Outlook

In this chapter, a method was developed for quickly investigating the relationship between light intensity and growth rate for multiple cyanobacteria strains at single-cell resolution. This included choosing a technique for generating the light-intensity gradient, characterizing the chosen technique, designing tailor-made cultivation layouts, establishing a method for assigning a light intensity to each growth chamber on the cultivation layout, and coding Python notebooks to automate light-intensity assignment and post-experimental data analysis. The resulting calibration data is then passed directly to the post-experimental data analysis workflow. The outcome from the light-intensity cultivation were comparable to the results generated under homogeneous growth light illumination, whereby the time to generate the data was drastically reduced. For homogeneous illumination the experiments were conducted over 32 days, whereas the data for gradient light-intensity cultivation was gathered in four days.

The main advantage of the technique is that gradient generation is integrated into the additional light path. Therefore, the gradient can be activated or deactivated by opening or closing the shutter. Also, image quality was unaffected. Therefore, this technique enables a light-intensity gradient to be generated without placing obstacles in the light path for microscopy or placing an additional PDMS layer to the cultivation layout. This facilitates CO_2 control, as is demonstrated in the next chapter. Part II of this thesis demonstrates how the technique can be used to characterize strains in fundamental biological research.

The major drawback of the method is the limited light intensity range. Sometimes multiple experiments were needed to find the right light-intensity range for a specific strain. When cultivating strains with highly differing kinetics, it was complicated to choose a light-intensity range that worked for all strains. For strains with a high $PFD_{1/2}$ this resulted in a compromise between achieving a wide range of light intensities and ensuring good coverage at low light intensities. One approach to increase the usable light-intensity range would be to add a higher-order polynomial term to Eq. 5.1. Although the calibration process would need to be modified, the task is highly feasible. Also, a project is underway to simulate the light cone emitted by the ringlight using algebraic equations. This simulation is expected to optimize the ringlight's coverage, resulting in a

steeper light-intensity gradient, thus overcoming the issue of the limited light-intensity range.

Although it is already being used in research to study the fundamental properties of cyanobacteria, there is potential to further improve the experimental workflow with homogeneous illumination and with the linear light-intensity gradient. During work on this thesis the lamp was controlled by a different software than the software performing the time-lapse measurement. A problem arose during the day/night experiments. When the time-lapse was stopped to correct the PFS, a time offset occurred between the microscope and the lamp software. Since pictures were only taken every one to two hours, a ten-minute offset was considered negligible. Integrating the control of the growth-light into the microscope software would have solved this problem. The light-intensity sensor (Fig. 3.5) can be integrated into the microscope software via the DAQ-device. Integrating both the lamp and the sensor into the software can further automate light-intensity measurements and calibration of the light-intensity gradient. Further automation of the experimental workflow, including automated chamber selection and image pre-processing, would reduce experimental effort. Other researchers at the institute are currently working on this.

An additional challenge was selecting the growth chambers to be observed in a way that minimizes the time needed for the microscope to move to each position. While in this chapter the problem was solved by making the cultivation chip slimmer, it could also easily be solved by using a newer microscope with a faster x-y-stage.

6 Dynamic CO_2 control

Parts of this chapter have been published in peer-reviewed journals or on preprint servers (I and III) [1, 94]. Some results were presented as an oral presentation (II) or posters (II, V) at international conferences. Data and the applied code are publicly available (I - III). The simulations were carried out in collaboration with the Modeling and Simulation group at the IBG-1. The conceptualization of the simulation, literature research, and interpretation of the results were carried out together with Birgit Stute. She then implemented and executed the simulation.

6.1 Introduction

As evident from the data presented in chapters 4 & 5 the growth rate of cyanobacteria is mainly governed by two parameters. The amount of photons impinging of a cell, refereed to as light-intensity, and the availability of CO_2. Control of the light-intensity was extensively demonstrated in the last three chapters, culminating in the development of a spatial light-intensity gradient for fast growth behavior characterization. This chapter in contrast will show the development of a system for controlling the CO_2 during microfluidic cultivation. The design of the CO_2-perfusion chamber was based on previously published results [72, 73]. As demonstrated in chapter 4 cyanobacteria growth was not limited within the microfluidic device when working with ambient air. Hence, to explore growth kinetics, the CO_2 concentration should be lowered compared to ambient air.

6.2 Materials & Methods

6.2.1 Experimental design

Supply with CO_2 depleted gas

As demonstrated in Chapter 4, the growth of cyanobacteria was not limited by CO_2 availability within the microfluidic device when ambient air was used. Therefore, in order to explore growth kinetics, the concentration of CO_2 should be lower than that of ambient air. The concentration of CO_2 in the ambient air was monitored using a conventional air quality control device (Air CO_2ntrol 5000, TFA Dostmann, Germany). The measured CO_2 concentration in the lab with the microscope and in the lab with the MC was between 400

and 500 ppm. In order to get the desired CO_2 molar fractions O_2 and N_2 were supplied from the building gas supply network, for CO_2 a bottle containing 200 ppm CO_2 in synthetic air was used. To mix the gas streams a block of three mass flow controllers were used (red-y, Voegtlin Instruments GmbH, Switzerland). The supplier calibrated the controllers for the desired gas. However, for the synthetic air, a controller calibrated for N_2 was used. The mass flow rates were controlled using the supplier's software (red-y, Voegtlin Instruments GmbH, Switzerland) for the preflushing with gas and with an in-house developed LabView software. The desired volumetric flow rates were calculated using Eq. 6.1, 6.2, and 6.3.

$$\dot{V}_{Synthetic\ air} = \dot{V}_{Final} \cdot \frac{y_{CO_2,\,Final}}{y_{CO_2,\,Bottle}} \tag{6.1}$$

$$\dot{V}_{N_2} = \left[\dot{V}_{Final} - \dot{V}_{\text{Synthetic air}}\right] \cdot 0.79 \tag{6.2}$$

$$\dot{V}_{O_2} = \left[\dot{V}_{Final} - \dot{V}_{\text{Synthetic air}}\right] \cdot 0.21 \tag{6.3}$$

Therein $\dot{V}_{Final}$ is the volumetric flow rate of the final gas mixture, $\dot{V}_{Synthetic\ air}$ is the volumetric flow rate from the synthetic air bottle, $\dot{V}_{N_2}$ is the volumetric flow rate of pure N_2 gas, $\dot{V}_{O_2}$ is the volumetric flow rate of pure O_2 gas, $y_{CO_2,\,Bottle}$ is the molar fraction of CO_2 in the synthetic air bottle and $y_{CO_2,\,Final}$ is the molar fraction of CO_2 in the final gas mixture.

The volumetric flow rate of the final mixture $\dot{V}_{Final}$ was constrained by two factors: (i) The minimal flow rate applicable to the mass flow controller connected to the synthetic air bottle (1 mL·min^{-1}). (ii) The maximum flow rate of the mass flow controller connected to the pure N_2 (10 mL·min^{-1}). Based on these constraints, a total flow rate of 13.5 mL·min^{-1} was selected for $\dot{V}_{Final}$.

Device design & fabrication

The cultivation design used for the CO_2 control experiments was based on layout i from wafer #1. For CO_2 control experiments, the final cultivation chip consisted of a thin cultivation layer and a rectangular box for perfusion of CO_2-depleted air as seen in Fig. 6.1.

Cultivation layer: Particular emphasis was placed on molding the cultivation chip to be as thin as possible. Therefore, 25 g of PDMS and 2.5 g curing agent were used, as opposed to the 60 g PDMS and 6 g curing agent used for standard-height cultivation chips. Due to the inherent flexibility of the PDMS, it was difficult to measure the height of the cultivation chip exactly. However, an approximate height of 1 mm was measured using a caliper. The washing step was performed as always and chips were stored until further usage.

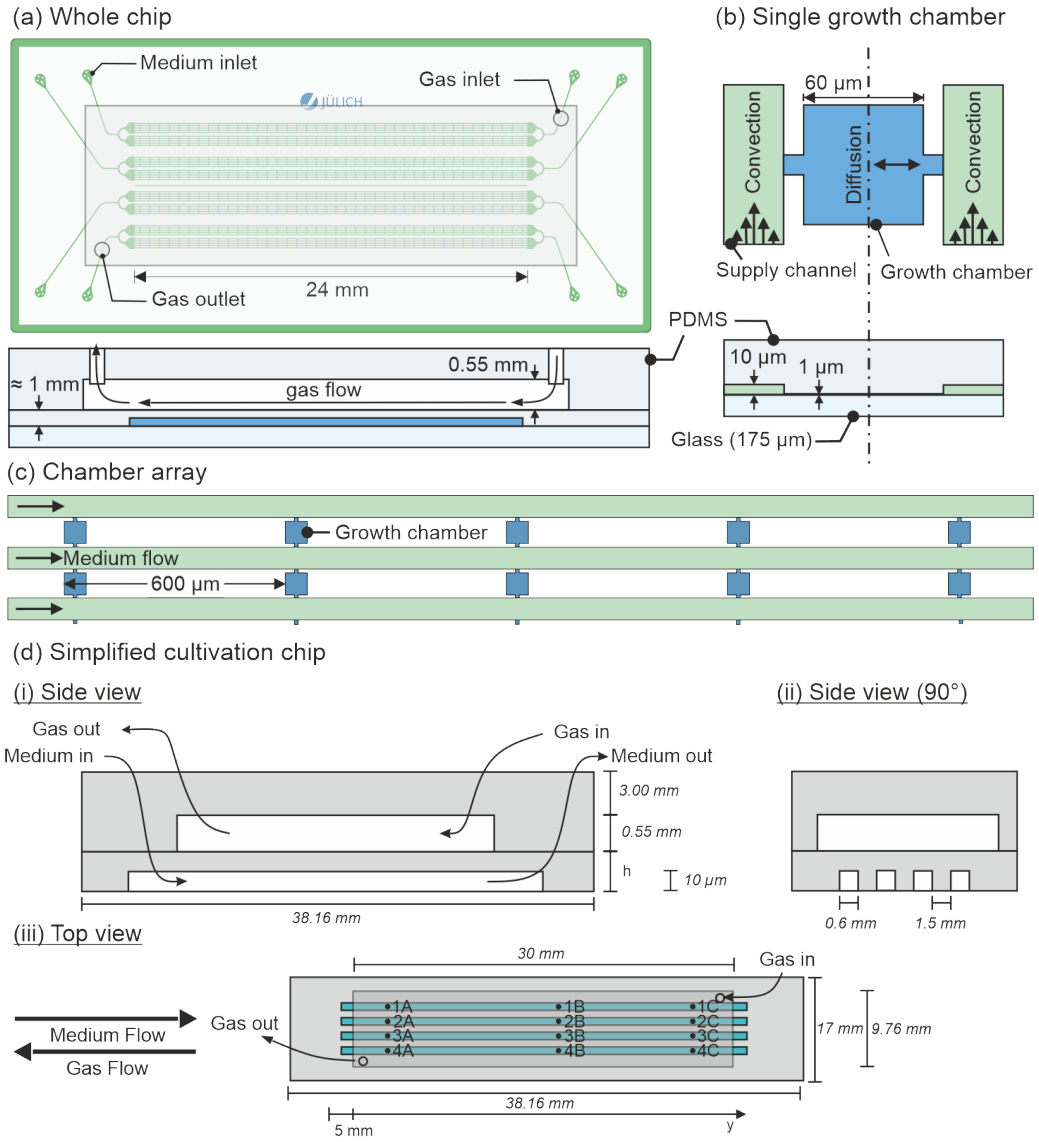


Fig. 6.1: The cultivation device used for CO_2 control experiment. (a) Cultivation chips of approximately 1 mm thickness (the cultivation layer) were used for experiments with CO_2 control to minimize the thickness of the gas exchange membrane. The CO_2 perfusion chamber was bonded onto the cultivation layer enabling the perfusion of air with a defined molar fraction of CO_2. (b) Each chamber is connected to medium supply channels (10 µm in height), resulting in diffusive mass transfer within the chamber. The chambers have a surface area of 60 µm x 60 µm and a height of approximately 1 µm. (c) The cultivation layer contains four arrays, each 24 mm long and containing eight rows of forty evenly distributed growth chambers. (d) Simplified model of the cultivation chip for Computational fluid dynamics (CFD) simulation. The figure was reproduced from Ref. [1] with permission from the Royal Society of Chemistry.

CO_2 perfusion chamber: The replication master for the CO_2 perfusion chamber (See App. C: Fig. C.13) was designed using the 3D printing protocol described in chapter 2, with the fabrication details listed in Tab. 2.5. The design incorporates a rectangular box measuring 30 x 9.76 x 0.55 mm for homogeneous gas supply. Molding of the gas layer involved mixing of PDMS with the curing agent at a ratio of 10:1 (30 g PDMS + 3 g curing agent), degassing, casting the PDMS and baking it at 80 °C for 2 hours. The polymerized PDMS was then removed from the replication master, cut and stored until required. Before starting an experiment inlet and outlet holes were created.

Final assembly: First, the CO_2 perfusion chamber was first bonded onto the cultivation chip, thereby enabling gas supply to the cultivation chambers as well as additional mechanical stability when handling the thin PDMS chips. Then the inlet and outlet holes were created. Finally, the cultivation chip was bonded onto the glass slide. A detailed description is provided in chapter 2.

Time-lapse microscopy & Data analysis

Time lapse microscopy was mainly performed according to the protocol given in chapter 2. Before starting the experiment the light-intensity gradient was applied according the description in chapter 5. The growth light was programmed to emit Planck's radiation distribution at 5800 K, mimicking the spectrum emitted by the sun [109]. The two main deviations to the standard protocol are:

Medium flow rate: A volumetric flow rate of BG11 of 400 $nL{\cdot}min^{-1}$ was applied in contrast to the default 200 $nL{\cdot}min^{-1}$, to prevent drying out of chambers by the perfusion of dry air.

Preflushing of air: Prior to inoculation, the resulting airflow was connected to the inlet, and air containing 100 ppm CO_2 was flushed through the system for a period of time to allow it to reach equilibrium. Prior to connecting the gas flow, it was verified that CO_2 was actually arriving at the outlet tubing using a conventional air quality control device. Once the gas flow was connected, a drop of DI water was sprinkled onto the outlet of the CO_2 perfusion chamber to confirm that the gas flow was functioning correctly. The LabView script was started simultaneously with the time-lapse microscopy. The CO_2 flow was always operated in counter-current to the medium flow. The molar fraction of CO_2, the volumetric flow rates and the time points for the experiment shown in this chapter are listed in Tab. 6.1.

Tab. 6.1: Molar fraction of CO_2 and volumetric flow rates for the CO_2-control experiment.

y_{CO_2} [ppm]	c_{CO_2} [µM]	$\dot{V}_{Syntheticair}$ [mL·min^{-1}]	$\dot{V}_{0_2}$ [mL·min^{-1}]	$\dot{V}_{N_2}$ [mL·min^{-1}]	Cultivation time [h]
100	2.56	6.75	1.42	5.33	0 -24
50	1.28	3.38	2.13	8	24 - 48
15	0.38	1.01	2.62	9.87	48 - 72
0	0	0	2.66	10	72 - 96

With regard to data analysis, the procedure described in Chapter 2 was mostly followed, except that the growth rates were calculated based on the 24-hour intervals, shown in Tab. 6.1. Also, before starting the analysis, it was confirmed that growth had actually stopped at 0 ppm. Growth channels where this was not the case were not used in the analysis. Placing the CO_2 perfusion chamber above the cultivation layer impaired the image quality, resulting in more frequent segmentation errors. Therefore, growth rates were calculated with extraordinary attention in this chapter. The calculation intervals were reviewed manually for each chamber and changed, if necessary, to correct segmentation errors. Growth rates corrupted by segmentation errors or a chamber that was already full (an issue especially prominent for PCC7942) were omitted from the final plot. The curated data was then imported into Origin2020 Pro for curve fitting and plotting.

6.2.2 Calculations

Estimation of the aqueous CO_2 concentration

At moderate temperatures and at low pressures the equilibrium between CO_2 in a gas phase and in a liquid phase can be described by the Henry equation [115]

$$x_{CO_2} \cdot H_{CO_2,\,H_2O} = y_{CO_2} \cdot P \tag{6.4}$$

Therein x_{CO_2} is the molar fraction of CO_2 in water, H_{CO_2,H_2O} is the Henry-coefficient for CO_2 in water, y_{CO_2} is the molar fraction of CO_2 in the air and P is the total pressure.

The concentration of CO_2 in water was calculated from the molar fraction using equation 6.5.

$$c_{CO_2} = \frac{x_{CO_2} \cdot \rho_{H_2O}}{M_{H_2O}} \tag{6.5}$$

Therein C_{CO_2} is the concentration of CO_2 in water, x_{CO_2} is the molar fraction of CO_2 in water, ρ_{H_2O} is the density of water (1000 g/L), M_{CO_2} is the molar weight of CO_2 (44.01 g·mol^{-1}) and M_{H_2O} is the molar weight of water (18.015 g·mol^{-1}).

For calculating the Henry-coefficient the correlation given by Carroll et al. was used [115]. This correlation was calculated from data at higher partial pressures than used in this thesis. For proof, the calculated solubility's at ambient CO_2 (320 ppm = 0.032 %) were compared to tabular data given in Boyd et al. [22] and Maki et al. [116]. The deviations were found to be negligible.

A dual parameter growth model

For modelling the dependency of the growth rate on external nutrients such as CO_2 Monod kinetic models are often applied [33].

$$\mu(y_{CO_2}) = \mu_{sat} \frac{y_{CO_2}}{K_{CO_2} + y_{CO_2}} \tag{6.6}$$

Therein μ is the growth rate, y_{CO_2} is the molar fraction of CO_2 in the air, μ_{sat} is the growth rate when neither CO_2 nor the light-intensity are limiting growth and K_{CO_2} is the molar fraction of CO_2 at which half of μ_{sat} is reached.

The dual parameter growth model was derived by inserting Eq. 6.6 into Eq. 1.9 resulting in Eq. 6.7.

$$\mu(PFD, y_{CO_2}) = \frac{\mu_{sat} \cdot y_{CO_2}}{K_{CO_2} + y_{CO_2}} \cdot \tanh \frac{\alpha \cdot PFD}{\frac{\mu_{sat} \cdot y_{CO_2}}{K_{CO_2} + y_{CO_2}}} \tag{6.7}$$

Therein μ is the growth rate, PFD is the applied photon flux density, y_{CO_2} is the molar fraction of CO_2 in the air, μ_{sat} is the growth rate when neither CO_2 nor the light-intensity are limiting growth, K_{CO_2} is the molar fraction of CO_2 at which half of μ_{sat} is reached and α is the initial slope of the model.

The model was parameterized in OriginPro 2020, which included the following steps:

1. The hyperbolic tangent model (Eq. 1.9) was fitted onto the growth rate over light-

intensity curve for each CO_2 molar fraction.

2. At 0 ppm CO_2 no growth was observed. Instead of fitting Eq. 1.9 the mean of all growth rates was calculated.
3. The Monod kinetic model (Eq. 6.6) was fitted onto the μ_{max} over y_{CO_2} curve.
4. The resulting values for μ_{sat} and K_{CO_2} were inserted into Eq. 6.7.
5. As derived in Eq. 1.1.2 α represents the slope in the light-limited region, where the CO_2 concentration does not inhibit growth. Accordingly, no correlation between the initial slope α and y_{CO_2} was observed. The mean of all values for α was calculated and inserted into Eq. 6.7.

Estimation of the aqueous CO_2 concentration in the MC

Estimation of the aqueous CO_2 concentration in the MC under ambient air supply included the following steps:

- Retrieving the μ_{max} for growth of UTEX2973 in the MC under ambient air supply from Tab. 4.4.
- Count based growth rates were more comparable to the growth rates in the MC. The growth rates presented in this chapter were based on colony area. Using Eq. 1.9 and the data in Tab. 4.4 the μ_{max} in the MC was transformed into the corresponding area based growth rate at the same light intensity.
- This growth rate was inserted into Eq. 6.6 and solved for y_{CO_2}.
- The aqueous CO_2 concentration was then calculated using Eq. 6.4 and 6.5.

Tab. 6.2: Estimation of the half maximum CO_2 concentration of RuBisCo.

Parameter	Value	Source
Half maximum CO_2 concentration K_{CO_2}	172 µM	[117, 118]
Half maximum O_2 concentration K_{O_2}	585 µM	[117, 118]
Henry coefficient O_2 in water at 37 °C $H_{O_2,\,H_2O}$	0.0011 mol·kg^{-1}atm^{-1}	[119]
$c_{CO_2,\,1/2}$	240.29 µM	Eq. 6.8

Calculation of comparative data from the literature

Literature research was performed to find comparative data on the affinity of *S. elongatus* towards inorganic carbon. Data on the catalytic rates of RuBisCo were found for PCC7942 using the review by Flamholtz et al. [117]. The original experiment was performed at 25 °C and a pH of 8.1 [118]. The CO_2 concentration at the half maximum catalytic rate of RuBisCo under 21 % O_2 was estimated using literature data (See Tab. 6.2 and Eq. 6.8).

$$c_{CO_2,\,1/2} = K_{CO_2} \cdot \left[1 + \frac{H_{O_2,\,H_2O} \cdot 0.21}{K_{O_2}}\right] = 240.29\ \mu M \tag{6.8}$$

Therein $c_{CO_2,\,1/2}$ is apparent half maximum concentration of CO_2 under a given inhibitory O_2 concentration (Here 21 % O_2 in air), K_{CO_2} is the half maximum concentration of CO_2, K_{O_2} is the half-maximum inhibitory concentration of O_2 and $H_{O_2,\,H_2O}$ is the Henry coefficient O_2 in water at 37 °C.

6.2.3 Simulation of the cultivation system

Conventional CO_2 sensors rely on measuring the pH change resulting from the equilibrium shown in Eq. 1.6. The change in pH leads to a change in voltage between a measurement and a reference electrode, that can be correlated to the aqueous CO_2 concentration. However, due to the low fluid volumes, these devices are not applicable here. In microfluidics, some authors report measuring the pH change with fluorescence optodes or pH-sensitive dyes and correlating this to the CO_2 concentration (Compare Tab. 1.3). If synthetic air without CO_2, would be flushed through the CO_2 perfusion chamber and a resulting fluorescence signal was measured, it would be impossible to know whether this fluorescence signal actually corresponds to a CO_2 concentration of 0 mg/L. Consequently, these methods are more useful for measuring dynamics than for measuring absolute values. In this thesis, a COMSOL simulation was performed to validate the CO_2 concentration inside the cultivation device. The study was aimed at answering two main questions:

- **CO_2 perfusion chamber:** Can a homogeneous distribution of CO_2 be assumed within the CO_2 perfusion chamber? If so, does it contain the desired molar fraction of CO_2?
- **Cultivation layer:** Can it be assumed that the CO_2 in the CO_2 perfusion chamber is in equilibrium with the aqueous CO_2 according to Henry's law?

To answer these questions the design of the cultivation chip was simplified to reduce computational complexity (Subfigure 6.1 d). First, the growth chambers were omitted, because the fluid within them is stagnant and the volume of the chambers is small compared to the

volume of the supply channels. Then, the supply channels were merged into one channel with an equivalent volume, therefore keeping the velocity of the fluid constant. The gas layer was not simplified. The mass transfer coefficients for the simulation were taken from Mäki et al. [116]. The simulations were performed in COMSOL Multiphysics 6.2 (COMSOL Inc., USA).

6.3 Results & Discussion

6.3.1 Simulation results

In the simulation perfusion of CO_2 depleted air was started at t = 0 s. An equilibrium was reached after roughly 15 minutes for all simulations. At the applied imaging rate of 1 image every 2 h, this was sufficient to exclude an effect of the equilibrium kinetics on the observed growth rates. As can be seen from Fig. 6.2, the assumption that CO_2 is distributed homogeneously in the CO_2 perfusion chamber is well justified, hence answering the first question. When synthetic air containing 0 ppm CO_2 was perfused, a maximum of 2.7 ppm CO_2 was observed at location 1A. The maximum CO_2 concentration in the B and C row was 1.6 ppm. It is noteworthy, that the virtual measurement points were placed, to resemble the outer border of the chamber array. Furthermore, the light-intensity gradient was applied with the lowest light intensity to be projected onto row A and the highest

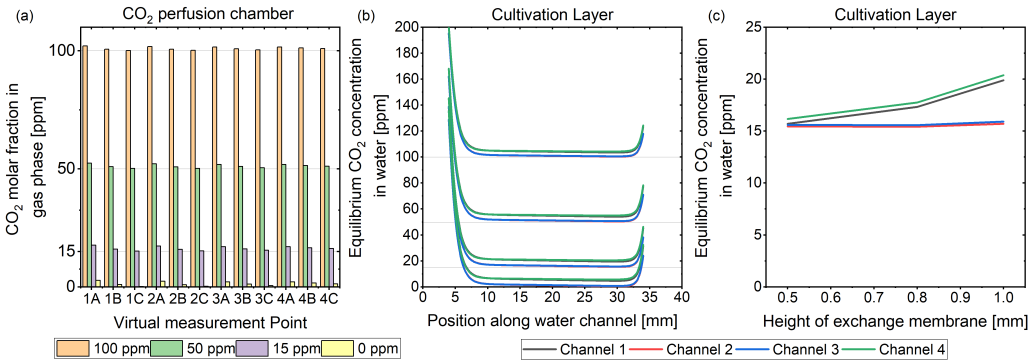


Fig. 6.2: Results from the COMSOL Simulation of the CO_2 control device. (a) CO_2 molar fraction in the CO_2 perfusion chamber at the virtual measurement points after 75 minutes perfusion of synthetic air with a defined CO_2 concentration. (b) CO_2 concentration in the cultivation layer along the length of the simplified chamber array. CO_2 concentrations are expressed as corresponding equilibrium CO_2 molar fractions. Here the distance between CO_2 perfusion chamber and cultivation layer h was at 1 mm (c) CO_2 concentration at the y-coordinate of 30 mm for different heights of the exchange membrane between CO_2 perfusion chamber and cultivation layer (h). The CO_2 concentrations are expressed as corresponding equilibrium CO_2 molar fractions.

light intensity in row C. Therefore, the slightly higher CO_2 concentration in row A does not affect the estimation of μ_{max}, because under the projected light intensities, growth is limited by light rather than CO_2.

Answering the second question is more difficult. Although the CO_2 concentration decreases rapidly due to the countercurrent flow of CO_2-depleted air, a higher CO_2 concentration is clearly present in the outer channels than in the inner channels at a distance of 1 mm between the cultivation layer and the CO_2 perfusion chamber. This is due to CO_2 diffusion from the sides. Reducing the height of the exchange membrane to 0.5 mm resolved this difference in CO_2 concentration.

During the simplification of the model, the focus was on maintaining the volume of the flow channels, which reduced the exchange surface area compared to the original design. Additionally, the growth chambers, which were ten times thinner, were omitted entirely, further reducing the exchange surface area. Going forward, it was planned to take the results from the simulation of the CO_2, perfusion chamber and simulate only a small section of the cultivation layout with the detailed structure. Ideally, this section should be taken from the inlet of an outer channel to create the most conservative scenario (See App. D). However, due to time constraints, this simulation has not yet been carried out.

6.3.2 Light-intensity gradient cultivation under decreasing CO_2 molar fractions

The experimental results are shown in Fig. 6.3. All parameters from fitting Eq. 1.9 and 6.6 are listed in Tab. 6.3: In this experiment one growth array was inoculated with UTEX2973, one with PCC7942, growth in the other arrays failed. Although both successful cultivations were from the outer arrays, only the inner sub-array was used to select the growth chambers for imaging. As seen from Subfigures (a) and (b) a light-intensity gradient between ≈ 10 and 80 $\mu E \cdot m^{-2} \cdot s^{-1}$ was simultaneously applied. For UTEX2973 no reduction of the growth rate was observed between 100 and 50 ppm. At 15 ppm the value for μ_{max} was reduced. At 0 ppm growth had stopped. As usual PCC7942 grew faster overall, and a reduction was already observed between 100 and 50 ppm CO_2. Overall, fewer data points are available for PCC7942, particularly at high light intensities, the growth chambers were already full when switching to 15 ppm CO_2. Although it was not possible to derive a growth rate, it was clear from visual inspection that growth had completely stopped at 0 ppm. For both cases the proposed dual-parameter growth model worked well to explain the data.

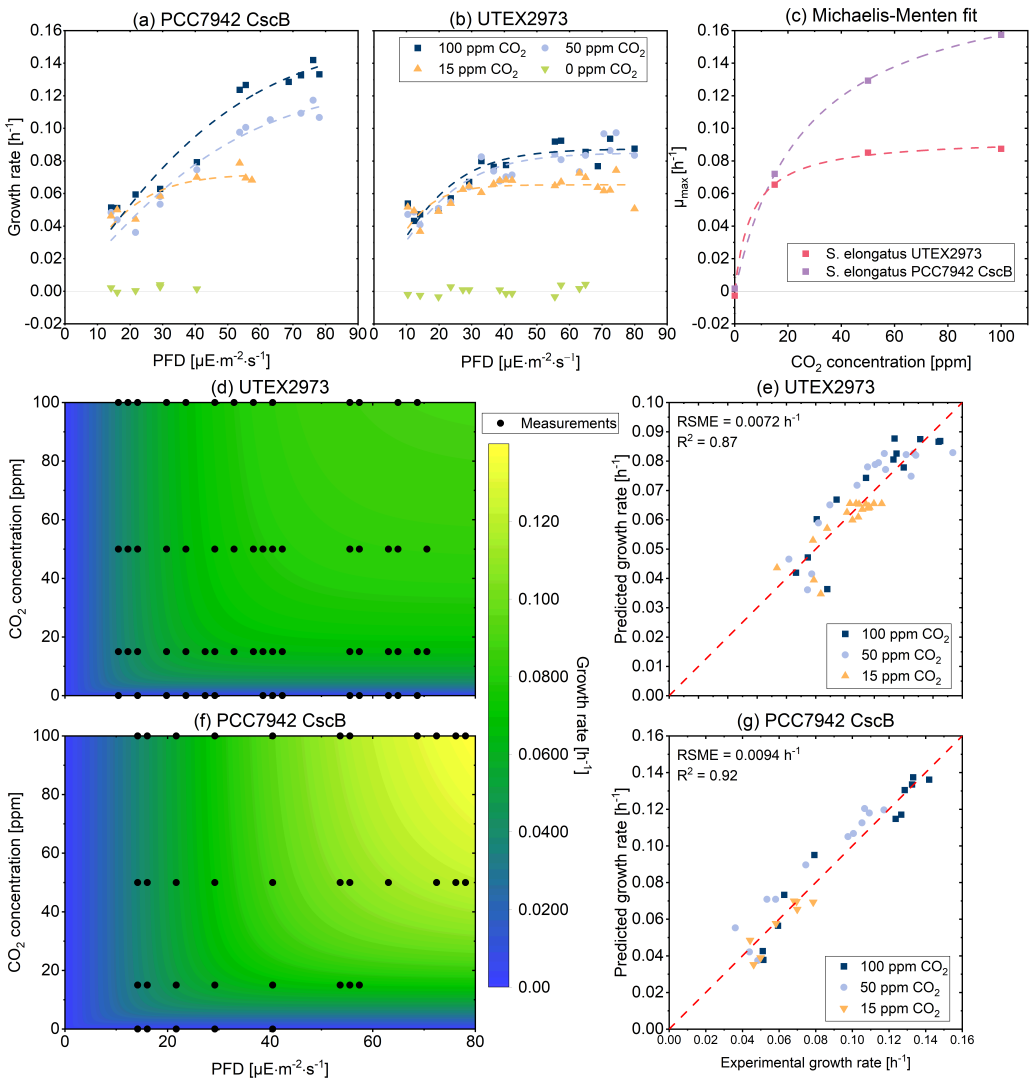


Fig. 6.3: Cultivation of S. elongatus with an applied light-intensity gradient and decreasing CO_2 molar fractions. Growth rate over light intensity curves for (a) PCC7942 cscB and (b) UTEX2973. Each data point represents growth within a distinct growth chamber illuminated with a given light intensity. Growth rates were determined for each 24-hour interval separately (indicated by colour and shape). The dotted line shows the fit of Eq. 1.9 to the data. (c) Curve of μ_{sat} over the CO_2 molar fractions for both strains. The dotted line shows the fit of Eq. 6.6 onto the data. The resulting dual-parameter growth model for (d) UTEX2973 and (f) PCC7942 cscB. The data is displayed as CO_2 molar fraction versus light intensity. The growth rate is indicated by color. The measurement points are indicated as black dots. The growth rate predicted by the model is shown against the experimentally determined growth rate for (e) UTEX2973 and (g) PCC7942 cscB. Subfigure (b) was reproduced from Ref. [1] with permission from the Royal Society of Chemistry.

The comparison with the literature data shows that all the tested CO_2 concentrations (Tab. 6.1) are below the affinity values for RuBisCo towards carbon dioxide shown in Tab. 6.2. Meaning the CCM was active during the whole duration of the experiment. According to the applied correlation, around 10.26 µM CO_2 should be dissolved in the BG11 growth medium under ambient conditions ($\sim$ 400 ppm). Therefore, under ambient conditions, the CO_2 concentration in the carboxysome must increase by about 50-fold compared to outside the cell to saturate RuBisCo. For 50 ppm and 15 ppm, the increase is 390-fold and 1.299-fold, respectively. Assuming a maximum 1,000-fold increase in CO_2 in the carboxysome, as stated by Badger et al. [26], the tested values appear to be within the correct magnitude to overwhelm the CCM. This calculation further supports the statement in Chapter 4 that growth is not limited by CO_2 under ambient air. Furthermore, under the same assumptions, the external CO_2 concentration required for half the catalytic rate is 0.24 µM external CO_2. Here, the corresponding aqueous CO_2 concentrations for the calculated K_{CO_2} values were 0.16 µM and 0.68 µM for UTEX2973 and PCC7942, respectively (Tab. 6.3). Similar values for the affinity of *Synechococcus* strains towards external CO_2 were previously reported in other studies [120, 121]. This shows that, although the tested values seem extraordinarily low at first, they are in the right magnitude.

During microfluidic cultivation, CO_2 containing gas is continuously supplied via the top PDMS layer resulting in diffusive gas exchange occurring across the interfacial PDMS layer. This thin interface acts as a gas-permeable membrane between the gas-supply channel and the underlying monolayer growth chambers, resulting in a high 'gas exchange-surface' to 'monolayer cultivation-volume' ratio of 0.97 μm^{-1}. During cultivation, all cyanobacteria are constantly aerated (and illuminated) over roughly half of their surface area. In addition, the growth medium is supplied continuously, resulting in very homogeneous growth conditions.

Therefore, for the microfluidic cultivation, the following can be assumed: As long as gas is supplied continuously at relatively high flow-rates, concentration changes in the gas supply can be neglected. Thus, during photoautotrophic growth, the resulting CO_2 concentration in the growth chamber is at equilibrium with the supplied gas (according to Henry's law [115]), and is not limited by the actual mass-transfer rates. Inefficient mass transfer in process aeration, often a growth limiting aspect at larger cultivation scales, did not limit continuous single-cell growth under the applied growth conditions.

The analytical precision presented here allows considering the single-cell resolution based growth data as a standard to characterize other technical cultivation systems, such as the laboratory-scale MC. This comparison yielded an effective CO_2 concentration of c_{CO_2} = 9.60 ppm. According to Henry's law [115], this is equivalent to a concentration of 0.0108 $mg \cdot L^{-1}$ CO_2 in the culture medium of the MC.

The initial slope of the growth curve characterizes the dependency between light intensity and growth rate in the light-limited region of phototropic growth. It is reasonable to assume that the light intensity in the microfluidic device is the actual light intensity impinging on the cells. This allows to quantify the deviation between the incident light intensity (given by the MC device manufacturer) and the effective light intensity within the culture medium of the MC. Thus, the initial slope at 15 ppm in the microfluidic device was compared to the initial slope at ambient air in the MC, resulting in the conclusion that the effective light intensity in the MC is 4.6 times lower than the incident light intensity as given by the manufacturer.

Tab. 6.3: Model parameters for the data presented in Fig. 6.3.

	Hyperbolic tangent fit		
x_{CO_2} [ppm]	μ_{max} [h^{-1}]	α [$h^{-1}\cdot(\mu E\cdot m^{-2}\cdot s^{-1})^{-1}$]	$PFD_{1/2}$ [$\mu E\cdot m^{-2}\cdot s^{-1}$]
PCC7942 cscB			
100	0.157	$2.75\cdot10^{-3}$	31.47
50	0.011	$2.55\cdot10^{-3}$	31.56
15	0.072	$3.16\cdot10^{-3}$	12.53
0		0.00166 ± 0.00168	
UTEX2973			
100	0.087	$3.56\cdot10^{-3}$	13.48
50	0.085	$3.26\cdot10^{-3}$	14.34
15	0.065	$4.31\cdot10^{-3}$	8.33
0		-0.0027 ± 0.0109	
	Dual parameter growth model		
Strain	μ_{sat} [h^{-1}]	K_{CO_2} [ppm]	α [$h^{-1}\cdot(\mu E\cdot m^{-2}\cdot s^{-1})^{-1}$]
PCC7942 cscB	0.199	26.61	$2.72\cdot10^{-3}$
UTEX2973	0.094	6.5	$3.71\cdot10^{-3}$

6.4 Conclusion & Outlook

Microfluidic CO_2 control cultivation was successfully established. However, more work needs to be put into the experimental workflow and into correctly simulating the device. Going forward the following recommendations are made:

Simulation the microfluidic CO_2 control device: Of the two questions posed above regarding the device, only the first could be answered definitively. Assuming homogeneously distributed CO_2 in the CO_2 perfusion chamber is well justified. The second question - whether the CO_2 in the CO_2 perfusion chamber is at equilibrium with the CO_2 in the growth medium - could not be answered. However, it became clear that the height of the exchange membrane is a critical parameter. An optimized simulation strategy has been developed, but has not yet been executed (See App. D: Fig. D.15).

Experimental approach: Two recommendations can be derived from the simulation results for the experimental approach: (i) Use the device fabrication technique developed by Keitaro Kasahara for thin exchange membranes [73]. If possible, use the inner growth arrays; if not, use the inner sub-array of the outer array, as in the successful experiment displayed above. This ensures that the cultivation remains shielded from the diffusion of CO_2 from the side by the outer sub-array, because of inward diffusion, CO_2 is transported toward the outlet by convective mass transfer.

New cultivation layout: The cultivation layout on wafer #2 (Fig. 5.4) was designed with CO_2 control in mind. For this, the master moulds for the CO_2 perfusion chamber were produced by photolithography on a silicon wafer. This process has three expected advantages:

- Faster gas flow rates at the same volumetric flow rate yielding better mass transfer.
- No compromise on the image quality due better surface quality of the resulting mold.
- The CO_2-perfusion chambers were designed as a separate CO_2-perfusion channels above each growth array. This allows all arrays to be perfused with the same concentration of CO_2 or different concentrations for each array. Hence, it improves experimental flexibility and allows parallel control experiments. The modular design also allows placing a big CO_2-perfusion chamber onto the whole device.

For the layout the reader is refereed to App. B: Fig. B.2 - Fig. B.4.

This technique has great potential for investigating the cyanobacteria CCM at a high level of precision, for example by knocking out certain parts of the CCM and observing the effect on cyanobacterial growth. If the image quality could be improved, it could also be used to study the formation and dissociation of carboxysomes. Growth of cyanobacteria in commercial photobioreactors is often limited by CO_2 rather than by light availability. Therefore, the precise correlations between growth rate and CO_2 obtained in these experiments could serve as ground-truth data for photobioreactor modeling approaches.

A major problem during the CO_2 control experiments was that the size of the growth chambers limited how long an experiment could last for fast-growing strains. When 0 ppm CO_2 was applied, visual inspection confirmed that cell growth had indeed stopped. However, this could not be quantified. One solution for this issue would be to use mother machines instead of growth chambers. This works well for rod-shaped cells. However, it is unclear if this works for coccoid cell such as *Synechocystis*, therefore limiting the application. Another approach would be to spatially implement CO_2 control in an orthogonal direction to the light-intensity gradient. For this, an mCGG could be used to generate the CO_2 gradient, as described in other publications [76, 77]. The outlets of the mCGG could then be fed into different CO_2 perfusion channels, each of which is placed above a different growth array. On the one hand, this allows day/night rhythms to be implemented in the time dimension. However, it eliminates the possibility of investigating multiple strains at once and limits the amount of applied concentrations. The size of the growth chambers is mainly limited by the FOV of the microscope. Making small adjustments to the light path allows for the use of larger growth chambers. As an alternative, since cell division were highly synchronous doubling times could also be derived from the mean single-cell area over time plot. This would allow for the measurement of growth rates in full growth chambers. Depending on their experimental needs, researchers could decide whether to implement CO_2 control spatially or time-dependently, as was done in this work.

While the first part was focused on device development, the final two chapters demonstrate how the cultivation technique can be used to answer biological questions.

Part II

Biological use cases

7 Engineering building blocks for a synthetic vacuole

The results shown in this chapter stem from a collaboration with the HHU and Bielefeld University (BU). The project is part of the Collaborative Research Centers program (CRC 1535, 'MibiNet: Microbial Networking — From Organelles to Cross-Kingdom Communities') from the German Research Foundation (Deutsche Forschungsgemeinschaft). The CRC is primarily based at the HHU, but also involves collaborations with nearby research institutions, such as the FZJ and BU. The goal of this subproject (Number A07) is to recreate the process of endosymbiosis by encapsulating engineered cyanobacteria within customized microfluidic environments. While researchers at HHU and BU are engineering cyanobacteria model strains to resemble the early endosymbiont, researchers at FZJ are developing microfluidic cultivation devices that resemble the host cell. Parts of this chapter have been presented at international conferences as a poster (III, VI - IX). Some data is included in a manuscript (V).

7.1 Introduction

Endosymbiosis is a widely accepted evolutionary theory that explains the origin of key organelles in eukaryotic cells, including chloroplasts. It states that eukaryotic plastids evolved from a cyanobacterium that was engulfed by a protist approximately 1.5 billion years ago. While the engulfment of bacteria as prey is a common phenomenon, today's plastids must have originated from a single engulfed cyanobacterium. It is believed that the ability to generate and store glycogen was lost in the early stages of this process [122], forcing the endosymbiont to become dependent on the host at night. This required a metabolic connection between the endosymbiont and the host cell. Key developments for establishing such a connection must include: [14]

- Loss of the endosymbiont cell wall
- Integration of new transporters into the plasma membrane of the endosymbiont to allow controlled nutrient exchange
- Gene transfer between host and endosymbiont

In simpler terms: A single cyanobacteria cell was retained in a small amount of fluid and kept alive at night by providing nutrients. This reframing led to the idea of recapitulating endosymbiosis using microfluidic growth chambers as synthetic host cells. The concept is

depicted in Fig. 7.1. The most crucial aspects for the development of the synthetic inclusion and the potential early endosymbiont include:

Synthetic cytoplasm:

- Precise control of environmental parameters such as light intensity and CO_2.
- Dynamic medium switching to simulate nutrient supply by the host cell.
- Implementation of extracellular biosensors for quantification of the nutrient supply to the host cell.

Early endosymbiont:

- Deletion of the ability to synthesize and store glycogen ($\Delta glgC$).
- Introduction of transporters to take up nutrients from the host cell.
- Implementation of intracellular biosensors to read out cytosolic nutrient concentrations.

The first bullet point regarding the synthetic inclusion has been addressed in previous chapters of this thesis. This chapter partly addresses the second bullet point. Work on the third bullet point did not progress beyond preliminary testing. A major part of this chapter focuses on mutants where the gene encoding for the enzyme ADP-glucose pyrophosphorylase (glgC)

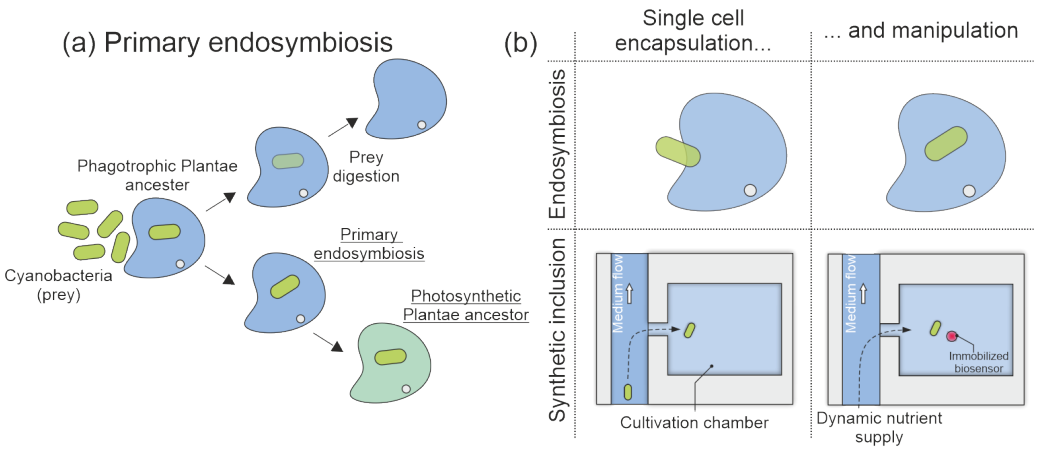


Fig. 7.1: Synthetic recapitulation of synthetic endosymbiosis. (a) The process of primary endosymbiosis. The figure was adapted from Reyes-Prieto et al. [14] with permission from Annual Reviews. (b) Synthetic recapitulation of primary endosymbiosis using single-cell microfluidic cultivation technology.

has been knocked out, which catalyzes the conversion of Glucose-1-phosphate (G-1-P) and ATP to ATP-glucose (See Fig. 1.2). Therefore, the glgC knockout mutants cannot store energy in the form of glycogen [123].

Tab. 7.1: List of investigated strains in this chapter.

Strain	Abbreviation	Resistance
Synechocystis sp. PCC6803 WT	WT	-
Synechocystis sp. PCC6803 Δ*glgC*-1	Δ*glgC*-1	Km
Synechocystis sp. PCC6803 Δ*glgC*-6	Δ*glgC*-6	Km

7.2 Materials & Methods

7.2.1 Characterization of Synechocystis sp. PCC6803 ΔglgC mutants

Laboratory scale culture conditions

All mutants were generated at the Institute for Plant Biochemistry at HHU. Two independent mutant cell lines were generated and characterized. The different mutant cell lines are indicated by the number appended onto their name. The mutants were transferred to the FZJ and cultivated in a permanent shake flask culture for the duration of the experiments. It was quickly found that the Δ*glgC* mutants are characterized by a long initial lag phase. Therefore, a two-step precultivation was necessary to prepare the strains for microfluidic cultivation. In the first step, all strains were inoculated into the MC and cultivated at 30 °C and 80 $\mu E \cdot m^{-2} \cdot s^{-1}$. After 96 hours of cultivation, all strains were back-diluted to an OD_{720} of 0.1 after which they were cultivated for an additional 24 hours. A sample was then taken to inoculate the microfluidic chip.

Microfluidic culture conditions

Three types of experiments were carried out to characterize the Δ*glgC* mutants. (i) Experiments under homogeneous illumination with a sequence of day and night phases. (ii) Experiments with an applied light-intensity gradient under constant illumination. (iii) Experiments with an applied light-intensity gradient and day and night phases. Concerning the experiment under homogeneous illumination, one experiment was conducted with sequentially longer night phase (24, 23/1, 22/2, 18/6 and 12/12) on a 24-hour basis. In another

experiment, the strains were first grown under 72 hours of constant light and then exposed to a 48-hour dark phase.

Tab. 7.2: Microfluidic experimental conditions applied in this chapter. The notation in the *Cultivation layout* column is defined in Fig. 5.4 and Tab. 5.1.

Illumination mode	PFD [$\mu E \cdot m^{-2} \cdot s^{-1}$]	Imaging rate [h]	Cultivation layout [Layout, Wafer]	Day/Night cycle
Homogeneous	30	0.25	iii., #1	Yes
Homogeneous	30	0.25	iii., #1	Yes
Gradient	-	2	i., #1 & ii., #2	No
Gradient	-	2	i., #1	Yes

7.2.2 Dynamic medium switching for nutrient spiking

Other authors have published microfluidic cultivation systems, that allow dynamic switching between two different types of growth medium [40, 55]. The goal here, however, was to integrate the medium switching into the existing setup. Calculations showed that adding a valve was not an option because the residence time in the valve and tubing dead volumes would exceed the switching period at the low flow rates applied. In order to achieve nearly instantaneous switching, two holes were punched into the inlet channel on layout iii. from wafer #1 (Fig. 5.4). One into the designated area and a second one in middle between the first hole and the beginning of the chamber array. These holes can then be connected to syringes containing different medium types. In principle, using the technique it should be possible to integrate dynamic medium switching into all similar cultivation layouts. For validation experiments 100 mg of fluorescein were weighted into 10 mL of H_2O. The resulting solution was diluted using DI water to a final concentration of 0.01 g/L. The script function of QmixElements was used to time the discharge of the respective syringes. Two types of validation experiments were performed with the fluorescein solution. (i) Whole chip scale using the 2x objective (ii) Chamber level with the 100x objective. For the experiments with the 100x objective one or multiple growth chambers were selected for imaging. The fluorescein fluorescence was imaged using a filter block designed for YFP HC (Ex: 500 $\pm$ 24 nm; DM: 520 nm; 542 $\pm$ 27 nm). Time-lapse acquisition was performed with the microscope software. For data analysis Region of interest (ROI)s were cropped out. The pixel intensity of the fluorescence channel was measured using the *Multi Measure* PlugIn in Fiji.

The Reynolds number, which is the ratio of inertial to viscous forces, is used to compare fluid flows across different scales. The Reynolds number for flow through a circular tube

is shown in Eq. 7.1. Experiments have shown that laminar flow can be considered for Re smaller than 2100 for flow through circular tubes [124].

$$Re = \frac{u \cdot \rho \cdot d}{\eta} = \frac{Q \cdot \rho \cdot d}{A_{cross} \cdot \eta} \tag{7.1}$$

Therein, u is the linear flow rate, Q is the volumetric flow rate, A_{cross} is the cross-sectional area, ρ is the fluid density (Here 995.6 kg·m^{-3} [111]), η is the dynamic viscosity of the fluid (Here 7.97 · 10^{-4} Pa · s [111]) and d is the pipe diameter.

Note that, in order to compare the tubing with the rectangular supply channel, an equivalent diameter was calculated from its cross-section. All calculations were performed under the assumption of a volumetric flow rate of 200 nL·min^{-1}. The Reynolds numbers calculated for the different sections along the path of the liquid are shown in Tab. 7.3.

Tab. 7.3: Dimensions and flow properties in different sections along the path of the liquid.

Section	Dimensions	A_{cross} [m^2]	u [mm·min^{-1}]	Re [-]
PTFE Tubing	Inner diameter: 0.5 mm	1.96·10^{-7}	1.02	10.60·10^{-3}
Dispense-tip	Inner diameter: 0.33 mm	8.55·10^{-8}	2.34	16.07·10^{-3}
Supply channel	Height: 10 µm, Width: 77 µm	7.70·10^{-10}	259.74	0.17

One potential issue with the applied switching concept is that the two syringes are connected to the same inlet channel. Therefore, solutes could theoretically diffuse from one syringe to the other. Calculations were made under the assumption that the medium containing the solute is being pumped while the medium without the solute is stagnant. In this case, the solute could diffuse into the stagnant medium towards the syringe. When the medium components are switched, tailing occurs. To make a rough estimate, Fick's second law was applied under the following assumptions:

- The concentration of the solute was considered constant across the width of the channel. Therefore, the problem was considered one-dimensional.
- Because the solute-containing medium is being pumped, the solute concentration *c(x,t)* in the solute containing medium is constant (*c(0,t)*) and does not deplete.

- The initial concentration of the solute in the solute-free medium is zero ($c(x,0) = 0$).
- The concentration of the solute at an infinite distance stays at zero ($c(\infty,t) = 0$).

Given these constraints, an analytical solution can be derived for the one-dimensional version of Fick's second law (Eq. 7.2) [124]. Example calculations were performed for the diffusion of glucose at 30 °C.

$$\frac{\partial c(t,x)}{\partial t} = D\frac{\partial^2 c(t,x)}{\partial x^2} \Leftrightarrow \frac{c(x,t)}{C(0)} = 1 - \left[\mathrm{erf}\left(\frac{x}{\sqrt{4Dt}}\right)\right] \tag{7.2}$$

Therein, c is the concentration of the solute (Glucose), x is the coordinate along the one-dimensional axis, t is the time and D is the diffusion coefficient ($D_G = 5.4 \cdot 10^{-10}$ m^2 s^{-1}) [111].

7.3 Results & Discussion

7.3.1 Characterization of Synechocystis sp. PCC6803 ΔglgC mutants

The mutants were transferred to the FZJ and kept in permanent shake flask culture for the duration of the experiments. All strains grew without complication in shake flasks and were characterized by a dark green color. Neither visual inspection of the shake flasks nor regular OD_{720} measurements revealed a difference in growth (Compare Fig. 7.2). After establishing the two-step MC preculture, all strains grew well in the microfluidic device. Fig. 7.3 shows the successful growth of PCC6803 WT in a standard growth chamber. Three aspects that required special attention when cultivating these strains were identified during the experiments.

- A common issue with this strain is its tendency to adhere to PDMS or glass surfaces. During long experiments with high growth rates, this has sometimes led to clogged growth channels, limiting the nutrient supply. Therefore, the channels should be flushed extra thoroughly and inoculated from the outlet.
- PCC6803 tended to grow to a high cell diameter at higher light intensities. As can be seen in Fig. 7.3 using standard growth chambers, the cells look squashed. Unlike the cultivation of *G. sulphuraria* (Compare Fig. 4.1) this led to frequent cell bursting. These experiments were conducted before higher growth chambers were available.
- For successful growth of Δ*glgC* mutants, it is important to inoculate only from the exponential phase during the second step of the two-step preculture. Therefore, when

working with these mutants, the operator must be patient. The length of the lag-phase was not reproducible but always lasted between three and five days (See Fig. 7.2). During the second step of preculture, all strains rapidly transitioned to exponential growth. No difference in growth rates was observed during this phase.

Fig. 7.3 shows an example image containing lysed cells. Since the segmentation was performed on phase-contrast images, the algorithm failed to differentiate between live and dead cells. Therefore, a single-cell autofluorescence filter was added to the script. The filtering included the following steps:

1. Plot a histogram of all single-cell autofluorescence values.
2. Manually select an autofluorescence threshold value.
3. Discard all cells with single-cell autofluorescence values below the threshold.
4. Plot a histogram of all single-cell autofluorescence values higher than the threshold.

With the updated script, it was possible to differentiate between live and dead cells. This distinction becomes important in the latter parts of this chapter.

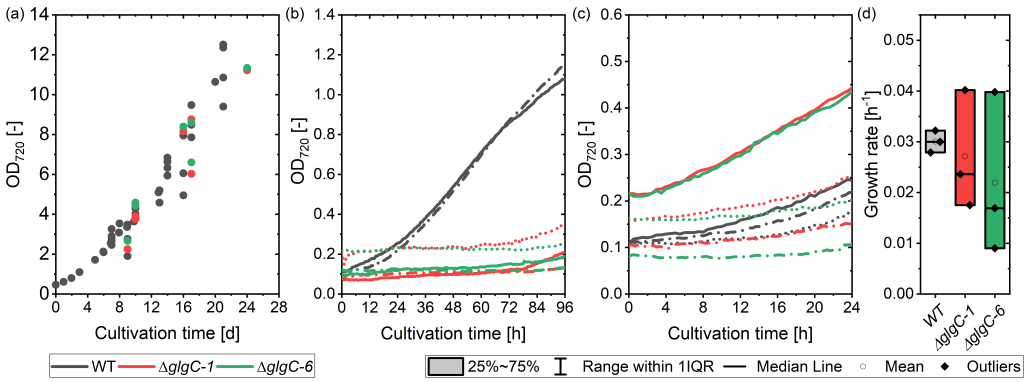


Fig. 7.2: Two-step preculture for microfluidic cultivation of PCC6803 ΔglgC mutants. (a) Growth of *Synechocystis* in the permanent shake flask culture. OD_{720} values were obtained from regular measurements of the OD_{720} to inoculate the MC (b) In the first cultivation step, the strains were cultivated for approximately 96 hours. While the WT (black) exhibited rapid growth, the Δ*glgC* mutants (colored) were characterized by a long lag-phase. The difference in line style indicates independent experimental runs. (b) In the second step, all strains exhibited a rapid transition to exponential growth. (c) Boxplot of the growth rates during the second preculture step.

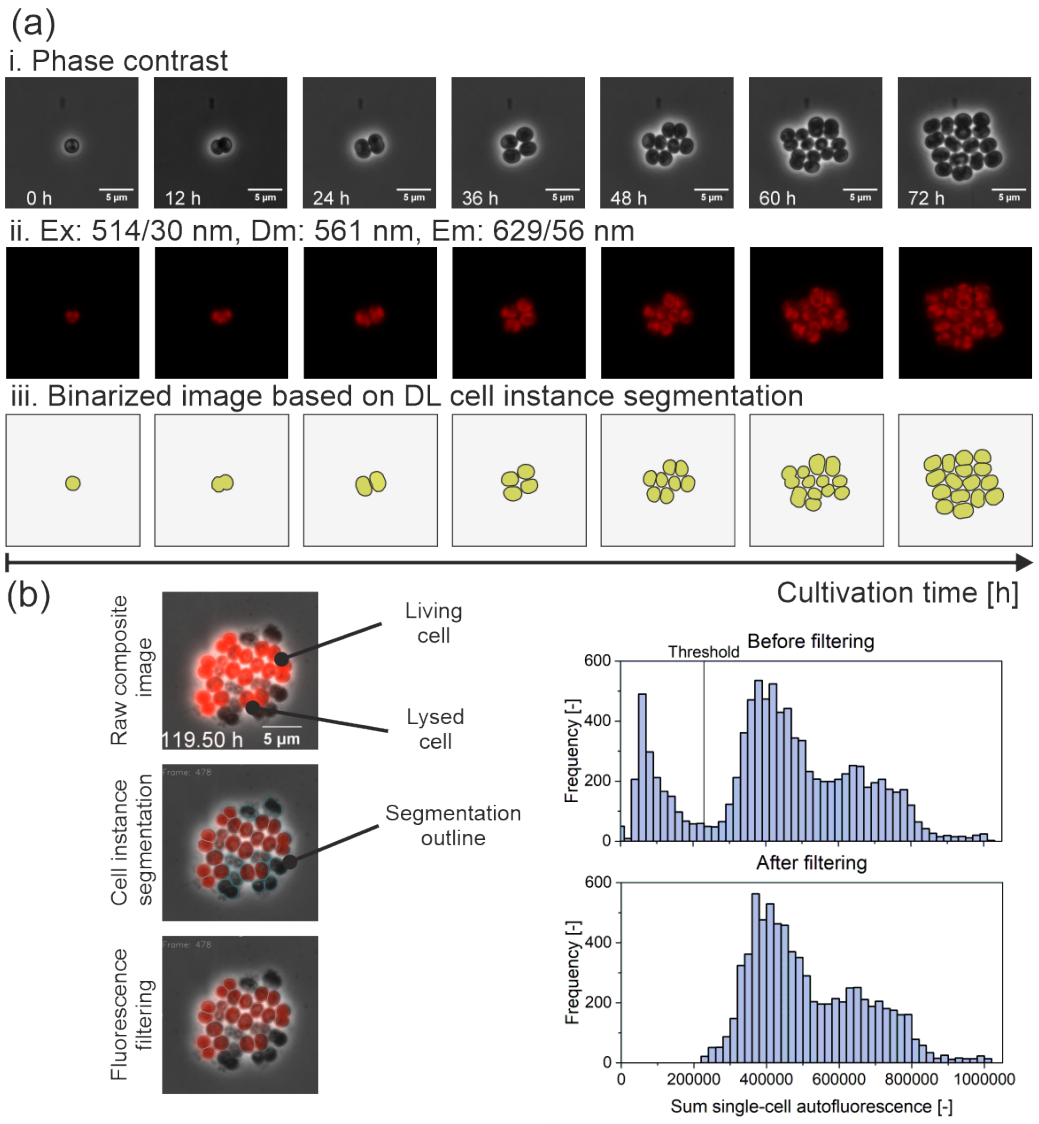


Fig. 7.3: Growth of Synechocystis sp. PCC6803 WT in a microfluidic cultivation chamber. (a) The figure displays time-lapse microscopy images acquired by phase-contrast (i) and fluorescence microscopy (ii). The fluorescence images (ii) are obtained using the indicated filter cube and visualize chlorophyll autofluorescence. The third row (iii) shows binary images based on the DL cell segmentation. (b) A single-cell autofluorescence filter is applied to distinguish lysed cells from live cells.

Sensitivity to high light-intensities

The results from the light-intensity gradient experiments done with the Δ*glgC* mutants displayed in Fig. 7.4 show the limited ability of the mutants to tolerate high light intensities. Growth chambers were selected for all strains over the entire length of the growth array, and the same gradient was applied to all arrays. However, in the arrays where the Δ*glgC* mutants were inoculated, many cells on the side of the array facing higher light intensities did not grow. Even an initial expansion of the cell area or an initial cell division followed by rapid cell death, which was often seen in *Synechococcus* strains, was not observed. These cells were considered dead; therefore, no data point is shown for these chambers in Fig. 7.4. As in Chapter 5 results from multiple experiments were stitched together to yield the plot. The data for the WT was generated in a separate experiment then the results for the Δ*glgC* mutants and were previously discussed in another context in Chapter 5. However, the ability of the WT to grow at these high light intensities was validated over multiple experiments. Two experiments were conducted for the Δ*glgC* mutants, yielding similar results.

Towards higher light intensities, the growth rates of the Δ*glgC* mutants decreased compared to the WT. The maximum light intensity that the Δ*glgC* mutants could tolerate roughly coincided with the transition from the light-limited to the light-saturated growth region. Cell sizes were independent of light intensity in the light-limited region for both WT and mutant cells. However, in the light-saturated region, WT cells were significantly larger than in the light-limited region. Impaired growth rates for a Δ*glgC* mutant were also observed by Kato et al. [125]. Given the results of Part 1 of this thesis, it is impossible to compare these culture conditions here to the ones in given in literature. However, the results shown here indicate that the growth of the *glgC* mutants is only impaired at light intensities approaching the light-saturated region of growth.

Behavior of mutants during night

Three independent experiments were conducted to investigate the behavior of the Δ*glgC* mutants in contrast to the WT at night. The experimental conditions are shown in Tab. 7.2. Fig. 7.5 (a) shows an experiment in which the strains were cultivated for a total of 140 hours under sequentially larger night phases (1, 2, 6, and 12 hours). The plots of the colony area respectively the cell count over the cultivation time show that the WT performed the best under these conditions. While no cell division occurs for all strains during the night, it appears that the WT cells keep increasing in size after the onset of the night. It is also evident that the Δ*glgC* mutants require more time to begin growing again after the night phase ends. This effect is especially evident in the colony area over cultivation

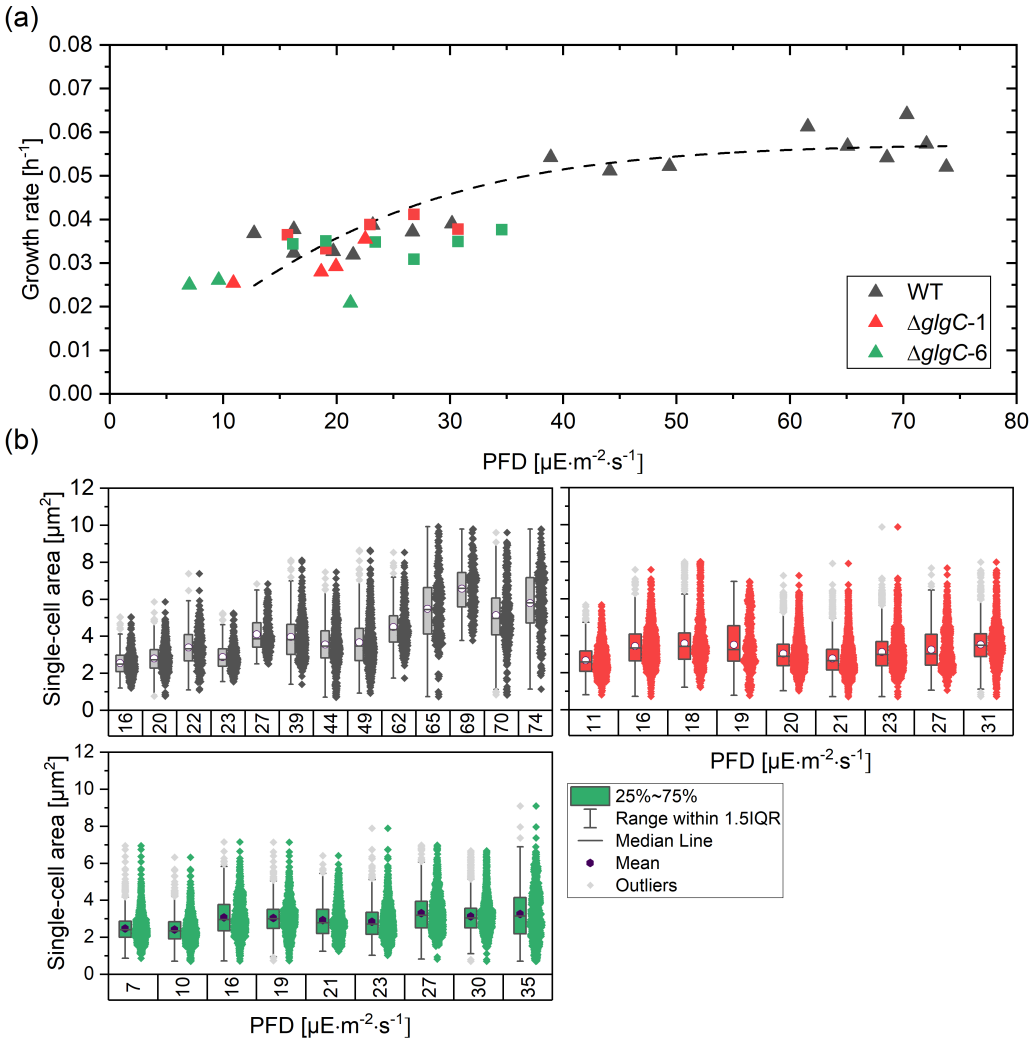


Fig. 7.4: Results from light-intensity gradient experiments with ΔglgC mutants. (a) Curve of growth rate over light intensity for the WT (black) and the Δ*glgC* mutants (colored). Each data point represents the growth rate from one distinct growth chamber. The dotted red line shows the fit of the growth model in Eq. 1.9 to the WT data. The WT data are also displayed in Fig. 5.5 (c). Two distinct experiments were conducted for the Δ*glgC* mutants. One experiment used layout i. from wafer #1 (triangle), and the other used layout ii. from wafer #2 (square). (b) Boxplots of the single-cell areas extracted from cell instance segmentation for the WT (black), Δ*glgC*-1 (red) and Δ*glgC*-6 (green). Each data point represents an individual cell recognized by the algorithm. The data for each box stems from a distinct colony illuminated at the indicated light intensity.

time plot in 7.5 (a). After the 12-hour night phase ends, WT strains resume growth immediately, whereas the Δ*glgC* mutants need time to transition back to exponential growth. During the final phase (area based, 120 - 140 h), the growth rates of the Δ*glgC* mutants were lower than those of the WT: 0.018 ± 0.06 h^{-1} and 0.013 ± 0.007 h^{-1} for mutants 1 and 6, respectively, compared to 0.029 ± 0.010 h^{-1} for the WT.

In another experiment (Fig. 7.5 (b), the strains were first grown in homogeneous growth light mode for 72 hours. Then, the growth light was shut off for 48 hours. During the light phase of the experiment no significant difference in the growth rate could was observed (0.037 ± 0.006 h^{-1}, 0.037 ± 0.008 h^{-1} and 0.032 ± 0.007 h^{-1} for the WT, and the Δ*glgC*-1 and Δ*glgC*-6 mutant). Examining the colony area and cell count plots over cultivation time at night initially suggests that the WT performed worse than the Δ*glgC* mutants. However, the mean cell area plot shows that the area of single cells increased for about 12 hours after the start of the night. This effect coincided with a decrease in cell number in the WT colonies. Two possible explanations are plausible for this effect: (i) Small cells die while big cells survive. (ii) All cells increase in size, and some die. Visual inspection of the time-lapse videos and single-cell traces (See App. D: Fig. D.14) revealed that the size of all WT cells increased during the night, with some of these cells lysing. It is also noteworthy that the fluctuation in the mean cell area curve is due to segmentation errors. Often, it is unclear whether a cell has divided. This causes the algorithm to sometimes recognize a cell as one large cell and, in another frame, as two separate cells.

In the experiment shown in Fig. 7.5 c the linear light-intensity gradient (see Chapter 5) and a 12-hour light/12-hour dark cycle were applied. Growth rates were determined at 12-hour intervals to compare growth during the day versus night. The mean phase-contrast intensity for each segmented cell was extracted and averaged for each frame. The figure shows the traces for each growth colony separately, as well as the mean of all traces. In this experiment, only the WT was successfully grown; therefore, the data lacks a control experiment. Consequently, these results are preliminary. Nevertheless, two findings can be extracted from the data: (i) The rate of cell swelling at night depends on light intensity. Before applying the exponential fit (Eq. 1.7) to the colony area at night, it was verified for each colony that the increase lasted the entire night. (ii) The Phase contrast seems to decrease at night and increase during the day. This phenomenon is discussed more thoroughly in the next chapter.

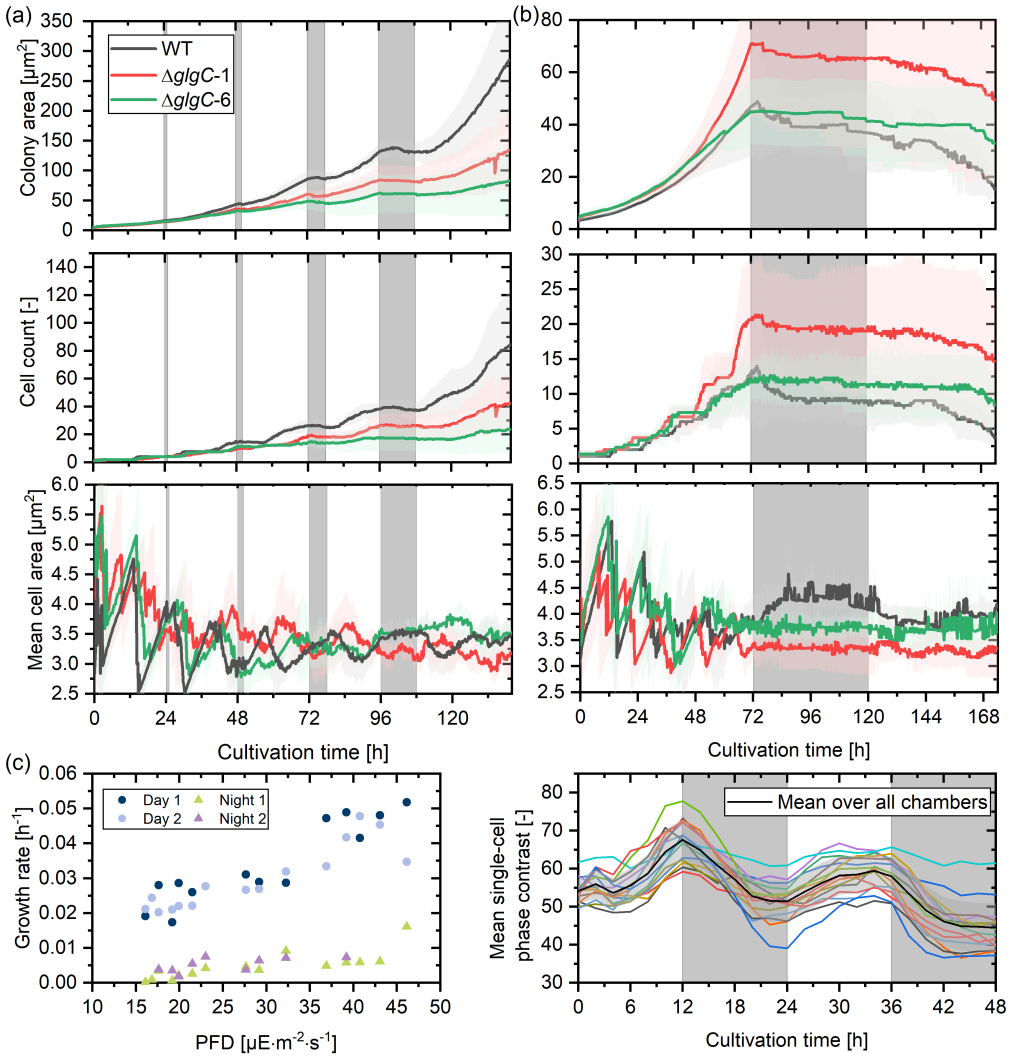


Fig. 7.5: Behavior of ΔglgC mutants at night. The figure displays results from three independent experiments. (a) Homogeneous growth light cultivation under sequentially longer night phases. For each strain, the mean and standard deviation of three growth colonies are shown. (b) Homogeneous growth light cultivation with 72 hours of light followed by 48 hours of darkness. For each strain, the mean and standard deviation of three growth colonies are shown. (c) A gradient growth light experiment with a 12-hour day and 12-hour night cycle applied over two days. Only data for the WT is shown here. The dark phases are indicated by the gray background in all graphs.

In summary, three growth patterns can be distinguished from the presented data:

Continuous low light-intensity illumination: The growth of the strains under continuous illumination with moderate light intensities is hardly distinguishable. The only exception is that knockout mutants have a longer lag phase during MC cultivation. The initial expectation that the WT would grow more slowly under continuous illumination because it allocates some carbon towards glycogen production rather than cell growth could not be confirmed. Further investigation is recommended to determine how much glycogen is generated depending on the light intensity under continuous illumination. Fig. 7.5 (c) shows initial evidence of light intensity-dependent glycogen production.

Continuous high light-intensity illumination: With increasing light intensity, the Δ*glgC* mutants initially exhibited reduced growth rates and, at higher light intensities, ceased growth entirely. In cyanobacteria, glycogen can function as a metabolic sink. As light intensity increases, carbon fixation via the CBB is enhanced. In the absence of an adequate metabolic sink, this imbalance may impair growth. However, it has been shown that Δ*glgC* mutants can partially compensate by synthesizing and exporting alternative metabolites that serve as energy sinks [125].

Cell behavior during night: Using single-cell microfluidics, it was demonstrated that the size of WT cells increased after the growth light was turned off. However, this effect coincided with a higher likelihood of WT cells lysing. Although single-cell analysis enabled differentiation between an increase in cell size and the death of some cells, the cause of the increase in cell size remained unclear. Two options would be plausible: (i) The cells break down glycogen and use the energy from metabolizing the resulting glucose for cell growth. (ii) The cells break down glycogen purely for cell maintenance. However, generating monomers from a large polymer changes the osmotic pressure, causing water to diffuse into the cell. This effect could explain the lysis of some cells. Of course, a mixture of these effects is also plausible. It is also noteworthy that the Δ*glgC* mutants survived even 12 hours of darkness, although they needed longer to recover from the night. This proves that these mutants must have an alternative energy storage mechanism.

Obviously, based on this data alone, any explanations for these phenomena would be speculative. Here, microfluidic analysis can only serve as one analytical method alongside others to gain a more detailed understanding on the impact of the knockout of *glgC* on PCC6803. As transcriptomic and metabolic analyzes are being carried out the HHU and BU more insights

will be revealed. It will be of special interest what metabolites Δ*glgC* mutants generate as an alternative carbon storage and whether differential gene expression can be observed during night and under high light-intensities.

7.3.2 Dynamic medium switching for nutrient spiking

As previously mentioned, stable symbiosis between host cells and endosymbiont requires the host cells to supply the endosymbiont with nutrients. In the case of a photosynthetic endosymbiont, as in this study, this means that the host cell must provide nutrients to the endosymbiont in the dark because photosynthesis cannot occur at night. The first step towards developing such an endosymbiont was the knockout of *glgC*, taking away the ability of PCC6803 to store energy in the form of glycogen. The next logical step from the early endosymbiont engineering side will be to implement transporters into the cell membrane of a Δ*glgC* mutant to take up energy rich nutrients during night to compensate the lack of glycogen. On the side of engineering a synthetic cytoplasm this means a system for dynamic medium exchange in the growth chambers is required. The following expectations should be met by such a system:

- **Integrable:** Ideally the system should be integrated into the existing cultivation setup.
- **Switching periods:** The period for switching should be in the range of hours rather than minutes or seconds.
- **Designed for component spiking:** Rather than completely exchanging the growth medium, one component should be spiked.

Low-magnification microscope pictures of the proposed technique are shown in Fig. 7.6 (a). Two holes were punched into the inlet channel from wafer #1 (See Fig. 5.4). The hole farther back was connected to a syringe containing a fluorescein solution, and the hole in the middle of the channel was connected to a syringe containing DI water. The solutions were pumped by turning the respective syringe on and off using the syringe pump software. The analysis of the indicated ROIs shows, that the fluid within the growth chamber arrays was exchanged rapidity. These results were further validated on growth chamber level using a 100x objective (Fig. 7.6 (b). Here, multiple consecutive 15 min and 20 min switches were investigated. As in the graph in Fig. 7.6 (a) tailing of the fluorescein could not be avoided. Also, when the syringe containing fluorescein was turned on, the height of the maximum fluorescence did not appear to be completely stable. Lastly, tests were made whether the mixing of fluids is possible using the proposed technique. The height of the fluorescence peak was approximately what was expected. However, as in the previous subfigure, the peak height was unstable.

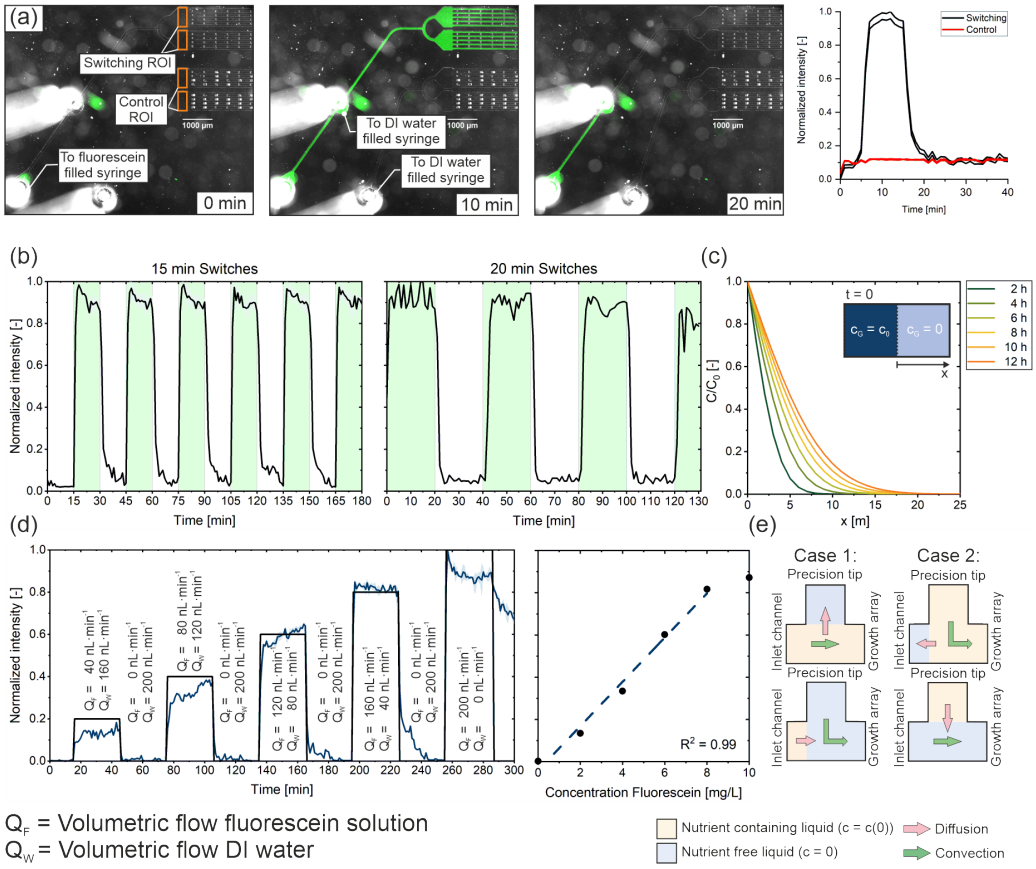


Fig. 7.6: The proposed dynamic medium switching concept. (a) Images from a time-lapse sequence taken during medium switching. The pixel intensity was evaluated in the indicated ROIs and plotted. (b) Fluorescence intensity traces within microfluidic growth chambers during switching. Tests were performed at 15- and 20-minute intervals. (c) Diffusion of glucose in the direction of the syringe that does not contain glucose. (d) Fluorescence intensity traces recorded within microfluidic growth chambers at different mixing ratios of medium-filled syringes. (e) Schematic side view onto the junction of the two media inlets and the main supply channel. The illustration shows the two possible ways to connect the medium containing syringes.

Eq. 7.2 was solved for the case displayed in Fig. 7.6 under the above stated assumptions. To simulate nutrient supply during night, the switching duration should be in the range of hours rather than minutes or seconds. For approximating the tailing two problems need to be considered:

1: Nutrient containing liquid stagnant, nutrient free liquid flowing: In this case, a steady state occurs, where nutrient from the stagnant fluid is constantly diffusing into the flowing liquid through the hydrodynamic boundary layer. Although this constitutes a complex mass transfer problem, the following considerations can be made: The extremely low Reynolds number in the supply channel (See Tab. 1) implies a rather thick hydrodynamic boundary layer and thus slow diffusion. The diffusive particle stream depends directly on the exchange surface area. As shown in Fig. 7.6 (e), for Case 1 the exchange surface area corresponds to the cross-section of the inlet channel, whereas for Case 2 it corresponds to the cross-section of the metal precision tip. Because the latter is more than 100 times larger than the former, less nutrient diffusion is expected in Case 1, hence it is beneficial.

2: Nutrient containing liquid flowing, nutrient free liquid stagnant: Based on the above assumptions, an analytical solution to Fick's second law can be derived in this case. The solutions for the relevant time steps are shown in Fig. 7.6 c). In the extreme case of a 12-hour switching period, the normalized concentration drops below 0.01 at a distance of 17–18 cm into the tubing.

Case 1: The length of the dispense-tip is around 2 mm. For Case 1, this means that the nutrient does not reach the thicker PTFE tubing. Using the fluid velocity for the dispense-tip from Tab. 7.3, 18 minutes of tailing are expected. To speed up the clearing of the tailing after long switching times, the volumetric flow rate could be set higher for the first few minutes. For instance, at 1000 $nL \cdot min^{-1}$, the tailing for 12 h switching is cleared within 3.5 minutes for Case 1.

Case 2: Here, the nutrient first diffuses into the supply channel (approximately 3.5 mm in length) and then into the dispense-tip via the inlet hole. The time needed to reduce the amount of nutrient in the stream to under 0.01 is reduced to 14.23 minutes because of the much higher fluid velocity in the supply channel. For the cases displayed in Fig. 7.6 (a) and (b), the normalized concentration drops below 0.01 after 2-3 mm for 20-minute intervals and 3-4 mm for 30-minute intervals. This implies that the tailing sometimes observed in the figures must be caused by other factors, e.g. the general inertia of the system. Also, due to the extremely low Reynolds numbers, the fluid velocity is not distributed evenly along the channel profile. Towards the wall, the fluid velocity approaches zero. The nutrients diffuse toward the middle and are transported from there by convective transport, which leads to nutrient tailing. However, the duration of this process is independent of the duration of the switching interval.

In conclusion, the following assumptions are made: (i) the length of the tailing along the velocity profile and system inertia is independent of switching time; and (ii) diffusion into the stagnant fluid can be resolved within ten minutes of faster flow after switching. This means that, when deciding whether to apply Case 1 or Case 2 (Fig. 7.6 e), only the first problem needs to be considered. Therefore, Case 1 is beneficial overall. Finally, the following recommendations are made for successful experiments using the medium-switching technique.

- **Tubing:** Rigid tubing (e.g., PTFE tubing) is recommended. Non-rigid tubing can expand radially when pressure is applied, thus increasing the system's inertia.
- **Needle positioning:** It is recommended that the syringe containing the nutrient to be spiked be connected to the original inlet hole (Case 1). The dispense-tip containing the fluid without the nutrient should be connected to the additional hole. In this case, the nutrient mainly diffuses into the larger diameter of the fluid dispense-tip, leading to longer tailing. However, this issue can be resolved with a faster fluid velocity immediately after switching. The advantage is the smaller cross-sectional area for diffusion when the nutrient-containing liquid is stagnant.
- **Thoroughly check the experimental setup:** For a successful experiment, check the setup extra thoroughly for air bubbles in the tubing and make sure that no liquid is dripping out of the needles and syringes. Also, ensure that the needle in the additional hole is not inserted so deeply that it blocks the flow of the medium.

7.4 Conclusion & Outlook

The previous chapter summarizes the research that has been conducted thus far within the CRC1535 framework. The aim of the subproject was to emulate the process of primary endosymbiosis using microfluidic cultivation technology to simulate the host organism and genetic engineering to recreate an artificial endosymbiont.

The first step in the development of the synthetic endosymbiont was to delete the ability of PCC6803 to synthesize intracellular glycogen by knocking out the *glgC* gene. Microfluidic cultivation technology revealed differences in growth behavior under high light-intensities (More than 40 $\mu E \cdot m^{-2} \cdot s^{-1}$) and in the dark: At high light-intensities growth of the Δ*glgC* mutants was highly inhibited. In most cases, no growth was observed, while the WT cells continued to grow. At night the WT cells kept increasing in size, while the cell size of the Δ*glgC* mutants stayed constant. The WT also returned to exponential growth more quickly after the end of the night. No difference in behavior could be observed at moderate

light intensities. The next step towards a synthetic endosymbiont will be the integration of transporters into an Δ*glgC* mutant to compensate the lack of glycogen. The synthetic host then supplies nutrients to compensate the lack of glycogen.

In preparation for this experiment, a technique for nutrient spiking during microfluidic cultivation was developed and evaluated. It was demonstrated that this technique is suitable for this specific use case. At the required high switching intervals, the observed tailing becomes negligible. The following experiment is proposed to proceed: A light-intensity gradient experiment with a low light-intensity range, ideally under 40 $\mu E \cdot m^{-2} \cdot s^{-1}$ with an additional 12-hour day and 12-hour night cycle to compare the growth of the WT, a Δ*glgC* mutant and a Δ*glgC* + transporter mutant.

- **Growth array 1:** Inoculated with WT as control, no nutrient provision during night.
- **Growth array 2:** Inoculated with Δ*glgC* + transporter mutant, nutrient provision during night.
- **Growth array 3:** Inoculated with WT as control, nutrient provision during night.
- **Growth array 4:** Inoculated with Δ*glgC* + transporter mutant, no nutrient provision during night.

To demonstrate that the integration of the transporter leads to metabolic connectivity between the host and the endosymbiont, the following outcome is expected:

- There is no difference in growth behavior between channels 1 and 3. This means that providing the nutrient at night does not influence the WT because it lacks the appropriate transporter and contains glycogen. Consequently, the difference in growth behavior between channels 2 and 4 must be linked to the knockout of the *glgC* gene and, therefore, to the missing glycogen metabolism.
- The Δ*glgC* + transporter mutant in channel 2 behaves like the controls in channel 1 and channel 3. This indicates that the supplied nutrient was able to compensate for the absence of intercellular glycogen. Metabolic connectivity was established between the synthetic host and the endosymbiont.
- The Δ*glgC* + transporter mutant in channel 4 behaves analogously to the results previously shown for the Δ*glgC* mutants in this chapter.

As shown in this chapter of this thesis, the preparations for this particular experiment are complete. At least concerning the microfluidic aspects.

8 Reporter-free observation of the circadian rhythm in individual Synechocystis cells

The results shown in this chapter originate from a cooperation with the institute for synthetic microbiology at the HHU and constitute an example how microfluidic single-cell analysis can unravel phenomena masked in bulk fermentation. Parts of the results have been published at international conferences as a poster (I & IV) or oral presentation (I). An abstract containing data from this chapter was awarded with the Outstanding Young Student Award at the 18th International Symposium on Phototrophic Prokaryotes (Qingdao China, 2025). Some data presented in this chapter was analyzed as part of Julius Nohr's bachelor thesis. Some data is included in a manuscript (IV). Underlying data and code was published in a data repository (IV)

8.1 Introduction

Cyanobacteria possess a protein-based circadian oscillator that enables them to anticipate the time of day. While investigating this so-called circadian clock in *Synechocystis* sp. PCC6803, researchers at the HHU observed an $\sim$ 24 h oscillation in the backscatter signal of *Synechocystis* shake flask cultivation [126, 127]. In these experiments, the culture was exposed to constant light, meaning no day/night rhythm was applied. Under such conditions, circadian researchers refer to the two 12-hour phases as "subjective day" and "subjective night". During subjective night, illumination remains on, but the organism's internal oscillator indicates a night phase.
Although being able to attribute this oscillation to the internal circadian clock of *Synechocystis* it remained unclear what exactly is causing the oscillation in the backscatter signal. From a physical standpoint the backscatter measures the fraction of a light-beam scattered by a probe. When using a bacterial culture as a probe, the backscatter depends on the concentration and the optical properties of the bacteria, the probe's thickness and the intensity of the incident light beam. Since the thickness and the incident light beam are unlikely to change periodically, the reason must lie in the culture density or the optical properties. The following reasons for the oscillation are therefore plausible:

Concentration

- Cells divide only during certain times of the day (Gating of cell division).
- Cell growth is faster during the subjective day or night.

Optical properties

- Periodic synthesis and consumption of intracellular macromolecules e.g. glycogen.
- Periodic migration of cell components within the cytosol.

Or a combination of multiple effects.

8.1.1 The circadian clock in cyanobacteria

An extensive introduction into the field of circadian (24-h rhythmic) regulation in cyanobacteria lies beyond the scope of this thesis. For this, the reader is refereed to other authors [47, 53, 126–128]. In short, a biological clock is considered a circadian clock if it fulfills the following three criteria: [129]

- A stable $\sim$ 24 h period.
- Stability against environmental changes e.g. temperature, pH.
- Ability to be entrained by an external stimulus.

In cyanobacteria three proteins KaiA, KaiB and KaiC form the core oscillator. Whereby the hexameric KaiC protein gets phosphorylated and dephosphorylated by KaiA and KaiB over a 24 h period. The phosphorylation status of KaiC in turn regulates cellular processes like the transcription of genes. In *Synechocystis* sp. PCC6803 two protein oscillators are involved in generating a stable circadian oscillation [126, 127]. In many publications, these rhythms are visualized by expressing fluorescent or luminescent proteins under the control of promoters that are indirectly regulated by the phosphorylation status of *kaiC*. In these experiments the fluorescence or luminescence can be monitored for bacterial colonies on a BG11 plates [130, 131]. As an alternative, the fluorescence or luminescence can be assessed in individual cells using either non-structured agarose pads [54] or a microstructured agarose pads or PDMS-based systems [52, 53, 55]. Further, researchers have used single-cell imaging to investigate how the division behavior of *S. elongatus* is regulated by the circadian clock [47, 50]. The reader is referred to the review by Yokoo et al. for a broader overview [49]. However, all

the experiments require knowledge of a suitable promoter and genetic accessibility. Until recently, the gene-reporter method that has long been established in *S. elongatus* has proven difficult to transfer to other cyanobacteria such as *Synechocystis* [131]. Here, a reporter-free method for visualizing the circadian rhythm in individual *Synechocystis* cells is described. This enables visualization of the circadian rhythm in WT strains.

8.2 Materials & Methods

8.2.1 Strains & shake flask cultivation

It is worth mentioning, that the experiments in this chapter were conducted using a PCC6803 retrieved from different lab, than the one refereed to in the previous chapters. All strains investigated in this chapter are listed in Tab. 8.1. All listed strains were generated at the HHU, transferred to the FZJ and kept in shake flask until the experiments were conducted.

Tab. 8.1: *Synechocystis* sp. PCC6803 strains investigated in this chapter. All strains were generated by project partners at the HHU

Strain	Comment	Resistance
WT	Wildtype	-
Δ*glgC*	no glycogen synthesis	Km
Δ*kaiA1B1C1*	1^{st} oscillator knocked out	Km
Δ*kaiC1*	*kaiC1* gene knocked out	Km
Δ*kaiA3B3C3*	2^{nd} oscillator knocked out	Km & Cl
Δ*kaiA3*	*kaiA3* gene knocked out	Km
Δ*kaiB3*	*kaiB3* gene knocked out	Km
Δ*kaiC3*	*kaiC3* knocked out	Cl
Δ*kaiC3* + *kaiC3*	*kaiC3* reinserted into native locus	Sp
Δ*kaiA1B1C1* Δ*kaiA3B3C3*	Both oscillators knocked out	Km, Cl & Sp

8.2.2 Microfluidic cultivation

The precultivation in the MC was conducted according to the description in chapter 2 with the exception, that the device was programmed to perform a 12-hour day and 12-hour night cycle to synchronize the circadian clock (Fig. 8.2 a). Samples were taken approximately 1 h after the end of the night. It is noteworthy, that in shake flask the nutritional upshift resulting from diluting down a culture with fresh medium, can be sufficient to synchronize

a culture [126]. The standard cultivation parameters in this chapter are listed in Tab. 8.2. The cultivation layout (Fig. 8.1) was chosen because of the open design of the boxes, and it's height.

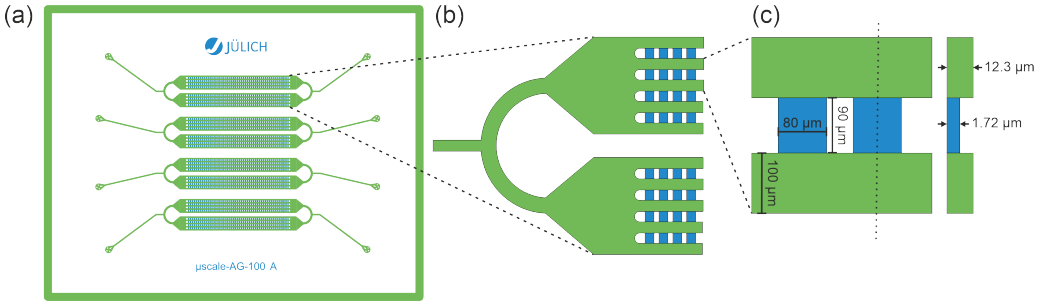


Fig. 8.1: The cultivation chip layout used for observing the circadian clock in Synechocystis. (a) The cultivation layout includes 4 cultivation arrays (Height 10 µm). (b) Each array includes 8 rows of 50 chambers, that are interconnected by shared supply channels. (c) The growth chambers are 80 x 90 µm in size and 1.72 µm high

Tab. 8.2: Standard cultivation parameters for circadian clock experiments.

Parameter	Value
Light-intensity growth-light	4 or 7 µE·m^{-2}·s^{-1} 5800 K black body radiation
Incubator temperature	30 °C
Imaging rate	1 h
Total cultivation time	168 h
Camera	DS-Fi3 with color disabled
Intermediate magnification	1.5 x magnification
Flow rate syringe pump	200 nL·min^{-1}

8.2.3 Data analysis

The post-experimental process was mostly conducted in accordance with the description in Chapter 2. Unlike all the other chapters, the data analysis was fully automated in Python. To achieve this, a designated post-segmentation data analysis pipeline was developed. This includes Python notebooks at the chamber, channel, experiment and project levels. A master notebook was placed within a folder containing folders for each conducted experiment Executing the master notebook copies the analysis notebooks into the respective subfolders at the experiment or channel level for data analysis. The data is then retrieved, and

a meta-analysis is performed on all experiments. Using this pipeline the following analyses were performed:

Timing of cell division: To investigate whether gating of cell division occurs in *Synechocystis* a superordinate Python script was used. The script iterates through all folders in the project, grabbing the file containing the cell count over cultivation time from each growth chamber containing the WT. A representative plot is shown in Fig. 8.2 (c). Subsequently, the script iterates through each time series, checking whether the previous entry in the column is equal to the current one. In the case, that the value for the number of cells has increased, cell division has occurred, thus the respective value for the cultivation time is saved.

Growth rate: The growth rates were calculated according to the exponential model in Eq. 1.7. This was done either for the cultivation time or based on 12-hour intervals. In both cases, the first 24 hours were omitted. The growth rates were then sorted according to whether they belonged to subjective day or night, and plotted accordingly.

Phase-contrast intensity: Extracting circadian rhythms from the raw phase-contrast intensity in image data involved the following steps:

1. For each cyanobacteria cell the mean intensity of all pixels within the border of the cell was calculated.
2. These values were then averaged per frame. It is important to note that due to the low light intensity applied, only a small amount of cyanobacteria were included in this average.
3. The course of the mean phase-contrast per frame was plotted over the cultivation time and approximated using a 6^{th} degree polynomial fit. The residuals from the fit over time constitute the signal.
4. The signal was smoothed using *numpy.convolve* [83]. In this case, the settings were configured to apply a six-point moving average to the signal.
5. Using *numpy.fft.fft* a Discrete Fourier transformation (DFT) was performed on the signal. The result is an array of complex numbers and their corresponding frequencies. The absolute value of the complex number is the magnitude M and the angle is the phase angle φ. The dominant frequency is the frequency f with the highest magnitude.

In order to reconstruct the signal at the dominant frequency the amplitude can be calculated from the magnitude using Eq. 8.1 [132].

$$A = \frac{2 \cdot M}{\text{Number of datapoints in signal}} \tag{8.1}$$

Therein A is the amplitude of a given frequency and M is the magnitude of a given frequency.

6. The dominant frequency and the corresponding amplitude and phase were then used as the initial parameter guess for fitting Eq. 8.2 onto the signal using *curve_fit* from *scipy.optimize* [113]. The function *curve_fit* uses non-linear least squares to fit a predefined function onto given data.

$$A \cdot cos(2\pi \cdot f \cdot t + \varphi) \tag{8.2}$$

Therein A is the amplitude, f is the frequency, t is the time and φ is the phase angle of the oscillation.

The time shift τ can be calculated from the phase angle using Eq. 8.3.

$$\tau = \frac{\varphi}{2\pi \cdot f} \tag{8.3}$$

Therein τ is the time shift, φ is the phase angle and f is the frequency.

The period (P) of the cosine oscillation and the timing ($T_{\text{First Peak}}$) of the first peak on the positive x-axis were calculated using Eq. 8.4 and 8.5.

$$P = \frac{1}{f} \tag{8.4}$$

$$T_{\text{First Peak}} = -\tau + \text{P} \tag{8.5}$$

Therein P is the period of the oscillation, f is the frequency of the oscillation, $T_{First\ Peak}$ is the timing of the first peak and τ is the time shift.

The code for the polynomial fit and the smoothing was adapted from Berwanger et al. [126]. In their study, the operations were applied to the backscatter signal from shake flask cultivations.

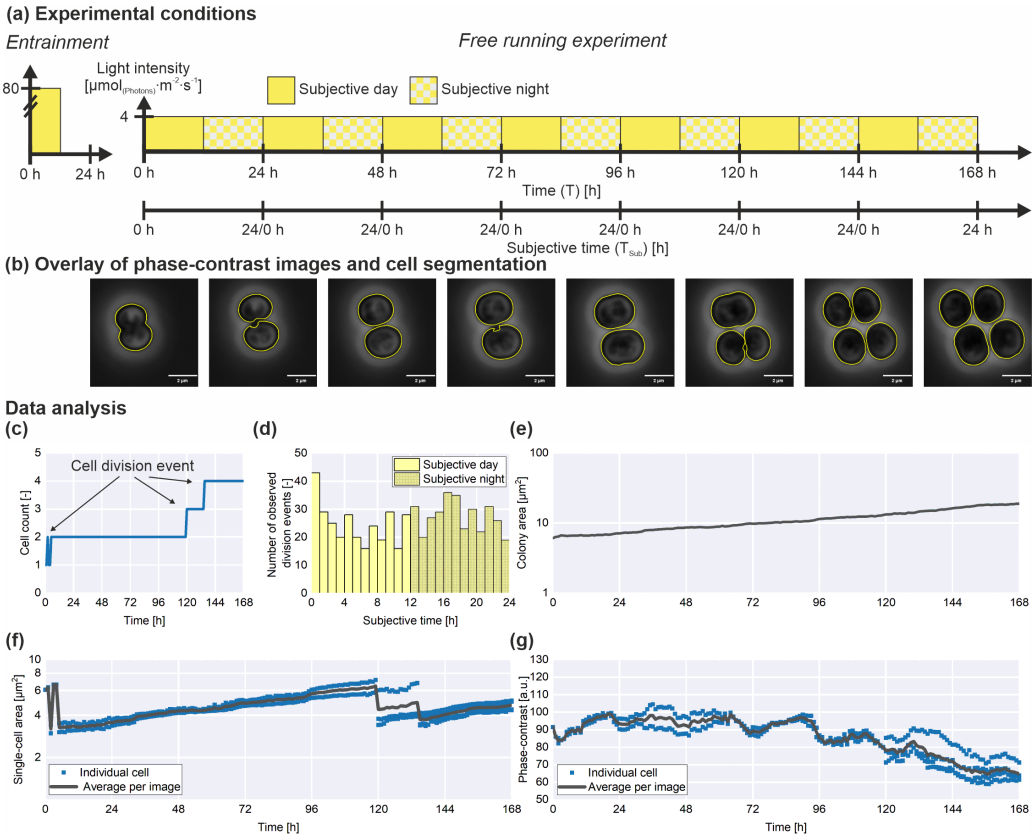


Fig. 8.2: Observation of the circadian rhythm in individual Synechocystis cells. Shown are the results from an exemplary WT colony. (a) The strains were precultivated and synchronized in the MC. During microfluidic cultivation constant white light at 4 or 7 $\mu E \cdot m^{-2} \cdot s^{-1}$ was applied over 168 h. The 168 h of cultivation time (T) were subdivided into seven subjective days (T_{Per}). According to the entrainment, each subjective day consists of a 12-h subjective night and a 12-h subjective day. (b) Example image sequence of a *Synechocystis* strain growing in a microfluidic cultivation chamber. During time-lapse microscopy phase-contrast and fluorescence images (Ex: 514/30 nm; Dm: 561 nm; Em: 629/56 nm) were taken every hour. Cells were segmented using a previously published data processing pipeline [94]. (c) Plot of the number of cells in an image (cell count) over time. (d) These plots can be used to analyze the subjective time at which cell division occurred. A total of 624 division events were detected in 141 image sequences from 9 independent experiments and plotted over the subjective time. Furthermore, the method allows the size of individual cells (single-cell area) (e) and the cumulative area occupied by a cell colony (colony area) (f) to be distinguished. (g) Furthermore, the brightness of individual cells within phase-contrast images (phase-contrast) can be extracted.

8.3 Results & Discussion

8.3.1 Validation of the phase-contrast signal pipeline

In contrast to similar studies done on PCC7942 [47, 50] no evidence for gating of cell division could be observed (Fig. 1 d). Additionally, both single-cell and colony growth were exponential and did not exhibit superimposed oscillations (Fig. 1 e & f). Also, no difference in the growth rate between subjective day and subjective night could be found. However, an app. 24 h oscillation in the mean phase-contrast of individual cyanobacteria cell was found. Fig. 8.5 (a) shows the mean phase-contrast intensity for individual cells. Since an image can contain multiple cells, multiple data points are shown per time point. However, due to the low cell numbers, cell lineages can easily be recognized. A separate plot is shown for each image sequence. Because the oscillation is still apparent the averaged data per frame (Fig. 8.3 a & b) single-cell oscillations must be highly synchronized across generations within a colony. When data from multiple colonies was averaged, the oscillation remained visible (Fig. 8.3 d). Hence, oscillations must be synchronized for all cells within an array on the microfluidic chip. Due to the high flow rates, communication between cells is unlikely, so the oscillation must have been stable from the synchronization step in the MC onwards.

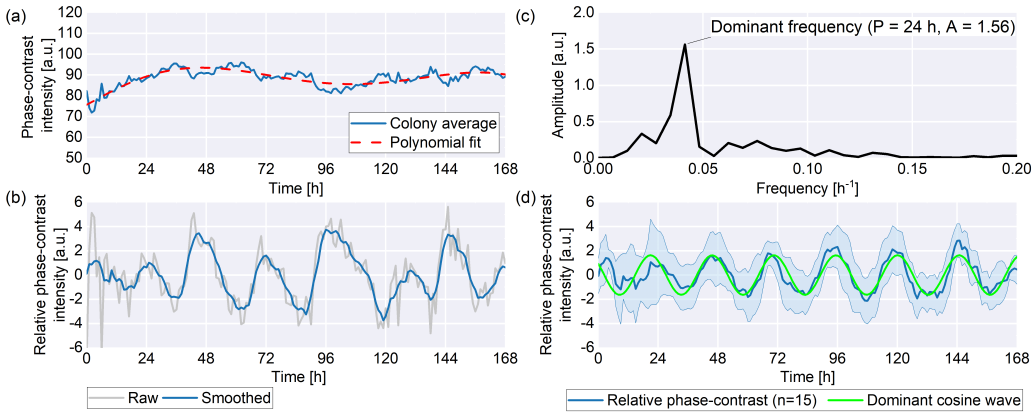


Fig. 8.3: The circadian data analysis pipeline (a) Raw phase-contrast intensity (blue) and polynomial fit (red) of an example image sequence (b) The relative phase-contrast (gray) is obtained by subtracting the raw phase-contrast intensity from the polynomial fit. A moving average filter for data smoothing is then applied. (c) Discrete Fourier transformation performed on the mean relative phase contrast of 15 chambers. The frequency with the highest amplitude is the dominant frequency. (d) Relative phase contrast of 15 chambers (blue) and the reconstructed dominant cosine wave (green).

In the example shown in Fig. 8.5 (a) only two cell division were observed over the 168 h of cultivation. From this the colony-area based doubling time was calculated to be around 100 h. Hence, the cell division cycle can be excluded as a cause for the phase-contrast oscillation. After confirming the presence of phase-contrast oscillations, a data analysis pipeline was developed to compare the parameters of these oscillations for multiple strains. The DFT yielded robust estimates of the oscillation parameters. For example, in the data shown in Fig. 8.3, the magnitude of the dominant frequency accounts for 27 % of the total magnitude. During the first hours of the experiment, small corrections to the PFS were sometimes needed to compensate for the thermal expansion offset of the chip, even though the chip was preheated overnight. This resulted in sharp increases or decreases in the phase-contrast value. Therefore, it was found beneficial to exclude the first 24 hours from the DFT. The main disadvantage of the DFT is, that it is calculated on a discrete number of frequencies. On the upper end the number of frequencies is limited by the sampling rate. Here, an imaging rate of one per hour implies, that the lowest detectable period would be 2 h, corresponding to a frequency of 0.5 h^{-1}. The number of discrete frequencies in-between 0.5 h^{-1} and 0 is limited by the length of the signal [132]. Hence, the non-linear least-square optimization was performed, to improve the results. Hereby, all real frequencies above zero were possible answers.

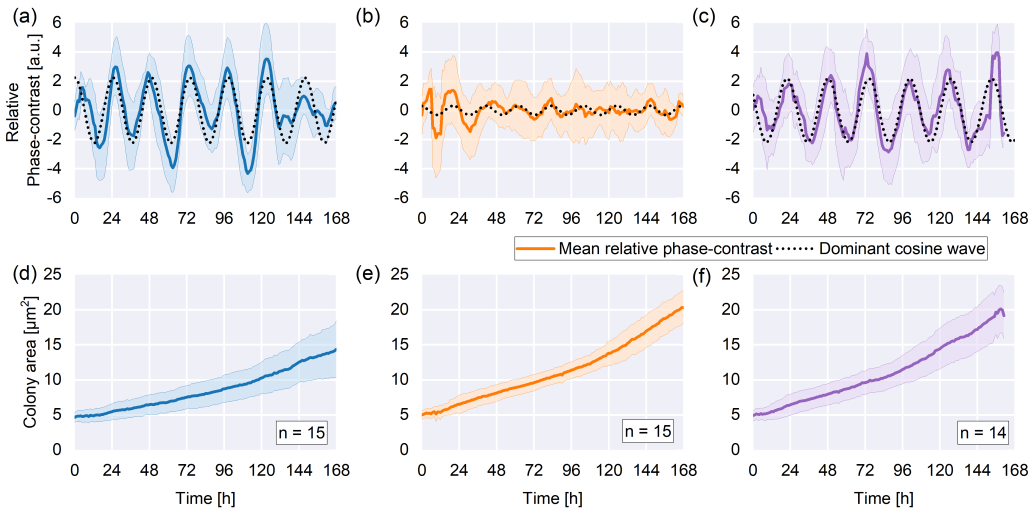


Fig. 8.4: Comparison of the WT, the kaiC3 knockout and the complementation mutant. (a)-(c) Relative phase-contrast intensity and the dominant cosine wave for the WT (blue; average of the data shown in Fig. 8.5) a), *kaiC3* knockout (orange; average of the data shown in Fig. 8.5 b) and the Δ*kaiC3* + *kaiC3* complementation mutant (purple; average of the data shown in Fig. 8.5 c). (d)-(f) Colony area over time for WT, *kaiC3* knockout mutant and Δ*kaiC3* + *kaiC3* complementation mutant. For each strain, the mean and standard deviation for multiple colonies is shown.

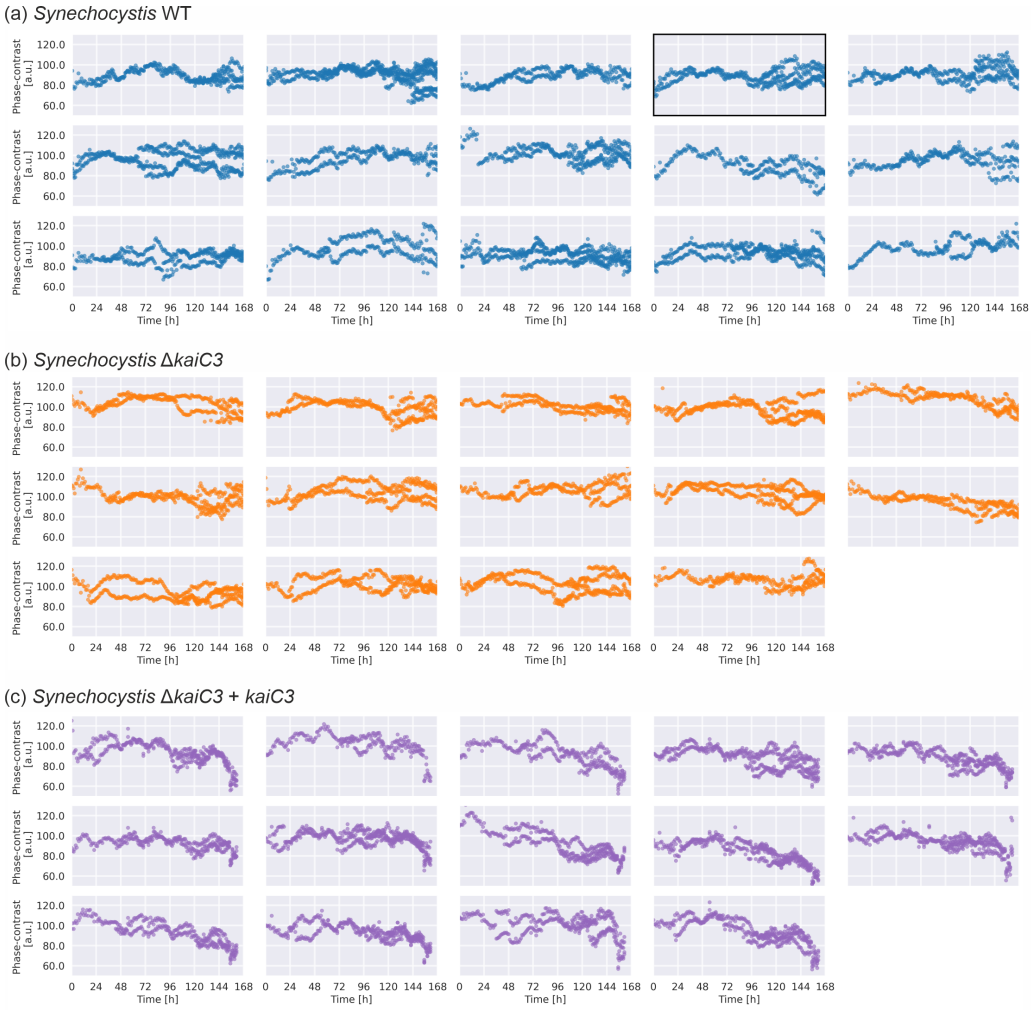


Fig. 8.5: Single-cell phase-contrast oscillations. The figure shows the single-cell phase-contrast intensity for the PCC6803 WT (a), the Δ*kaiC3* knockout mutant (b) and the Δ*kaiC3* + *kaiC3* complementation mutant (c). Each individual plot contains data from a time-lapse image sequence of a single colony acquired during a continuous microfluidic experiment. Colonies shown within the same subplot originated from separate growth chambers belonging to the same array of chambers on the microfluidic chip. Therefore, they are interconnected by shared supply channels. Each data point represents the mean intensity of all pixels within the boundary of an individual *Synechocystis* cell. The data from the subplot in (a) that is outlined in black is also shown in Fig. 8.3.

8.3.2 Biological interpretation of the results

Prove that the phase-contrast oscillation is orchestrated by the circadian oscillator

That the observed phase-contrast intensity oscillations are indeed caused by the circadian oscillator was proved by investigating a *kaiC3* knockout mutant in the microfluidic chip. Further, a complementation mutant in which the gene had been synthetically reinserted into its native position was investigated as a control. The results from the data analysis pipeline for this particular experiment is shown in Fig. 8.4. The single-cell phase contrast intensities for both mutant strains are shown in Fig. 8.5 (b) and 8.5 (c). The data Fig. 8.5 (b) demonstrates that knocking out *kaiC3* led to dissimilar single-cell oscillation phenotypes within populations. Although some Δ*kaiC3* cells exhibited phase-contrast oscillations, the amplitudes were lower than those observed in the WT and the oscillations were inconsistent within a colony. Other cells did not exhibit oscillations at all. Overall, this variation in phenotype results in the apparent damped phenotype, as seen in the averaged colony data. Following the synthetic reinsertion of the gene, however, the oscillation was recovered. Hence, proving that the phase-contrast oscillations are linked to the circadian oscillator. The reconstructed and optimized cosine wave for the WT suggest a stable circadian oscillation (Period: 24.63 h, Amplitude: 2.24, Time shift: 5.99 h), for the *kaiC3* knockout the oscillation was abolished. By reintroducing the *kaiC3* gene synthetically, the circadian oscillation was recovered (Period: 26.29 h, Amplitude: 2.18, Time shift: 11.04 h). While the cell areas did not seem to differ greatly, the growth rates were a bit lower for the WT.

Testing of various clock mutants

Fig. 8.6 provides an overview of the optimized dominant cosine fit. The growth rates are displayed in Fig. 8.7 (a), the single-cell areas are shown in Fig. 8.7 (b). Overall, the single-cell area, period, time shift and growth rate were highly reproducible for the WT across experiments. However, the amplitude varied, even within a single experiment. Therefore, more caution is needed when comparing these parameters. The following considerations were then made regarding the fitting parameters of the cosine function:

Period: In all experiments, growth arrays inoculated with WT exhibited a reproducible period of 24.99 $\pm$ 0.65 h. For experiments i. - vi. as well as viii - ix. the mean overall growth rates were reproducible. For experiment vi., a slightly lower growth rate was observed. The higher growth rate in experiment x. can be explained by the increased light-intensity (7 $\mu E \cdot m^{-2} \cdot s^{-1}$ compared to 4 $\mu E \cdot m^{-2} \cdot s^{-1}$ for the others. to vii.) Overall, the growth rates correspond to doubling times of between 65.14 and 155.38 hours. Therefore, cell division

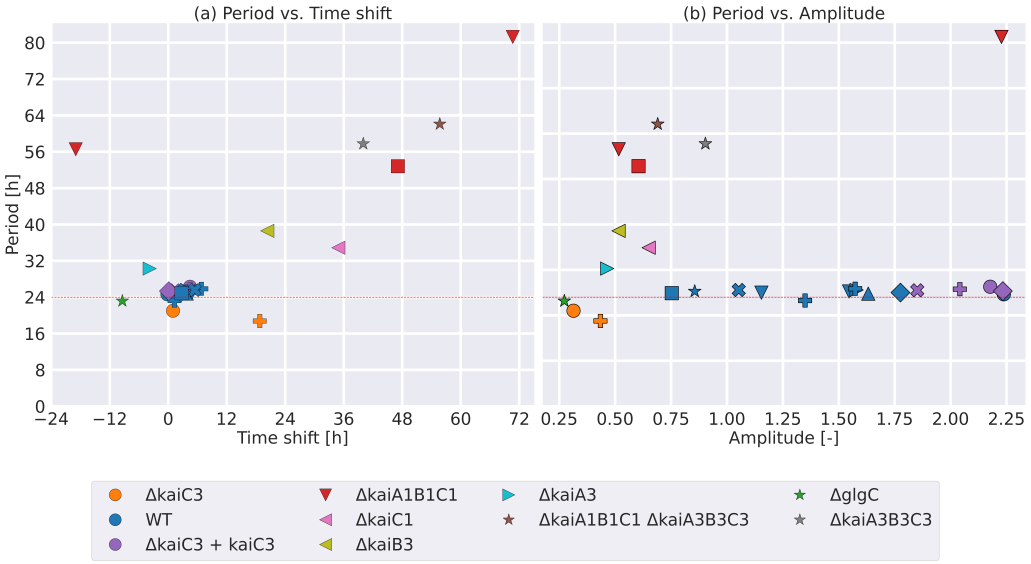


Fig. 8.6: Summary of the fitted cosine parameters for various strains. Optimized dominant period versus time shift (a) and optimized dominant period versus amplitude (b) for all investigated strains. Different strains are indicated by color. Independent experiments can be distinguished by marker shape.

cannot be the cause of the approximately 24-hour oscillation because the value did not correspond to the period value, and a change in doubling time did not influence it. From the plot and visual inspection of the data, it can be concluded that the following knockout mutation lead to a loss of the observed circadian signal:

- The simultaneous knockout of both oscillators: Δ*kaiA1B1C1* Δ*kaiA3B3C3*
- The knockout of one of the two oscillators: Δ*kaiA1B1C1*, Δ*kaiA3B3C3*
- The knockout of certain parts of the oscillators: Δ*kaiC1*, Δ*kaiB3*, Δ*kaiA3*

Since this method most likely only visualizes a physiological function downstream of the circadian oscillator, it does not definitively mean that the circadian clock is entirely lost. Results from experiment i. show that the circadian rhythm can be restored by reintroducing the native Δ*kaiC3* protein into the knockout mutant.

Time shift: The time shift was reproducible in all eleven growth arrays inoculated with the WT (3.81 ± 0.43 h). In experiment iii., two independent arrays were filled with the WT, the time shift was the same in both arrays. This clearly demonstrates that the second of

the above-stated criteria for a circadian rhythm is also met. However, it remains unclear whether it is the 12-hour night during the preculture, the inoculation into the microfluidic chip, or both processes that reset the rhythm. In each experiment, the time between the end of the night phase in the MC and inoculation into the microfluidic chip, and the time between inoculation and the start of the time-lapse, varied considerably. The time at which the first peak of the cosine oscillation occurred was calculated from these values according to Eq. 8.5. The calculation showed that the first peak occurred, on average, 21.19 ± 1.54 h after the experiment began. Thus, it occurred towards the end of the subjective night.

Amplitude: The amplitude of the optimized dominant cosine oscillation was not reproducible, even between different WT arrays on a single growth chip. The intensity of a pixel in a microscopic picture depends on a variety of settings. While the imaging settings (e.g. exposure time, LED intensity, gain) were kept the same throughout all experiments, the microscope settings (e.g. the degree of opening of the various diaphragms, the distance between the condenser and the chip) were difficult to reproduce. Also, each culture chip is slightly different, and segmentation errors did occur. Hence, the variety in the observed amplitudes.

Unlike conventional bright-field microscopy, which visualizes light transmission through a probe, phase-contrast microscopy images the probe's refractive index. The refractive index in turn is the ratio of the speed of light in the probe to the speed of light through a vacuum [133] and can be correlated to the volumetric density of a probe and subsequently to the optical properties of the bacteria. The most likely explanation for this rhythmic change in the phase-contrast intensity of the cells is a cellular process (e.g. synthesis and degradation of glycogen, displacement of DNA or carboxysomes) downstream of the circadian clock happening in the cytoplasm and influences its volumetric density and, consequently, its refractive index.

Although the underlying reason for the change in refractive index remains unclear, it can be concluded that the oscillation observed in the cell's refractive index during single-cell analysis also causes the backscatter oscillation. It is proposed that, during batch cultivation, each cell oscillates independently, as observed during single-cell analysis. However, the entire population exhibits similar periods and phases. This results in a cumulative backscatter signal that oscillates with the same parameters.

In all experiments growth arrays inoculated with the WT a reproducible period of $\sim$ 24 h was observed. The Δ*glgC* mutant, however, exhibited a significantly lower single-cell

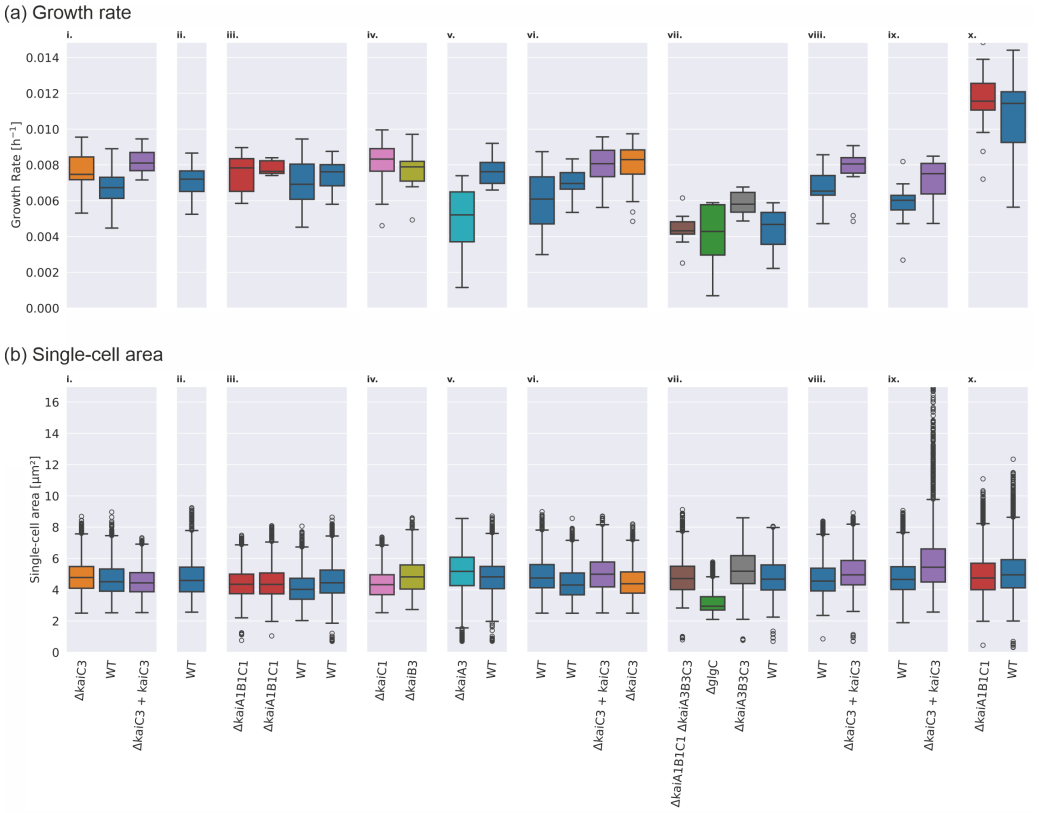


Fig. 8.7: Summary of the growth rates and single-cell areas for various strains. The figure displays the growth rate (a) and single-cell area (b) boxplots for all investigated strains. Each plot summarizes results from an independent experiment. Each box summarizes data from multiple growth chambers within an array. Arrays containing the WT are always coloured in dark blue. The middle line inside each box represents the median. The box shows the quartiles of the dataset. The whiskers extend to show the rest of the distribution, excluding points identified as outliers.

area (3.25 μm^2) compared to the rest, while displaying a highly damped oscillation, as previously observed using the backscatter method [126]. This is most likely due to an absence of glycogen, a macromolecule. This suggests that all the other mutants must contain glycogen, which makes glycogen synthesis and degradation less likely to be the cause of the observed oscillation in the WT. However, it does not completely rule it out. Perhaps in mutants that do not display the rhythm, the synthesis and degradation of glycogen are not timed correctly instead of showing a complete lack of glycogen. The effect of the timed synthesis and degradation of glycogen on single-cell size in the WT is most likely masked by the general increase in cell size caused by biomass accumulation.

To determine the cause of the refractive index oscillations, researchers should attach fluorescence tags to the target molecules and conduct the experiment with these strains. If the intensity of the fluorescence from the tagged components exhibits similar oscillations as the phase-contrast oscillations, it is likely that the components are subject to circadian regulation. This could be due to their localization, or concentration, or both. One challenge will be to find suitable fluorescence markers and differentiate between the oscillating concentrations of the markers themselves and the tagged components.

8.4 Conclusion & Outlook

The results in this chapter demonstrate the effectiveness of single-cell microfluidics. Using this technique, effects that were masked in shake flask culture because multiple parameters were combined in the backscatter value could be disentangled. In this example, the common assumption when performing OD measurements that the optical properties of the cells do not change over time was found to be incorrect. Furthermore, it was possible to differentiate between an increase in cell diameter and cell division. This showed that cell division was not restricted to certain times of the day under permanent illumination. The growth rate was also independent of the time of day, meaning a combined cause of the oscillation could be ruled out. The size of the cells could also be determined online without the use of external equipment, e.g. cell counting devices.

However, this method is better suited to qualitative measurements than to do high-throughput quantification of oscillation parameters on multiple strains. For this, the determination of parameters was not reliable enough; the amplitude in particular was hardly reproducible. Using shake flask measurements also allows more strains to be investigated in parallel. Even if a new chip were designed with more arrays, the system would not achieve the same level of parallelization. Further, one image loop during microfluidic cultivation lasted roughly 3–5 minutes. During this time, the lamp providing light for photosynthesis was switched off, which constrained the measurement rate to a maximum of one image per hour. During shake flask cultivation, the backscatter was measured every 20 seconds without interrupting the cultivation. The microfluidic experiments also suffered from frequent experimental failure due to channels drying out, an issue that was especially prominent in long-term cultivation.

To make the most of the advantages of both techniques, the shake flask technique should be used for quantitative comparisons of oscillation parameters to assess the effect of circadian clock mutations on oscillations. Experiments involving different temperatures should also

use the shake flask technique since temperature changes cause the microfluidic method to lose focus. Conversely, the microfluidic method should be used to investigate interesting strains in detail, to further investigate the cause of oscillation, as well as to conduct experiments on the influence of environmental parameters such as light spectrum, day/night rhythms and nutrient spiking (e.g. glucose) on circadian oscillations. Experiments involving fluorescence-tagged components (e.g. glycogen, DNA and carboxysomes) are recommended to investigate the cause of the oscillation.

9 Conclusion & Outlook

The first part of this thesis focused on updating the existing microfluidic technology to study phototrophic microorganisms. Fig. 1 provides an overview of the proposed cultivation platform. Most cultivations were performed with cyanobacteria from the genera *Synechococcus* and*Synechocystis*. However, cultivating eukaryotic microalgae for up to twelve days at a temperature of 40 °C and a pH of 2 demonstrated the long-term stability and versatility of the platform. First, the microscope was equipped with a ringlight-based illumination system to drive photosynthesis. This created an additional light path, enabling the diascopic light-path to be configured for optimal imaging. Experiments proved that the growth light provided homogeneous and stable illumination of the cultivation chip. Since the cells are grown in a monolayer, the applied light intensity can be considered the actual intensity of photons impinging on the cells. Furthermore, under ambient air, no CO_2 limitations were observed, and since the growth medium is supplied continuously, nutrient limitations did not occur. To accelerate the acquisition of growth data, a concept was pioneered for creating a linear light-intensity gradient across the chip. This was used for high-throughput strain characterization (See Chapter 5). In order to investigate the dependence of cyanobacteria growth on the CO_2 concentration, dynamic CO_2 control was integrated using a CO_2 perfusion chamber connected to a premixed CO_2-bottle (See Chapter 6). The ability to precisely control the light intensity and CO_2 concentration to which the cells are exposed makes the generated correlations between these parameters and the growth rates of cyanobacteria suitable for use as ground-truth data in photobiotechnology. This will enable comparisons between different photobioreactors, thus facilitating photobioreactor scale-up. In conclusion, all the requirements defined in the first chapter were met. The platform's design is **Simple and user-friendly**, restricting growth to **monolayers** and enabling growth data acquisition at **single-cell resolution**. Additionally, **dual-parameter** characterization of **light intensity** and **CO_2** was demonstrated.

The second part of this thesis presented two applications for the proposed platform. (i) The characterization of mutants lacking the ability to synthesize intracellular glycogen as carbon storage (Δ*glgC* mutant). No differences in growth behavior were observed under moderate continuous light. When a day/night rhythm was applied, the following observations were made: During the night, the size of the mutant cells remained constant, while the size of WT cells continued to increase. When the light was switched back on, the WT cells were able to switch back to exponential growth faster. (ii) A method was developed for reporter-free observation of the circadian rhythm in individual *Synechocystis* cells. Circadian oscillations in the phase-contrast intensity of individual cells were identified and recorded

using time-lapse imaging with single-cell resolution. A Python-based analysis workflow was designed to analyze and compare these oscillations across a set of circadian clock mutants. This proved that the observed oscillations are indeed caused by the circadian oscillator. Both case studies demonstrate how microfluidic analysis can separate phenomena that were previously lumped together in bulk cultivation.

Although it is already being used in research to study the fundamental properties of cyanobacteria, there is potential to further improve the experimental workflow with homogeneous illumination and with the linear light-intensity gradient. As discussed in detail in the respective chapters, further automation of the pre- and post-experimental procedures is necessary. Additionally, expanding the usable range of the linear light-intensity gradient would greatly improve the results. The experiment with the CO_2 perfusion chamber did not reach further than proof-of-concept status. One major challenge will be to improve the simulation of the CO_2 mass transfer. Furthermore, researchers should implement either bigger growth chambers or mother-machines to eliminate the problem of overflowing growth chambers limiting the experimental duration.

Overall, the developed cultivation technology for phototropic microorganisms has great potential for application in microbiology research laboratories. First, due to the issue of cellular self-shading that is always present in conventional photobioreactors most researchers still do not know the exact intensity and spectrum of light that their cells are exposed to. This makes comparing results across different cultivation platforms difficult. It is only possible to know exactly how much light is impinging on a microalgae cell when applying single-cell resolved monolayer growth. This also enables reliable energy balances. Furthermore, using a lamp such as the STL light engine used in this work allows time-resolved dynamic changes of the light regime. Here data generated using the presented microfluidic approach can serve as ground-through data to compare growth rate correlations across laboratories and facilitate reactor scale-up. Another benefit of this technology is its potential for high-quality live cell imaging. This would enable researchers to dynamically study the localization of fluorescent molecules under precisely controlled environmental conditions. For instance, the assembly of carboxysomes depending on the CO_2 concentration or the synthesis and degradation of glycogen depending on the time of day. Furthermore, using single-cell resolution time-lapse imaging researchers can discriminate between cell growth, cell division and morphological changes. When working with backscatter or OD measurements, these effects are combined and can only be distinguished by sampling and subsequent offline measurements using, for instance, a cell counter. To date many research labs perform single-cell resolution experiments on agarose pads [47, 48, 54]. These have several disadvantages, such as the inability to supply the growth medium continuously and limited environmental control.

The major hurdles hindering the further spread of the technology are (i) the relatively long training needed to successfully perform a microfluidic experiment (ii) the high cost of the specialized equipment needed to perform them. Regarding the first hurdle, it is recommended that environmental control (e.g. light-intensity gradient, day/night, CO_2 mixing, nutrient spiking) be integrated into the microscope periphery rather than into cultivation chip itself, as done in this thesis. This reduces the likelihood of experimental failures related to cultivation chip, e.g. leaking of liquid or insufficient attachment of PDMS to PDMS. In general, to make the technology more accessible, an emphasis should be placed on keeping experimental procedures simple. For instance, revising the approach for connecting the tubing containing the medium to the cultivation chip. This could be achieved by incorporating commercial microfluidic connectors. Regarding the second hurdle the infrastructure needed to perform such experiments can be divided into three groups:

- Pre-experimental
  - A clean room for wafer production.
  - A clean workbench and plasma oven for cultivation chip assembly.
- Experimental
  - A microscope equipped with a motorized stage and a temperature incubator.
  - An applicable pump to perfuse growth medium.
- Post-experimental
  - A server for storing and accessing large image datasets.
  - A cell segmentation pipeline.

Most biological research institutions possess microscopes that could be upgraded with a temperature incubator and a motorized stage if needed. Time-lapse experiments and image segmentation can be performed using commercial software, such as NIS-Elements, or open-source software, such as µManager [134], Fiji [88] or the acia-workflows [94]. However, maintaining the infrastructure necessary for assembling and producing PDMS-based microfluidic cultivation chips may not be feasible for every research laboratory. In this thesis, the cultivation chips were assembled either on the day the experiment began or the day before. However, collaborating with partners has shown that successful experiments can be performed with cultivation chips assembled several months ago. To further spread the technology, it is recommended that cultivation chips be produced in large quantities by specialized personnel at a specialized production facility and then

distributed to dedicated research labs. This approach keeps the production cost per chip low by maximizing equipment utilization and enables microbiology specialists to perform the experiments themselves. Further, experiments are conducted close to where mutant strains are generated, eliminating the need to ship strains across research labs. To conclude, this concept would allow microbiology specialists to save money and time while benefiting from the advantages of single-cell resolution time-lapse data.

Bibliography

1. Witting, L. *et al.* A microfluidic system for the cultivation of cyanobacteria with precise light intensity and CO2 control: enabling growth data acquisition at single-cell resolution. *Lab on a Chip* **25,** 319–329. (2025).
2. Posten, C. in *Integrated bioprocess engineering* 182–219 (De Gruyter, Berlin, 2018). ISBN: 978-3-11-031539-4.
3. Olatunji, O. in *Aquatic Biopolymers: Understanding their Industrial Significance and Environmental Implications* 5–31 (Springer International Publishing, Cham, 2020). ISBN: 978-3-030-34709-3.
4. Sharma, N. K. in *Cyanobacteria : an economic perspective* (eds Rai, A. K. & Stal, L. J.) 3–39 (Wiley Blackwell, Chichester, England, 2014). ISBN: 9781118402221 (e-book).
5. Tanaka, T. *et al.* in *Handbook of Marine Biotechnology* (ed Kim, S.-K.) 1., 51–59 (Springer, Berlin, Heidelberg, 2015). ISBN: 978-3-642-53971-8.
6. Shih, P. M. Photosynthesis and early Earth. *Current Biology* **25,** R855–R859. (2015).
7. Abed, R., Dobretsov, S. & Sudesh, K. Applications of cyanobacteria in biotechnology. *Journal of Applied Microbiology* **106,** 1–12. (2009).
8. Kratzl, F., Kremling, A. & Pflüger-Grau, K. Streamlining of a synthetic co-culture towards an individually controllable one-pot process for polyhydroxyalkanoate production from light and CO2. *Engineering in Life Sciences* **23,** e2100156. (2023).
9. Hays, S. G. *et al.* Synthetic photosynthetic consortia define interactions leading to robustness and photoproduction. *Journal of Biological Engineering* **11,** 4. (2017).
10. Masojidek, J., Torzillo, G. & Koblizek, M. in *Handbook of microalgal culture : applied phycology and biotechnology* (eds Richmond, A. & Hu, Q.) 2nd edition, 21–36 (Wiley Blackwell, Chichester, West Sussex, U.K., 2013).
11. Arias, P. A. *et al.* in *Climate Change 2021: The Physical Science Basis. Contribution of Working Group I to the Sixth Assessment Report of the Intergovernmental Panel on Climate Change* 33–144 (Cambridge University Press, Cambridge, UK and New York, NY, USA, 2023).
12. Bindoff, N. L. *et al.* in *The Ocean and Cryosphere in a Changing Climate: Special Report of the Intergovernmental Panel on Climate Change* 447–588 (Cambridge University Press, Cambridge, 2022). ISBN: 978-1-009-15796-4.
13. Liu, F. *et al.* An array microhabitat device with dual gradients revealed synergistic roles of nitrogen and phosphorous in the growth of microalgae. *Lab on a Chip* **20,** 798–805. (2020).
14. Reyes-Prieto, A., Weber, A. P. & Bhattacharya, D. The Origin and Establishment of the Plastid in Algae and Plants. *Annual Review of Genetics* **41,** 147–168. (2007).

15. Kaneko, T. *et al.* Sequence Analysis of the Genome of the Unicellular Cyanobacterium Synechocystis sp. Strain PCC6803. II. Sequence Determination of the Entire Genome and Assignment of Potential Protein-coding Regions. *DNA Research* **3,** 109–136. (1996).

16. Kaneko, T. *et al.* Sequence Analysis of the Genome of the Unicellular Cyanobacterium Synechocystis sp. strain PCC6803. I. Sequence Features in the 1 Mb Region from Map Positions 64% to 92% of the Genome. *DNA Research* **2,** 153–166. (1995).

17. Hill, R. & Rich, P. R. A Physical Interpretation for the Natural Photosynthetic Process. *Proceedings of the National Academy of Sciences of the United States of America-Biological Sciences* **80,** 978–982 (1983).

18. Vermaas, W. F. *Photosynthesis and Respiration in Cyanobacteria* (John Wiley & Sons, Ltd, 2001., 2001).

19. Hahn, U. in *Physik für Ingenieure. Band 2, Elektrizität und Magnetismus, Optik, Messungen und ihre Auswertung* (ed Hahn, U.) 2. Auflage., 761–951 (De Gruyter Oldenbourg, Berlin, Germany, 2015). ISBN: 978-3-11-037724-8.

20. Zhu, X. G., Long, S. P. & Ort, D. R. Improving Photosynthetic Efficiency for Greater Yield. *Annual Review of Plant Biology, Vol 61* **61,** 235–261 (2010).

21. Chen, M. & Blankenship, R. E. Expanding the solar spectrum used by photosynthesis. *Trends in Plant Science* **16,** 427–431. (2011).

22. Boyd, C. E. in *Water Quality: An Introduction* 105–122 (Springer, Boston, MA, 2000). ISBN: 978-1-4615-4485-2.

23. Markou, G., Vandamme, D. & Muylaert, K. Microalgal and cyanobacterial cultivation: The supply of nutrients. *Water Research* **65,** 186–202 (2014).

24. Loerting, T. & Bernard, J. Aqueous Carbonic Acid (H2CO3). *Chemphyschem* **11,** 2305–2309 (2010).

25. Mills, A. in *Sensors for Environment, Health and Security: Advanced Materials and Technologies* (ed Baraton, M.-I.) 347–368 (Springer Netherlands, Dordrecht, 2009). ISBN: 978-1-4020-9009-7.

26. Badger, M. R. & Price, G. D. CO2 concentrating mechanisms in cyanobacteria: molecular components, their diversity and evolution. *Journal of Experimental Botany* **54,** 609–622 (2003).

27. Badger, M. R., Hanson, D. & Price, G. D. Evolution and diversity of CO2 concentrating mechanisms in cyanobacteria. *Functional Plant Biology* **29,** 161–173 (2002).

28. Daneshvar, E. *et al.* Insights into upstream processing of microalgae: A review. *Bioresource Technology* **329,** 124870. (2021).

29. Monod, J. The Growth of Bacterial Cultures. *Annual Review of Microbiology* **3,** 371–394. (1949).

30. Ferenci, T. 'Growth of bacterial cultures' 50 years on: towards an uncertainty principle instead of constants in bacterial growth kinetics. *Research in Microbiology* **150,** 431–438. (1999).

31. Schmelling, N. M. & Bross, M. What is holding back cyanobacterial research and applications? A survey of the cyanobacterial research community. *Nature Communications* **15,** 6758. (2024).

32. Grünberger, A. *et al.* A disposable picolitre bioreactor for cultivation and investigation of industrially relevant bacteria on the single cell level. *Lab on a Chip* **12,** 2060. (2012).

33. Lee, E., Jalalizadeh, M. & Zhang, Q. Growth kinetic models for microalgae cultivation: A review. *Algal Research* **12,** 497–512. (2015).

34. Jassby, A. D. & Platt, T. Mathematical formulation of the relationship between photosynthesis and light for phytoplankton. *Limnology and Oceanography* **21,** 540–547. (1976).

35. Bannister, T. T. Quantitative description of steady state, nutrient-saturated algal growth, including adaptation. *Limnology and Oceanography* **24,** 76–96. (1979).

36. Benner, P. *et al.* Lab-scale photobioreactor systems: principles, applications, and scalability. *Bioprocess and Biosystems Engineering* **45,** 791–813 (2022).

37. Morschett, H. *et al.* Design and validation of a parallelized micro-photobioreactor enabling phototrophic bioprocess development at elevated throughput. *Biotechnology and Bioengineering* **114,** 122–131. (2017).

38. Chen, M. *et al.* Optical microplates for high-throughput screening of photosynthesis in lipid-producing algae. *Lab on a Chip* **12,** 3870. (2012).

39. Heo, J. *et al.* PhotoBiobox: A tablet sized, low-cost, high throughput photobioreactor for microalgal screening and culture optimization for growth, lipid content and CO2 sequestration. *Biochemical Engineering Journal* **103,** 193–197. (2015).

40. Täuber, S. *et al.* dMSCC: a microfluidic platform for microbial single-cell cultivation of Corynebacterium glutamicum under dynamic environmental medium conditions. *Lab on a Chip* **20,** 4442–4455. (2020).

41. Battat, S., Weitz, D. A. & Whitesides, G. M. An outlook on microfluidics: the promise and the challenge. *Lab on a Chip* **22,** 530–536. (2022).

42. Anggraini, D. *et al.* Recent advances in microfluidic devices for single-cell cultivation: methods and applications. *Lab on a Chip* **22,** 1438–1468. (2022).

43. Merkel, T. C. *et al.* Gas sorption, diffusion, and permeation in poly(dimethylsiloxane). *Journal of Polymer Science Part B-Polymer Physics* **38,** 415–434 (2000).

44. Goodman, A. L. A Comparison Study of Carbon Dioxide Adsorption on Polydimethylsiloxane, Silica Gel, and Illinois No. 6 Coal Using in Situ Infrared Spectroscopy. *Energy & Fuels* **23,** 1101–1106 (2009).

45. Cardenas-Valencia, A. M. *et al.* Spectrometric determination of the refractive index of optical wave guiding materials used in lab-on-a-chip applications. *Applied Spectroscopy* **60,** 322–329 (2006).

46. Kaganovitch, E. *et al.* Microbial single-cell analysis in picoliter-sized batch cultivation chambers. *New Biotechnology. Implementation of Microreactor Technology in Biotechnology – IMTB 2017* **47,** 50–59. (2018).

47. Martins, B. M. C. *et al.* Cell size control driven by the circadian clock and environment in cyanobacteria. *Proceedings of the National Academy of Sciences* **115,** E11415–E11424. (2018).

48. Moore, K. A. *et al.* Mechanical regulation of photosynthesis in cyanobacteria. *Nature Microbiology* **5,** 757–767. (2020).

49. Yokoo, R., Hood, R. D. & Savage, D. F. Live-cell imaging of cyanobacteria. *Photosynthesis Research* **126,** 33–46. (2015).

50. Dong, G. *et al.* Elevated ATPase Activity of KaiC Applies a Circadian Checkpoint on Cell Division in *Synechococcus elongatus*. *Cell* **140,** 529–539. (2010).

51. Yang, Q. *et al.* Circadian Gating of the Cell Cycle Revealed in Single Cyanobacterial Cells. *Science* **327,** 1522–1526. (2010).

52. Teng, S.-W. *et al.* Robust Circadian Oscillations in Growing Cyanobacteria Require Transcriptional Feedback. *Science* **340,** 737–740. (2013).

53. Eremina, A. *et al.* Environmental and molecular noise buffering by the cyanobacterial clock in individual cells. *Nature Communications* **16,** 3566. (2025).

54. Mihalcescu, I., Hsing, W. & Leibler, S. Resilient circadian oscillator revealed in individual cyanobacteria. *Nature* **430,** 81–85. (2004).

55. Luke, C. S. *et al.* A Microfluidic Platform for Long-Term Monitoring of Algae in a Dynamic Environment. *Acs Synthetic Biology* **5,** 8–14 (2016).

56. Kim, B. J. *et al.* An array microhabitat system for high throughput studies of microalgal growth under controlled nutrient gradients. *Lab on a Chip* **15,** 3687–3694. (2015).

57. Castaldello, C. *et al.* Microfluidic Platform for Microalgae Cultivation under Non-limiting CO_2 Conditions. *Industrial & Engineering Chemistry Research* **58,** 18036–18045. (2019).

58. Liu, F. *et al.* A high throughput array microhabitat platform reveals how light and nitrogen colimit the growth of algal cells. *Scientific Reports* **14,** 9860. (2024).

59. Liu, F. *et al.* Microscope-based light gradient generation for quantitative growth studies of photosynthetic micro-organisms. *Lab on a Chip* **22,** 3138–3146. (2022).

60. Graham, P. J., Riordon, J. & Sinton, D. Microalgae on display: a microfluidic pixel-based irradiance assay for photosynthetic growth. *Lab on a Chip* **15,** 3116–3124. (2015).

61. Nguyen, B., Graham, P. J. & Sinton, D. Dual gradients of light intensity and nutrient concentration for full-factorial mapping of photosynthetic productivity. *Lab on a Chip* **16,** 2785–2790. (2016).

62. Kim, H. S. *et al.* A microfluidic photobioreactor array demonstrating high-throughput screening for microalgal oil production. *Lab on a Chip* **14,** 1415–1425 (2014).

63. Zheng, G. *et al.* An integrated microfluidic device in marine microalgae culture for toxicity screening application. *Marine Pollution Bulletin* **72,** 231–243. (2013).

64. Bae, S. *et al.* An integrated microfluidic device for the high-throughput screening of microalgal cell culture conditions that induce high growth rate and lipid content. *Analytical and Bioanalytical Chemistry* **405,** 9365–9374. (2013).

65. Yang, C.-C. *et al.* Using a Microfluidic Gradient Generator to Characterize BG-11 Medium for the Growth of Cyanobacteria Synechococcus elongatus PCC7942. *Micromachines* **6,** 1755–1767. (2015).

66. Paik, S.-M., Sim, S.-J. & Jeon, N. L. Microfluidic perfusion bioreactor for optimization of microalgal lipid productivity. *Bioresource Technology* **233,** 433–437. (2017).

67. Zheng, G. *et al.* Development of Microfluidic Dilution Network-Based System for Lab-on-a-Chip Microalgal Bioassays. *Analytical Chemistry* **90,** 13280–13289. (2018).

68. Yu, F. B. *et al.* Long-term microfluidic tracking of coccoid cyanobacterial cells reveals robust control of division timing. *Bmc Biology* **15** (2017).

69. Westerwalbesloh, C. *et al.* A microfluidic photobioreactor for simultaneous observation and cultivation of single microalgal cells or cell aggregates. *Plos One* **14** (2019).

70. Eu, Y.-J. *et al.* A microfluidic perfusion platform for cultivation and screening study of motile microalgal cells. *Biomicrofluidics* **8,** 024113. (2014).

71. Kwak, H. S., Kim, J. Y. H. & Sim, S. J. A microscale approach for simple and rapid monitoring of cell growth and lipid accumulation in Neochloris oleoabundans. *Bioprocess and Biosystems Engineering* **38,** 2035–2043. (2015).

72. Kasahara, K. *et al.* Enabling oxygen-controlled microfluidic cultures for spatiotemporal microbial single-cell analysis. *Frontiers in Microbiology* **14.** (2023).

73. Kasahara, K. *et al.* Unveiling microbial single-cell growth dynamics under rapid periodic oxygen oscillations. *Lab on a Chip* **25,** 2234–2246. (2025).

74. Deng, T. *et al.* Versatile Microfluidic Platform for Automated Live-Cell Hyperspectral Imaging Applied to Cold Climate Cyanobacterial Biofilms. *Analytical Chemistry* **93,** 8764–8773. (2021).

75. Choi, S. Microscale microbial fuel cells: Advances and challenges. *Biosensors and Bioelectronics* **69,** 8–25. (2015).

76. Xu, Z. *et al.* Microfluidic chip for automated screening of carbon dioxide conditions for microalgal cell growth. *Biomicrofluidics* **11,** 064104. (2017).

77. Abdulla Yusuf, H. *et al.* A Hybrid Microfluidic Differential Carbonator Approach for Enhancing Microalgae Growth: Inline Monitoring Through Optical Imaging. *Arabian Journal for Science and Engineering* **46,** 6765–6774. (2021).

78. Forry, S. P. & Locascio, L. E. On-chip CO2 control for microfluidic cell culture. *Lab on a Chip* **11,** 4041–4046 (2011).

79. Takano, A., Tanaka, M. & Futai, N. On-chip CO2 incubation for pocket-sized microfluidic cell culture. *Microfluidics and Nanofluidics* **12,** 907–915. (2012).

80. Takano, A., Tanaka, M. & Futai, N. On-chip multi-gas incubation for microfluidic cell cultures under hypoxia. *Biomicrofluidics* **8,** 061101. (2014).

81. Probst, C. *et al.* Microfluidic growth chambers with optical tweezers for full spatial single-cell control and analysis of evolving microbes. *Journal of Microbiological Methods* **95,** 470–476. (2013).

82. Lindemann, D. *et al.* Microbial single-cell growth response at defined carbon limiting conditions. *RSC Advances* **9,** 14040–14050. (2019).

83. Harris, C. R. *et al.* Array programming with NumPy. *Nature* **585,** 357–362. (2020).

84. Albrecht, W., Moers, J. & Hermanns, B. HNF - Helmholtz Nano Facility. *Journal of large-scale research facilities JLSRF* **3** (2017).

85. Gruenberger, A. *et al.* Microfluidic Picoliter Bioreactor for Microbial Single-cell Analysis: Fabrication, System Setup, and Operation. *JoVE (Journal of Visualized Experiments),* e50560. (2013).

86. Probst, C. *et al.* Rapid inoculation of single bacteria into parallel picoliter fermentation chambers. *Analytical Methods* **7,** 91–98. (2015).

87. Burmeister, A. *et al.* A microfluidic co-cultivation platform to investigate microbial interactions at defined microenvironments. *Lab on a Chip* **19,** 98–110. (2019).

88. Schindelin, J. *et al.* Fiji: an open-source platform for biological-image analysis. *Nature Methods* **9,** 676–682. (2012).

89. Parslow, A., Cardona, A. & Bryson-Richardson, R. J. Sample drift correction following 4D confocal time-lapse imaging. *Journal of Visualized Experiments: JoVE,* 51086 (2014).

90. Allan, C. *et al.* OMERO: flexible, model-driven data management for experimental biology. *Nature Methods* **9,** 245–253. (2012).

91. Scherr, T. *et al.* microbeSEG: A deep learning software tool with OMERO data management for efficient and accurate cell segmentation. *PLOS ONE* **17,** e0277601. (2022).

92. Seiffarth, J. *et al.* ObiWan-Microbi: OMERO-based integrated workflow for annotating microbes in the cloud. *SoftwareX* **26.** (2024).

93. Cutler, K. J. *et al.* Omnipose: a high-precision morphology-independent solution for bacterial cell segmentation. *Nature Methods* **19,** 1438–1448. (2022).

94. Seiffarth, J. *et al. acia-workflows: Automated Single-cell Imaging Analysis for Scalable and Deep Learning-based Live-cell Imaging Analysis Workflows* 2025.
95. Grossmann, G. *et al.* The RootChip: An Integrated Microfluidic Chip for Plant Science. *The Plant Cell* **23,** 4234–4240. (2011).
96. Morschett, H. *et al.* Laboratory-scale photobiotechnology—current trends and future perspectives. *FEMS Microbiology Letters* **365.** (2018).
97. Hirooka, S. *et al.* Life cycle and functional genomics of the unicellular red alga Galdieria for elucidating algal and plant evolution and industrial use. *Proceedings of the National Academy of Sciences* **119,** e2210665119. (2022).
98. Gross, W. & Schnarrenberger, C. Heterotrophic Growth of Two Strains of the Acido-Thermophilic Red Alga Galdieria sulphuraria. *Plant and Cell Physiology* **36,** 633–638. (1995).
99. Miyagishima, S. & Wei, J. L. in *Cyanidioschyzon merolae: A New Model Eukaryote for Cell and Organelle Biology* (eds Kuroiwa, T. *et al.*) 31–41 (Springer, Singapore, 2017). ISBN: 978-981-10-6101-1.
100. Dvořák, P. *et al.* Synechococcus: 3 billion years of global dominance. *Molecular Ecology* **23,** 5538–5551. (2014).
101. Yu, J. J. *et al.* Synechococcus elongatus UTEX 2973, a fast growing cyanobacterial chassis for biosynthesis using light and CO2. *Scientific Reports* **5** (2015).
102. Golden, S. S. The international journeys and aliases of Synechococcus elongatus. *New Zealand Journal of Botany* **57,** 70–75. (2019).
103. Ducat, D. C. *et al.* Rerouting Carbon Flux To Enhance Photosynthetic Productivity. *Applied and Environmental Microbiology* **78,** 2660–2668. (2012).
104. Abramson, B. W. *et al.* Increased Photochemical Efficiency in Cyanobacteria via an Engineered Sucrose Sink. *Plant and Cell Physiology* **57,** 2451–2460. (2016).
105. Korelusová, J., Kasˇtovský, J. & Komárek, J. Heterogeneity of the Cyanobacterial Genus Synechocystis and Description of a New Genus, Geminocystis1. *Journal of Phycology* **45,** 928–937. (2009).
106. Stanier, R. Y. *et al.* Generic Assignments, Strain Histories and Properties of Pure Cultures of Cyanobacteria. *Microbiology* **111,** 1–61. (1979).
107. Stanier, R. Y. *et al.* Purification and Properties of Unicellular Blue-Green Algae (Order Chroococcales). *Bacteriological Reviews* **35,** 35 (1971).
108. Allen, M. M. Simple conditions for growth of unicellular blue-green algae on plates. *Journal of Phycology* **4,** 1–4 (1968).
109. Zhu, X. G., Long, S. P. & Ort, D. R. What is the maximum efficiency with which photosynthesis can convert solar energy into biomass? *Current Opinion in Biotechnology* **19,** 153–159 (2008).
110. Albertano, P. *et al.* The taxonomic position of Cyanidium, Cyanidioschyzon and Galdieria: An update. *Hydrobiologia* **433,** 137–143 (2000).

111. Westerwalbesloh, C. *et al.* Modeling and CFD simulation of nutrient distribution in picoliter bioreactors for bacterial growth studies on single-cell level. *Lab on a Chip* **15,** 4177–4186. (2015).

112. McKinney, W. Data Structures for Statistical Computing in Python. In *Proceedings of the 9th Python in Science Conference* (eds van der Walt, S. & Millman, J.) 56–61 (Austin, Texas, 2010).

113. Virtanen, P. *et al.* SciPy 1.0: fundamental algorithms for scientific computing in Python. *Nature Methods* **17,** 261–272. (2020).

114. Sabri, S., Nielsen, L. K. & Vickers, C. E. Molecular Control of Sucrose Utilization in Escherichia coli W, an Efficient Sucrose-Utilizing Strain. *Applied and Environmental Microbiology* **79,** 478–487. (2013).

115. Carroll, J. J., Slupsky, J. D. & Mather, A. E. The Solubility of Carbon-Dioxide in Water at Low-Pressure. *Journal of Physical and Chemical Reference Data* **20,** 1201–1209 (1991).

116. Maki, A. J. *et al.* Modeling carbon dioxide transport in PDMS-based microfluidic cell culture devices. *Chemical Engineering Science* **137,** 515–524 (2015).

117. Flamholz, A. I. *et al.* Revisiting Trade-offs between Rubisco Kinetic Parameters. *Biochemistry* **58,** 3365–3376. (2019).

118. Occhialini, A. *et al.* Transgenic tobacco plants with improved cyanobacterial Rubisco expression but no extra assembly factors grow at near wild-type rates if provided with elevated CO2. *The Plant Journal: For Cell and Molecular Biology* **85,** 148–160 (2016).

119. Tromans, D. Temperature and pressure dependent solubility of oxygen in water: a thermodynamic analysis. *Hydrometallurgy* **48,** 327–342. (1998).

120. Luisa Rodríguez-Buey, M. & Isabel Orús, M. The response of *Synechococcus* PCC7942 (Cyanophyta) to changes in CO2 supply in relation to the acclimation of the CO2-concentrating mechanism. I: physiological study. *Journal of Plant Physiology* **158,** 325–334. (2001).

121. Price, G. D. *et al.* Modes of active inorganic carbon uptake in the cyanobacterium, *Synechococcus* sp. PCC7942. *Australian Journal of Plant Physiology* **29,** 131–149. (2002).

122. Ball, S. G. *et al.* Metabolic Effectors Secreted by Bacterial Pathogens: Essential Facilitators of Plastid Endosymbiosis? *The Plant Cell* **25,** 7–21. (2013).

123. Luan, G. *et al.* Progress and perspective on cyanobacterial glycogen metabolism engineering. *Biotechnology Advances* **37,** 771–786. (2019).

124. Bird, R. B., Steward, W. E. & Lightfoot, E. N. in *Transport Phenomena* 2nd ed., 620–656 (John Wiley & Sons Ltd, New York, NY, 2002). ISBN: ISBN 0-471-41077-2.

125. Kato, Y. *et al.* Glycogen deficiency enhances carbon partitioning into glutamate for an alternative extracellular metabolic sink in cyanobacteria. *Communications Biology* **7,** 233. (2024).

126. Berwanger, L. C. *et al.* Self-sustained rhythmic behavior of Synechocystis sp. PCC 6803 under continuous light conditions in the absence of light–dark entrainment. *PNAS Nexus* **4,** pgaf120. (2025).

127. Köbler, C. *et al.* Two KaiABC systems control circadian oscillations in one cyanobacterium. *Nature Communications* **15,** 7674. (2024).

128. Ditty, J., Williams, S. & Golden, S. A Cyanobacterial Circadian Timing Mechanism. *Annual Review of Genetics* **37,** 513–543. (2003).

129. Paranjpe, D. A. & Sharma, V. K. Evolution of temporal order in living organisms. *Journal of Circadian Rhythms* **3,** 7. (2005).

130. Kondo, T. *et al.* Circadian rhythms in prokaryotes: luciferase as a reporter of circadian gene expression in cyanobacteria. *Proceedings of the National Academy of Sciences of the United States of America* **90,** 5672–5676 (1993).

131. Zhao, C. *et al.* Synechocystis: A model system for expanding the study of cyanobacterial circadian rhythms. *Frontiers in Physiology* **13.** (2023).

132. Press, W. H. *et al.* in *Numerical Recipes: The Art of Scientific Computing*. 3rd ed., 600–637 (Cambridge University Press & Assessment, Cambridge, UK., 2003). ISBN: 978-0-521-88068-8.

133. Pedrotti, F. L. in *Optik für Ingenieure: Grundlagen ; mit 28 Tabellen* 3., bearb. und aktualisierte Aufl, 1–8 (Springer, Berlin Heidelberg, 2005). ISBN: 978-3-540-22813-4.

134. Edelstein, A. *et al.* Computer Control of Microscopes Using μManager. *Current Protocols in Molecular Biology* **92,** 14.20.1–14.20.17. (2010).

Publications

Peer-Reviewed Journal Articles

I. **Lennart Witting**, Johannes Seiffarth, Birgit Stute, Tim Schulze, Jan Matthis Hofer, Katharina Nöh, Marion Eisenhut, Andreas P. M. Weber, Eric von Lieres, and Dietrich Kohlheyer, 'A microfluidic system for the cultivation of cyanobacteria with precise light intensity and CO_2 control: enabling growth data acquisition at single-cell resolution', Lab on a Chip, vol. 25, no. 3, pp. 319–329, 2025.

II. Aleksandra Eremina, Christian Schwall, Teresa Saez, **Lennart Witting**, Dietrich Kohlheyer, Bruno M. C. Martins, Philipp Thomas, and James C. W. Locke, 'Environmental and molecular noise buffering by the cyanobacterial clock in individual cells', Nat Commun, vol. 16, no. 1, p. 3566, Apr. 2025.

III. Johannes Seiffarth, Keitaro Kasahara, Michelle Bund, Benita Lückel, Richard D. Paul, Matthias Pesch; **Lennart Witting**, Michael Bott, Dietrich Kohlheyer and Katharina Nöh, 'acia-workflows: Automated Single-cell Imaging Analysis for Scalable and Deep Learning-based Live-cell Imaging Analysis Workflows', *arXiv*, under revision.

IV. **Lennart Witting**[†], Florian Stirba[†], Julius Nohr, Ekatarina Ivanova, Petra Kolkhof, Dietrich Kohlheyer, Anika Wiegard and Ilka Axmann, 'Live-cell imaging enables reporter-free monitoring of the circadian rhythm in individual *Synechocystis* cells', *bioRxiv*, under revision.

V. Jan Mathis Hofer[†], Tim Schulze[†], **Lennart Witting**, Bianca Laker, Stephan Krüger, Philipp Westhoff, Jeannine Volke, Dietrich Kohlheyer, Andreas P.M. Weber, and Marion Eisenhut, 'Acclimation response of the cyanobacterium *Synechocystis* sp. PCC 6803 towards glycogen deficiency', *bioRxiv*, revised.

VI. Philipp Ernst, Jan Vanselow, Max Denter, Wen Li, **Lennart Witting**, Jochem Gätgens, Vlada B. Urlacher, Dietrich Kohlheyer, Michael Feldbrügge and Julia Frunzke, 'Systematic evaluation of *Cyanidioschyzon merolae* across photobioreactor systems: Linking reactor design to biomass production and biochemical composition', *bioRxiv*, under revision.

[†] Equal contribution

Peer-Reviewed Journal Articles (not related to this thesis)

I. Juliane Diehm, **Lennart Witting**, Frank Kirschhöfer, Gerald Brenner-Weiß, and Matthias Franzreb, 'Micro simulated moving bed chromatography-mass spectrometry as a continuous on-line process analytical tool', Anal Bioanal Chem, vol. 416, no. 2, pp. 373–386, Jan. 2024.

International Conference Contributions (oral presentation)

‡ LW attended the conference and was the presenting author
+ LW attended the conference but was **not** the presenting author
* LW did **not** attend the conference

I. **Lennart Witting**, Florian Stirba, Anika Wiegard, Ilka Axmann and Dietrich Kohlheyer, 'Markerless detection of the circadian rhythm in *Synechocystis* sp. PCC6803 using single-cell microfluidics' *18th International Symposium on Phototrophic Prokaryotes*, September 2025, (Qingdao, China). ‡

II. **Lennart Witting**, Marion Eisenhut, Andreas Weber, Tim Schulze, Keitaro Kasahara, Johannes Seiffarth and Dietrich Kohlheyer, 'In vitro evolution of a synthetic organelle inside a picoliter habitat' *Annual conference 2023 of the Association for General and Applied Microbiology (VAAM)*, Sep. 2023 (Göttingen, Germany). ‡

International Conference Contributions (poster)

‡ LW attended the conference and was the presenting author
+ LW attended the conference but was **not** the presenting author
* LW did **not** attend the conference

I. **Lennart Witting**, Florian Stirba, Anika Wiegard, Ilka M. Axmann and Dietrich Kohlheyer, 'Reporter-free observation of the circadian rhythm in individual *Synechocystis* cells using single-cell resolution time-lapse imaging' *Annual conference 2026 of the Association for General and Applied Microbiology (VAAM)*, March 2026, (Berlin, Germany). ‡

II. **Lennart Witting**, Jan Matthis Hofer, Tim Schulze, Andreas P. M. Weber, Marion Eisenhut and Dietrich Kohlheyer, 'A versatile microfluidic platform for the cultivation of cyanobacteria at single-cell resolution' *Annual conference 2025 of the Association for General and Applied Microbiology (VAAM)*, March 2025, (Bochum, Germany). ‡

III. Jan Matthis Hofer, Tim Schulze, **Lennart Witting**, Jeanine Volke, Dietrich Kohlheyer, Marion Eisenhut and Andreas P. M. Weber, 'From cyanobacteria to cell organelle – Engineering and studying minimal endosymbiotic metabolism' *Annual conference 2025 of the Association for General and Applied Microbiology (VAAM)*, March 2025 (Bochum, Germany). +

IV. Florian P. Striba, **Lennart Witting**, Niklas Küppers, Anika Wiegard, Fynn Kolkhof, Dietrich Kohlheyer, Annegret Wilde and Ilka M. Axmann, 'Unraveling the role of a new input receiver in a complex cyanobacterial circadian clock' *Annual conference 2025 of the Association for General and Applied Microbiology (VAAM)*, March 2025 (Bochum, Germany). +

V. **Lennart Witting**, Keitaro Kasahara and Dietrich Kohlheyer, 'Cyanobacteria at single-cell resolution: From analyzing distinct colonies to multi-parameter growth models' *13th International CeBiTec Research Conference*, Sep. 2024 (Bielefeld, Germany). ‡

VI. Jan Hofer, Tim Schulze, **Lennart Witting**, Dietrich Kohlheyer, Marion Eisenhut and Andreas Weber 'Establishing a Minimal Endosymbiotic Metabolism in Cyanobacteria' *12th Workshop on the Biology of Cyanobacteria (EWBC)*, Sep. 2024 (Seville, Spain). *

VII. Tim Schulze, Jan Hofer, **Lennart Witting**, Dietrich Kohlheyer, Marion Eisenhut and Andreas Weber 'From cyanobacteria to cell organelle - Engineering and studying a synthetic cyanobacterial endosymbiont' *12th Workshop on the Biology of Cyanobacteria (EWBC)*, Sep. 2024 (Seville, Spain). *

VIII. Jan Hofer, Tim Schulze, **Lennart Witting**, Dietrich Kohlheyer, Marion Eisenhut and Andreas Weber 'Establishing a Minimal Endosymbiotic Metabolism in Cyanobacteria' *International Conference of the German Society for Plant Sciences*, Sep. 2024 (Halle/Saale, Germany). *

IX. Tim Schulze, Jan Hofer, **Lennart Witting**, Dietrich Kohlheyer, Marion Eisenhut and Andreas Weber 'From cyanobacteria to cell organelle - Engineering and studying a synthetic cyanobacterial endosymbiont' *International Conference of the German Society for Plant Sciences*, Sep. 2024 (Halle/Saale, Germany). *

X. Tim Schulze, Jan Hofer, **Lennart Witting**, Dietrich Kohlheyer, Marion Eisenhut and Andreas Weber 'In vitro recapitulation of plastid evolution' *German Association for Synthetic Biology (GASB7)*, Sep. 2023 (Freiburg, Germany). *

Other Conference Contributions

‡ LW attended the conference and was the presenting author
+ LW attended the conference but was **not** the presenting author
* LW did **not** attend the conference

I. **Lennart Witting**, Keitaro Kasahara and Dietrich Kohlheyer, 'Single-Cell Microfluidics: A Highly Interdisciplinary Endeavor' *Evaluation of Helmholtz Earth & Environment Topic 7 - Bioeconomy*, June 2025 (Jülich, Germany), poster. ‡

II. **Lennart Witting** and Dietrich Kohlheyer, 'Cyanobacteria at single-cell level: New insights into population dynamics' *Fall meeting Topic 7: Towards a Sustainable Bioeconomy – Resources, Utilization, Engineering and AgroEcosystems*, December 2023 (Jülich, Germany), poster. *

III. **Lennart Witting**, Keitaro Kasahara and Dietrich Kohlheyer, 'Microfluidic cultivation of cyanobacteria' *General Assembly 2023 of the Program "Changing Earth - Sustaining our Future"*, May 2023 (Karlsruhe, Germany), poster. ‡

Data & code publication related to this thesis

I. **Lennart Witting**, Johannes Seiffarth, Birgit Stute, Tim Schulze, Jan Matthis Hofer, Katharina Nöh, Marion Eisenhut, Andreas P. M. Weber, Eric von Lieres, and Dietrich Kohlheyer, 'A microfluidic system for the cultivation of cyanobacteria with precise light intensity and CO_2 control: enabling growth data acquisition at single-cell resolution' [Data set]. DataPLANT. https://doi.org/10.60534/g22mf-11z54

II. **Lennart Witting**, (2024). Supplement to Witting et al. 2024 [Data set]. Zenodo. https://doi.org/10.5281/zenodo.13220517

III. **Lennart Witting**, JuBiotech/Supplement-to-Witting-et-al.-2024. (Mar. 11, 2025). Jupyter Notebook. IBG-1: Biotechnology. Accessed: May 27, 2025. [Online]. Available: https://github.com/JuBiotech/Supplement-to-Witting-et-al.-2024

IV. **Lennart Witting**†, Florian Stirba†, Julius Nohr, Ekatarina Ivanova, Petra Kolkhof, Dietrich Kohlheyer, Anika Wiegard and Ilka Axmann (2026). Live-cell imaging enables reporter-free monitoring of the circadian rhythm in individual Synechocystis cells [Data set]. DataPLANT. https://doi.org/10.60534/w3pyw-ds524

† Equal contribution

Invited seminar presentations

I. **Lennart Witting**, 'Microfluidic cultivation of cyanobacteria - the new gold standard for growth quantification of phototrophic microorganisms?' *Seminar of the synthetic microbiology group at University of Düsseldorf*, March 2025 (Düsseldorf, Germany), oral presentation.

II. **Lennart Witting**, 'Markerless observation of circadian rhythms in *Synechocystis* sp. PCC6803 at single-cell resolution' *Seminar of the synthetic microbiology group at University of Düsseldorf*, April 2025 (Düsseldorf, Germany), oral presentation.

III. Keitaro Kasahara & **Lennart Witting**, 'Advancing environmental control in microfluidic single cell analysis - on-chip gas control and light intensity gradient cultivation' *Seminar of the microsystems in bioprocess engineering group at KIT*, April 2025 (Karlsruhe, Germany), oral presentation.

Supervision of bachelor & master theses

Aurian Andree *Microfluidic Platform for the Study of Stable Co-Cultures: Phototrophic and Heterotrophic Microorganisms in Sucrose-Driven Carbon Exchange.* University of Bonn. 27.05.2025, master thesis.

Julius Nohr *Data analysis of circadian clock mutants cultivated in a microfluidic system* University of Düsseldorf. 02.06.2025, bachelor thesis.

Awards

Outstanding Young Student Award, *18th International Symposium on Phototrophic Prokaryotes*, September 2025, (Qingdao, China).

Further activities related to this thesis

JuDocs transferable skills curriculum

- **Management of a doctoral project** September 2022
- **Good Research Practice** October 2022
- **Scientific Presentation** September 2023
- **Scientific Writing** September 2023
- **Entrepreneurship** December 2024

Activities related to CRC1535 MibiNet

- **Kick off meeting** March 2023, Düsseldorf, Germany.
- **Progress report I** May 2023, oral presentation, Düsseldorf, Germany.
- **Onboarding week** May 2025, Düsseldort & Colone, Germany.
- **MibiNet Retreat I** November 2025, oral presentation, Königswinter, Germany.
- **MibiNext Journal Club** November 2023, presentation and discussion of a research paper by Kim et al. [56].
- **MibiNext Workshop - Synthetic design and analysis of microbial communities** 14-May 2023, Düsseldorf, Germany.
- **Progress report II** August 2024, oral presentation, Jülich, Germany.
- **MibiNet Retreat II** September 2024, oral and poster presentation, Kalkar, Germany.
- **MibiNext career day: Mentorship Matters - Building Bridges to Career Success.** February 2025, Düsseldorf, Germany.
- **Progress report III** April 2025, oral presentation, Jülich, Germany.
- **MibiNet Retreat III** September 2025, oral and poster presentation, Rösrath, Germany.

Activities related the Helmholtz Innovation Pool project "High CO2 – metabolic responses and bioeconomic opportunities"

- **Biyearly status update** February 2023, oral presentation.
- **Biyearly status update** June 2023, oral presentation.
- **Biyearly status update** April 2024, oral presentation.
- **Biyearly status update** November 2024, oral presentation.

Teaching

MibiNext Workshop on Optogenetics and Microfluidics at FZJ. Participated in organisation. Designed and hosted a workstation on droplet microfluidics. April 2025, Jülich.

Microbial Single-cell analysis in microfluidic environments – Practical training. Designed and hosted a 3 h practical training lecture on analysing single-cell time-lapse microscopy data. Part of the *QBio402:Biotechnology and Synthetic Biology* course at University of Düsseldorf. May 2025, Düsseldorf.

List of Figures

1 Overview of the proposed microfluidic cultivation platform to study phototrophic microorganisms. vii

2 Übersicht über die mikrofluidische Kultivierungsplattform zur Untersuchung phototropher Mikroorganismen. ix

1.1 Development of the oxygen concentration in the Earth's atmosphere. . . . 1

1.2 Photosynthesis in cyanobacteria. 3

1.3 The spectrum of electromagnetic waves. 6

1.4 The dependency of microalgae growth on the light intensity. 10

1.5 Concepts for investigating different media or light regimes in a microfluidic experiment. 15

2.1 Growth of cyanobacteria model organisms in a shake flask culture. 29

2.2 Multi-Cultivator 1000-OD photobioreactor. 30

2.3 Moulding and assembly of microfluidic cultivation chips. 34

2.4 Frequently experienced reasons for experimental failure. 37

3.1 The proposed ringlight illumination system. 43

3.2 Custom-built components for STL to ringlight illumination system. 43

3.3 Pictures of the proposed illumination system. 47

3.4 Characterization of the STL to ringlight illumination system. 49

3.5 LI190R quantum sensor mounted into microscope objective turret. 51

4.1 Growth of extremophile microalgae. 58

4.2 Synechococcus growth at different light-intensities under homogeneous and constant growth-light illumination. 60

4.3 Distribution of the single-cell area in a distinct growth colony. 61

4.4 Growth of UTEX2973 in the microfluidic chip and MC. 63

5.1 Alternative light-intensity gradient concepts. 68

5.2 Characterization of the light cone emitted by the ringlight. 74

5.3 The pre-experimental calibration procedure. 75
5.4 Progression of microfluidic cultivation layouts. 77
5.5 Results from various light-intensity gradient experiments. 80
5.6 Combined day/night rhythm and light-intensity gradient cultivation. 83

6.1 The cultivation device used for CO_2 control experiment. 88
6.2 Results from the COMSOL Simulation of the CO_2 control device. 94
6.3 Cultivation of *S. elongatus* strains with an applied light-intensity gradient and decreasing CO_2 molar fractions. 96

7.1 Synthetic recapitulation of synthetic endosymbiosis. 103
7.2 Two-step preculture for microfluidic cultivation of PCC6803 Δ*glgC* mutants. 108
7.3 Growth of *Synechocystis* sp. PCC6803 WT in a microfluidic cultivation chamber. 109
7.4 Results from light-intensity gradient experiments with Δ*glgC* mutants. . . . 111
7.5 Behavior of Δ*glgC* mutants at night. 113
7.6 The proposed dynamic medium switching concept. 116

8.1 The cultivation chip layout used for observing the circadian clock in *Synechocystis*. 123
8.2 Observation of the circadian rhythm in individual *Synechocystis* cells. . . . 126
8.3 The circadian data analysis pipeline 127
8.4 Comparison of the WT, the *kaiC3* knockout and the complementation mutant. 128
8.5 Single-cell phase-contrast intensity oscillations. 129
8.6 Summary of the fitted cosine parameters for various strains. 131
8.7 Summary of the growth rates and single-cell areas for various strains. . . . 133

A.1 Default values for image registration with the *Correct 3D drift* Fiji plugin. . xli

B.1 Cultivation layout #1. xlii
B.2 Cultivation layout #2 xliii
B.3 CO_2 perfusion channels for cultivation layout #2. xliv
B.4 Overlay of cultivation layout #2 and CO_2 perfusion channels. xlv

C.1 Connector between the STL and the ringlight as used for reference measurements and measurements with the aspheric condenser lenses. xlvi
C.2 Connection ring between STL and shutter. xlvii
C.3 Dimensions of the adapter ring between the connection ring and the shutter. xlvii
C.4 Dimensions of the shutter. xlviii
C.5 Connector between the shutter and the ringlight input xlviii
C.6 Dimensions of the STL light engine. xlix
C.7 Connector between the rebuild STL and the shutter. l
C.8 Comparison of the two approaches to maximise the intensity emitted onto the cultivation plane. li
C.9 Assembled ringlight fixation lii
C.10 Dimensions of the spacer to fix the ringlight around the microscope condenser. lii
C.11 Dimensions of the connector plate between the spacer and the half-circle cover. liii
C.12 Dimension of the Half-circle cover to generate a linear light-intensity gradient. liii
C.13 Master mold for replication of the CO_2 perfusion chamber. liv
C.14 Master mold for the tilted chip concept liv
C.15 Li190R to objective turret connector lv
C.16 Fixed-spectrum LED to ringlight connection lvi

D.1 Spectrum and spectral stability of the mounted LED. lvii
D.2 Output characteristic of the mounted LED lvii
D.3 Homogeneity of the mounted LED lviii
D.4 Mean single-cell area across growth colonies with a growth array lix
D.5 Mean single-cell area across growth colonies with a growth array lx
D.6 Single-cell area distribution for UTEX2973 at 140 $\mu E \cdot m^{-2} \cdot s^{-1}$. lxi
D.7 Single-cell area over the distance to the colony center for UTEX2973 at 140 $\mu E \cdot m^{-2} \cdot s^{-1}$. lxii
D.8 Single-cell area distribution for UTEX2973 at 20 $\mu E \cdot m^{-2} \cdot s^{-1}$. lxiii
D.9 Single-cell area over the distance to the colony center for UTEX2973 at 140 $\mu E \cdot m^{-2} \cdot s^{-1}$. lxiv
D.10 Single-cell area over the distance to the colony center for UTEX2973 at 140 $\mu E \cdot m^{-2} \cdot s^{-1}$. lxv

D.11 Single-cell area over the distance to the colony center for UTEX2973 at 140 µE·m^{-2}·s^{-1}. lxv
D.12 Single-cell area over light-intensity for UTEX2973. lxvi
D.13 Single-cell area over light-intensity for PCC7942 CscB. lxvi
D.14 Single-cell traces for the experiment displayed in Fig. 7.5. lxvii
D.15 Improved simulation approach lxviii

List of Tables

1.1 Microfluidic devices for the investigation of lighting conditions. 18
1.2 Microfluidic devices for the investigation of medium composition. 21
1.3 Microfluidic devices with On-Chip CO_2-Control. 23
1.4 Comparison of microfluidic devices for the cultivation of microalgae. 25
1.5 Design aspects of the microfluidic experimental platform presented in this thesis. 27

2.1 Concentration of antibiotics during permanent shake flask culture. 29
2.2 Composition of the BG11 liquid growth medium. 31
2.3 Standard parameters for oxygen plasma treatment. 34
2.4 Microscopy setup and peripheral devices. 35
2.5 Process parameters for 3D printing 40

3.1 Cost comparison of different growth light sources. 45

4.1 Cultivation parameters for extremophile microalgae. 55
4.2 Number of analyzed chamber growth chamber with cell growth for the data shown in Fig. 4.4 and 4.2 F. 60
4.3 Growth rate and quantum yields calculated for distinct colonies of UTEX2973. 61
4.4 Model parameters for cultivation of UTEX2973 and PCC7942 in the microfluidic device and in the MC under homogeneous growth-light illumination. 65

5.1 Design parameters of microfluidic layouts designed for light-intensity gradient cultivation. 76
5.2 Model parameters for the data presented in Fig. 5.5 and Fig. 5.6 82

6.1 Molar fraction of CO_2 and volumetric flow rates for the CO_2-control experiment. 90
6.2 Estimation of the half maximum CO_2 concentration of RuBisCo. 92
6.3 Model parameters for the data presented in Fig. 6.3. 98

7.1 List of investigated strains in this chapter. 104
7.2 Microfluidic experimental conditions applied in this chapter. 105
7.3 Dimensions and flow properties in different sections along the path of the liquid. 106

8.1 *Synechocystis* sp. PCC6803 strains investigated in this chapter. 122
8.2 Standard cultivation parameters for circadian clock experiments. 123

A.1 Process parameters for both layers of the replication master for layout #1. xl

Appendix

A Supplementary protocols

A.1 Fabrication of the replication master with maskless lithography

The replication master were produced at the Helmholtz Nano facility (HNF). Fabrication details of the 2-step process are listed beneath.

Tab. A.1: Process parameters for both layers of the replication master for layout #1.

Layer 1 - approximately 1 µm high	
Process step	Parameter
Dehydration	150 °C, 2 min
Spin coating	Photoresist: SU-8 200 (Micro resist technology, Germany); 1900 rpm
Soft bake	On hot plate: 1 min at 65°C and 1 min at 95 °C
Maskless lithography	DWL66+ (Heidelberg-instruments, Germany); 13 h writing time
Post exposure bake	On hot plate: 1 min at 65°C and 1 min at 95 °C
Developer	mrDEV600 (Micro resist technology, Germany) + Isopropanol
Layer 2 - approximately 10 µm high.	
Process step	Parameter
Dehydration	150 °C, 2 min
Spin coating	Photoresist: SU-8 2001 (Micro resist technology, Germany); 2300 rpm
Soft bake	On hot plate: 3 min at 65°C and 3 min at 95 °C
Maskless lithography	DWL66+ (Heidelberg-instruments, Germany); 6 h writing time
Post exposure bake	On hot plate: 3 min at 65°C and 3 min at 95 °C
Developer	mrDEV600 (Micro resist technology, Germany) + Isopropanol

After the fabrication of the second layer the wafer was baked on a hot plate for 5 h at 150 °C.

A.2 Default values for image registration with the Correct 3D drift Fiji plugin

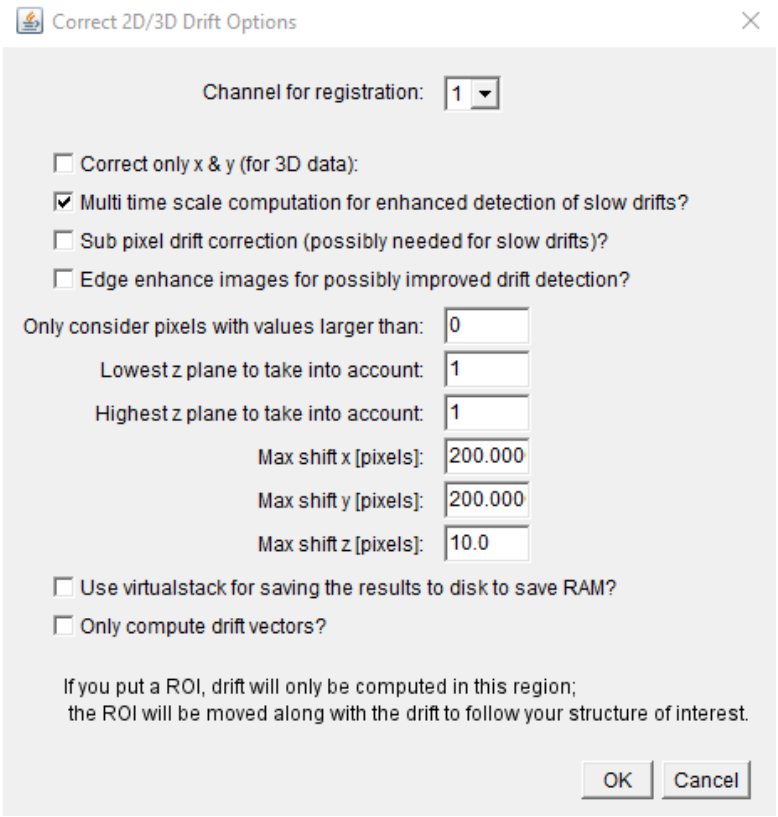


Fig. A.1: Default values for image registration with the Correct 3D drift Fiji plugin. Prior to activating the plugin a ROI was selected. If possible, the markers outside the growth chambers were selected. The code of the *Correct 3D drift* plugin[89] for Fiji [88] has been modified to show this setting by default. This was regularly used to prepare the image sequences for segmentation.

B Master mold designs for soft lithography

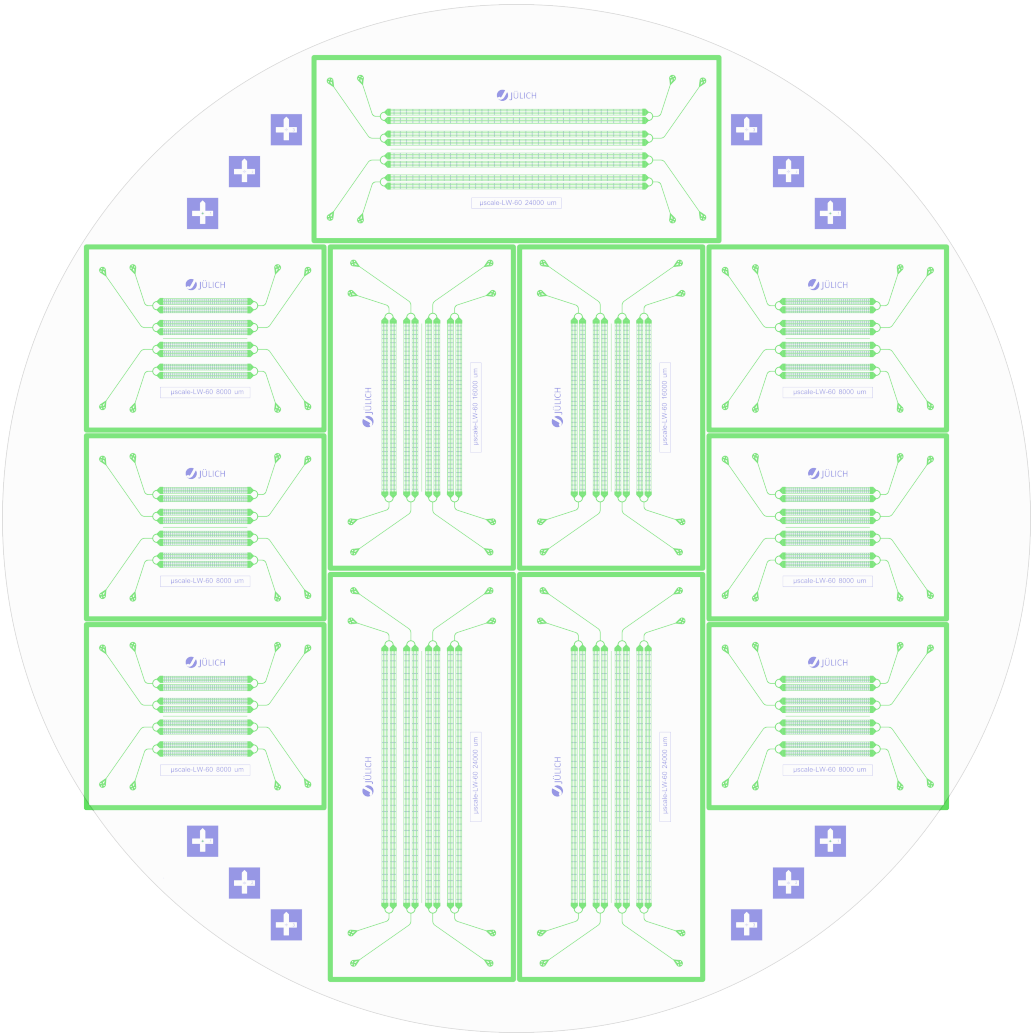


Fig. B.1: Cultivation layout #1. Full cultivation layout #1 on a 4" silicon wafer. The Wafer includes three identical copies of layout i., two copies of layout ii. and six copies of layout iii.. Layer 1 (Green) is ≈ 10 µm high. Layer 2 is ≈ 1.026 µm high.

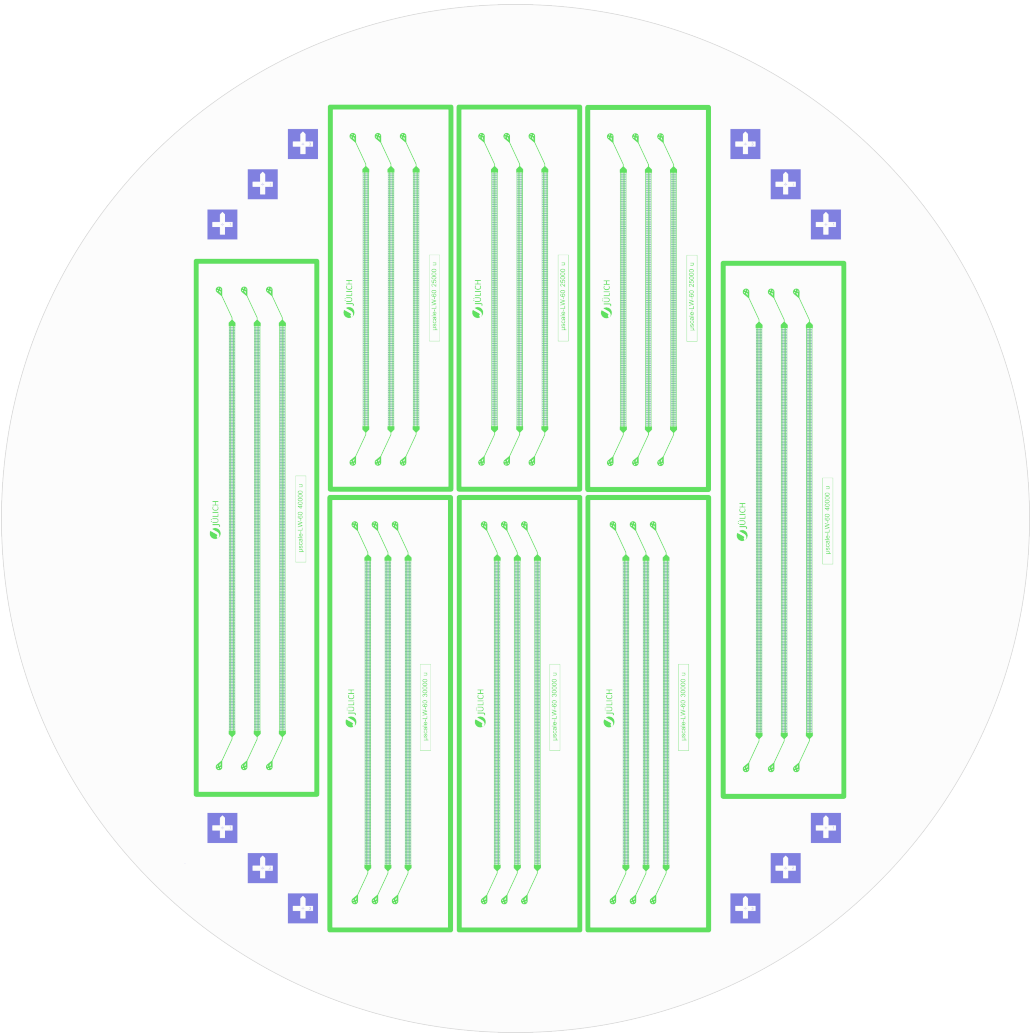


Fig. B.2: Cultivation layout #2. Full cultivation layout #2 on a 4" silicon wafer. The wafer includes three identical copies of layout i., three copies of layout ii. and two copies of layout iii.. Layer 1 (Green) is ≈ 10.97 µm high. Layer 2 (Blue) is ≈ 1.062 µm high.

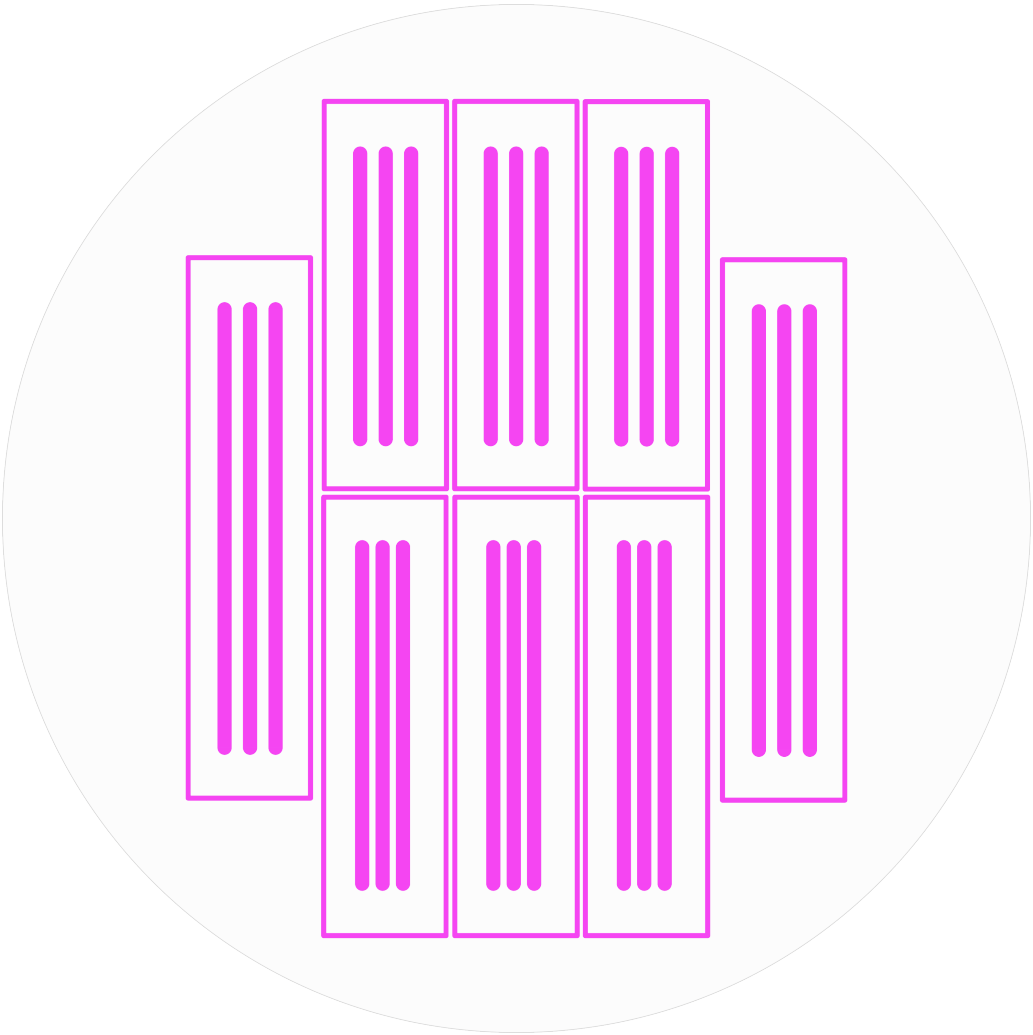


Fig. B.3: CO_2 perfusion channels for cultivation layout #2. The design was produced twice on a 4" silicon wafer.

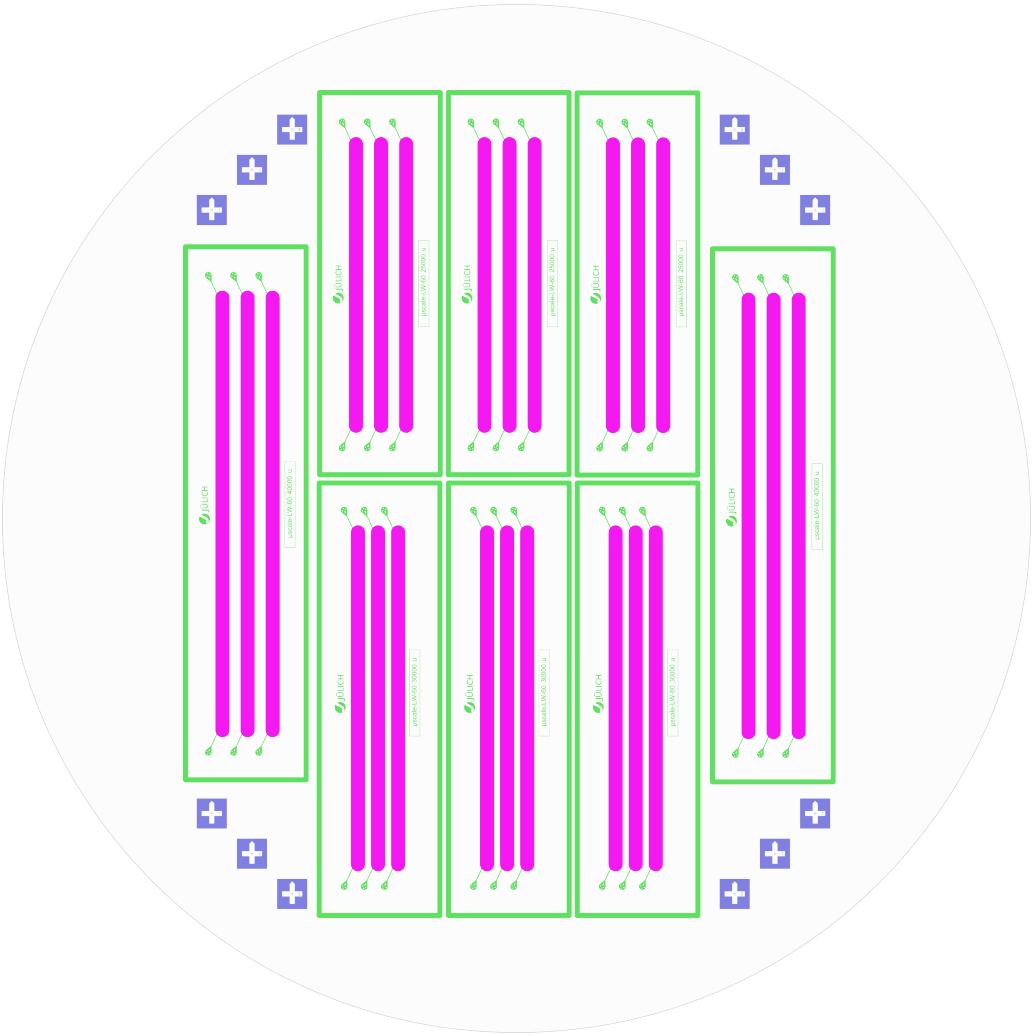


Fig. B.4: Overlay of cultivation layout #2 and CO_2 perfusion channels.

C Technical drawings

C.1 Connection of the STL light engine to the ringlight input used for reference measurements and measurements with the aspheric condenser lenses.

The custom-built components were conceptualized in collaboration with Daniel Klein from the IBG-1 workshop. The drawings created by Daniel Klein are indicated in the figure caption.

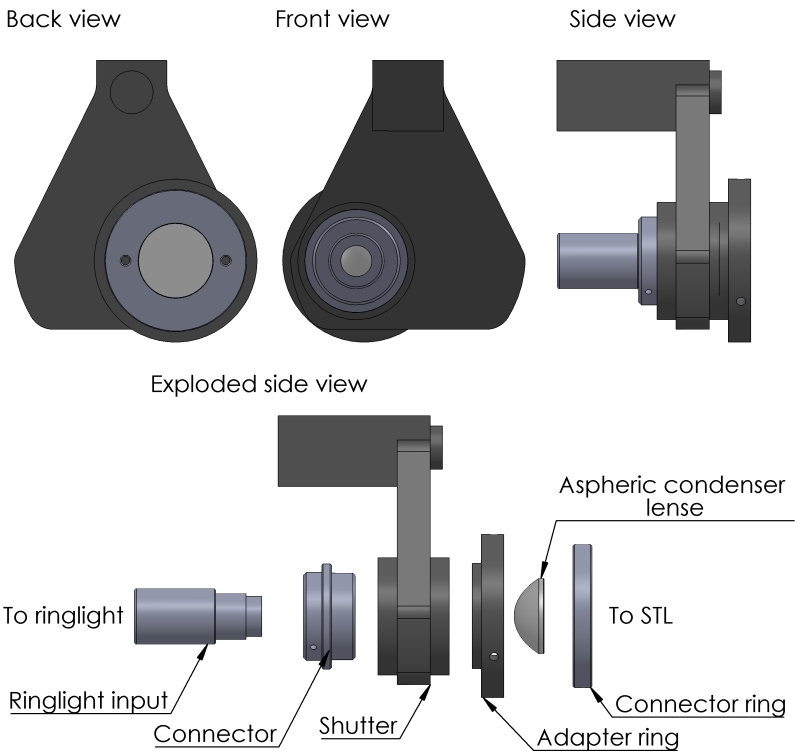


Fig. C.1: Connection between the STL and the ringlight as used for reference measurements and measurements with the aspheric condenser lenses. The connector between the ringlight input and shutter was the same as for the reduced distance approach. The adapter ring was included with the shutter. The connector ring between the shutter and the STL holds the condenser lens. For reference measurements, the lens was omitted.

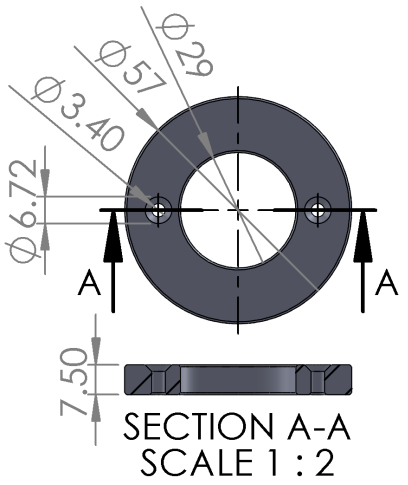


Fig. C.2: Connection ring between STL and shutter. The STL has built-in holes for connecting a commercial C-mount adapter ring. The ring is fixed onto the STL via these holes. Then, the lens can be pushed into the ring. However, this method only works with the 3D-printed ring because its material is soft. For reference measurements, the lens was omitted. All dimension are in mm.

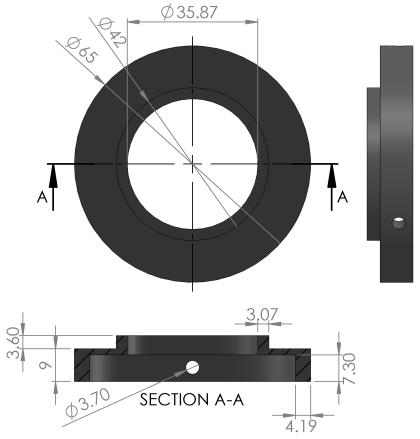


Fig. C.3: Dimensions of the adapter ring between the connection ring and the shutter. The adapter was an accessory for the shutter, and the drawing was created based on manual measurements. The smaller diameter of the adapter has a thread that allows it to be screwed into the inner thread of the shutter. All dimensions are in mm.

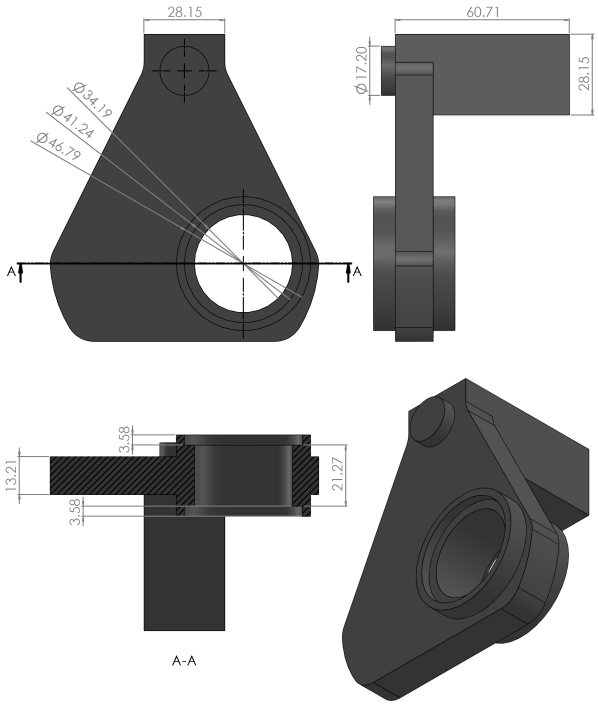


Fig. C.4: Dimensions of the shutter. The drawing was created based on manual measurements of the shutter. The shutter has built-in M42x0.75 inner threads on both sides.

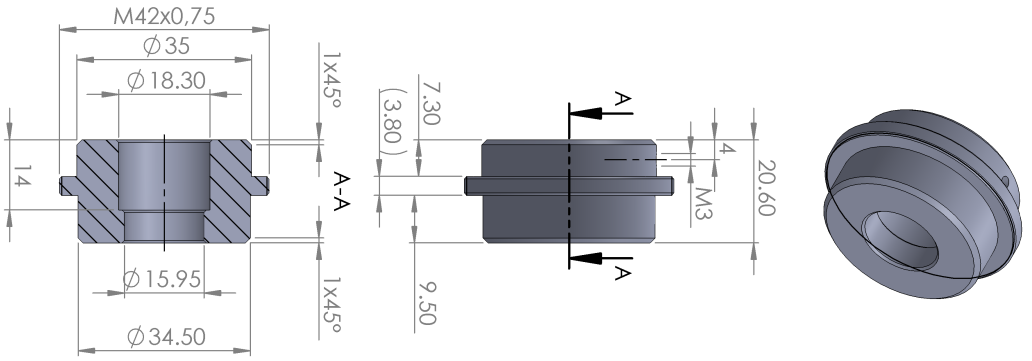


Fig. C.5: Connector between the shutter and the ringlight input. The connector was screwed to the shutter using its built-in inner thread. All dimension are in mm. Drawing by DK.

C.2 Connection of the STL light engine to the ringlight input with reduced distance

This section displays the individual components of the assembled connection, as shown in Fig. 3.2. The connector between the shutter and the ringlight input is the same as in Fig C.5.

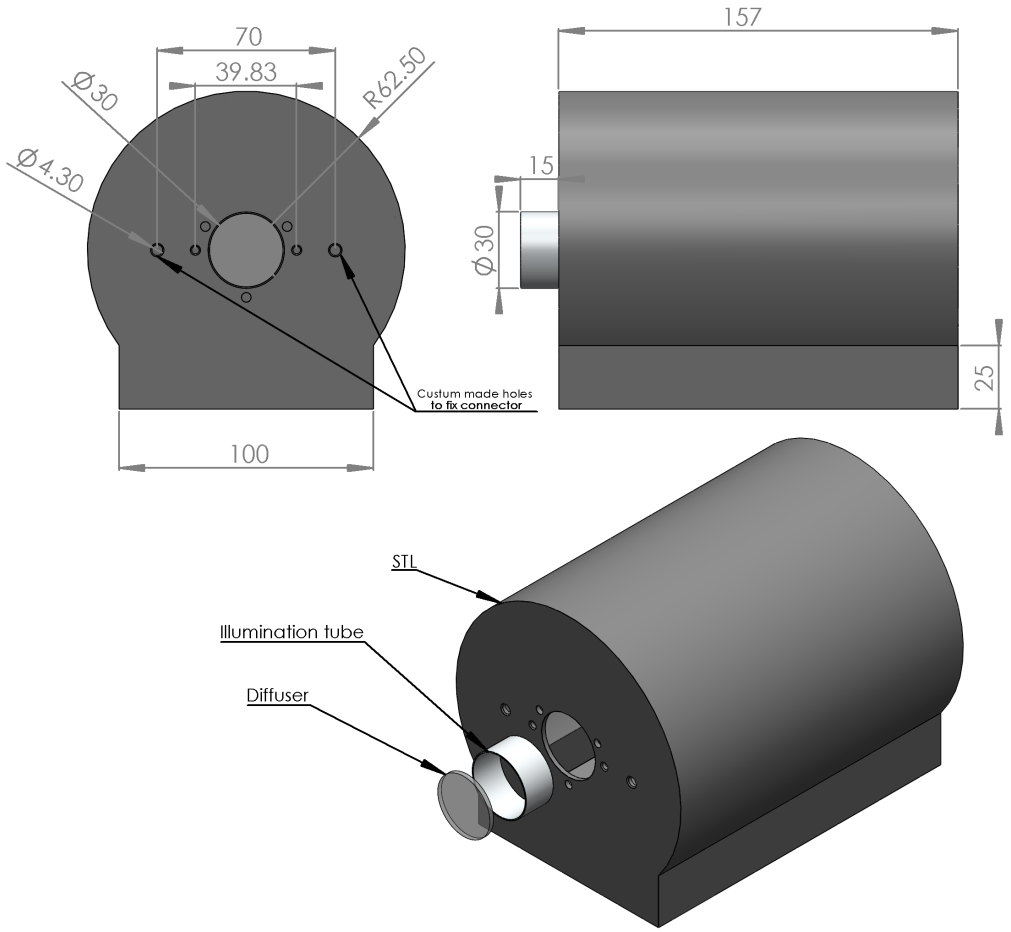


Fig. C.6: Dimensions of the STL light engine. The drawing was created based on manual measurements of the STL. Dimensions off the STL light engine are displayed after reconstruction of the front panel. Two custom holes were drilled into the cover plate to fix the connector. All dimension are in mm.

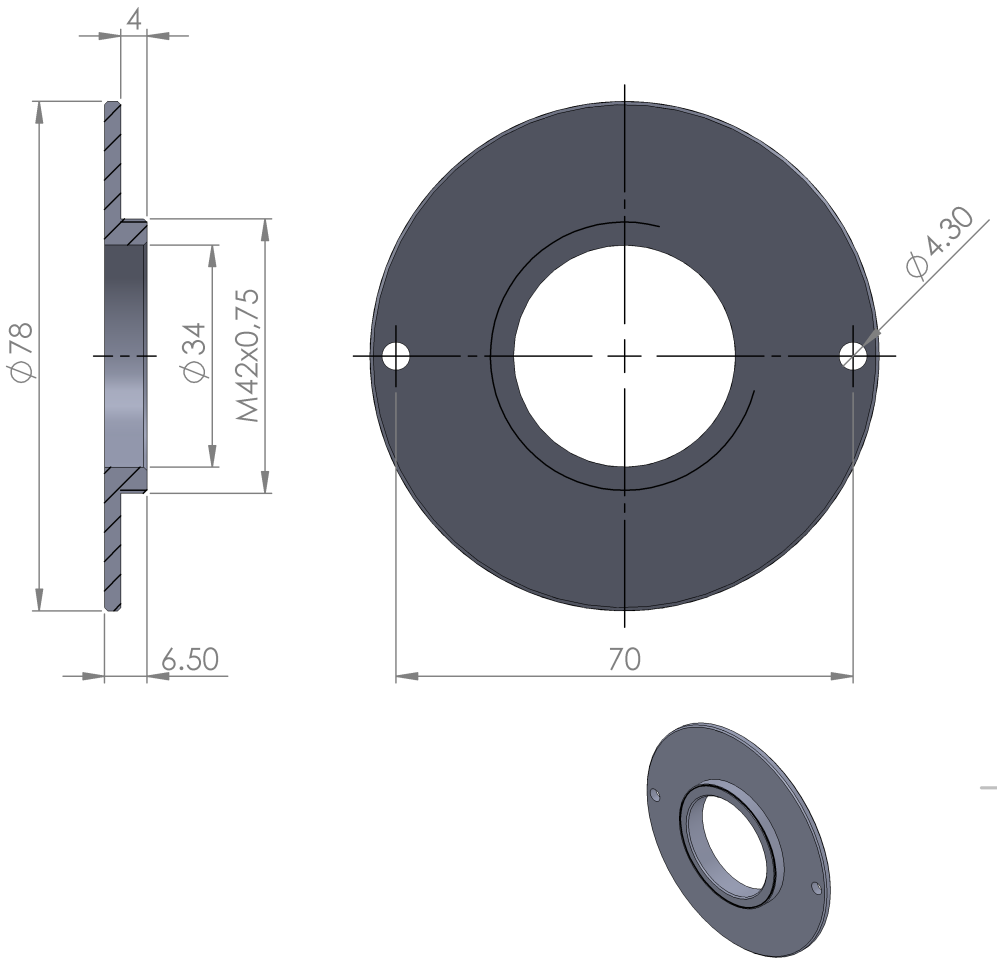


Fig. C.7: Connector between the rebuild STL and the shutter. Holes were drilled in the STL cover plate so that the wider diameter of the connector could be fixed to it. The shutter was then screwed to the connector using its built-in thread. All dimension are in mm. Drawing by DK.

C.3 Comparison of the two approaches to maximize the intensity emitted onto the cultivation plane

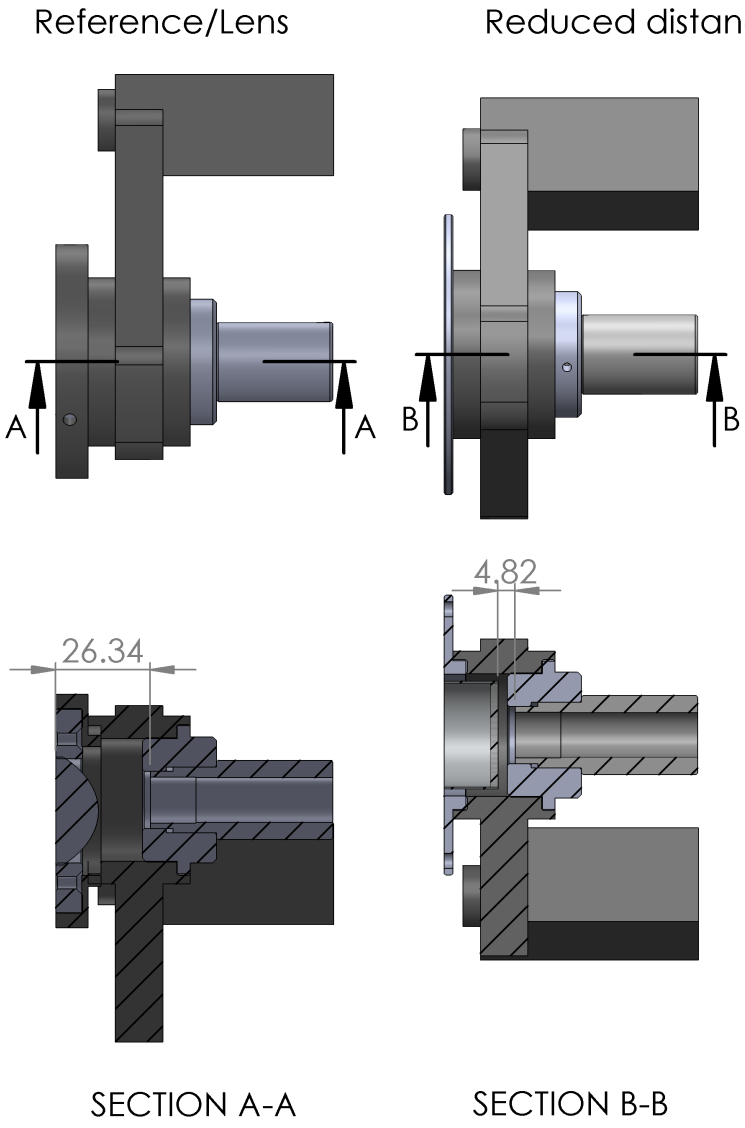


Fig. C.8: Comparison of the two approaches to maximise the intensity emitted onto the cultivation plane. Left is the reference/aspheric condenser lens. Here the distance between lamp output and the STL input was 26.34 mm. For reference measurements the lens was removed. After rebuilding the lamp the distance was reduced to 4.82 mm.

C.4 Fixation of the ringlight around the microscope condenser

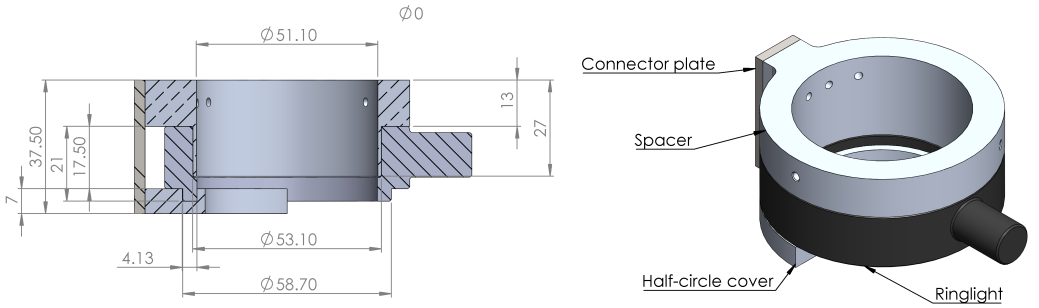


Fig. C.9: Assembled ringlight fixation. All dimension are in mm. Drawing by DK.

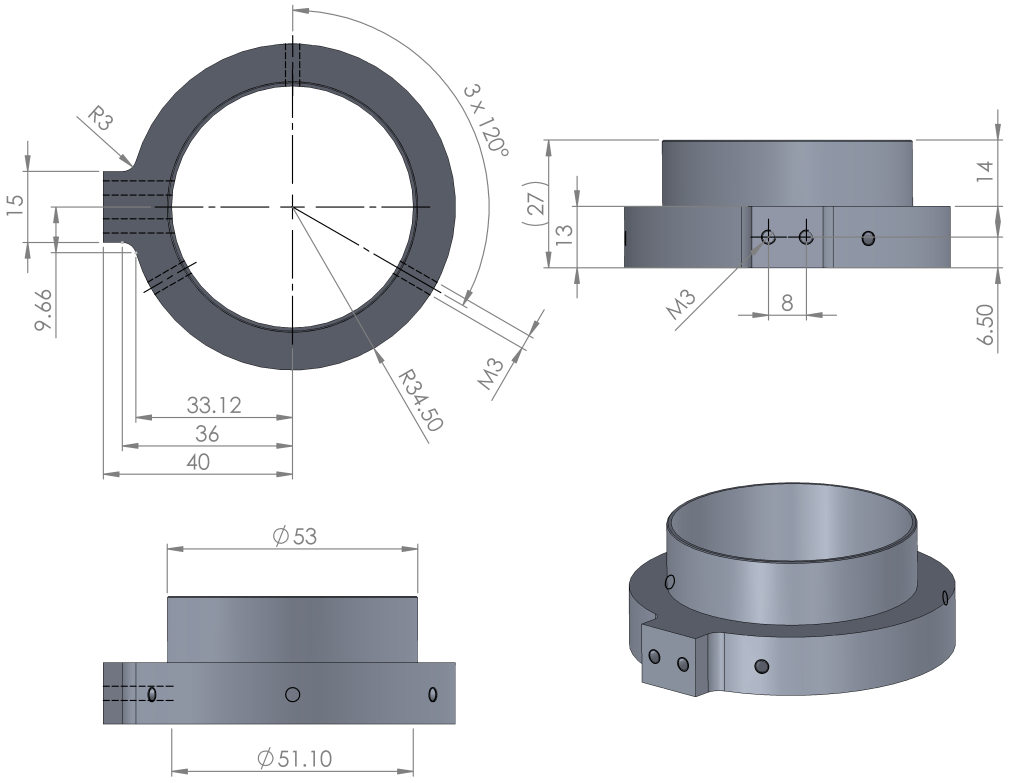


Fig. C.10: Dimensions of the spacer to fix the ringlight around the microscope condenser. All dimension are in mm. Drawing by DK.

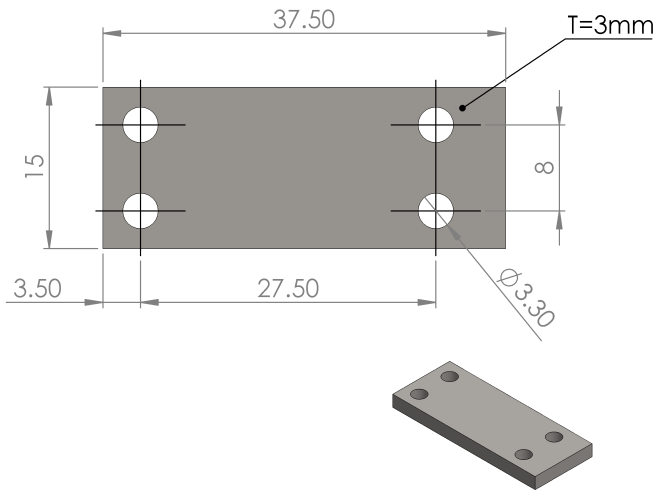


Fig. C.11: Dimensions of the connector plate between the spacer and the half-circle cover. All dimension are in mm. Drawing by DK.

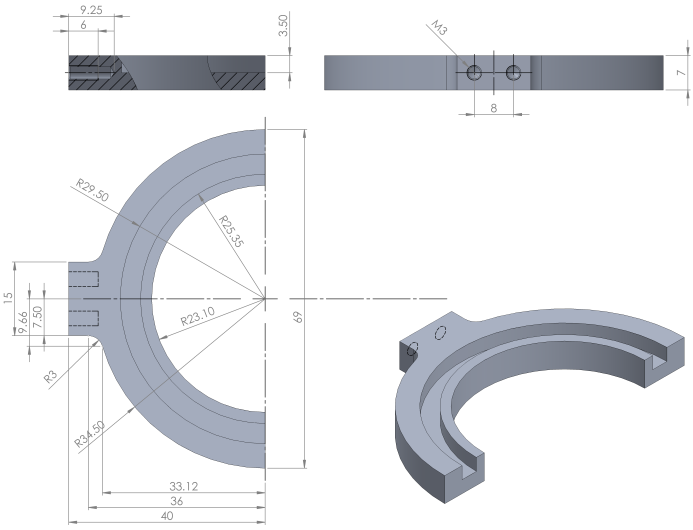


Fig. C.12: Dimension of the Half-circle cover to generate a linear light-intensity gradient. All dimension are in mm. Drawing by DK.

C.5 3D printed master molds for soft lithography

The master molds were based on previously published designs from the group [73]. The files from the cited work were uploaded into SolidWorks and modified.

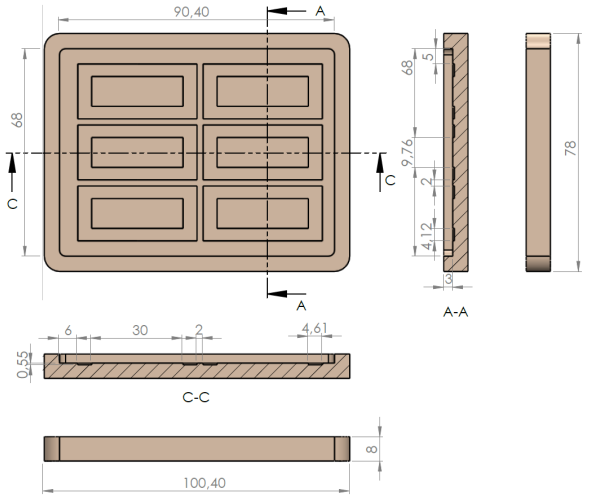


Fig. C.13: Master mold for replication of the CO_2 perfusion chamber. The master mold was produced by 3D printing. All dimensions are in mm.

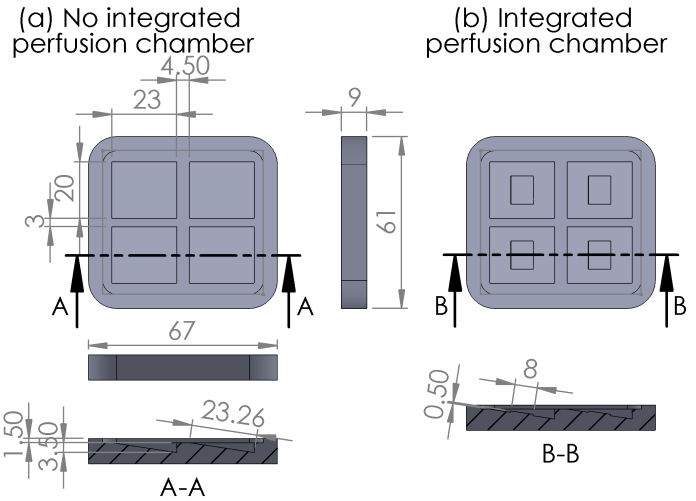


Fig. C.14: Master mold for the tilted chip concept. (a) Without integrated gas perfusion chamber. (b) With integrated gas perfusion chamber. All dimensions are in mm.

C.6 Miscellaneous

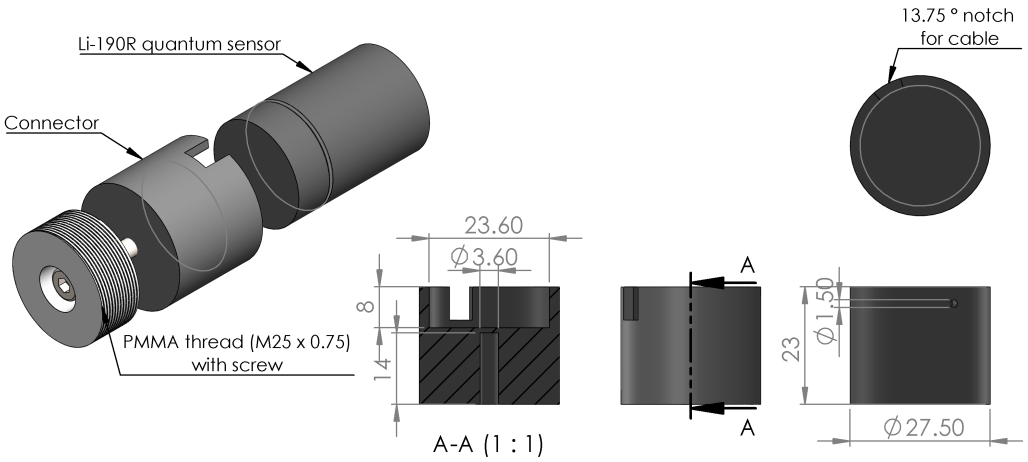


Fig. C.15: Li190R to objective turret connector. The custom designed connector between the Li190R and objective turret of the microscope. All dimension are in mm.

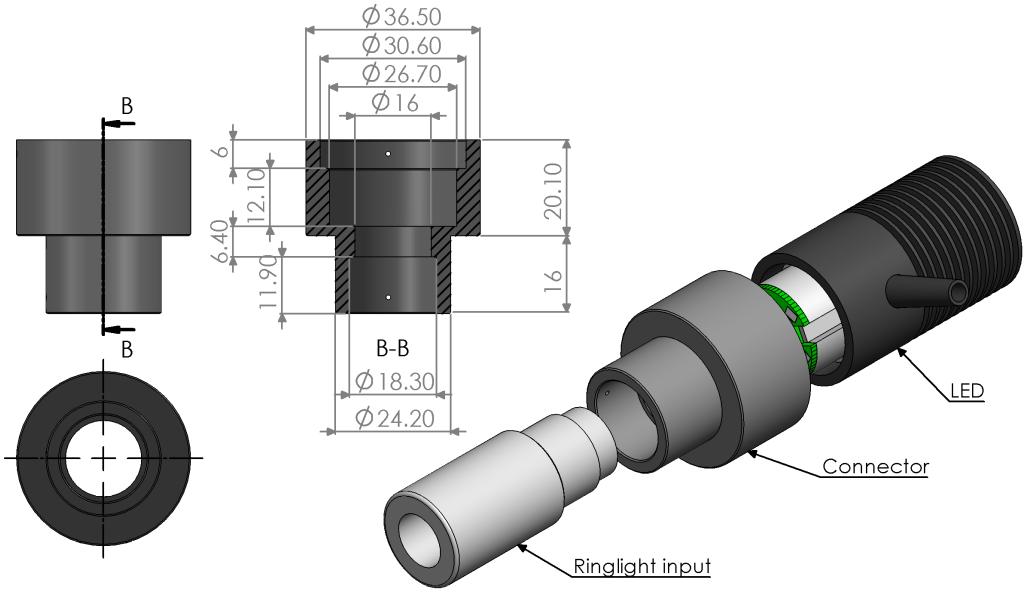


Fig. C.16: Fixed-spectrum LED to ringlight connection. The custom designed connector between the fixed-spectrum LED and the ringlight input. All dimension are in mm. The 3D model of the fixed-spectrum LED was downloaded from the supplier's website and imported into SolidWorks. The supplier also provided a 3D model of the ring light input.

D Supplementary data

D.1 Characterization of the Mounted LED

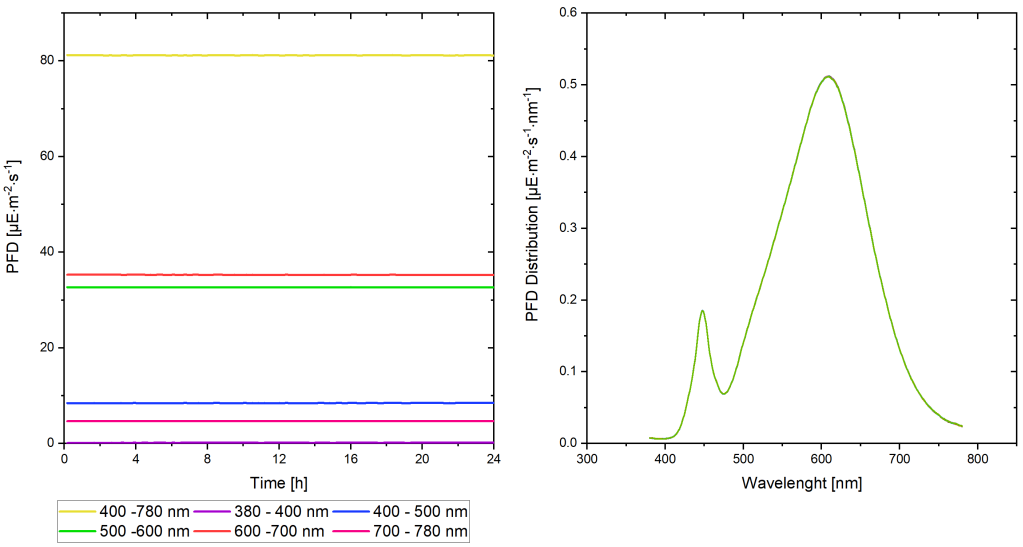


Fig. D.1: Spectrum and spectral stability of the mounted LED. The LED was coupled into the ringlight, which was set to emit approximately 80 $\mu E \cdot m^{-2} \cdot s^{-1}$. The Li180 spectrometer was placed at a vertical distance comparable to the distance between the ringlight and the cultivation plane during phototrophic cultivation (31.3 mm). The PFD was then recorded for 24 hours, and the standard deviation was found to be 0.024 µE·m^{-2}·s^{-1}.

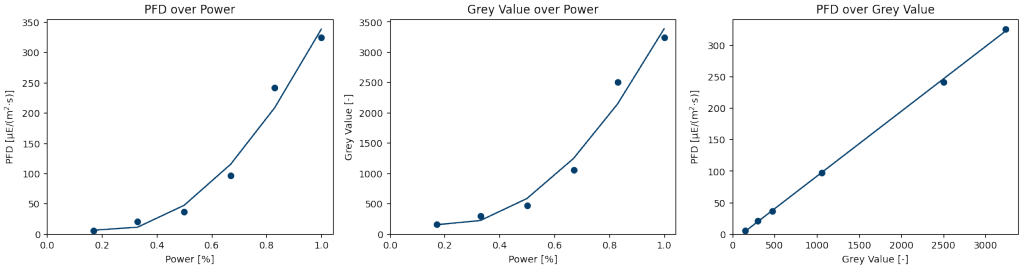


Fig. D.2: Output characteristic of the mounted LED Calibration was performed according to the description in Chapter 5. The calibration revealed the non-linear output characteristic of the mounted LED.

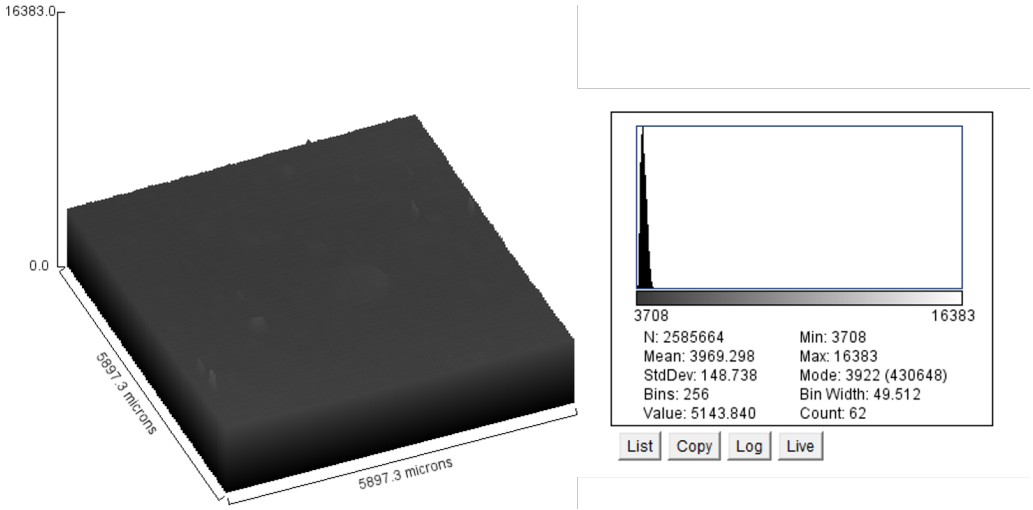


Fig. D.3: Homogeneity of the mounted LED The picture was taken analogously to the description in Chapter 3, except that the image was kept at 16-bit. The pixel value of the 16-bit image deviated by less than 3.75 %. The figure displays screenshots made from the analysis in Fiji.

D.2 Mean Single-cell area across colonies

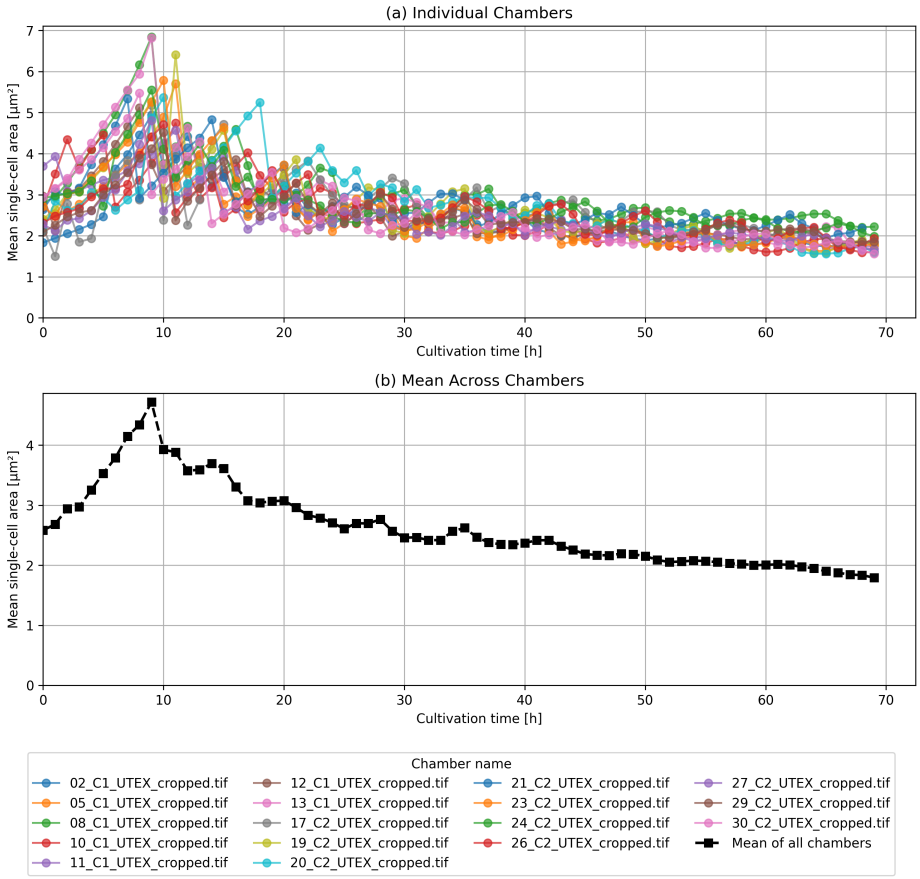


Fig. D.4: Mean single-cell area across growth colonies with a growth array. The data for the experiment at 140 µE·m^{-2}·s^{-1}. is shown. (a) Mean single-cell area from individual growth colonies. (b) Mean single-cell area curve for all chambers.

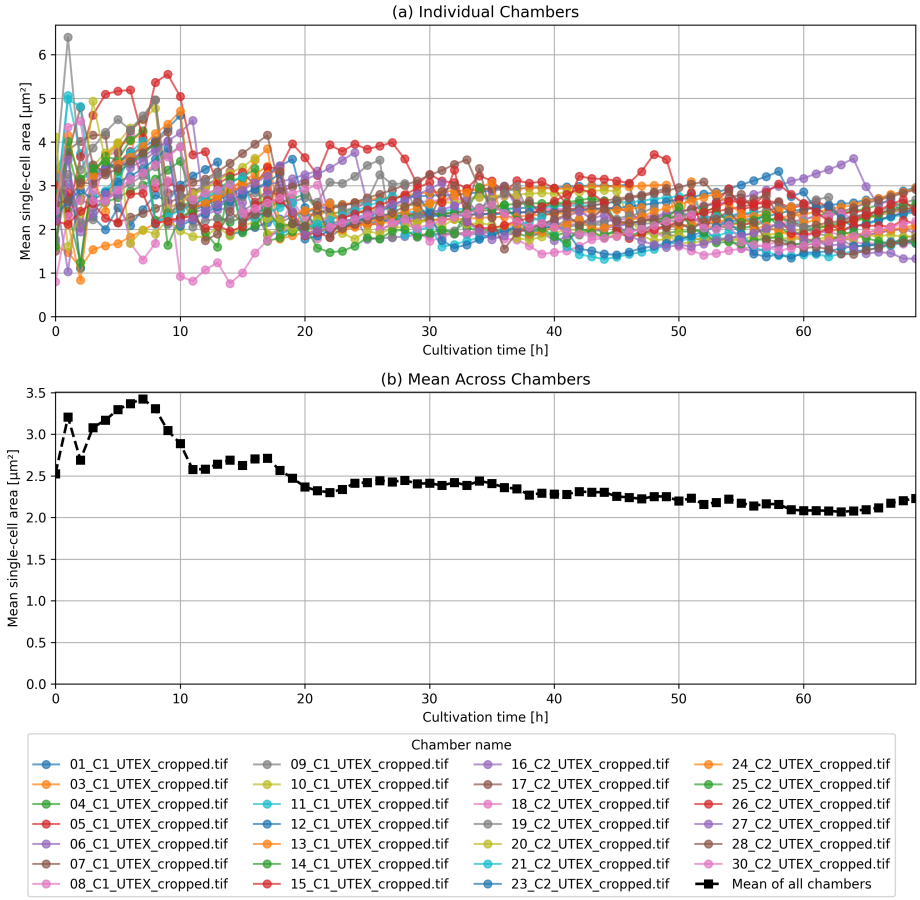


Fig. D.5: Mean single-cell area across growth colonies with a growth array. The data for the experiment at 20 µE·m^{-2}·s^{-1}. is shown. (a) Mean single-cell area from individual growth colonies. (b) Mean single-cell area curve for all chambers.

D.3 Single-cell area distribution analysis

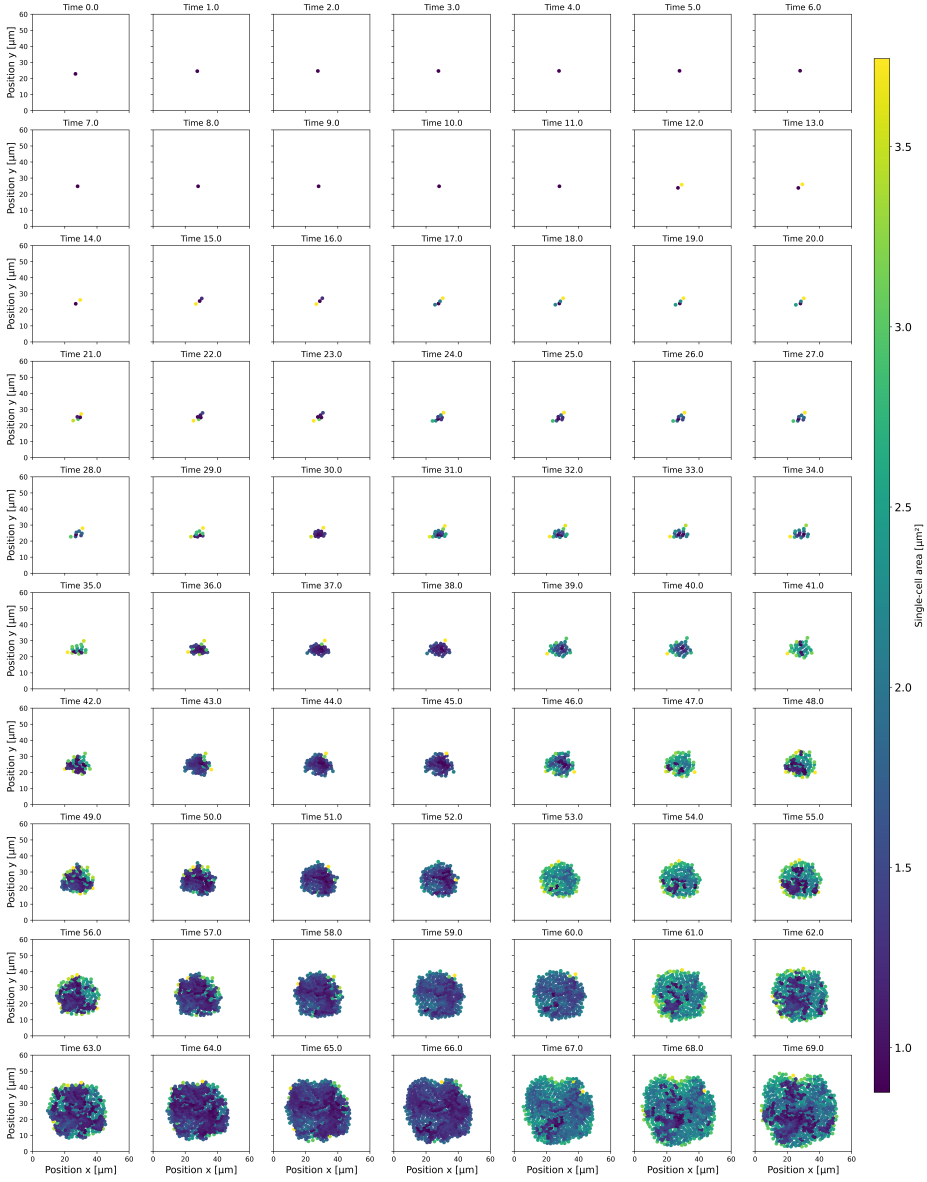


Fig. D.6: Single-cell area distribution for UTEX2973 at 140 µE·m^{-2}·s^{-1}. Each plot represents a frame from a time-lapse microscopy series. Images were taken every hour. Each data point represents the position of a detected cell within the image frame. The area of the respective cell is marked by colour.

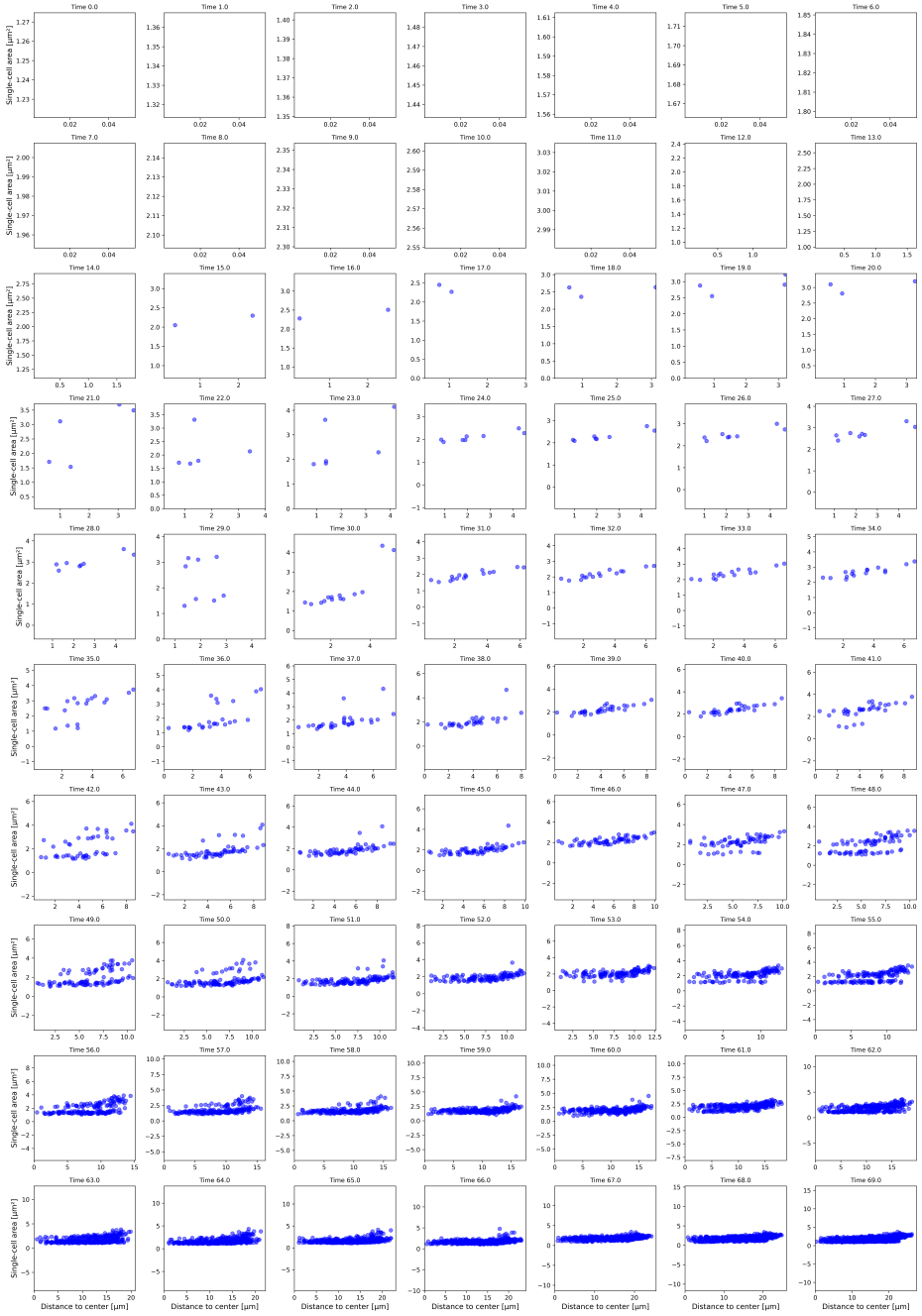


Fig. D.7: Single-cell area over the distance to the colony center for UTEX2973 at 140 µE·m^{-2}·s^{-1}. Each plot shows a frame from a time-lapse microscopy series. Images were taken every hour. The colony center and the distance to the colony center were calculated based on the data from D.7 with Equ. 4.1 and 4.2.



Fig. D.8: Single-cell area distribution for UTEX2973 at 20 µE·m^{-2}·s^{-1}. Each plot represents a frame from a time-lapse microscopy series. Images were taken every hour. Each data point represents the position of a detected cell within the image frame. The area of the respective cell is marked by colour.

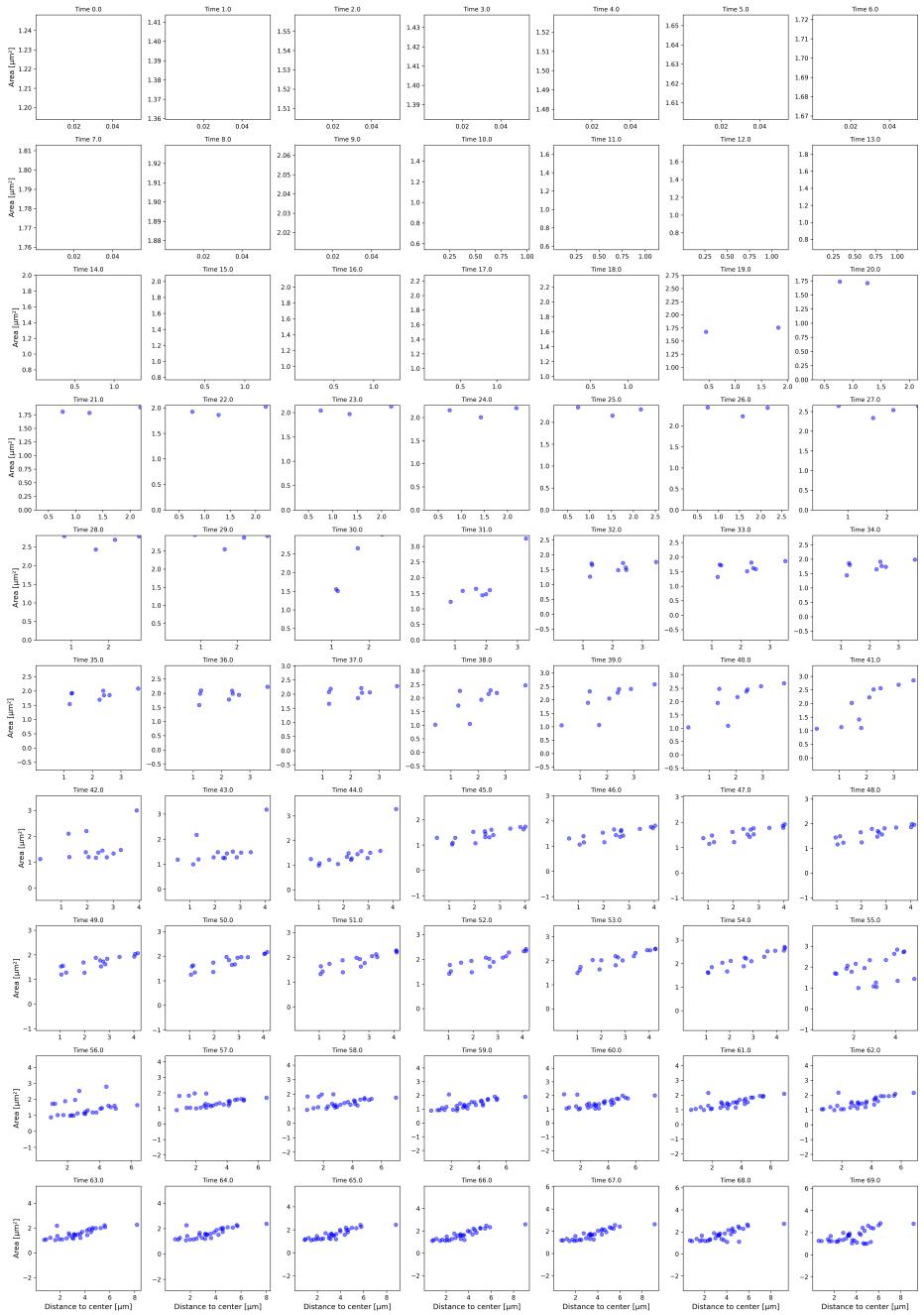


Fig. D.9: Single-cell area over the distance to the colony center for UTEX2973 at 20 µE·m^{-2}·s^{-1}. Each plot shows a frame from a time-lapse microscopy series. Images were taken every hour. The colony center and the distance to the colony center were calculated based on the data from D.9 with Equ. 4.1 and 4.2.

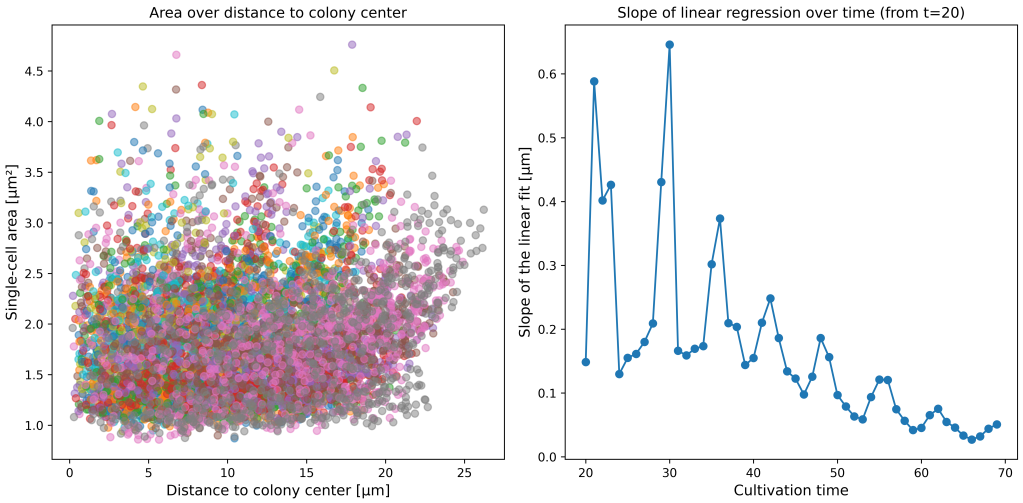


Fig. D.10: Single-cell area over the distance to the colony center for UTEX2973 at 140 µE·m^{-2}·s^{-1}. Left Overlay of all single-cell area plot (Fig. D.7) over distance to colony center. **Right** A linear regression was fitted through each plot in Fig. D.7 and the slope were plotted over the respective cultivation time.

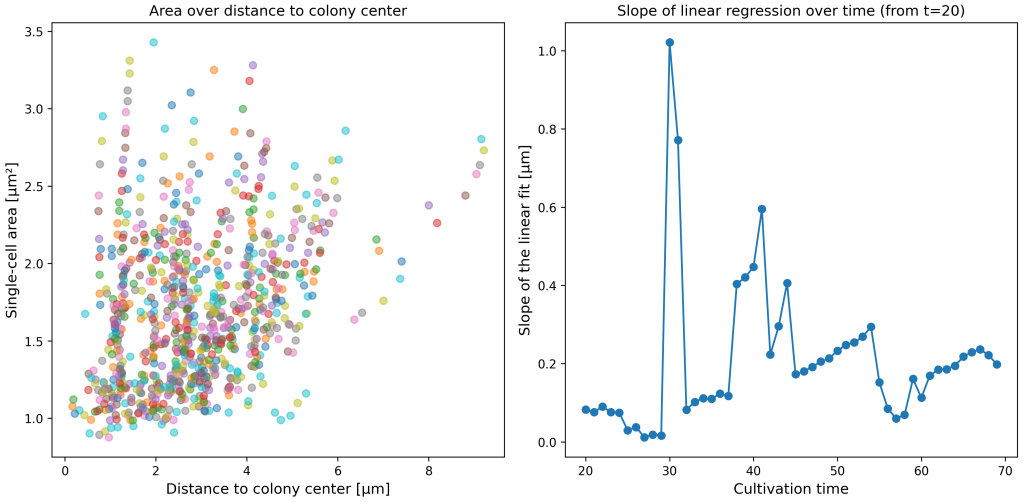


Fig. D.11: Single-cell area over the distance to the colony center for UTEX2973 at 20 µE·m^{-2}·s^{-1}. Left Overlay of the single-cell area over distance to colony center. **Right** Each plot represents a frame from a time-lapse microscopy series. Images were taken every hour. Each data point represents the position of a detected cell within the image frame. The area of the respective cell is marked by colour.

D.4 Single-cell area over light-intensity analysis

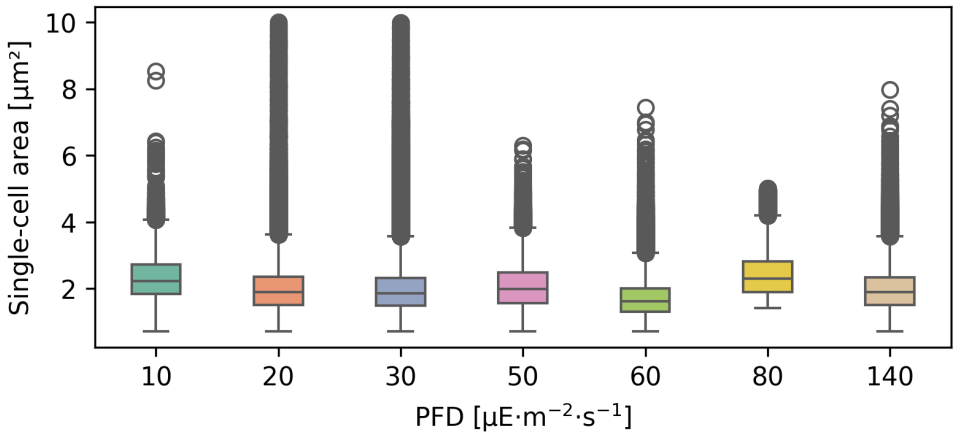


Fig. D.12: Single-cell area over light-intensity for UTEX2973. The single-cell areas from all chambers of a continuously performed experiment were grouped and plotted against the light intensity at which the experiment was performed. The horizontal line in the boxplot shows the mean and the box shows the dataset's quartiles. The whiskers extend to show the remainder of the distribution, excluding points identified as outliers.

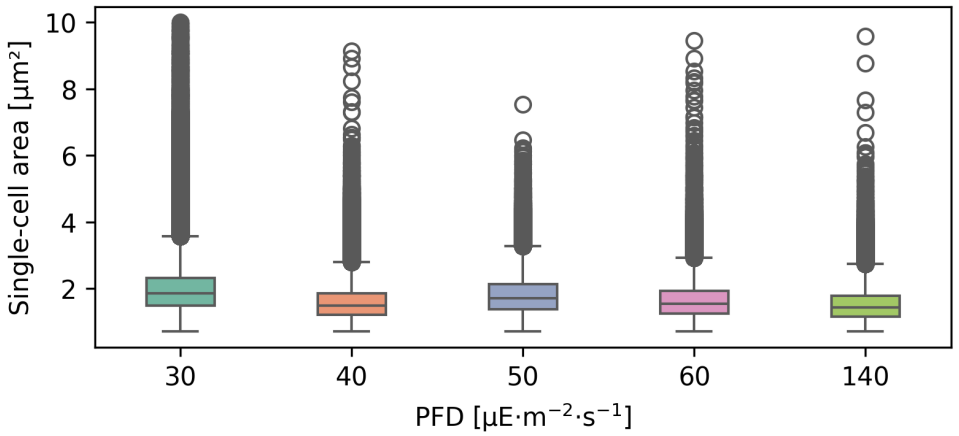


Fig. D.13: Single-cell area over light-intensity for PCC7942 CscB. The single-cell areas from all chambers of a continuously performed experiment were grouped and plotted against the light intensity at which the experiment was performed. The horizontal line in the boxplot shows the mean and the box shows the dataset's quartiles. The whiskers extend to show the remainder of the distribution, excluding points identified as outliers.

D.5 Single-cell traces for the experiment displayed in Fig. 7.5 (b)

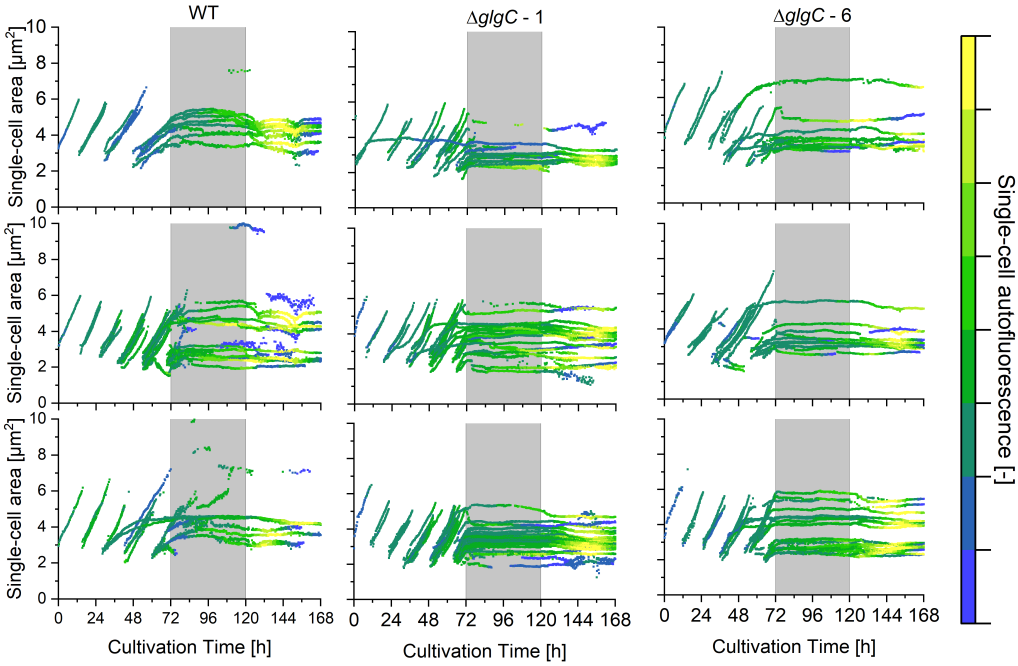


Fig. D.14: Single-cell traces for the experiment displayed in Fig. 7.5 (b) for the WT, the Δ*glgC*-1 and the Δ*glgC*-6 mutant. Each plot contains data from an individual growth chamber. Each data point represents the value measured for a distinct cell within the respective image frame. During the day (white background), the light was set to 30 µE·m^{-2}·s^{-1}, at night (grey background), the light was turned off. The colour of the datapoint indicates the measured single-cell autofluorescence.

D.6 Improved simulation approach

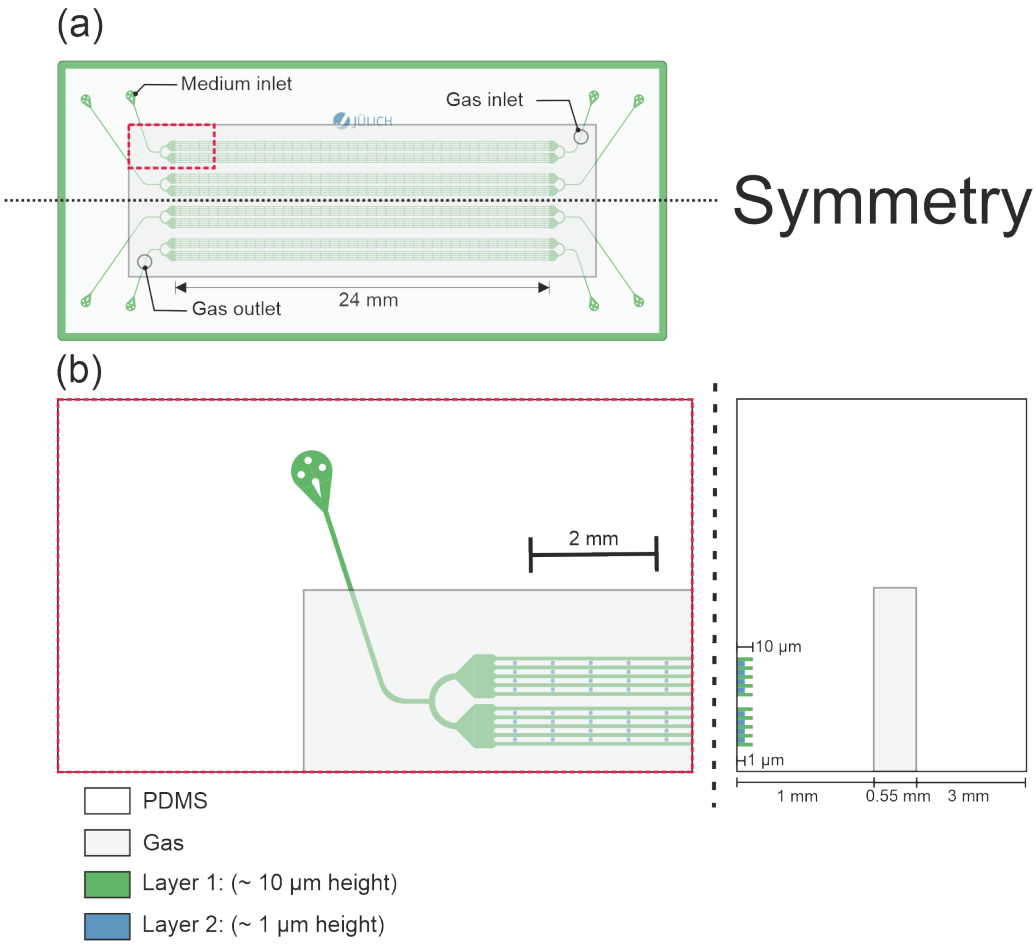


Fig. D.15: Improved simulation approach (a) In order to be able to simulate the more details the approach aims at taking advantage of the symmetry of the layout. (b) Thereby only a small part of the chip needs to be simulated in full detail to make an estimate whether CO_2 in the growth channels is at equilibrium with the CO_2 perfusion chamber.